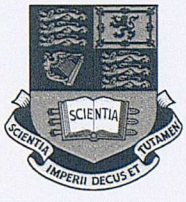
To my Dad and Mum

Composite Cathodes for Intermediate Temperature Solid Oxide Fuel Cells

Gopiraj Sivasundram

A thesis submitted for the degree of Doctor of Philosophy of the

University of London and for the Diploma of Imperial College London



Department of Materials Science and Engineering,
Imperial College,
University of London,
London SW7 2BP

January 2006

Abstract

High temperature solid oxide fuel cell (SOFC) operation causes many serious materials problems; such as degradation of the components, a limited choice of materials, etc. With the drive to lower operating temperatures for the solid oxide fuel cell, several critical components within each cell require further improvement. Arguably, the cathode is the component that requires the greatest improvement. Composite cathodes offer the possibility of developing a high performance electrode for intermediate temperature (500-600°C) SOFC operation. Therefore this project aims at improving the performance of the composite cathode of a SOFC operating between 500-600°C. The target in this project is to reach an area specific resistance (ASR) for the cathode in the order of 0.1 Ωcm^2 at 600°C. To this end the electrochemical properties of $La_{0.6}Sr_{0.4}Co_{0.2}Fe_{0.8}O_{3-\delta}$ (LSCF)/$Ce_{0.8}Gd_{0.2}O_{2-\delta}$ (CGO20-80), $Gd_{0.6}Sr_{0.4}CoO_3$ (GSC)/CGO20-80, $Sm_{0.5}Sr_{0.5}CoO_3$ (SSC)/CGO20-80 composite cathodes on a $Ce_{0.9}Gd_{0.1}O_{2-\delta}$ (CGO10-90) electrolyte have been investigated for use in intermediate temperature SOFC, using an AC impedance spectroscopy. Here the composite cathodes on the CGO10-90 electrolyte are all sintered at 1050°C before testing in AC impedance spectroscopy between 400-700°C. This will allow to co-sinter all the components at one temperature (around 1000°C), which can reduce the processing cost. LSCF/CGO20-80 composite cathode is very dense (around 80 %), hence pore former (carbon) was used to promote porosity in this electrode. The microstructures of the cathodes were examined using a secondary electron microscopy (SEM) and focussed ion beam secondary ion microscopy (FIB-SIMS). The CGO20-80/LSCF/carbon electrode on a clean electrolyte (a cleaned electrolyte was produced by cleaning both the surface of an as sintered electrolyte with a 1200 grid (5-15 micron) silicon carbide paper and then etched by 40 % HF acid for two minutes) and iso-statically pressed had 5 times lower ASR of 2.33 $\Omega.cm^2$ at 503°C, 0.75 $\Omega.cm^2$ at 552°C and 0.29 $\Omega.cm^2$ at 601°C than CGO20-80/LSCF cathode without a pore former. The CGO/GSC cathode on a clean electrolyte and iso-statically pressed had the best ASR of 2.02 $\Omega.cm^2$ at 503.5°C, 0.88 $\Omega.cm^2$ at 553°C and 0.33 $\Omega.cm^2$ at 602°C. Compared to the other two composite cathodes, the CGO20-80/SSC cathode on a clean electrolyte and iso-statically pressed had the best ASR value of 2.02 $\Omega.cm^2$ at 502°C, 0.64 $\Omega.cm^2$ at 551°C and 0.23 $\Omega.cm^2$ at 599°C.

Acknowledgements

I bow my head God Almighty and give thanks for His never failing grace and blessings.

I am truly indebted to my supervisor, Prof. J.A. Kilner, for his invaluable support and guidance through out the course of this work. His patience and encouragement is very much appreciated. This thesis is a tribute to him.

I am very grateful to the 'groupies' for their assistance and support; namely Dr. Naoki, and Dr Edwin Raj without who I could never have completed this work. Naz and manjit (soon to be Dr) for entertaining me for these last three years and also special thanks to Dr. A. Esquirol and Dr. Baron.

I would like to thank Richard Sweeney, Mike Haddon, Bob Rudkin, Nick Royall and Mahmood Ardakani for their help with the experimental work.

Also a very special mention to fellow PhD's and my friends; Amit and Massod who provided much hilarity to the delight of us all. Iman who is truly an inspiration to all PhD students (she will know why!), Naz, the SIMS addict, Manju and I should add Anju too as she was there as much as him; Muthiah. Chris, Ian and Chandra deserve a mention too. I would also like to thank my friend Susie who has spend her valuable time proof-reading my thesis.

I would like to offer my sincere thanks to my family for their immense love, faith in my abilities and constant encouragement, which gave me strength to complete this work successfully.

Finally a big thank you to the EPSRC for their funding of this work.

Table of Contents

Abstract.....i

Acknowledgements.....ii

Table of Contents.....iii

List of Tables.....viii

List of Figures.....ix

Chapter 1 Introduction

1.1 Introduction 1

1.2 History.....1

1.3 Fundamental operation of fuel cell.....2

1.3.1 Types of fuel cells.....5

1.3.1.1 Alkaline fuel cell.....5

1.3.1.2 Proton exchange membrane fuel cell (PEMFC).....6

1.3.1.3 Molten carbonate fuel cell.....6

1.3.1.4 Phosphoric acid fuel cell 7

1.3.1.5 Solid oxide fuel cell (SOFC).....7

1.4 References 9

Chapter 2 Solid Oxide Fuel Cell

2.1 Introduction.....10

2.2 Operating principle of SOFC.....11

2.2.1 Efficiency.....12

2.2.2 Voltage of the cell.....15

2.2.3 Voltage lossed in fuel cells.....16

2.2.3.1 Activation polarization.....16

2.2.3.2Ohmic polarization.....17

2.2.3.3 Concentration polarization.....17

2.2.4 Cell components of SOFC.....17

2.2.4.1 Interconnect.....18

2.2.4.2 Anode.....19

2.2.4.3 Electrolyte.....20

2.2.4.4 Cathode.....21

2.2.4.1.1 Oxygen reduction in a cathode.....22
2.2.4.1.2 Oxygen reduction model in a cathode.....24
2.2.5 SOFC designs.....28
2.2.5.1 Tubular design.....28
2.2.5.2 Planar design.....30
2.2.5.3 Monolithic design.....31
2.2.6 Advantages of SOFC and problems to be solved.....32
2.2.7 Advantages of Intermediate temperature SOFC.....33
2.3 References.....35

Chapter 3 Structure, Defects and Conductivity

3.1 Fluorite structure.....38
3.2 Perovskite structure.....38
3.3 Defect chemistry.....41
3.3.1 Doping effects.....44
3.3.2 Defects in perovskite oxides.....45
3.4 Ionic, electronic and mixed conductivity.....48
3.4.1 Conductivity in perovskite oxides.....49
3.5 References.....51

Chapter 4 Materials Literature Review

4.1 Materials for interconnect.....53
4.2 Materials for Anode.....54
4.3 Materials for electrolyte.....54
4.4 Materials for cathodes.....58
4.4.1 Composite cathode materials.....65
4.4.2 Microstructure and performance of cathode.....69
4.5 Summary.....70
4.6 Objective of the research work.....74
4.7 References.....75

Chapter 5 Experimental Procedure

5.1 Introduction.....80

5.2 Glycine-nitrate Combustion Synthesis.....80
5.3 Composite Powder Preparation.....81
5.4 Sample Preparation.....82
5.4.1 For Dilatometry.....82
5.4.2 For AC Impedance Spectroscopy.....82
5.5 Density Measurements.....83
5.6 Powder Characterisation Techniques.....84
5.6.1 Particle Size Analysis.....84
5.6.2 Dilatometry.....84
5.6.3 X-ray Diffraction.....85
5.6.4 Scanning Electron Microscopy.....87
5.6.5 Focussed Ion Beam Secondary Ion Electron Microscopy.....87
5.6.6 AC Impedance Spectrocopy.....88
5.6.6.1 Introduction.....88
5.6.6.2 Theory.....88
5.6.6.3 Equivalent circuit model.....92
References.....95

Chapter 6 Results and Discussion

6.1 Powder characterisation.....96
6.1.1 Particle Size Measurement.....96
6.1.2 Dilatometry.....97
6.1.3 Electrolyte Characterisation by AC Impedance Spectroscopy.....99
6.2 CGO/LSCF.....102
6.2.1 Powder Characterization.....102
6.2.2 Sintering Studies.....105
6.2.3 Electrochemical Performance.....107
6.2.3.1 CGO/LSCF on an as sintered electrolyte.....107
6.2.3.2 CGO/LSCF on a cleaned electrolyte.....110
6.2.3.3 CGO/LSCF on a cleaned electrolyte and iso-pressed.....115
6.2.4 Microstructural Characterisation.....118
6.2.5 Comparison with the Adler Model.....119
6.3 CGO/LSCF/LSM.....123

6.4 CGO/LSCF/PMMA.....128
6.5 CGO/LSCF/carbon.....129
6.5.1 Powder Characterization.....129
6.5.2 Sintering Studies.....131
6.5.3 Microstructural Studies by SEM.....132
6.5.4 Microstructural Studies by FIM-SIMS.....135
6.5.5 Electrochemical Performance.....137
6.5.5.1 CGO/LSCF/carbon on an as sintered electrolyte.....137
6.5.5.2 CGO/LSCF/carbon on a cleaned electrolyte.....140
6.5.5.3 CGO/LSCF/carbon on a cleaned electrolyte and iso-pressed.....143
6.5.6 Comparison with the Adler Model.....147
6.6 CGO/LSCF/carbon in Water Atmosphere.....150
6.7 CGO/GSC.....154
6.7.1 Powder Characterization.....154
6.7.2 Sintering Studies.....155
6.7.3 Microstructural Studies by SEM.....156
6.7.4 Microstructural Studies by FIM-SIMS.....159
6.7.5 Electrochemical Performance.....161
6.7.5.1 CGO/GSC on an as sintered electrolyte.....162
6.7.5.2 CGO/GSC on a cleaned electrolyte.....165
6.7.5.3 CGO/GSC on a cleaned electrolyte and iso-pressed.....167
6.7.6 Comparison with the Adler Model.....169
6.8 CGO/SSC.....172
6.8.1 Powder Characterization.....172
6.8.2 Sintering Studies.....174
6.8.3 Microstructural Studies by SEM.....174
6.8.4 Microstructural Studies by FIM-SIMS.....177
6.8.5 Electrochemical Performance.....180
6.8.5.1 CGO/SSC on an as sintered electrolyte.....180
6.8.5.2 CGO/SSC on a cleaned electrolyte.....183
6.8.5.3 CGO/SSC on a cleaned electrolyte and iso-pressed.....185

6.8.6 Comparison with the Adler Model.....187
6.9 References.....189

Chapter 7 Summary and Conclusion.....192

Chapter 8 Suggestions for Future Work.....198

List of Tables

Chapter 1

Table 1.1: Principle of fuel cell type [5] p. 8

Chapter 2

Table 2.1:- Westinghouse SOFC: cell components p. 30

Chapter 3

Table 3.1: Defects symbols p. 42

Chapter 6

Table 6.1.1:- Particle size analysis results of the powders p. 96

Table 6.1.2:-Resistivity ρ, capacitance C and conductivity σ for bulk and grain boundary of $Ce_{0.9}Gd_{0.1}O_{2-x}$ calcined at 1400°C p. 100

Table 6.1.3:- ASR values of the composite cathodes at various temperatures p. 115

Table 6.1.4:- ASR values of the composite cathodes at various temperatures p. 146

Table 6.1.5:- ASR of all the CGO20-80/GSC at various temperatures p. 168

Table 6.1.6:- ASR of all the CGO20-80/SSC at various temperatures p. 186

Chapter 7

Table 7.1:- ASR values CGO/LSCF p. 192

Table 7.2:- ASR values CGO/LSCF/C p. 194

Table 7.3:- ASR values CGO/GSC and CGO/SSC p. 196

List of Figures

Chapter 1

Fig 1.1: - Schematic diagram of fuel cell diagram [6] p. 3

Chapter 2

Fig 2.1:- Schematic diagram of chemical reactions in SOFCs [15] p. 12
Fig 2.2: Energy Conversion in Fuel cells p. 13
Fig 2.3: Carnot vs Hydrogen fuel cell p. 14
Fig 2.4: Fuel cell voltage/current characteristics p. 16
Fig 2.5: - Fuel Cell Stack Components [5] p. 18
Fig 2.6 (a) oxygen reduction at the triple phase boundary (electronic conductor) p. 23
Fig 2.6 (b) oxygen reduction through a mixed conductor p. 23
Fig 2.7: Schematic representation of the ALS model [49] p. 25
Fig 2.8:- Tubular design SOFC [17] p. 30
Fig 2.9:- Flat plate design SOFC (exploded view) [16] p. 31
Fig 2.10:- Monolithic design SOFC [5] p. 32

Chapter 3

Fig 3.1: - Fluorite Structure [60] p. 38
Fig 3.2:- The cubic perovskite unit cell [63] p. 39
Fig 3.3:- Perovskite distortion from cubic (left) to Orthorhombic (right) [63] p. 40
Fig 3.4: Schematic representation of (1) Frenkel defect (vacancy-interstitial pair) and (2) *Schottky defect (a pair of cation and anion vacancies) in an ionic crystal.* p. 44
Fig 3.5: Brouwer diagram of partial pressure vs concentration p. 47

Chapter 4

Figure 4.1:- Temperature dependence of electrical conductivity for oxide ion conductors (lower temperature range) [64] p. 56
Figure 4.2: - Total electrical conductivity as a function of oxygen partial pressure p. 57
Figure 4.3: - Total electrical conductivity as a function of oxygen partial pressure p. 58
Figure 4.4:- Log σT versus 1000/T in air for La1-xSrxCo0.2Fe0.8O3 as function of Sr content (mol) [112] p. 62
Figure 4.5:- A.C. impedance spectroscopy of LSCF/CGO/LSCF at 700°C: effect of 7.5 $\mu g/cm_2$ Pd addition to LSCF [119] p. 63
Figure 4.6:- Impedance plot of LSM electrodes (left) and LSM-YSZ electrodes (right) at a) T = 650°C and b) T = 850°C in air [83] p. 66
Figure 4.7:- AC Impedance Spectroscopy spectra of LSCF and Composite electrode on CGO electrolyte at 590°C [139] p. 67

Figure 4.8:- Temperature dependence of the polarization resistance for pure LSCF and various LSCF-GDC cathode composition measured over a temperature range of 500-750°C in air [140] p. 68

Figure 4.9:- Comparison of the area specific resistance for each cathode material on CGO electrolyte p. 73

Chapter 5

Figure 5.1:- Reflection of x-rays from two planes of atoms in a solid p. 86

Figure 5.2:- Schematic of an AC measurement result p. 91

Figure 5.3:- Equivalent circuit to which data fit p. 91

Chapter 6

Fig 6.1.1:- Dilatometry trace for a pure CGO20-80 powder sample p. 98

Fig 6.1.2:- Dilatometry trace for a pure LSCF powder sample p. 98

Fig 6.1.3:- Dilatometry trace for a pure LSM powder sample p. 98

Fig 6.1.4:- Complex impedance spectra of $Ce_{0.9}Gd_{0.1}O_{2-x}$ pellets with silver electrodes p. 99

Figure 6.1.5:- Arrhenius graph of the grain boundary resistivity of CGO10-90 electrolyte p. 101

Figure 6.2.1: X-ray diffraction pattern of $Ce_{0.9}Gd_{0.1}O_{2-x}$ (electrolyte material) using Cu-K_α radiation (λ = 1.5406 Å) p. 103

Figure 6.2.2: X-ray diffraction pattern of $Ce_{0.8}Gd_{0.2}O_{2-x}$ using Cu-K_α radiation (λ = 1.5406 Å) p. 103

Figure 6.2.3: X-ray diffraction pattern of $La_{0.6}Sr_{0.4}Co_{0.2}Fe_{0.8}O_{3-\delta}$ using Cu-K_α radiation (λ = 1.5406 Å) p. 104

Figure 6.2.4: X-ray diffraction pattern of $Ce_{0.8}Gd_{0.2}O_{2-x}/La_{0.6}Sr_{0.4}Co_{0.2}Fe_{0.8}O_{3-\delta}$ composite using Cu-K_α radiation (λ = 1.5406 Å) p. 105

Figure 6.2.5:- Dilatometric traces of 3 CGO/LSCF composite powders p. 106

Figure 6.2.6:- Dilatometric traces of CGO, LSCF and CGO (30 weight %)/LSCF composite powders p. 106

Figure 6.2.7: AC Impedance Spectroscopy spectra of CGO20-80/LSCF Composite cathode on an as sintered CGO10-90 electrolyte at various temperatures p. 108

Figure 6.2.8: Equivalent circuit, LR(CPE(R)) p. 109

Figure 6.2.9: Arrhenius plot of the CGO20-80/LSCF composite cathode on an as sintered CGO10-90 electrolyte p. 110

Figure 6.2.10: AC Impedance Spectroscopy spectra of CGO20-80/LSCF composite cathode on a cleaned CGO10-90 electrolyte at various temperatures p. 111

Figure 6.2.11: Normalized AC Impedance Spectroscopy spectra of CGO20-80/LSCF composite cathode on an as sintered and cleaned CGO10-90 electrolyte at various temperatures p. 112

Figure 6.2.12: Arrhenius plot of the CGO20-80/LSCF composite cathode on cleaned CGO10-90 electrolyte p. 113

Figure 6.2.13: SEM micrographs taken at low and high magnification of an as sintered CGO10-90 electrolyte at 1400°C p. 114

Figure 6.2.14: SEM micrographs taken at low and high magnification of a cleaned CGO10-90 electrolyte p. 114

Figure 6.2.15: AC Impedance Spectroscopy spectra of CGO20-80/LSCF composite cathode on a cleaned CGO electrolyte and iso-statically pressed p. 116

Figure 6.2.16: Arrhenius plot of the CGO20-80/LSCF composite cathode on a cleaned CGO10-90 electrolyte and iso-statically pressed p. 117

Figure 6.2.17:- SEM micrograph of CGO-LSCF sintered at 1050°C. Top surface p. 118

Figure 6.2.18:- SEM micrograph of CGO-LSCF sintered at 1050°C. Fractured surface p. 118

Figure 6.2.19:- Arrhenius plot of the oxygen tracer diffusion coefficients and surface exchange coefficients for the CGO/LSCF samples exchanged around 880 mbar and 200 mbar [11] p. 119

Figure 6.2.20: Comparison of the measured impedance and that predicted by Adler's model p. 121

Fig 6.3.1:- Dilatometry trace of CGO20-80/LSCF/LSM p. 124

Fig 6.3.2:- AC Impedance Spectroscopy spectra of CGO20-80/LSCF/LSM on CGO10-90 electrolyte calcined at 1050°C in air p. 125

Fig 6.3.3:- Arrhenius plot of the CGO20-80/LSCF/LSM composite cathode on an as sintered CGO10-90 electrolyte p. 126

Fig 6.3.4:- SEM micrograph of CGO-LSCF-LSM sintered at 1050°C. Top surface. p. 127

Fig 6.3.5:- SEM micrograph of CGO-LSCF-LSM sintered at 1050°C. Fractured surface. p. 127

Fig 6.4.1:- SEM micrograph of CGO-LSCF-PMMA sintered at 1050°C. Top surface p. 128

Fig 6.4.2:- SEM micrograph of CGO-LSCF-PMMA sintered at 1050°C. Top surface p. 128

Figure 6.5.1:- Carbon and PVB burn-out profile [23] p. 129

Figure 6.5.2: X-ray diffraction pattern of $Ce_{0.8}Gd_{0.2}O_{2x}/La_{0.6}Sr_{0.4}Co_{0.2}Fe_{0.8}O_{3\delta}$/carbon composite before sintering using Cu-K_α radiation (λ = 1.5406 Å) p. 130

Figure 6.5.3: X-ray diffraction pattern of $Ce_{0.8}Gd_{0.2}O_{2-x}/La_{0.6}Sr_{0.4}Co_{0.2}Fe_{0.8}O_{3-\delta}$/carbon composite after sintering using Cu-K_α radiation (λ = 1.5406 Å) p. 130

Fig 6.5.4: - Dilatometry trace for a composite CGO/LSCF/carbon sample p. 132

Fig 6.5.5:- SEM micrograph of CGO-LSCF-carbon sintered at 900°C p. 133

Fig 6.5.6:- SEM micrograph of CGO-LSCF-carbon sintered at 1050°C p. 133

Fig 6.5.7:- SEM micrograph of CGO-LSCF-carbon sintered at 1050°C. Iso-pressed p. 133

Figure 6.5.8:- SEM micrograph of the cross-section of CGO-LSCF-Carbon onto a CGO electrolyte, iso-statically pressed and sintered at 1050°C p. 134

Figure 6.5.9:- (A) Focus ion beam image (FIB) of the surface of a CGO20-80/LSCF composite cathode sintered at 1050°C. (B) Focus ion beam image (FIB) of the top view of an ion-milled crater on the surface of the cathode (30kev Ga^+ primary bombardment) p. 135

Figure 6.5.10:- Focused ion beam image (FIB) of an ion-milled crater after tilting at 30° ((30kev Ga+ primary bombardment) p. 136

Figure 6.5.11: AC Impedance Spectroscopy spectra of CGO20-80/LSCF/carbon composite cathode on an as sintered CGO10-90 electrolyte at various temperatures p. 138

Figure 6.5.12: Equivalent circuit model for the responses in Figure 6.511 p. 139

Figure 6.5.13: Normalized AC Impedance Spectroscopy spectra of CGO20-80/LSCF-carbon composite cathode on an as sintered electrolyte at various temperatures p. 139

Figure 6.5.14: Arrhenius plot of the CGO20-80/LSCF/carbon composite cathode on an as sintered CGO10-90 electrolyte p. 140

Figure 6.5.15: AC Impedance Spectroscopy spectra of CGO20-80/LSCF/carbon composite cathode on a cleaned CGO10-90 electrolyte at various temperatures p. 142

Figure 6.5.16: Arrhenius plot of the CGO20-80/LSCF/carbon composite cathode on a cleaned CGO10-90 electrolyte p. 143

Figure 6.5.17: AC Impedance Spectroscopy spectra of CGO20-80/LSCF/carbon composite cathode on a cleaned CGO electrolyte and iso-statically pressed p. 144

Figure 6.5.18: Normalized AC Impedance spectroscopy spectra of CGO/LSCF-carbon p. 145

Figure 6.5.19:- Arrhenius plot of the CGO20-80/LSCF/carbon composite cathode on a cleaned CGO10-90 electrolyte and iso-statically pressed p. 146

Figure 6.5.20:-Comparison of the ASR values of - from the present study and values reported in the literature p. 147

Figure 6.5.21: Comparison of the measured impedance and that predicted by Adler's model p. 149

Figure 6.6.1:- AC Impedance Spectroscopy spectra of CGO20-80/LSCF/carbon composite cathode in dry and wet conditions at various temperatures p. 151

Figure 6.6.2:- Normalized plot of the AC impedance spectra of CGO-LSCF/carbon in dry and wet conditions p. 152

Figure 6.6.3:- AC Impedance Spectroscopy spectra of CGO20-80/LSCF/carbon composite cathode in dry and wet conditions at various temperatures p. 153

Figure 6.7.1: X-ray diffraction pattern of $Gd_{0.6}Sr_{0.4}CoO_{3-\delta}$ using Cu-K_α radiation (λ = 1.5406 Å) p. 154

Figure 6.7.2: X-ray diffraction pattern of $Ce_{0.8}Gd_{0.2}O_{2-\delta}/Gd_{0.6}Sr_{0.4}CoO_{3-\delta}$ composite using Cu-K_α radiation (λ = 1.5406 Å) p. 155

Figure 6.7.3: Dilatometry trace for a composite CGO/GSC p. 156

Fig 6.7.4:- SEM micrograph of CGO-GSC sintered at 1050°C p. 157

Fig 6.7.5:- SEM micrograph of CGO-GSC sintered at 1050°C. Iso-pressed p. 157

Figure 6.7.6:- SEM micrograph of the cross-section of CGO-GSC onto a CGO electrolyte, sintered at 1050°C p. 158

Figure 6.7.7:- SEM micrograph of the cross-section of CGO-GSC onto a CGO electrolyte, iso-statically pressed and sintered at 1050°C p. 158

Figure 6.7.8:- (A) Focused ion beam image (FIB) of the surface of a CGO20-80/GSC composite cathode sintered at 1050°C. (B) Focused ion beam image (FIB) of the top view of an ion-milled crater on the surface of the cathode (30kev Ga^+ primary bombardment) p. 159

Figure 6.7.9:- Focused ion beam image (FIB) of an ion-milled crater after tilting at 30° ((30kev Ga+ primary bombardment) p. 160

Figure 6.7.10:- Temperature dependence of the polarization resistance for various CGO-GSC cathode compositions measured over a temperature range of 400-650°C p. 161

Figure 6.7.11: AC Impedance Spectroscopy spectra of CGO20-80/GSC composite cathode on an as sintered CGO10-90 electrolyte at various temperatures p. 163

Figure 6.7.12:Equivalent circuit model p. 163

Figure 6.7.13: Normalized AC Impedance Spectroscopy spectra of CGO20-80/GSC composite cathode on an as sintered electrolyte at various temperatures p. 164

Figure 6.7.14: Arrhenius plot of the CGO20-80/GSC composite cathode on an as sintered CGO10-90 electrolyte p. 165

Figure 6.7.15: AC Impedance Spectroscopy spectra of CGO20-80/GSC composite cathode on a cleaned CGO10-90 electrolyte at various temperatures p. 166

Figure 6.7.16: Arrhenius plot of the CGO20-80/GSC composite cathode on a cleaned CGO10-90 electrolyte p. 167

Figure 6.7.17: AC Impedance Spectroscopy spectra of CGO20-80/GSC composite cathode on a cleaned CGO electrolyte and iso-statically pressed p. 169

Figure 6.7.18: Arrhenius plot of the CGO20-80/GSC composite cathode on a cleaned CGO10-90 electrolyte and iso-statically pressed p. 169

Figure 6.7.19: Comparison of the measured impedance and that predicted by Adler's model p. 171

Figure 6.8.1: X-ray diffraction pattern of $Sm_{0.5}Sr_{0.5}CoO_{3-\delta}$ using Cu-K_α radiation (λ = 1.5406 Å) p. 173

Figure 6.8.2: X-ray diffraction pattern of $Ce_{0.8}Gd_{0.2}O_{2-\delta}/Sm_{0.5}Sr_{0.5}CoO_{3-\delta}$ composite using Cu-K_α radiation (λ = 1.5406 Å) p. 173

Figure 6.8.3: Dilatometry trace for a composite CGO/SSC p. 174

Figure 6.8.4:- SEM micrograph of CGO-SSC sintered at 900°C p. 175

Figure 6.8.5:- SEM micrograph of CGO-SSC sintered at 1050°C p. 175

Figure 6.8.6:- SEM micrograph of CGO-SSC sintered at 1050°C. Iso-pressed p. 176

Figure 6.8.7:- SEM micrograph of the cross-section of CGO-SSC onto a CGO electrolyte, iso-statically pressed and sintered at 1050°C p. 177

Figure 6.8.8:- (A) Focused ion beam image (FIB) of the surface of a CGO20-80/SSC composite cathode sintered at 1050°C. (B) Focused ion beam image (FIB) of the top view of an ion-milled crater on the surface of the cathode (30kev Ga^+ primary bombardment) p. 178

Figure 6.8.9:- Focused ion beam image (FIB) of an ion-milled crater after tilting at 30° ((30kev Ga+ primary bombardment) p. 179

Figure 6.8.10: AC Impedance Spectroscopy spectra of CGO20-80/SSC composite cathode on an as sintered CGO10-90 electrolyte at various temperatures p. 181

Figure 6.8.11: Equivalent circuit model p. 181

Figure 6.8.12: Normalized AC Impedance Spectroscopy spectra of CGO20-80/SSC on an as sintered CGO10-90 electrolyte at various temperatures p. 182

Figure 6.8.13: Arrhenius plot of the CGO20-80/SSC composite cathode on an as sintered CGO10-90 electrolyte p. 182

Figure 6.8.14: AC Impedance Spectroscopy spectra of CGO20-80/SSC composite cathode on a cleaned CGO10-90 electrolyte at various temperatures p. 184

Figure 6.8.15: Arrhenius plot of the CGO20-80/SSC composite cathode on a cleaned CGO10-90 electrolyte p. 184

Figure 6.8.16: AC Impedance Spectroscopy spectra of CGO20-80/SSC composite cathode on a cleaned CGO electrolyte and iso-statically pressed p. 186

Figure 6.8.17: Arrhenius plot of the CGO20-80/SSC composite cathode on a cleaned CGO10-90 electrolyte and iso-statically pressed p. 187

Figure 6.8.18: Comparison of the measured impedance and that predicted by Adler's model p. 188

Figure 7.1:- Arrhenius plot of CGO/LSCF, CGO/LSCF/C, CGO/GSC and CGO/SSC composite cathodes p. 197

Chapter 1 – Introduction

1.1 Introduction

Public perception towards energy conservation and reduction of pollution has radically changed in the last 25 years. The energy crisis of the 1970's caused a considerable increase in fuel cost. There have been rather pessimistic predictions showing that during the first half of the next century there will be a progressive shortfall between the energy produced by the conventional sources and the demand for electricity **[1].** Therefore the demand for energy services worldwide is likely to substantially increase over the next two decades. There are growing concerns over global environmental issues such as increasing CO_2 emissions and their contribution to the greenhouse effect, increasing NO_x and SO_x emissions and the damage caused by acid rain. In addition, safety concerns have led to the environmental opposition to the expansion of hydroelectric schemes and the use of nuclear energy. All of these factors are hastening the search for clean, efficient, modular power generation systems, which can be sited close to the consumer and operated on a variety of fuels. Recent international summits dedicated to the global regulations of CO_2 emissions show that an understanding of these global problems has reached a wider audience. Consequently, any energy conversion systems promising increased efficiency of fuel utilisation and reduction of CO_x and NO_x emissions have attracted a lot of attention. The automobile industry is also changing, primarily due to a tightening of the legislation concerning emissions from cars. In particular, the new legislation that requires 10% of the vehicles sold in the state of California to be Zero emitting by 2003 **[2]**, is encouraging the major auto manufacturers to develop electrically powered vehicles. Therefore, it is not surprising that there is a renewed interest in electrochemical devices for energy conversion and storage, and in particular fuel cells. Fuel cells could potentially be used to replace conventional power equipment in many cases. The main applications are likely to be in stationary power generation, transportation, and battery replacement.

1.2 History

The origin of the fuel cell dates back to 1839 when Sir William Grove first described its principle and demonstrated a fuel cell at room temperature using a liquid electrolyte **[3]**. His fuel cell used a dilute sulphuric acid electrolyte, a hydrogen anode and an oxygen cathode and operated at room temperature. At that time no conventional batteries were

yet available and so four fuel cells were connected in series and were applied to the electrolysis of water to produce electricity. Ludwig Mond and Charles Langer first created the term "fuel cell" in 1889. They attempted to build a working fuel cell using air and industrial coal gas. From 1889 until the early twentieth century many people tried to develop fuel cells that could convert coal or carbon to electricity directly. These attempts failed because not enough was known about materials or electricity. It was not until Walther Nernst discovered the solid oxide electrolyte in 1899 that the ceramic fuel cell could be conceived. Nernst suggested that zirconium oxide, stabilised with yttrium oxide (now known as yttria stabilised zirconia) could be used as a glowing filament in lamps. This idea was taken up, but while the filaments were alight, electrolysis took place – in a process that was the reverse of fuel cell operation. In 1935 walter Schottky followed this up and suggested that the yttria-stabilised zirconia (YSZ) could be used as a solid fuel cell electrolyte, replacing liquid electrolytes such as sulphuric acid.

In 1932, Francis Bacon developed the first successful fuel cell **[4]**, with a hydrogen-oxygen cell using a less corrosive alkaline electrolytes and nickel electrodes – inexpensive and alternatives to the catalysts used by Mond and Langer. Due to a substantial number of technical hurdles, it was not until 1959 that Bacon and company first demonstrated a practical five-kilowatt fuel cell system. Harry Karl Ihrig presented his now-famous 20-horsepower fuel cell-powered tractor that same year.

Also in the sixties, a little known federal agency called National Aeronautics and Space Administration (NASA) began to build a compact electricity generator for use on space missions. After discharging nuclear reactors as too risky, batteries as too heavy and short lived, NASA turned to fuel cells. NASA soon came to fund hundreds of research contracts involving fuel cell technology. Fuel cells now have a proven role in the space program, after supplying electricity to several space missions.

Since the late eighties, the major efforts are presently focused on developing fuel cells for uses from stationary power units to portable and mobile applications, i.e. mobile phones, laptop and electric vehicles.

1.3 Fundamental Operation of the Fuel Cell

A fuel cell is an electrochemical device that converts the chemical energy in fuels (such as hydrogen, methane, butane or even petrol and diesel) directly into electrical energy by exploiting the natural tendency of oxygen and hydrogen to react. In principle, a fuel

cell operates like a battery, however it differs from a typical battery in several aspects. The battery is an energy storage device, that is, the maximum energy that is available is determined by the amount of chemical reactant stored in the battery itself. Thus, the battery will cease to produce electrical energy when the chemical reactants are consumed (i.e. discharged). In a secondary battery, the reactants are regenerated by recharging, which involves putting energy into the battery from an external source. The fuel cell, on the other hand, is an energy conversion device, which theoretically has the capability of producing electrical energy in the form of electricity and heat by electrochemical combination of the fuel with an oxidant for as long as the fuel and oxygen is supplied to the cell. So unlike a battery, a fuel cell does not run down or require recharging.

A fuel cell is composed of two porous electrodes: an anode (negative electrode) and a cathode (positive electrode) separated by an ionically conductive dense electrolyte, which prevents gas transport and is impervious to the fuel and oxidant **[5]** (Figure 1.1). The fuel is oxidised on an anode and electrons are released into the external circuit, oxidant is fed to the cathode where it is reduced and electrons are accepted from the external circuit. The electron flow through the external circuit produces DC electricity. The role of the electrolyte is to conduct either anions (e.g. O^{2-}, CO_3^{2-}) from the cathode to the anode or cation (e.g. H^+) from the anode to the cathode. The anode, cathode and the electrolyte in fuel cells forms the basic unit of power called the single cell. Many single cells are electrically connected by an interconnect to produce a stack and by connecting several of these stacks (in series or parallel) power ranging from few hundred watts to megawatts can be generated.

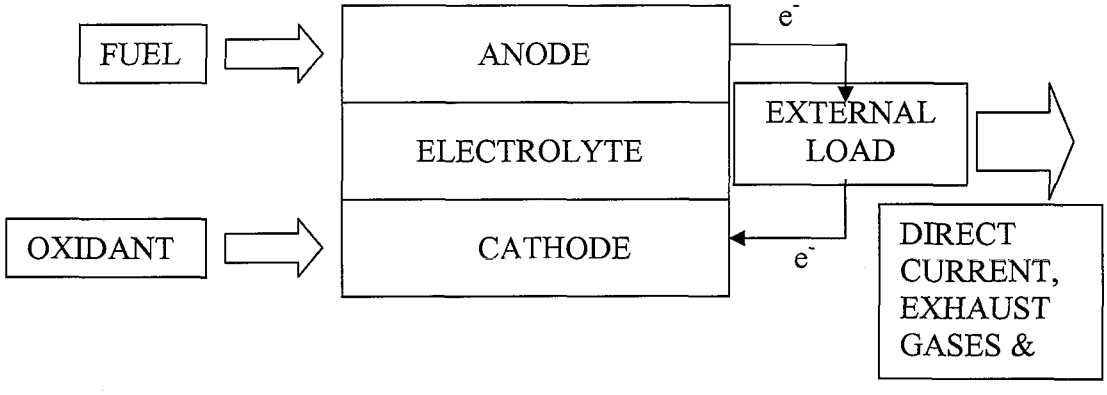


Figure 1.1: - Schematic diagram of fuel cell diagram **[6]**

Fuel cells have many advantages compared to conventional electric power generation systems, such as **[5]**:

- *High conversion efficiency*: As the chemical energy of the reagents is directly converted to electrical energy without the intermediate thermal energy, the efficiency of fuel does not depend on the Carnot limitation. Fuel (when hydrogen is used as a fuel)-to-electricity conversion efficiency is predicted to be around 45-60%, which is relatively independent of size **[7]**.
- *Environmental compatibility*: Emissions of key pollutants from fuel cells are several orders of magnitude lower than those produced by conventional power generators. Conventionally, electricity is generated by the combustion of fossil fuel with air at high temperatures, which produce CO, CO_2, SO_2, $(NO)_x$ causing greenhouse effect, acid rain, atmospheric pollution etc. Unlike the combustion process, fuel cells operate at extremely high efficiencies. This reduces carbon dioxide emissions and other emissions, which in turn should help in reducing global warming.
- Fuel cells are mechanically more reliable since they have no moving parts. Noise and vibration are virtually absent.
- *Modularity*: Fuel cell size can be easily increased or decreased, since the efficiency of a fuel cell is relatively independent of size. The construction of a fuel cell stack is essentially modular and it can be upgraded by connecting individual fuel cells in series and/or parallel as power demand grows. Moreover, in case of stack failure, the replacement of only a few individual cells is required.
- *Sitting flexibility*: Because fuel cells can be made in a variety of sizes, they can be placed at different locations with minimum sitting restrictions.
- *Multifuel capability*: Certain types of fuel cells have multifuel capability.
- Portable and consume less surface area per unit power produced.
- Fuel cell stacks can be connected in parallel with batteries, enabling fuel cells to operate as based-load generators, under varying load conditions.
- Appreciable amount of useful exhaust heat, thus fuel cells are well adapted for CHP operation

But these fuel cells do have their disadvantages too:

- Highly expensive due to exotic materials, and complicated design and assembly

- Highly sensitive to fuel contamination. Mandatory additional expense for procurement and maintenance of effective filters and cleaners
- Skilled personal needed for maintenance and overhaul
- Fuel cell technology has an unproven record, though cost-effective and reliable materials/technologies are under research and development for commercial power generation applications.

1.3.1 Type of Fuel cells

There are five main types of fuel cells. The most common are shown below. Each type uses different materials and operates at a different temperature. These Fuel cells are based on the type of electrolyte used and are summarised in Table 1.1.

1.3.1.1 Alkaline fuel cell

The alkaline fuel cell is operated between the temperatures of 60 and 250°C; the electrolyte in this fuel cell is concentrated (85 wt%) potassium hydroxide (KOH) for high temperature (~ 523 K), or less concentrated (35-50 wt%) KOH for lower temperature (< 393 K) operation. A wide range of electrocatalysts can be used (e.g. Ni, Ag, noble metals, spinels and metal oxides). The hydroxyl ions are the conducting species from the cathode to the anode through the electrolyte. Carbon monoxide (CO) is a poison and carbon dioxide (CO_2) will react with the KOH to form K_2CO_3 **[8 and 9]**, thus altering the electrolyte. So the fuel supply must be completely free from CO_2 and the fuel must be pure hydrogen. This low temperature fuel cell was developed by NASA and used extensively in the Apollo manned missions program during the years 1968 to 1988 **[10]**.

Electrochemical Equation

Anode: $H_2 + 2(OH)^- \rightarrow 2H_2O + 2e^-$
Cathode: $\frac{1}{2} O_2 + H_2O + 2e^- \rightarrow 2(OH)^-$
Cell: $H_2 + \frac{1}{2} O_2 \rightarrow H_2O$

1.3.1.2 Proton Exchange Membrane Fuel Cell (PEMFC)

Also known as Polymer Electrolyte Membrane Fuel Cell consists a solid, hydrated sheet of a sulphonated fluropolymer (Nafion) membranes as an electrolyte (which is a proton conducting membrane) sandwiched between two platinum catalysed porous carbon electrodes. Nafion is a fluorocarbon polymer backbone with attached sulfonic acid

groups. PEMFC's operate between 80°C and 100°C. This low temperature fuel cell is mainly used in vehicle applications **[11]** and space applications **[12 and 13]**. The only liquid in this fuel cell is water, hence this type of fuel cell offers the following advantages: (i) corrosion problems are minimal, (ii) CO_2 tolerance, (iii) simple fabrication, (iv) high power density and long life time (v) ability to operate with hydrogen and reformed fuels. The key barriers for commercial applications are (i) the electrode made of platinum are sensitive to carbon monoxide poisoning (ii) cost (iii) non-availability of cheap hydrogen fuel from renewable sources.

Electrochemical Equation

Anode: $H_2 \rightarrow 2H^+ + 2e^-$
Cathode: $\frac{1}{2} O_2 + 2H^+ + 2e^- \rightarrow H_2O$
Cell: $H_2 + \frac{1}{2}O_2 \rightarrow H_2O$

1.3.1.3 Molten Carbonate Fuel Cell (MCFC)

The electrolyte for the MCFC is usually a combination of alkali carbonates (e.g. 62:38 mol% Li_2CO_3 (lithium carbonate)/K_2CO_3 (potassium carbonate)). These types of fuel cells belong to the class of high operating temperature fuel cells as they operate at 600-700°C. The MCFC consists of two porous electrodes separated by this molten carbonate electrolyte, which serves to conduct carbonate ions (CO_3^{2-}) from the cathode (Ni oxide) to the anode (Ni). The electrolyte is very corrosive and consequently high-grade construction materials must be used. The major advantage of MCFC is that it yields high-grade surplus heat as by-product, which can be used profitably by a suitable bottoming cycle. Another striking feature of MCFC is that it can handle fuels rich in hydrogen and not necessarily free from carbonaceous gases. It can also be possible to reform internally the natural fuels inside the MCFC. The main difficulty associated with MCFC is the management of carbon dioxide resulted as product from the anode.

Electrochemical Equation

Anode: $H_2 + CO_3^{2-} \rightarrow H_2O + CO_2 + 2e^-$
Cathode: $\frac{1}{2} O_2 + CO_2 + 2e^- \rightarrow CO_3^{2-}$
Cell: $H_2 + \frac{1}{2} O_2 + CO_2 \rightarrow H_2O + CO_2$

1.3.1.4 Phosphoric acid Fuel Cell (PAFC)

Phosphoric acid fuel cells operate using a 100% concentrated phosphoric acid (H_3PO_4), which operates at 150-200°C. Platinum is required as a catalyst and platinum alloys for the construction of the electrodes. The matrix material used to retain the phosphoric acid is silicon carbide (SiC). At low temperatures, phosphoric acid is a poor ionic conductor and the carbon monoxide poisoning will degrade the performance of the pt-based anode electrocatalyst. The relative stability of concentrated phosphoric acid is high compared to other common acids; consequently the PAFC is capable of operating at elevated temperatures. The cell has advantage in that fuel based on coal gas or natural gas can be used without the danger of poisoning the electrolyte, but CO has to be converted/removed to avoid platinum poisoning.

Electrochemical Equation

Anode: $H_2 \rightarrow 2H^+ + 2e^-$
Cathode: $\frac{1}{2} O_2 + 2H^+ + 2e^- \rightarrow H_2O$
Cell: $H_2 + \frac{1}{2} O_2 \rightarrow H_2O$

1.3.1.5 Solid Oxide Fuel Cell (SOFC)

Solid oxide fuel cell is a high temperature fuel cell for power generation. The SOFC is an all solid-state energy conversion unit that uses an ionic conducting ceramic oxide electrolyte. These fuel cells operate between 500-1000°C.

The next chapter reviews the science and technology associated with solid oxide fuel cells since this thesis is concerned with this type of fuel cell.

Electrochemical Equation

Anode: $H_2 + O^{2-} \rightarrow H_2O + 2e^-$
Cathode: $\frac{1}{2} O_2 + 2e^- \rightarrow O^{2-}$
Cell: $H_2 + \frac{1}{2} O_2 \rightarrow H_2O$

Type of fuel cell	Typical components: electrolyte(E), anode(A), cathode(C)	Operating temperature, °C	Fuel requirements	Application
Alkaline Fuel Cell (AFC)	E: Concentrated KOH A: Ni compounds C: Rainey Ni	60 - 120	H_2 (pure), NH_3, C_2H_4	space applications
Proton Exchange Membrane Fuel Cell (PEM)	E: Hydrated organic polymer A: Pt based C: Pt based	20 - 120	H_2 (free of CO)	Transportation, small scale combined heat and power (CHP) generation
Phosphoric Acid Fuel Cell (PAFC)	E: Concentrated H_3PO_4 in supporting matrix A: Pt based C: Pt based	160 - 220	H_2 (free of CO, H_2S)	Large scale CHP generation
Molten Carbonate Fuel cell (MCFC)	E: Molten Li/Na/K carbonates in a lithium aluminate support A: Ni/ plus few percent of Cr_2O_3 and Al_2O_3 C: NiO	600 - 650	H_2 (free of CO, H_2S)	Stationary CHP generation
Solid Oxide Fuel cell (SOFC)	E: YSZ A: Ni/ YSZ cermet C: $La_{1-x}Sr_xMnO_3$	800 - 1000	H_2 (low purity), CH_3OH	Stationary CHP generation

Table 1.1: Principle of fuel cell type [5]

1.4 References

[1] R.H. Taylor, Alternative Energy Sources for the Centralised Generation of the Electricity, Adam Higler ltd, Briton 10 (1983).

[2] G. Hoogers, Physics World, 1998, p31-32.

[3] D. H. Scott, Advanced Power Generation from Fuel Cells – Implications for Coal, IEA Coal Research, London (1993).

[4] J. Mattei, L'expansion, 644, (2001), p98-100.

[5] N.Q. Minh, T. Takahasi, Science and Technology of Ceramic Fuel Cells.

[6] N.Q. Minh, Journal of American Ceramic Society, 76[3] (1993), p563.

[7] B.C.H. Steele, C.R. Academic Science, Paris, t-1. serie IIc, (1998), p533.

[8] N. Brandon, D. Hart, Introduction to Fuel Technology and Economics (1999). Centre for Energy Policy and Technology, London, UK.

[9] K. Joon, Journal of Power sources (1998), 71, p12-18.

[10] B.C.H. Steele, J. Mater. Sci., 36, (2001), p1053-1068.

[11] S. Thomas, M. Zalbowitz, "Fuel Cells, Green Power" (Los Alamos National Laboratory, 1999)

[12] J. Larmanie and A. Dicks, Fuel Cell systems explained, Chichester Wiley, (2000).

[13] K.D. Kreuer, J. Membrane Science, 185, (2001), p29-39.

Chapter 2 – The Solid Oxide Fuel Cell

2.1 Introduction

The present generation of SOFC's can be classified into two types; those based on oxygen-ion-conducting electrolytes and those based on proton-conducting electrolytes. An oxygen-ion-conducting SOFC can be considered as an oxygen concentration cell, and a proton-conducting SOFC as a hydrogen concentration cell. The major difference between the two SOFC types is the chamber in the fuel cell in which water is produced (the fuel side in oxygen-ion conducting cells and the oxidant side in proton-conducting cells). Out of these two types, the oxygen ion-conductor cell is the most technologically advanced. Work in this research programme is solely related to the oxygen-ion-conducting cell.

Compared with other fuel cells, the unique characteristics of SOFCs are as follows:

1. They have the highest efficiencies of any conventional fuel cell design
2. They have the potential to use many fuels including gasoline and diesel without expensive external reformers that create more volatile chemicals.
3. External facilities such as humidity controller, gas reformer, etc are not essential.
4. The polarization resistance at the electrodes is small and large current density can be extracted.
5. As all the components are solid state, they can be made into any shape.

SOFCs can operate at high temperatures promoting rapid reaction kinetics, which allows reforming of hydrocarbon fuels (natural gas, coal gas, bio-gas) within the fuel compartment. It also produces high-grade waste heat, or exhaust, which can be recovered and used for other applications, such as space heating and cooling, supplying homes with hot water, and even generating extra electricity by spinning a gas turbine linked to the unit **[1]**. For the military, SOFCs offer the possibility of delivering quiet, clean, and uninterruptible energy to armed forces stationed in remote locations. SOFCs can also serve as auxiliary power units in motor vehicles, and leading automotive companies are already working with industrial partners to exploit their potential. Furthermore, because all the components are solid, SOFCs can be fabricated in very thin layers, and cell components can be configured into unique shapes unachievable in fuel cell systems having a liquid electrolyte.

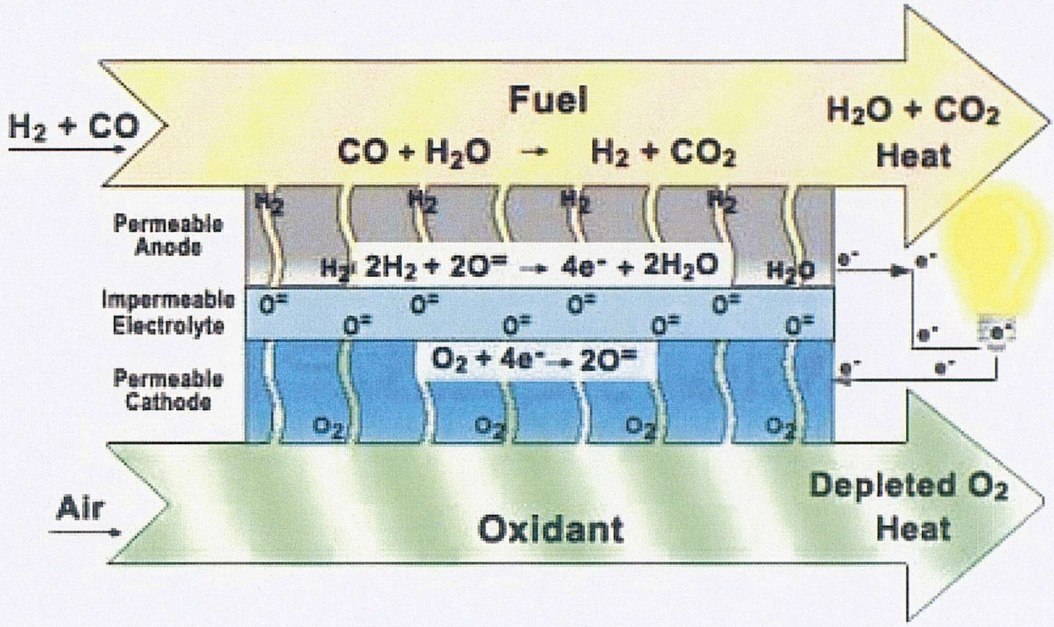
2.2 Operating Principle of SOFC

A SOFC single cell consists of a dense ion-conducting electrolyte sandwiched between two porous electrodes (an anode and a cathode). The electrode on the airside is the "cathode" on which oxygen molecules are reduced to oxide ions and incorporated into the electrolyte. The other electrode is the "anode" where the reactant gas is oxidised by oxygen ions, which comes through the electrolyte. The electron is extracted to the external circuit from the cathode to the anode. The driving force for the migrating oxygen ions is the difference in oxygen partial pressure between the electrodes. Thus the electron flow (from the anode to the cathode) through the external circuit produces direct-current (DC) electricity. The electrochemical transformation of the fuel and oxidant in a SOFC is isothermal; i.e., the fuel cell directly uses the available free energy in the fuel at the operating temperature. The driving force for the migrating oxygen ions is the difference in oxygen partial pressure between the electrodes. Contrary to conventional batteries, fuel cells do not undergo irreversible chemical change and it continues to operate as long as the reactants are present.

The combination of cathode/electrolyte/anode is called a "single cell". Another important component of the SOFC is the interconnect. Since the voltage generated by a single cell is not higher than 1V, several single cells should be connected in series to obtain a useful voltage. The interconnect is the material which connects the anode of one cell and the cathode of the next cell. The interconnect must separate the fuel and the oxidant of the neighbour cells. Thus, this component is called the "separator" from its function of gas separation.

The operating principle of a SOFC is shown in Figure 2.1. At the anode, hydrogen reacts with oxide ions transported through the electrolyte to form water. This is accompanied by the release of electrons to the external circuit. The electrons from the external circuit react with oxygen at the cathode and produce oxide ions. The overall process is the reaction of oxygen with hydrogen to produce water. Carbon monoxide can also be used, instead of hydrogen, and the corresponding reaction product will be carbon dioxide.

$$2CO + 2O^{2-} \rightarrow 2CO_2 + 4e^-$$
$$2H_2 + 2O^{2-} \rightarrow 2H_2O + 4e^-$$



$$O_2 + 4e^- \rightarrow 2O^{2-}$$

Figure 2.1:- Schematic diagram of chemical reactions in SOFCs [2]

2.2.1 Efficiency

The theoretical thermodynamic derivation of the Carnot Cycle shows that under ideal conditions, a heat engine cannot convert all the heat energy supplied to it into mechanical energy; some of the heat energy is rejected **[3]**. In an internal combustion engine, the engine accepts heat from a source at a high temperature (T_h), converts part of the energy into mechanical work and rejects the remainder into a heat sink at a low temperature (T_l). The greater the temperature differences between source and sink, the greater the efficiency. The maximum efficiency of a heat engine is subject to the Carnot efficiency limitation, which defines the maximum efficiency that any heat engine can have if its temperature extremes are known:

$$Carnot\ \ efficiency = \frac{T_h - T_l}{T_h}$$

Where T_h – absolute high temperature

T_l – absolute low temperature

The temperatures are in Kelvin (K).

For instance, for an engine operating at 800°C (1073K) and releasing exhaust at 60°C (333 K), the theoretical maximum efficiency is

$$h = \left(\frac{1073 - 333}{1073}\right) \times 100\%$$
$$= 69\%$$

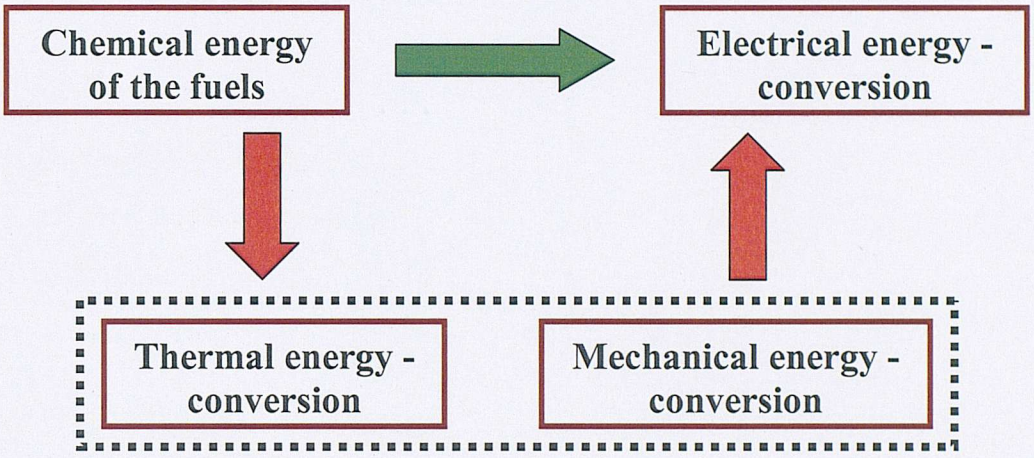


Fig 2.2: Energy Conversion in Fuel cells

There are 2 ways of converting chemical energy to electrical energy as shown in Figure 2.2. The red route is a general route for combustion process plus electricity generation in vehicles and power stations that use fossil fuels. The green route is however for fuel cells. A Fuel cell generates electricity by electrochemical reactions. It bypasses the thermal and mechanical energy conversions, and hence is more efficient. Because fuel cells convert chemical energy directly to electrical energy, this process does not involve conversion of heat to mechanical energy. Therefore, fuel cell efficiencies can exceed the Carnot limit even when operating at relatively low temperature, for example, 80°C (Figure 2.3).

The efficiency of a fuel cell is derived from the free energy (ΔG) of the electrochemical reactions taking place within the cells. However, their efficiency is usually expressed in terms of the heat of combustion (ΔH) of the fuel for convenience and also to allow the efficiency of the fuel cells to be directly compared with heat engines. The free energy released in the course of a chemical reaction is defined by the equation:

$$\Delta G = \Delta H - T\Delta S = -nFE$$

Where T is the absolute temperature, S is the entropy, n is the number of electron, F is Faraday's constant (F = 96 487 coulombs/mol electrons) and E is the thermodynamic potential of the cell.

In the case of the Grove hydrogen/oxygen fuel cell the overall reaction is:

$$H_2(gas) \div \frac{1}{2} O_2 \rightarrow H_2O(Liquid)\ \Delta H_f = -285.84\ \text{kJ/mole}\ \text{(higher heating value,HHV)}$$

$$\rightarrow H_2O(Steam)\ \Delta H_f = -241.83\ \text{kJ/mole}\ \text{(lower heating value,LHV)}$$

difference = 44.01 kJ/mole = molar enthalpy of vaporization of water.

The standard free energy change in this reaction (pure hydrogen and pure oxygen at 25°C and one atmosphere to liquid water) is -237.25 kJ/mole.

Thus, the theoretical maximum efficiency for the cell is therefore

$$\eta_{FC} = \frac{\Delta G}{\Delta H_f} = \frac{-237.25}{-285.84}$$

$$= 83\ \%(based\ on\ HHV)\ and\ 98.1\%\ (based\ on\ LHV)$$

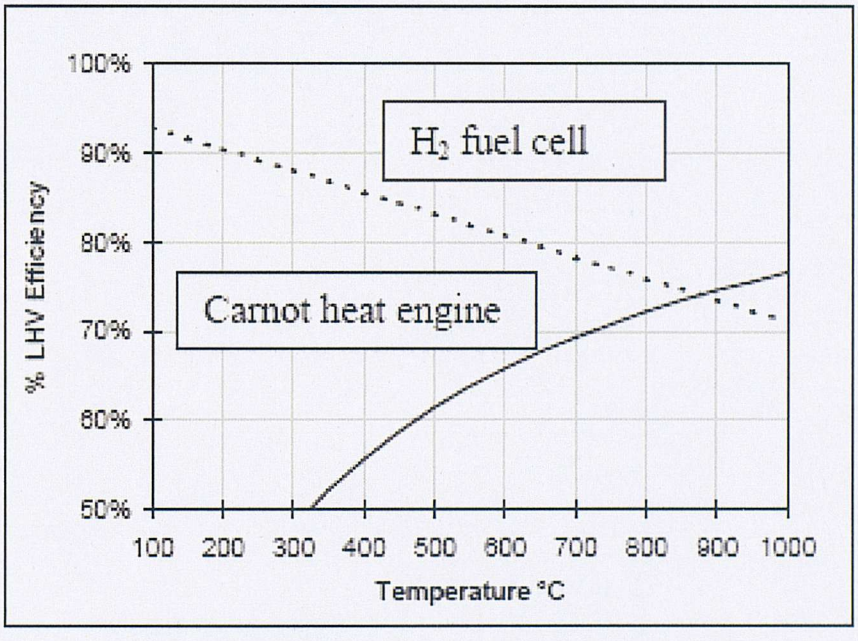


Fig 2.3: Carnot vs Hydrogen fuel cell [4]

2.2.2 Voltage of the Cell

The theoretical maximum voltage, the open circuit potential, of the hydrogen/oxygen fuel cell can also be derived.

$$\text{Reaction at the cathode : } \frac{1}{2}O_2 + 2e^- \rightarrow O^{2-}$$

$$\text{Reaction at the cathode : } H_2 \rightarrow 2H^+ + 2e^-$$

$$\text{Overall reation : } H_2 + \frac{1}{2}O_2 \rightarrow H_2O$$

The Gibbs free energy change for the overall reaction is given by:

$$\Delta G = \Delta G^o + RT \ln\left\{\frac{P_{H_2} \cdot (P_{O_2})^{\frac{1}{2}}}{P_{H_2O}}\right\}$$

in which R is the gas constant, T is the temperature (K), and P is the partial pressure of each gas of the overall reaction.

But $\Delta G = -nFE$ and $\Delta G^o = -nFE^0$

Where ΔG° and E° refer to the properties at equilibrium or standard state (298 K and pressure = 1 atm), n is the number of electrons taking part in the overall fuel cell reaction and F is a Faraday constant (F = 96487 Coulombs/mol electrons).

The electromotive force (emf) or reversible thermodynamic potential is given by the Nernst equation:

$$E = E^o + \frac{RT}{4F} \ln \frac{P_{H_2} \cdot (P_{O_2})^{\frac{1}{2}}}{P_{H_2O}}$$

The open circuit voltage (OCV) is the voltage produced by a fuel cell at zero current. It is equal to the Nernst voltage. The free energy of the overall reaction is 237.25 KJ/mole, so for fuel cell operating on hydrogen/oxygen at 25°C

$$OCV = -\frac{\Delta G}{2F} = \frac{237.25}{2 \times 96487}$$
$$= 1.23\ V$$

Practical SOFCs are not operated as single units, because a single cell produces less than 1 V under typical operating conditions (with hydrogen fuel and oxygen oxidant). They are rather connected using a component called interconnect which connects the cathode of one cell to the anode of the other in electrical series, parallel or both series and parallel, depending on a particular application to build a substantial voltage.

2.2.3 Voltage losses in Solid Oxide Fuel Cells

When current is flowing, the cell reaction deviates from the thermodynamically reversible process. Consequently the output voltage is also different from the open circuit voltage (OCV). The voltage losses are increased at higher currents. Several sources contribute to irreversible losses as shown in figure 2.4. The losses, which are often called polarization, overvoltage, or overpotential (η), originate primarily from three sources: activation polarization, η_{act}, ohmic polarization, η_{ohm}, and concentration polarization, η_{conc}. These losses are briefly discussed below in this section.

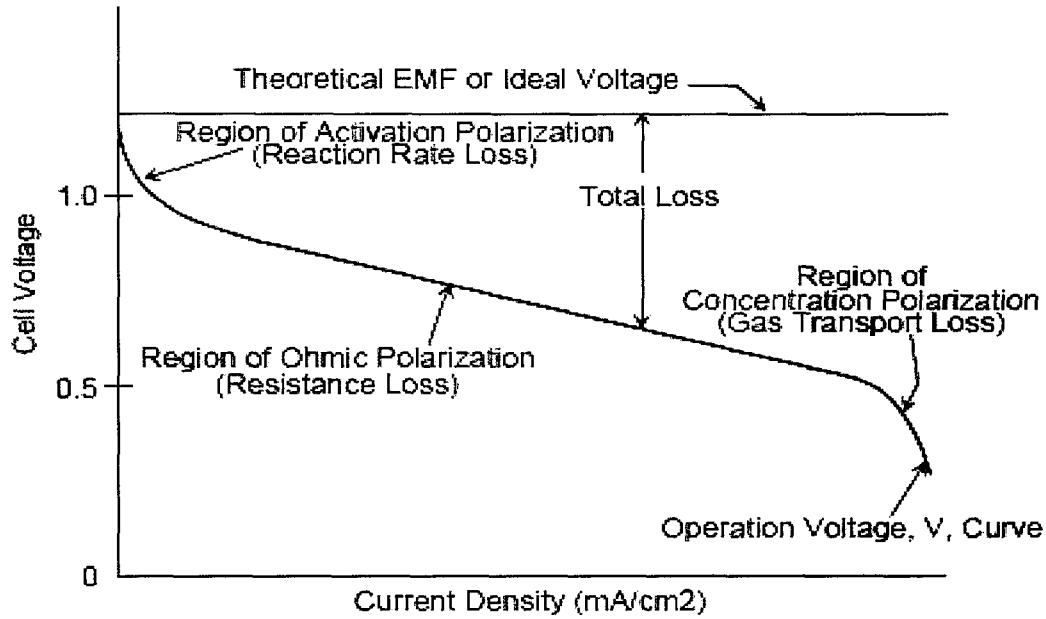


Fig 2.4: Fuel cell voltage/current characteristics [5]

2.2.3.1 Activation Polarization

The activation polarisation is significant at low current densities and it's the energy losses associated with the barrier that has to be overcome for the electrochemical reactions occurring both at cathode and anode. Under open circuit conditions, all reactions are at equilibrium but when a current is drawn one reaction rate must dominate to provide current flow. This requires a driving potential, which is lost from the open circuit voltage. Increasing the electrode area or catalytic activity of the electrodes can reduce the activation polarisation.

2.2.3.2 Ohmic Polarization

Summation of all the energy losses occurring due to electronic impedances through the electrodes, contacts, current collectors and at interfaces combined with the ionic impedance of the electrolyte. Ohmic losses simply follow Ohm's law as seen in equation below

$$\eta_{ohm} = I.R_{cell}$$

Here, I is the current density flowing through the cell, R_{cell} is the sum of the area specific resistance (ASR) of each components in the cell, which includes electronic, ionic and contact resistance. By choosing materials with high conductivities, the ohmic polarisation can be limited **[6 and 7]**.

2.2.3.3 Concentration Polarization

Concentration polarisation becomes significant at high current densities and it is due to the energy losses from mass transport effects such as reactants to diffuse to, or reaction products to diffuse away from the reaction sites. Increasing the reactant surface area by using porous electrodes with a fine particle size can reduce the concentration polarisation. In operational high temperature SOFC's, the polarisation curve is approximately linear and effects of concentration polarisation can usually be neglected.

2.2.4 Cell Components of SOFC

The four main components of a SOFC stack are the interconnect, the anode, the electrolyte, and the cathode (Figure 2.5). Each component plays a different role in the fuel cell and must meet the certain requirements. Each of the components must be chemically and physically compatible with other components in the cell. In addition, the components for ceramic fuel cells must have similar coefficients of thermal expansion to avoid separation or cracking during fabrication and operation. The electrolyte and the interconnect must be dense to prevent gas mixing, while the anode and cathode must be porous to allow gas transport to the reaction sites **[8]**. Materials selections for the components are discussed below.

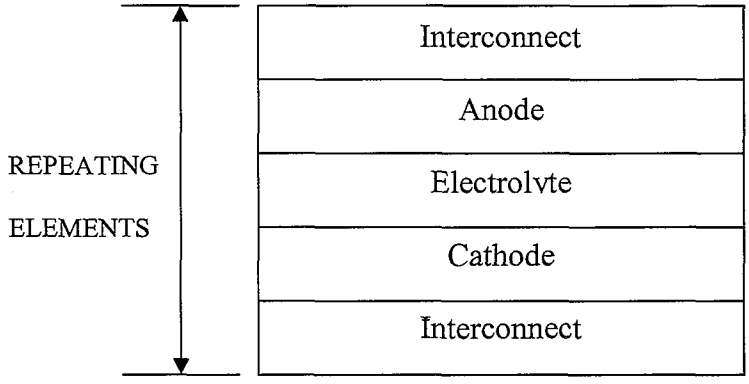


Fig 2.5: - Fuel Cell Stack Components [9]

2.2.4.1 Interconnect

The interconnect connects the cathode of a fuel cell to the anode of another fuel cell and hence forms a system of multicell modules. Besides, the interconnect will separate the fuel from the oxidant in adjoining the cells of a stack

Interconnect materials of relatively low cost in the final, fabricated form are essential for the expansion of fuel cell technology. In addition to having metallic conductivity and being capable of fabrication into appropriate configurations, any candidate material must **[5 and 9]**:

- Match the thermal expansion characteristics of the electrode materials, to ensure physical continuity of the interface and mechanical stability of the whole cell structure.

- Have a low resistance, stable interface with the electrode materials, (forming an adherent, conducting, stable or only slowly growing oxide film under the interface condition).

- Have scaling characteristics such that there is no damaging loss of section, or blockage of cell gas ports by friable scales.

- Have adequate strength at high temperatures, to maintain the required geometrical stability, and be sufficiently resistant to embrittlement during service.

- unconnected porosity is needed to avoid gas leakage.

In addition to these requirements, other desirable properties for the SOFC interconnect are high strength and toughness, fabricability and low cost.

2.2.4.2 Anode

The main functions of the SOFC anode are to facilitate the adsorption and oxidation of hydrogen from the fuel stream, thus permitting the oxygen ions from the electrolyte to combine with the hydrogen to form water and release electrons to the external circuit. Thus, the anode material must therefore be predominantly an electronic conductor, stable in the fuel reducing environment and catalytic activity for the fuel gas reaction at the operating conditions. Since the SOFC operates at temperatures between 500° to 1000°C, the anode must be thermally and chemically compatible with the other cell components (electrolyte and interconnect) from room temperatures to those operating temperatures and even higher temperatures at which the fuel cell is fabricated. The key requirements for the anode in the SOFC are:

- Porosity: For the transport of gas to the reaction sites, the anode must have sufficient porosity.

- Conductivity: The anode must possess sufficient electronic conductivity for electron flow in the reducing environment at the operating temperature.

- Thermal expansion: To avoid cracking, delamination during fabrication and operation, including thermal cycling, the anode must match the thermal expansion (from room temperature to operation and fabrication temperature) of other cell components (electrolyte and interconnect).

- Catalytic activity: The anode must have sufficient catalytic activity, thus low polarisation, for the electrochemical oxidation of the fuel.

- Stability: The anode must be chemically, dimensionally, and morphologically stable in the fuel environment.

- Compatibility: The anode must be chemically and physically compatible with other cell components, not only at the operating temperature, but also at the much higher temperatures at which the fuel cell ceramic structure is fabricated.

In addition to these requirements, other desirable properties for the SOFC anode are high strength and toughness, fabricability and low cost.

2.2.4.3 Electrolyte

The electrolyte material is exposed to both oxidising and reducing atmospheres during operation because of the porous nature of the cathode and anode (the electrolyte also separates the fuel from the oxidant in the fuel cell). The main function of the electrolyte is to transport the oxygen ions from the cathode to the anode to balance the charge from the electron flow and complete the electrical circuit in the cell. Other certain criteria also need to be fulfilled for the electrolyte to be used in a SOFC. It must be stable with respect to other cell components (air and fuel electrodes, interconnects, sealing materials for certain design fuel cells), adequate mechanical properties (strength, toughness, creep, mechanical and thermal shock resistance) in fuel cell operating conditions, structural and thermodynamic stability in both fuel and oxidising environments, matching thermal expansion coefficients with other cell components, and an ionic transport number close to unity. The electrolyte must be thin to minimise ohmic loss. The electrolyte for a SOFC requires the following characteristics:

- Conductivity: Once the molecular oxygen has been converted to oxygen ions it must migrate through the electrolyte to the fuel side of the cell. In order for such migration to occur, the electrolyte must possess a high ionic conductivity at the fuel cell operating temperature and no electronic conductivity to prevent voltage losses due to the electronic current flowing through the electrolyte. The transport number for oxygen ions, t_i close to unity is required and the transport number for electronic conduction as close to zero as possible.

- Porosity: The solid electrolyte must be free of porosity; it must be fully dense to prevent short-circuiting of reacting gases from one side of the electrolyte layer to the other.

- Stability: The electrolyte must be chemically, morphologically and dimensionally stable in the dual atmosphere (fuel oxidising atmosphere at the anode and oxygen reducing atmosphere at the cathode). Especially at the anode condition (low oxygen partial pressure), the electrolyte should not be reduced to give electronic conductivity.

- Thermal expansion: Thermal expansion compatibility of the electrolyte with the other cell components is required (from room temperature to operation and fabrication condition). This is to avoid cracking and delamination during fabrication and operation, including thermal cycling.

2.2.4.4 Cathode

A considerable part of the voltage losses in solid oxide fuel cells (SOFCs) arise on the cathode side. As a consequence of the temperature reduction in IT-SOFC from 1000°C to 700-500°C, higher interfacial polarisation and ohmic losses are anticipated. Therefore, the optimisation of cathode layers, the cathode/electrolyte and cathode/interconnect interfaces are desirable.

The main function of the cathode is to provide reaction sites for the electrochemical reduction of the oxidant. So a cathode material for solid oxide fuel cells should meet several requirements in respect to preparation and operating conditions:

- High electronic conductivity: The cathode must possess sufficient electronic conductivity to support electron flow in the oxidising environment at the operating temperature. In general, maximum possible cathode conductivity is desirable to minimise ohmic losses.

- Mixed ionic-and-electronic conductivity

- Porosity: The cathode must have sufficient porosity to allow gas transport to the reaction sites.

- High catalytic activity: The cathode must have sufficient catalytic activity, thus low polarisation, for the electrochemical reduction of the oxidant. It must also have high oxygen self-diffusion and surface exchange coefficients.

- Thermal expansion coefficient compatible (from room temperature to operation and fabrication temperature) with other cell components.

- Chemical compatibility with the other components, not only at the operating temperature, but also at the much higher temperature at which the fuel cell ceramic structure is fabricated.

- Stability (chemically, morphologically and dimensionally) in oxidant environment at high temperatures.

- Absence of destructive phase transitions in the operating temperature range

- Ability to be formed into films

In addition to these requirements, other desirable properties for the SOFC cathode are high strength and toughness, fabricability and low cost.

2.2.4.1.1 Oxygen Reduction in the Cathode

The electrochemical function of the cathode is to increase the rate at which oxygen from the gas phase is incorporated into the electrolyte, and to convert the electronic current in the connecting wires/current collecting material to the ionic current that passes through the electrolyte. The oxygen is reduced at the cathode by accepting electrons from the external circuit, and the overall reaction is simply:

$$O_2(gas) + 4e^- \rightarrow 2O^{2-}$$

There are many arguments about this reaction in the cathode and where it occurs. However, these are very much dependent on the properties of the cathode materials, such as diffusivity, surface exchange coefficient of oxygen and also its microstructure (thickness and porosity).

The electrode microstructure is an important parameter in the chemical processes of the oxygen reduction reaction. Two of the most important features are the triple phase boundary and the electrolyte/electrode (cathode) contact area. Generally in the case of the materials with low oxygen diffusion coefficient such as noble metals, or lanthanum manganite (LSM), the reactions occur near the triple phase boundary, under normal

SOFC operating conditions **[10-19]**. The triple phase boundary is defined as the area where the electrolyte, electrode and gas phase meet. This is shown in Figure 2.6a. Here the cathodic reduction reaction can be subdivided into several step reactions such as (i) oxygen transport in the gas phase, (ii) oxygen adsorption and dissociation on the electrode surface, (iii) oxygen diffusion in the electrode along the surface toward the triple-phase boundary (iv) ionization and ionic transfer across the interface between the electrode and electrolyte into the electrolyte **[20]**. The morphology of the electrode/electrolyte interface thus determines the polarization loss. A more promising approach is illustrated in Figure 2.6b: by utilizing a mixed conducting oxide (LSC, LSCF, GSC or SSC) or having a composite cathode (composed of an electronically conducting oxide or mixed conducting oxide and an ionically conducting oxide, this is discussed below). Here, the cathodic process is not limited to the triple phase boundaries, since the volume of the cathode can contribute to the electrochemical reduction reaction. This path consists of (i) gas diffusion (ii) adsorption on the cathode surface (iii) dissociation and ionization (iv) incorporation into the cathode (v) oxide ion transport through the electrode and (vi) the transfer of the ion into the electrolyte **[21-28]**.

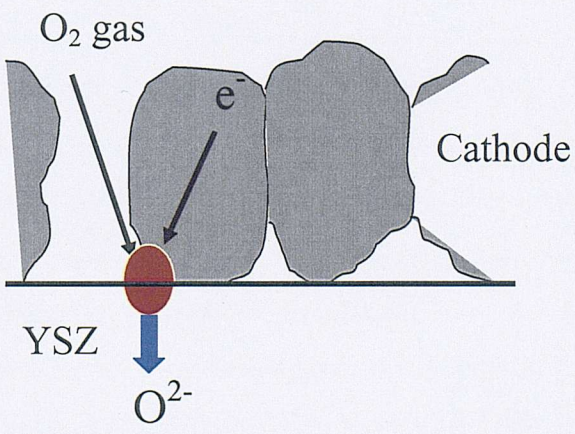
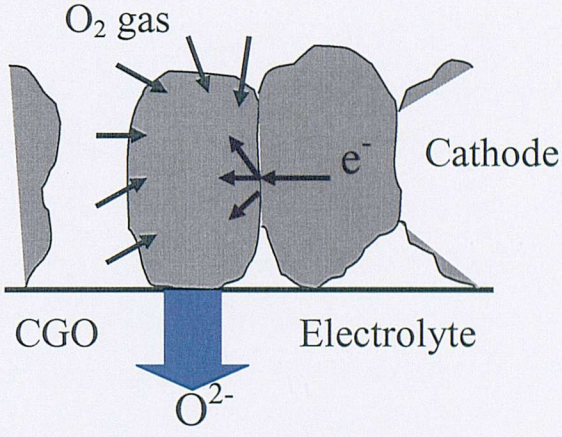


Fig 2.6: (a) Oxygen reduction at the triple phase boundary (electronic conductor)



(b) Oxygen reduction through a mixed conductor

2.2.4.1.2 Oxygen Reduction Model in a Cathode

Cathode reactions in SOFC systems involve a complex interaction of mobile electronic, ionic and molecular species. Under cathodic polarization the overall reaction is

$$\frac{1}{2}O_2(gas) + 2e^-(current\ collector) \rightarrow O^{2-}(electrolyte)$$

A lot of work has been carried out to model this reaction in SOFCs, unfortunately it is still not clearly understood how this reaction takes place in the cathode of a SOFC. It is generally accepted the reduction of oxygen is occurring locally at the triple-phase boundary where gas, ionic conductor (electrolyte) and electronic conductor (cathode) meet **[29]**. Yet it is unknown exactly what steps are involved in the reaction. Different researchers have taken different approaches to model the cathode behaviour. Wu et al predicted the ionic, electronic and ambipolar transport behaviour of a composite mixed conductor as a function of the volume fraction of each phase and porosity of the MIEC **[30]**. Here percolation theory was used to predict the electrical properties of randomly distributed two-phase composites using a resistor network approach. Tanner et al **[31]** theoretically examined the effect of porous composite cathodes on the overall charge-transfer process in SOFC by considering certain parameters such as electrolyte thickness, electrode thickness, intrinsic charge-transfer resistance and porosity. Sunde studied three different approaches of a model based on the physical aspect of the electrode: a thin film modelling, Monte Carlo simulations for randomly packed particles, and a macroscopic porous-electrode model of a disordered electrode structure **[32]**. Mitterdorfer et al **[33 and 34]** investigated the modelling of heterogeneous electrode reaction mechanisms in single-phase perovskite cathodes. Prestat and Gauckler took the state space approach for a description of heterogeneous reactions impedance directly from a reaction model. The equations of mass balance, transport and charge transfer equations are used to formulate a state-space model, which are linearised and undergoes a Laplace transform **[35]**. The resulting admittance transfer function enables the simulation of impedance data. Yamada et al **[36]** tried to model the behaviour of $Sm_{0.5}Sr_{0.5}O_3$ (SSC) cathodes to determine the rate-determining step of each material. The model, which was based on the mobility of oxygen ions on the electrode and rates of oxygen adsorption and desorption predicted the cathodic overpotential, which is dependent on the length of the triple phase boundary.

It has been shown by Kilner and De Souza **[37]**, that the surface exchange coefficient and tracer diffusion coefficient are related in the mixed conducting perovskite materials.

It is therefore likely that given certain electrode microstructures, the resistance to diffusion will be of a similar magnitude to the resistance due to the surface exchange process. In the case of a porous material, the exchange process is taking place over the entire volume of the electrode and diffusion can then occur from the site of exchange to the electrode/electrolyte boundary. Using this theory, a continuum model has been developed by Adler et al **[27, 28, 38 and 39].** He and his co-workers provided both theoretical and experimental evidence for understanding the linear AC polarisation values for single phase mixed conducting cathodes. This model indicates that for mixed conductors with fast ion transport (e.g. LSCF), the impedance can be dominated by O_2 surface exchange and diffusion processes. A schematic representation of the ALS model is provided in Figure 2.7.

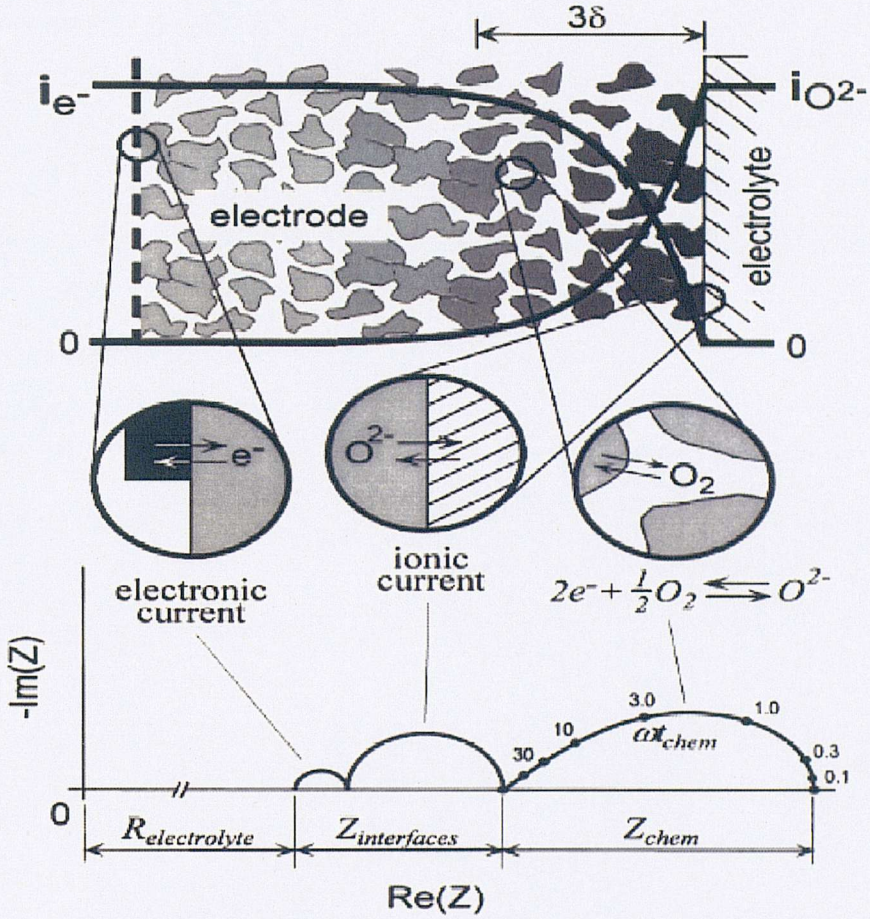


Fig 2.7: Schematic representation of the ALS model [40]

The electronic charge transfer impedance at the interface between the current collector and mixed conducting oxide cathode can usually be neglected. The second arc can be attributed to the ionic charge transfer across the mixed conducting cathode/electrolyte interface. This charge transfer impedance only makes a minor contribution to the total

electrode impedance provided that the interface is uncontaminated by siliceous impurities. Z_{chem} provides the major contribution, which is the convoluted contribution of non-charge transfer processes including oxygen surface exchange, solid-state diffusion, and gas-phase diffusion inside and outside the cathode **[34]**.

In the development of this model several assumptions have to be made and these are summarized below:

1. The electrolyte is treated as ohmic and of unity ionic transference.

2. The electronic conductivity of a mixed conductor is much greater than the oxygen ion conductivity.

3. There are no interactions between the oxygen vacancies so their chemical potential is determined directly from their concentration.

4. The diffusion of oxygen between the electrode/gas interface and electrode/electrolyte interface is driven by a chemical potential gradient.

5. The concentration of electrons is constant throughout the thickness of the electrode.

6. The thickness of the electrode is constant over the whole area of the electrode.

7. The equations are linearised around the trivial solution, i = 0 (zero bias).

Using these assumptions the heterogeneous chemical reaction contribution (R_{chem}) is given by Adler et al as: -

$$R_{chem} = \frac{RT}{2F^2}\sqrt{\frac{\tau}{(1-\varepsilon)aC_O{}^2 D^* k}}$$

Where: -
$D^* \rightarrow$ Oxygen self-diffusion coefficient
$k \rightarrow$ Oxygen surface exchange coefficient
$\tau \rightarrow$ Tortuosity
$\varepsilon \rightarrow$ Fractional porosity

a → Internal surface area/unit volume
R → Gas constant
T → Temperature
F → Faraday's constant
C_o → Molar concentration of oxygen ions

The time dependant impedance can then be expressed as,

$$Z_{chem} = R_{chem}\sqrt{\frac{1}{1-j\omega\tau_{chem}}}$$

Where τ_{chem} is the relaxation time defined as.

$$\tau_{chem} = \frac{\left[V_O^{\bullet\bullet}\right](1-\varepsilon)}{AakC_o}$$

A is a thermodynamic factor.

It is very noticeable from the equation above that the R_{chem} value (Area specific resistance, ASR) is dependent on both the kinetic and microstructural parameters. It would appear therefore that parameters D, Oxygen self diffusion coefficient (cm^2s^{-1}) and k, oxygen surface exchange coefficient (cms^{-1}) as well as microstructural parameters like particle size, porosity and tortuosity have an important role in determining the impedance of both porous and dense single phase mixed conducting oxide. The kinetic parameters are fixed by the choice of materials; however the microstructural variables can, in principle be controlled by controlled processing.

It is appropriate, therefore, to examine whether values D and k provide a qualitative understanding of impedance values generated by composite electrodes. Steele **[38]** examined whether the Adler approach for single phase mixed conducting oxide can provide useful insights into the behaviour of composite cathodes. It was suggested that the D and k values around 10^{-8} cm^2s^{-1} and 10^{-6} cms^{-1}, respectively, are required if the phase predominantly responsible for transporting the ionic flux is going to produce the required electrode ASR values of 0.1 - 0.3 Ωcm^2 at 500°C.

The Adler model is not applicable to a composite material. Steele et al **[38]** used this concept to give some insight on the behaviour of composite cathodes. The ALS model was used to calculate the theoretical R_{chem} of LSM, YSZ, LSCF and CGO, which were then compared with the experimental ASR obtained from the AC impedance spectroscopy for these materials, as well as the composites. As a first approximation the material is treated as a homogeneous mixed conducting medium and assume that the surface exchange coefficient is determined by the electronically conducting perovskite

phase. Using this assumption we can estimate the expected ASR of a composite material.

Data (7) for D^* and k at 500°C are 2.0×10^{-8} cm^2s^{-1} (CGO) and 2.0×10^{-8} cms^{-1} (LSCF). The following typical values for the microstructural parameters were assumed and the fraction porosity was calculated from the Archimedes principle:

τ (tortuosity) = 1.5

a (internal surface area/unit volume) = 20000 cm^{-1}

Co = 0.08 mol O cm^{-1} in LSCF

$\varepsilon = 0.6$

These data were used to calculate the relevant R_{chem} values at 498°C and 550°C and they were found to be around 2.87 Ωcm^2 and 1.55 Ωcm^2, respectively.

2.2.5 SOFC Designs

A combination of the anode, electrolyte and cathode is known as a single cell. A stack is formed by connecting these cells together using an interconnect. As all the components are solid, the SOFC stack can be configured into unique shapes unachievable in other types of fuel cells **[9]**. There are currently a number of designs that are being considered each has its own particular advantages and disadvantages. At present, three common stack configurations have been proposed and fabricated for SOFCs.

2.2.5.1 Tubular Design

The schematic view of a tubular cell is shown in Figure 2.8. The tubular design is the most developed design, pioneered by Westinghouse around 1980. The cells are slender cylinders approximately 13mm in diameter. In this design the cell components are configured as thin layers on a closed-one-end tubular support. One distinct feature of this design is that it has no seals. Each tube, typically 0.5-1m in length, corresponds to a single cell. The support tube, which is closed at one end, provides mechanical strength for the thin cell components. Table 2.1 shows the processes used for the fabrication of a Westinghouse cell.

Component	Material	Thickness	Fabrication process
Interconnect	$LaCrMgO_3$	40 μm	Electrochemical vapour deposition, (EVD)
Cathode	$La(Sr)MnO_3$	1.4 mm	Slurry coat, sintering
Electrolyte	$ZrO_2(Y_2O_3)$	40 μm	EVD
Anode	$Ni\text{-}ZrO_2(Y_2O_3)$	100 μm	Slurry coat, EVD

Table 2.1:- Westinghouse SOFC: cell components[41]

The cells are connected in series by pushing this interconnect on the surface of the anode of the neighbour cell by using a nickel felt. Each cell is fixed to the casing only at the open end of the tube. The anode, which forms the outermost layer of each tube, are supplied with fuel by suspending the tubes in a chamber containing a continuously replenished supply of fuel gas. A part of the fuel is utilized for the electrochemical reaction. The unreacted gas is burnt for preheating the air, which, in turn, introduced from the top of the alumina tube inside the cell and diffuses through the porous support tube to the cathode. The gas separation is done only at the top of the pre-heating room by the contact of the tip on the air tube and the casing. With this design, no gas sealing material is necessary. The "Seal-less" design of the device allows generous tolerances to be used in the hot zones of the fuel cell. The generated electricity should go through the electrode layer to reach to the next cell. Since the electrode should be porous, the electrical conductivity is not high enough. The ohmic resistance dominates the total energy loss. Recently, improvement has been made so that the cathode material itself is used as the support tube to decrease the ohmic loss **[42]**.

The main drawbacks of this design are the costly fabrication of the electrolyte and reduced current densities associated with the long current path lengths, which leads to low power densities.

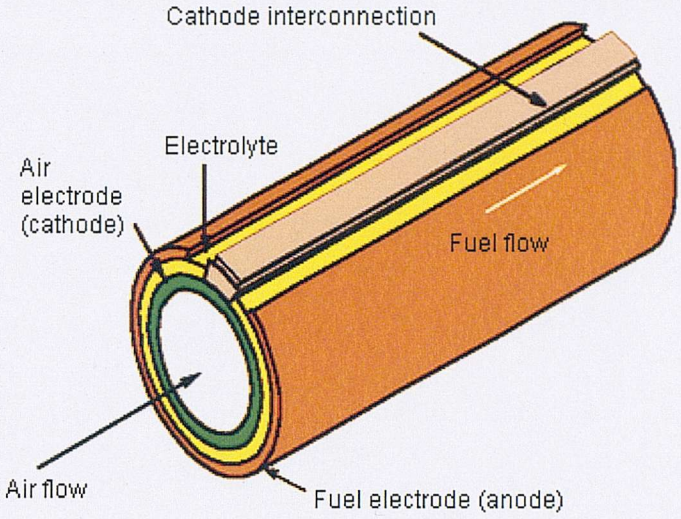


Fig 2.8:- Tubular design SOFC [43]

2.2.5.2 Planar Design

The conventional planar cell (Figure 2.9) configuration has an advantage over the tubular cell from a viewpoint of the electrical path and higher power density. Also the tubular design SOFCs has been criticised for their inefficient use of space. In theory, planar designs should allow the fuel cell elements to be stacked in a geometric pattern that uses space more efficiently and results in increased power density. Another advantage of this design is the cheap fabrication process required to make the components. In addition, the planar design may also include both intermediate and high temperature systems. Lastly, both thick and thin films can be used. The planar (flat-plate) configuration is the most common configuration for fuel cells. This permits a simple series electrical connection between cells without the need for external cell interconnections. These cell stacks should have an ohmic polarisation and improved stack performance when compared to tubular designs.

The flat-plate fuel cell consists of a single cell (anode/electrolyte/cathode) and interconnect configures as thin, flat plates. The interconnect, having ribs on both sides forms gas channels and serves as a bipolar gas separator contacting the anode and cathode of adjoining cells.

The technological problems in making a planar SOFC are (i) difficulty in gas sealing, (ii) fragility of the electrolyte and separator and (iii) large contact resistance. One of the solutions for these problems is the Co-firing technique in which the whole cell components are stacked and sintered together in one sintering process, however

satisfactory results have not been obtained yet. The major problem is the inter-diffusion of the materials during sintering process. Hence, the components in this design are fabricated by relatively cheap methods. The interconnect which have ribs on both sides is fabricated by either hot pressing or tape casting. The electrodes can be applied by plasma spraying, screen-printing, tape casting or slurry coating **[44]**. The electrolyte is either sintered or then co-sintered with the electrode applied or can be sintered with both electrodes as green bodies in one step.

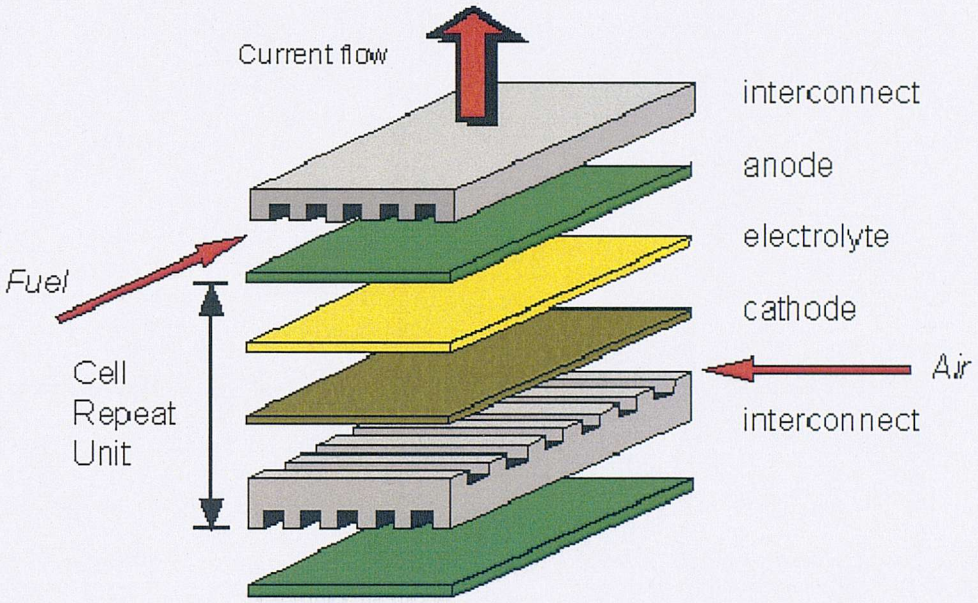


Fig 2.9:- Flat plate design SOFC (exploded view) [45]

2.2.5.3 Monolithic Design

Another planar fuel-cell system is the monolithic design of which a version was proposed by Argonne National Laboratory in 1984 **[46]**. The design has the potential to achieve high power density, because of its compact and lightweight structure. The feasibility of the monolithic design has only been demonstrated on a laboratory scale.

The monolithic structure is a more complex design of bipolar configuration for SOFCs. The schematic representation of a cross section of the monolithic structure proposed for SOFCs is presented in Figure 2.10. The structure resembles the corrugated assembly used in cardboard boxes. The small channels are formed from thin (25 to 100 μm) layers of the active cell components, and these channels serve for passage of the fuel and oxidant streams. In this design the anode, cathode and solid electrolyte are tape cast

into thin layer structures, and then the complete assembly is heat treated in air to produce the SOFC monolithic **[47]**.

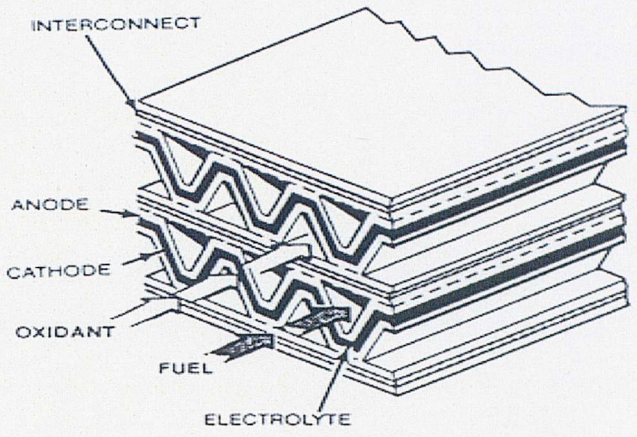


Fig 2.10:- Monolithic design SOFC [9]

2.2.6 Advantages of SOFC and Problems to be Solved

Solid oxide fuel cells have several distinct advantages over other type of fuel cells namely: the use of non-precious materials and no liquids involved in the fuel cell and invariant electrolyte. The use of solid electrolyte in ceramic fuel cells eliminates material corrosion and electrolyte management problems. The other attraction of solid oxide fuel cells includes the clean conversion of chemical energy to electricity, low levels of noise pollution, the ability to cope with different fuels, but most of all - high efficiency. The enhanced efficiency of SOFCs' in comparison with other energy conversion systems is born out of its high operating temperature, which in some designs may exceed 1000°C. The high operating temperature promotes rapid reaction kinetics, allows reforming of hydrocarbon fuels (natural gas, coal gas, bio-gas) within the fuel cell and produces high quality by-product, heat suitable for use in co-generation or bottoming cycle. Furthermore, because all the components are solid, ceramic fuel cells can be fabricated in very thin layers, and cell components can be configured into unique shapes, unachievable in fuel cell systems having a liquid electrolyte **[48-50]**.

The major problems associated with high temperature SOFC are (1) electrode sintering, (2) interfacial diffusion between electrode and electrolyte and (3) mechanical stress due to different thermal expansion coefficients, (4) severe restrictions on the choice of materials. Material costs are high, particularly for interconnect and construction

materials. Interconnects carry electrical current between individual cells in the stack and can also act as a separator between the fuel and oxidant supplies. In high temperature SOFC the interconnect may be a ceramic such as lanthanum chromite. In either case the interconnect represents a major proportion of the cost of the stack. Stack construction materials and balance of plant also need to be refractory enough to contain and manipulate the high temperature gas streams. A potential drawback to the use of chromium containing ceramics and alloys is the volatility of the material, which can result in contamination of the stack components. This has an increased significance for future reclamation of materials and components from used stacks where the presence of a toxic material such as Cr^{6+} would require special disposal procedures.

Another major problem reported in this device is the thermal mismatch of the components at the operation temperature **[40]**. Although, solid oxide fuel cell is an all-ceramic device, the inherent difficulties posed by the right choice of materials and the right techniques employed for their fabrication into thin sections of large area components with reproducible characteristics as yet remains to be solved.

Furthermore the mechanical and chemical stability of the materials could be affected after a long operating time. The formation of $La_2Zr_2O_7$ at high temperatures will lead to a conductivity three times lower than LSM resulting in an increase in polarisation. This has been observed in long-term tests **[42]**, which will lead to cathode layer being separated from the electrolyte/cathode interface **[51]**.

2.2.7 Advantages of Intermediate Temperature SOFC

Operation of the SOFC at a reduced temperature (between 500-600°C) can overcome some of the problems stated above and bring additional benefits. The primary advantages are (1) to arrive at an optimum between performance and lifetime of the stack and (2) to reduce the overall system cost **[52]**.

Other benefits include:

- Operation at less than 700°C means that low cost metallic materials e.g. ferritic stainless steels can be used as interconnect and construction materials. This makes both the stack and balance of plant cheaper and more robust. (Balance of Plant is widely assumed to constitute 50% of the cost of the SOFC system). Using ferritic

materials also significantly reduces the above-mentioned problems associated with Chromium.

- Thermal stress – Lower operating temperature can in general improve materials properties allowing greater geometrical flexibility and use of less material which in turn can improve overall area specific resistance.

- Lower temperature operation offers the potential for more rapid start up and shut down procedures.

- Reducing operating temperature simplifies the design and materials requirements of the balance of plant.

- Reducing the operation temperature significantly reduces corrosion rates.

- Heat loss – Less heat loss from the stack. In particularly radiation losses can be significantly less.

In order to operate at reduced temperatures several changes need to be made to cell and stack design, cell materials, reformer design and operation, and operating conditions.
For this purpose, four research strategies are being employed to develop cell materials that may produce a high power density even at low temperatures. The first is to produce a thin film of the electrolyte, the second is to develop alternate electrolyte material that may exhibit high oxygen ion conductivity (cerial gadolinia oxide, CGO has been found to have a higher ionic conductivity than YSZ and is now used as the electrolyte material for intermediate temperature SOFC operation), the third is to develop alternate active electrode catalyst with high electronic conductivity at lower temperatures **[53]** and finally the use of composite cathodes, which have some phases of electrolyte material (ionically conducting material) and the electronically conducting electrode material. This should also improve the electrode/electrolyte interface in a SOFC system.

2.3 References

[1] P.G. Bruce, Solid State Electrochemistry, Cambridge University Press, Uk, (1995).

[2] http://www.seca.doe.gov/fuelcellani.html

[3] N.Q. Minh, Journal of American Ceramic Society, 76[3] (1993), p563.

[4] B.C.H. Steele, Electronic Ceramics, Ed. B.C.H. Steele, Elsvier Science Publishers ltd, 1991.

[5] J. Larmanie and A. Dicks, Fuel Cell systems explained, Chichester Wiley, (2000).

[6] B.C.H. Steele, Mater. Sci. and Eng., B13, (1996), p79.

[7] B.C.H. Steele, P.H. Middleton, and R.A. Rudkin, Solid State Ionics, 40/41, (1990), p388.

[8] B.C.H. Steele, C.R. Academic Science, Paris, t-1. serie IIc, (1998), p533.

[9] N.Q. Minh, T. Takahasi, Science and Technology of Ceramic Fuel Cells.

[10] H. Fukunaga, M. Ihara, K. Sakakai and K. Yamada, Solid State Ionics, (1996), 86-88, p1179.

[11] A. Endo, M. Ihara, H. Komiyama and K. Yamada, Solid State Ionics, (1996), 86-88, p1191.

[12] F.H. Van Heuveln, H.J.M. Bouwmeester and F.P.F. Van Berkel, J. Electrochem. Soc., (1997), 144, p126.

[13] Y. Takeda, R. Kannno, M. Noda, Y. Tomida and O. Yamamoto, J. Electrochem. Soc., (1987), 134, p2656.

[14] A. Mitterdorfer and L.J. Gauckler, Solid State Ionics, (1998), 111, p185.

[15] J. Mizusaki, H. Tagawa, K. Tsuneyoshi and A. Sawata, J. Electrochem. Soc., (1991), 138, p1867.

[16] F.H. Van Heuveln and H.J.M. Bouwmeester, J. Electrochem. Soc., (1997), 144, p134.

[17] A. Hammouche, E. Siebert, A. Hammou and M. Kleitz, J. Electrochem. Soc., (1991), 138, p1212.

[18] B. Gharbage, T. Pagnier and A. Hammou, J. Electrochem. Soc., (1994), 141, p2118.

[19] H.Y. Lee, W.S. Cho, S.M. Oh, H-D. Wiemhofer and W. Gopel, J. Electrochem. Soc., (1995), 142, p2659.

[20] J. Fleig, Journal of Power Sources (2002), 105, p228-238.

[21] A. Endo, S. wada, C. Wen, H. Komiyama and K. Yamada, J. Electrochem. Soc., (1998), 145, pL35.

[22] A. Endo, H. Fukunaga, C. Wen and K. Yamada, Solid State Ionics, (2000), 143, p35.

[23] T. Inoue, N. Seki, K. Eguchi and H. Arai, J. Electrochem. Soc., (1990), 137, p2523.

[24] L.S. Wang and S.A. Barnett, J. Electrochem. Soc., (1992), 139, p3630.

[25] K. Huang, M. Feng, J.B. Goodenough and M. Schmerling, J. Electrochem. Soc., (1996), 143, p3630.

[26] T. Ishihara, M. Honda, T. Shibayama, H. Minami, H. Nishiguchi and Y. Takita, J. Electrochem. Soc., (1998), 145, p3177.

[27] S.B. Adler, J.A. Lane and B.C.H. Steele, J. Electrochem. Soc., (1996), 143, p355.

[28] S.B. Adler, Solid State Ionics, (1998), 111, p125-134.

[29] M. Godickemeier, K. Sasaki, L.J. Gauckler, Journal of the electrochemical society (1997), 144(5), p1635-1646.

[30] Z. Wu, M. Liu, Solid State Ionics (1997), 93, p65-84.

[31] C.W. Tanner, K-Z. Fung, A.V. Virkar, Journal of the Electrochemical Society (1997), 144(1), p21-30.

[32] S. Sunde, Journal of Electroceramics (2000), 5(2), p153-182.

[33] A. Mitterdorfer, L.G. Gauckler, Solid State Ionics (1999), 117, p203-207.

[34] A. Mitterdorfer, L.G. Gauckler, Solid State Ionics (1999), 117, p187-207.

[35] M. Prescat, L.J. Gauckler, H. Yokokawa, in SOFC-VII, S.C.S, The Electrochemistry Society (2001), p574-583.

[36] K. Yamada, in Fourth European SOFC Forum (2000), Lucerne, Switzerland.

[37] R.A. De Souza, PhD. Thesis, Imperial College, London (1996).

[38] B.C.H. Steele, K.M. Hori, S. Uchino, Solid State Ionics (2000), 135, p445-450.

[39] S.B. Adler, Solid State Ionics, 135, (2000), p603-612.

[40] T. Inagaki, K. Miura, H. Yoshida, R. Maric, S. Ohara, X. Zhang, K. Mukai and T. Fukui, J. Power Sources (2000), 86, p347-351.

[41] S.C. Singhal, Solid Oxide Fuel Cell Development at Westinghouse. In: The Second International Symposium on Solid Oxide Fuel Cells, Athens, Greece, 1991.

[42] Leo J.M.J. Blomen and Michael N. Mugerwa, Fuel Cell Systems, plenum press, New York and London.

[43] http://www.powergeneration.siemens.com/en/fuelcells/sofc/tubular/index.cfm

[44] Y.C. Hsiao, J.R. Selman, Solid State Ionics (1997), 98, p33-39.

[45] http://www.spice.or.jp/~fisher/sofc.html

[46] R.H. Taylor, Alternative Energy Sources for the Centralised Generation of the Electricity, Adam Higler ltd, Briton 10 (1983).

[47] D. Hart, A Solid Start to the Millenium, Chemistry and Industry, 1998.

[48] H-R. Rim, S-K. Jeung, H-K. Lee and J-S. Lee, Proc. Second International Fuel Cell Conference, Japan (1996), p469-472.

[49] R.N. Basu, S.K. Pratihar, M. Saha and H.S. Maiti, Matter. Lett. (1997), 32, p217-222.

[50] C. Ch. Kostogloudis and Ch. Ftikos, J. Euro. Ceram. Soc. (1999), 19, p497-505.

[51] D. Kuscer, J. Hole, M. Hrovat, S. Bernik, Z. Samardzija, D. Kolar, Solid State Ionics (1995), 78, p79-85.

[52] J.P.P. Huijsmans, F.P.F. Van Berkel and G.M. Christie, J. Power Sources, (1998), 71, p107-110.

[53] B.C.H. Steele, J. Mater. Sci., 36, (2001), p1053-1068.

Chapter 3: Structure, Defects and Conductivity

3.1 Fluorite Structure

Fluorite type oxides (Figure 3.1) are commonly ionic conductors and have been considered for use as electrolytes in SOFCs. The ideal fluorite structure has a general chemical formula of AO_2, where "A" (the green atoms) is a large tetravalent cation, e.g. Ce^{4+}, Zr^{4+}, Th^{4+} etc and "O" (the red atoms) is an anion. Oxides of the fluorite structure, particularly ZrO_2 and CeO_2, have great technological importance in structural, electrical, and chemical applications. It is a common structure for binary compounds in which the cation is large enough that eight-fold co-ordination is preferred. The fluorite structure is based on FCC close packing of the cations surrounded by eight oxygen ions with all tetrahedral interstices filled by anions. The co-ordination of the cations around anions is 4.

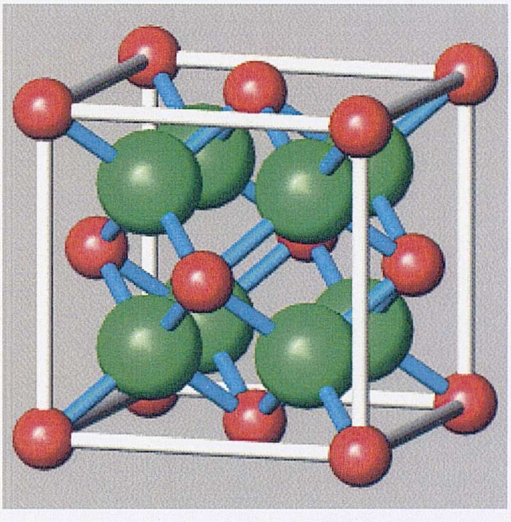


Fig 3.1: - Fluorite Structure [1]

3.2 Perovskite Structure

Perovskite structure stands out more among the variety of crystal structures found in nature or synthesised by man because of its peculiar ability to "tolerate" different types of distortion and imperfections. This leads to a very complex and occasionally unique interplay between structure, chemical composition and physical and chemical properties of the material.

The ideal perovskite structure has a general chemical formula of ABO_3, where "A" and "B" are cations and "O" is an anion. The "A" and "B" cations can have a variety of charges and in the original mineral perovskite ($CaTiO_3$) the A-cation is divalent and the B-cation is tetravalent. The A-cation is larger than the B-cation, but comparable with the radius of the oxygen anion **[2]**. The structure of a cubic perovskite is shown in Figure 3.2, **[3-6]** where the A-site cation is shown as the large blue spheres, which occupy the corners of the cube and have twelve-fold oxygen co-ordination, the B-site cation as the yellow sphere, situated at the centre of the cube, are octahedrally co-ordinated by six oxygen ions and oxygen ions as the red spheres, situated at the face centre of the cube. The perovskite structure can be also regarded as a cubic sequence of close packed AO_3 layers with B-cations occupying octahedral interstitial sites **[7]**.

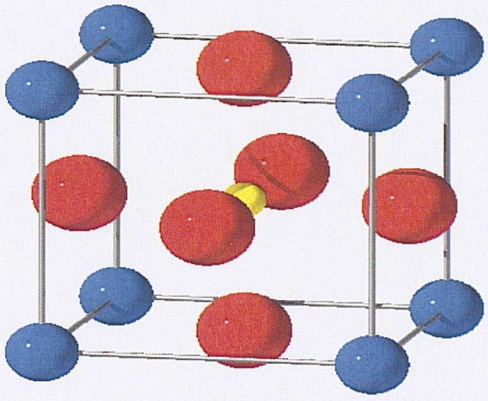


Fig 3.2:- The cubic perovskite unit cell [8]

Although the perovskite structure is very common, it is only one of several crystal structures found in the compounds with general formula ABO_3. The particular structure adopted by the ABO_3 compound is dependent on numerous factors (e.g. ionic radii, electronegativity, valence etc). For example, perovskites are formed when the radius of A cations is approximately equal to the radius of O anions whereas B cations are small enough to fill octahedral vacancies. On the other hand, when A and B cations are comparable in size and fit the octahedral interstitial sites of the close packed O framework, the corundum or ilmenite structures are formed.

Another description of the perfect cubic perovskite structure is to consider corner linked BO_6 octahedra with interstitial A cations. In an idealised cubic perovskite constructed or rigid spheres, each cation is large enough to be in contact with an oxygen anion, the radii of the ions can be related via:

$$R_A + R_O = \sqrt{2}(R_B + R_O)$$

Where R_A, R_B, and R_O are the relative ionic radii of the A-site and B-site cations and the oxygen ion respectively.

However, in a real structure, the ions are not rigid spheres and as the A cation decreases in size, there will become a point where it will be too small to remain in contact with the anions in the cubic structure. Therefore the B-O-B links bend slightly tilting the BO_6 octahedra to bring some anions into contact with the A cations **[9]**. To allow for this distortion, a constant, t, is introduced into the above equation, thus:

$$R_A + R_O = t\sqrt{2}(R_B + R_O)$$

Where t is known as the Goldschmidts tolerance factor and can be used as a measure of the degree of distortion of a perovskite from ideal cubic. Therefore, the closer to cubic, the closer the value of the tolerance factor is to unity **[10]**.

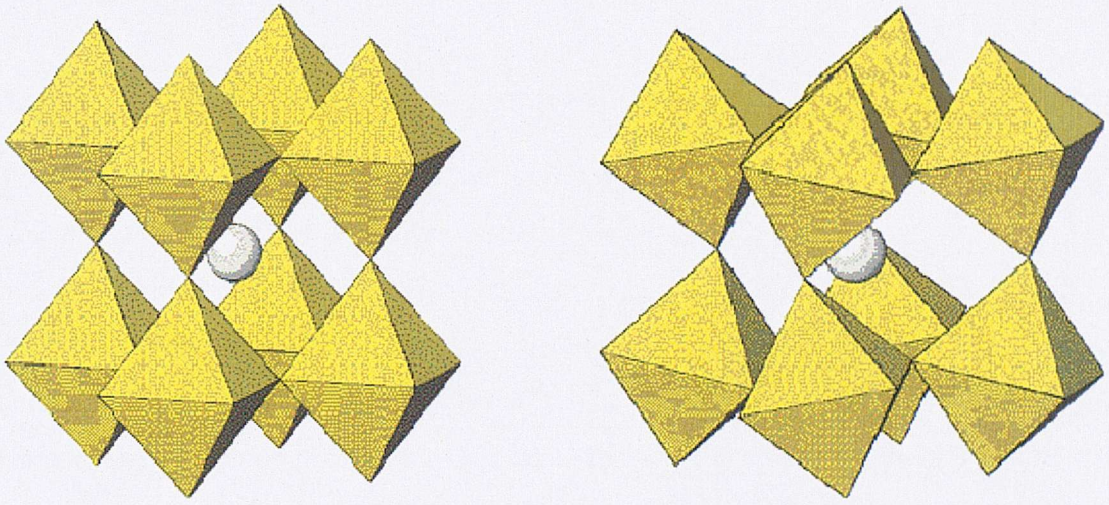


Fig 3.3:- Perovskite distortion from cubic (left) to Orthorhombic (right)

Limiting values for the tolerance factor have been determined through experiment and thus it can be said that the perovskite will be cubic if $0.9 < t < 1.0$, and will be orthorhombic if $0.75 < t < 0.9$ (Figure 3.3) **[9]**. When t values are smaller than 0.75, the ilmenite structure is often formed. Whereas, when $t > 1$, the phases with an increased proportion of hexagonally stacked AO_3 layers can appear (e.g. $SrMnO_3$) **[6]**.

3.3 Defect Chemistry

In a perfect crystal, all the atoms are at rest on their correct lattice positions. Only at the unattainable absolute zero Kelvin, will a crystal be perfect, in other words; at all real temperatures, the crystals are imperfect. The imperfections of crystals are called crystal defects **[11]**. In terms of the ideal perfect crystal, atomic vibrations and excited electrons can be regarded as defects. However, the degree of imperfection varies from compound to compound. There are always one or more defects in a crystal, and their presence can be explained thermodynamically.

$$\Delta G = \Delta H_f - T\Delta S$$

where G = free energy

H = enthalpy of formation of one defect

S = entropy of formation of one defect

T = absolute temperature

To form one defect at constant pressure (the usual situation), we have to add some energy to the crystal, ΔH_f, but the defect will create a disorder leading to a considerable increase of the entropy, ΔS. The free energy, ΔG, which is the difference between the enthalpy of formation of defect and the product of the entropy with the absolute temperature will then be minimized. The created disorder will become less important as the number of defects increases. There will be little change in the entropy energy as there will be less choice for the defect locations, and eventually the entropy energy will become stable. However, the enthalpy of formation of defects will continue to rise and hence the increase in the free energy too. The minimum free energy will be achieved at an equilibrium defect concentration **[12]**.

Defect reactions can be written in a similar format to normal chemical reactions, but using a special notation to describe the defects, this is called Kröger-Vink notation **[13]**. This notation is split into three sections: the main body, a subscript and a superscript.

- We define vacancies and interstitials as particles which occupy a defined site in a crystal and which may have a charge.
- Sites in a crystal are the points where the atoms, the interstitials, or the vacancies can be. The main body identifies whether the defect is an ion (e.g. Fe) or a vacancy "V". For a crystal composed of two kinds of atoms we have, e.g., the "A-sites" and the "B-

sites". The subscript shows where the defect is, i.e. what site is being occupied. An A-atom on an A-site we denote by A_A, a vacancy on a B-site is a V_B.

- This leaves the interstitials out of the picture. We therefore simply name all possible interstitials sites with their own place symbol and write A_i or B_i for an A-atom or a B-atom, respectively, on its appropriate interstitial site.
- The superscript (e.g. Fe_{Mg}^{X}) describes the effective charge on the defect: Positive effective charge is marked by a point or a dot (e.g. $A^{\bullet}$), and a dash or a hyphen represents a negative effective charge (e.g. $A^{/}$). If we consider a positively charged Na^{+} ion in the NaCl lattice, we write Na_{Na} as long as it is sitting on its regular lattice position, i.e. without a charge symbol. If we now consider a vacancy on the Na-site, the Na-ion as interstitial, or a Ca^{++} ion on the Na-site, we write V'_{Na}, $Na^{\bullet}_{i}$, and $Ca^{\bullet}_{Na}$ because this defines the net excess charge imposed by defect.
- Finally the defect has the same charge as the ion it is displacing, the subscript is an "X" (e.g. Fe_{Mg}^{X} represents a Fe^{2+} on a Mg^{2+} site). Defect reactions must conserve mass and charge **[14]**.

All the possible defects and its symbol are characterised in the Table 3.1:

TYPE OF DEFECT	SYMBOL
Cation atom	M
Anion atom	O
Vacant cation site	V_M''
Vacant anion site	$V_O^{\bullet\bullet}$
Cation on its site	M_M^X
Anion on its site	O_O^X
L^+ ion on M^{2+} site	L_M'
N^{3+} ion on M^{2+} site	$N_M^{\bullet}$
Cation interstitial site	$M_i^{\bullet\bullet}$
Anion interstitial site	O_i''
Free electron	e'
Free (electron) hole	$h^{\bullet}$
$^{\bullet}$ effective positive charge/ $^{/}$ effective negative charge/ ^{X} effective neutral charge	

Table 3.1: Defects symbols

Defects are present in all materials; these can be classified into the following:

- **Point defects** - atoms missing or in irregular places in the lattice (lattice vacancies, substitutional and interstitial impurities, self-interstitials). These can be divided into Frenkel and Schottky disorder, and these often occur in ionic crystals.
- **Linear defects** - groups of atoms in irregular positions (e.g. dislocations).
- **Planar defects** – the interfaces between homogeneous regions of the material (grain boundaries, stacking faults, external surfaces).

Defects can be either intrinsic or extrinsic. Intrinsic defects arise in pure materials due to lattice excitation whereas extrinsic defects arise from the addition of impurity or solute ions into the lattice **[15]**, these dopants can be aliovalent or isovalent, which will alter the compensation mechanism that will occur. The two most common disorders in crystalline ionic materials are Frenkel and Schottky (Figure 3.4). These are intrinisic disorders since they can be thermally generated in a perfect crystal.

Frenkel disorder is formed when an atom is displaced from its normal site into an interstitial site forming a defect pair: a vacancy and an interstitial. It is a pair of cation (positive ion) vacancy and a cation interstitial. Or it may also be an anion (negative ion) vacancy and anion interstitial. However anions are much larger than cations and it is not easy for an anion interstitial to form. The cation and anion Frenkel disorder for a binary oxide MO is represented in equation below by Kronger-Vink notation:

$$\text{Cation Frenkel} \quad M_M^{\,X} \Leftrightarrow M_i^{\bullet\bullet} + V_M^{''}$$

$$\text{Anion Frenkel} \quad O_O^{\,X} \Leftrightarrow V_O^{\bullet\bullet} + O_i^{''}$$

The Schottky disorder reaction is unique to metals and ionic crystals and is the simultaneous formation of both cation and anion vacancies with the creation on one formula unit of extra lattice **[16]**. The Schottky disorder for a binary oxide MO is represented in equation below by Kronger-Vink notation:

$$null \Leftrightarrow V_M^{''} + V_O^{\bullet\bullet}$$

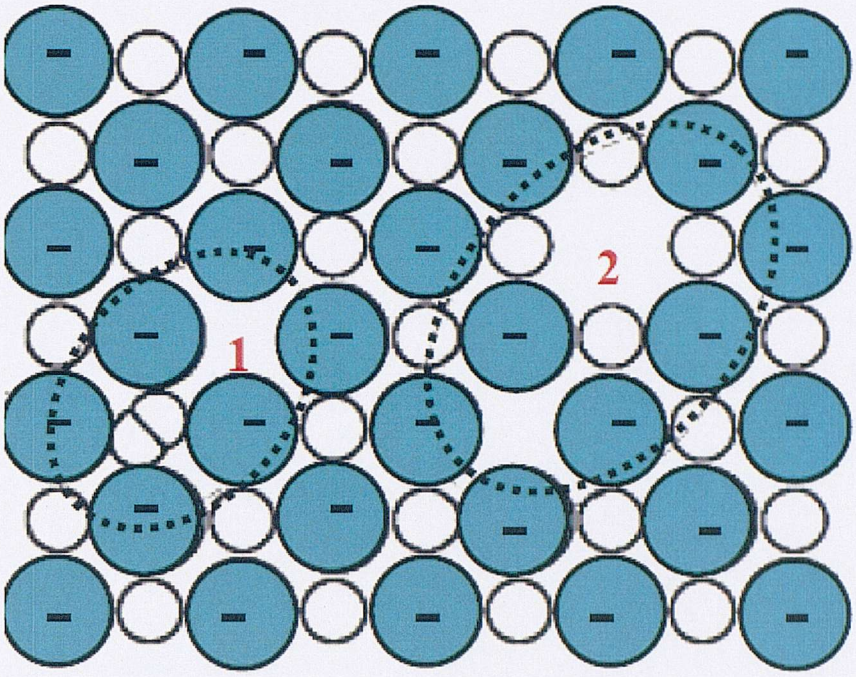


Fig 3.4: Schematic representation of (1) Frenkel defect (vacancy-interstitial pair) and (2) Schottky defect (a pair of cation and anion vacancies) in an ionic crystal.

As opposed to intrinsic defects, extrinsic defects are formed only by the addition of impurities or solutes. An interstitial defect is simply a foreign atom that has been forced into an interstitial position [17].

3.3.1 Doping Effects

An important practical way of increasing the concentration is by means of doping with aliovalent ions. This involves partial replacement of ions of one type by ions of different formal charge [18]. In order to retain charge balance, either interstitial ions or vacancies are formed which are able to migrate, so that dramatic increases in the conductivity can result.

Acceptor Doping involves the addition lower valent cations, which donates electrons to the conduction band.

Donor doping involves the addition of higher valent cations.

3.3.2 Defects in Perovskite Oxides

The Schottky reaction in the perovskite lattice of a general formula ABO_3 can be written as:

$$"null" \rightarrow V_A^{'''} + V_B^{'''} + 3V_0^{\bullet\bullet}$$

The other possible defect reactions are cation and anion Frenkel mechanisms; here the cations or the anions are displaced from their respective lattice positions and move into interstitial positions within the lattice leaving behind a vacancy. The reactions are given below in Kröger-Vink notation:

$$A_A^X \rightarrow A_i^{\bullet\bullet\bullet} + V_A^{'''}$$
$$B_B^X \rightarrow B_i^{\bullet\bullet\bullet} + V_B^{'''}$$
$$O_O^X \rightarrow O_i^{''} + V_O^{\bullet\bullet}$$

Another defect process is the anti-site reaction. The anti-site reaction is considered for the cation sub-lattice. The cations on the A-site and those on the B-site "swap" lattice positions. The reaction is shown below in Kröger-Vink notation:

$$A_A^X + B_B^X \rightarrow A_B^X + B_A^X$$

It can be seen from the equation that the reaction is charge neutral. This is only true for +3/+3 valence combination perovskites. But, for +2/+4 valence combination perovskites; e.g. $BaTiO_3$, then it would be:

$$Ba_{Ba}^X + Ti_{Ti}^X \Leftrightarrow Ti_{Ba}^{\bullet\bullet} + Ba_{Ti}^{''}$$

However, due to the significantly different ionic radii of the cations on the A- and B-sites, there will be a large distortion caused by this reaction.

For fuel cell applications, the electrical conductivity of the oxides is often enhanced by substituting acceptor- or donor-type cations for either the A or B sites. The most commonly used perovskite oxides for cathode in SOFCs are $LaMnO_3$. The electrical conductivity of $LaMnO_3$ is considered to be due to 3d electrons of Mn^{3+}ions. An increase in conductivity is expected when a lower-valence ion is substituted for either the La^{3+} or Mn^{3+} sites resulting in the formation of Mn^{4+}.

The cathode materials to be used in this research are LSCF ($La_{0.6}Sr_{0.4}Co_{0.2}Fe_{0.8}O_{3-\delta}$), GSC ($Gd_{0.6}Sr_{0.4}CoO_3$) and SSC ($Sm_{0.5}Sr_{0.5}CoO_3$). Here we shall look at the defect chemistry of the LSCF material. The ideal perovskite structure of this material is $LaCoO_3$ where the A site is being a rare earth, here Lanthanum (La is a trivalent cation)

and is doped by Strontium, and the B site is a transition metal, cobalt and is doped by iron **[19]**. The transition metal readily changes its oxidation state and it is largely responsible for the electronic conductivity of the oxide under different oxygen partial pressure (PO_2). A proposed defect chemistry of this perovskite-type oxide is discussed below.

The intrinsic schottky and electronic equilibrium of $LaCoO_3$ is represented by

$$null = V_{La}^{'''} + V_{Co}^{'''} + 3V_O^{\bullet\bullet}$$
$$K_S = \left[V_{La}^{'''}\right]\left[V_{Co}^{'''}\right]\left[V_O^{\bullet\bullet}\right]^3$$

$$null = e^{'} + h^{\bullet}$$
$$K_e = np$$

The K_S and K_e are the corresponding equilibrium constants.

The p-type nonstoichiometric reaction and is given as

$$\frac{3}{2}O_2 = V_{La}^{'''} + V_{Co}^{'''} + 3O_O^{X} + 6h^{\bullet}$$

but as $\left[V_{La}^{'''}\right] = \left[V_{Co}^{'''}\right]$, the cation stoichiometry must remain constant.

Hence, the equilibrium constant is given by

$$K = \left[V_{Co}^{'''}\right]^2 p^6 PO_2^{-\frac{3}{2}}$$

The Kröger-Vink notation below represents the dopant addition of SrO to $LaCoO_3$:

$$2SrO(LaCoO_3) \rightarrow 2Sr_{La}^{'} + V_O^{\bullet\bullet} + 2O_0^{X}$$

When $LaCoO_3$ is doped with SrO, the substitution of Sr^{2+} for the La^{3+} site results in the formation of $Sr_{La}^{'}$ which possesses one negative charge. This charge will be compensated for either by $Co^{3+} \rightarrow Co^{4+}$ **[20]** or by the formation of oxygen ion vacancies.

The electroneutrality condition then is expressed as

$$2\left[V_O^{\bullet\bullet}\right] + p = 6\left[V_{Co}^{'''}\right] + \left[Sr_{La}^{'}\right]$$

Where p represents the concentration of positive holes, i.e. $p = [h^{\bullet}]$.

Figure 3.5 summarises the defect behaviour in various oxygen partial pressure regions for $LaCoO_3$ perovskites doped with SrO acceptor dopant **[21]**.

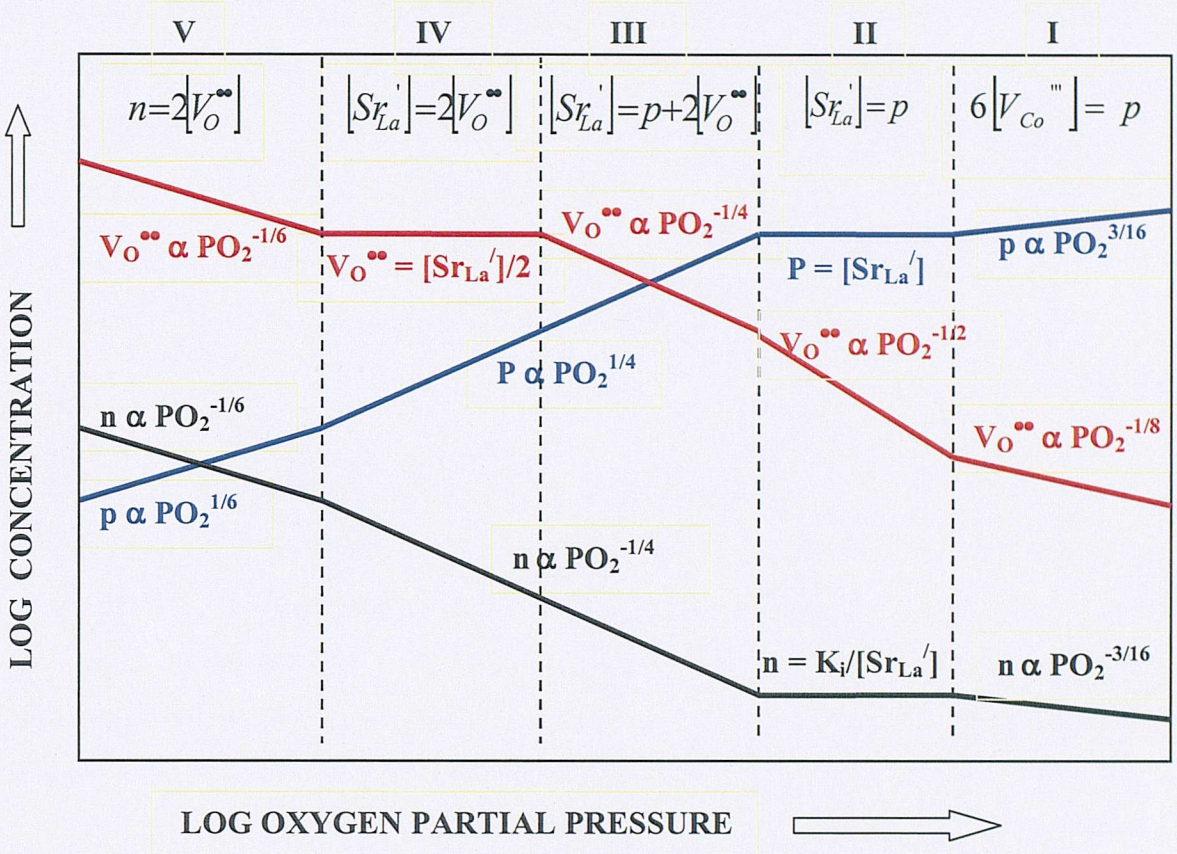


Fig 3.5: Brouwer diagram of partial pressure vs concentration

Region I : the oxygen partial pressure is very high, so native nonstoichiometry prevails as compensation is achieved by the formation of electron holes. Hence the electroneutrality becomes

$$6[V_{Co}''']= p$$

Region II: where the oxygen activity is slightly lower, both $[V_O^{\bullet\bullet}]$ and $[V_{Co}''']$ are smaller than the concentration of the dopant SrO, the electroneutality becomes

$$[Sr_{La}']=p$$

Region III: the oxygen partial pressure is decreased further; hence oxygen is lost to form oxygen-ion vacancies. The elecroneutrality condition is then represented by

$$[Sr_{La}']=p+2[V_O^{\bullet\bullet}]$$

Region IV: The loss of lattice oxygen continues with further decreases of the oxygen partial pressure until in this region where the dopant concentration exits total control and $[V_O^{\bullet\bullet}]$ is independent of the oxygen activity. The electroneutrality then becomes

$$[Sr_{La}']=2[V_O^{\bullet\bullet}]$$

Region V: with very low oxygen partial pressure, the transition metal ion, Co can be reduced further from Co^{3+} to Co^{2+}. The reduction then becomes the dominant reaction in this region.

$$n=2\left[V_O^{\bullet\bullet}\right]$$

Same effect is obtained when $LaCoO_3$ is doped with Fe_2O_3. Fe substitutes for Co to compensate the expansion coefficients associated with $LaCoO_3$.

3.4 Ionic, Electronic and Mixed Conductivity

The conduction process occurs by the diffusion of oxygen ions via the vacancies. Quantification of ion migration can be achieved under an applied electric field by the ionic conductivity, σ_i.

When the electric field is applied charge carriers are accelerated, the scattered carriers achieve a drift velocity, V. Thus the current density, J is given by:

$$J = nqV$$

n $\rightarrow$ concentration of a charge carrier

q $\rightarrow$ corresponding charge

Drift velocity can be defined as

$$V = \mu E$$

Where E is electric field.

Ohms law states that $J = \sigma E$, where σ is the conductivity.

Thus $\sigma = nq\mu$ and the ionic conductivity is expressed as:

$$\sigma_i = n_i q_i \mu_i$$

In general for an oxide, there are more than one charge carrier. In this case conductivity, σ can be rewritten as the sum of all the partial conductivities:

$$\sigma_t = \sum nq\mu$$

In the absence of an applied field, thermal vibrations proportional to kT cause ions and vacancies to exchange sites. The Nernst-Einstein equation links this process of self-diffusion coefficient, D_{self} with the ion drift (mobility) caused by an electric field as follows:

$$\mu_i = \frac{q_i D_{self}}{kT}$$

where K is the boltzmann's constant and T is the absolute temperature. By combining this equation and the conductivity equation, one can obtain a relationship for the ionic conductivity and diffusivity:

$$\sigma_i = \frac{n_i q_i^2 D_{self}}{kT}$$

Depending on the majority charge carriers, ceramic oxides can be classified as electronic conductors (electrons or electron holes), ionic conductors (ions) or mixed conductors, where both high ionic and electronic conductivities are possible. The total conductivity, σ_t, of a particular ceramic oxide will be the sum of the contributions from each species and can be represented by:

$$\sigma_t = \Sigma\sigma_j$$

where j represents the contributing species or charge carrier.

In order to specify the proportion of the total conductivity that results from each species, it is convenient to define a parameter known as the transference or transport number, t. In the case of electrolytes, it is the ionic conductivity that dominates and therefore the ionic transference number, t_i, can be defined as:

$$t_i = \frac{\sigma_i}{\sigma_i + \sigma_e}$$

Where

$\sigma_i \rightarrow$ ionic conductivity and

$\sigma_e \rightarrow$ electronic conductivity.

The ionic transport number for an ionic conductor should be close to 1 and can vary with oxygen partial pressure. By changing the partial pressure, it is possible to modify the defect structure and hence the conductivity of the material.

3.4.1 Conductivity in Perovskite Oxides

The total conduction process in a perovskite oxide is generally mixed ionic and electronic (MIEC). An oxide mixed ionic and electronic conductor requires oxygen vacancies and transition metal cations.

Sr, Mg, Ca, Fe, and Mn are all acceptor dopants. The Sr^{2+} ions have similar ionic radii to La^{3+} which substitute onto the A site in the perovskite-type $LaCoO_3$ lattice. Fe^{2+}, having a similar ionic radius to Co^{3+}, substitutes onto the B site.

For electronic compensation of the acceptor dopant, the charge imbalance in the lattice is accommodated by driving the oxidation state of the Co ion from 3+ to 4+. The lattice now contains Co^{3+} and Co^{4+} ions on equivalent sites, which is the model situation for electronic conduction by a small polaron hopping mechanism. Driving the oxidation state of the cobalt creates a hole available for conduction, but changing the oxidation state forces a change in the ionic radius of the ion, which produces polarisation of local regions of the lattice and effectively traps the charge. The combined ion, trapped charge and polarisation or lattice distortions are known collectively as a small polaron **[14]**. The small polarons formed can jump to equivalent sites in the lattice by a temperature activated hopping process. Electronic compensation therefore leads to the formation of mobile charge carriers and the electronic conductivity of the compound is significantly increased.

Another mechanism by which charge compensation for acceptor dopants can be achieved is termed ionic compensation. For ionic compensation, the charge lattice is corrected for by the formation of oxygen vacancies. In the case of ionic compensation, the formation of oxygen vacancies is likely to lead to a slight increase in the ionic conductivity of the ceramic, but no additional contribution to the electronic conductivity is anticipated.

Figure 3.5 is a Brouwer diagram for acceptor doped $LaCoO_3$ oxide. The Brouwer diagram is a plot of the logarithm of concentration of point defects as a function of the logarithm of partial pressure of oxygen. The concentrations of defects can be multiplied by their respective mobilities to give partial conductivity diagrams as a function of PO2. The diagram shows five regions of PO_2 over which compensation mechanisms or combination of compensation mechanisms are predicted to dominate. Regions I and V correspond to the formation of cation vacancies and the formation of extrinsic electrons respectively but these regions are at the extremes of the PO_2 range and rarely observed in practice. Region II corresponds to pure electronic compensation and region IV is pure ionic compensation. In region III, both electronic and ionic compensation mechanisms are achieved.

3.5 References

[1] S.J. Skinner and J.A. Kilner, Oxygen Ion Conductors, Materials Today, 2003.

[2] R.C. Evans, chapter 8, In: An Introduction to Crystal Chemistry, 2nd ed., Cambridge University press, 1964.

[3] D. Waller, J.A. Kilner, J.A. Lane and B.C.H. Steele, Solid State Ionics, 1996.

[4] B.C.H. Steele, Solid State Ionics (2000), 134(3).

[5] J.M. Ralph, J.T. Vaughey and M. Krumpelt, Electrochemical Society Proceedings, 16 (2001), p466-475.

[6] O. Yamamoto, Electrochimica Acta, 45 (2000), p2423-2435.

[7] J.M. Ralph, A.C. Scholer and M. Krumpelt, Journal of Materials Science, 36 (2001), p1161-1172.

[8] G.H. Haertling, Ceramic Materials for Electronics, edited by R.C. Buchanan, p 139, Marcel Dekker, New York (1986)

[9] N. Brandon, D. Hart, Introduction to Fuel Technology and Economics (1999). Centre for Energy Policy and Technology, London, UK.

[10] K. Joon, Journal of Power sources (1998), 71, p12-18.

[11] W.D. Kingery, H.K. Bowen, D.E. Uhlmann, Introduction to Ceramics ~ 2nd ed., John Wiley (1976), chapters 4, 6 and 17.

[12] Y-M. Chiang, I. Birnie, W.D. Kingery, Physical Ceramics: Principle for Ceramic Science and Engineering, John Wiley and Sons, (1997).

[13] F.A. Kroger, H.J. Vink, Solid State Physics, 307, (1956).

[14] P.A. Cox, The electronic structure and chemistry of solids, Oxford Science publications, Oxford University Press, Oxford, (1987).

[15] I. Bunget, M. Popescu, Physics of solid dielectrics, Elsevier, Amsterdam, (1984).

[16] H.L. Tuller, ceramic materials for electronics, Marcel Dekker INC, New York, (1986).

[17] J.L. Cohn, J.J. Neumeier, C.P. Popoviciu, K.J. McClellan, T. Leventouri, Physical Reviews B, 56, (1997), R8495-R8498.

[18] R.J.D. Tilley, Defect Crystal Chemistry and its Applications (1987), Blackie, Glasgow, p4.

[19] H.U. Anderson, in Proceedings of the 14th Riso International Symposium on Materials Science (eds. F.W. Poulsen, J.J. Bentzen, T. Jacobsen, E. Skou and M.J.L. Ostergard), (1993), p1.

[20] H.U. Anderson, Solid State Ionics, 52 (1993), p33.

[21] P. Kofstad and A. Petrov, in Proceedings of the 14th Riso International Symposium on Materials Science (eds. F.W. Poulsen, J.J. Bentzen, T. Jacobsen, E. Skou and M.J.L. Ostergard), (1993), p287.

Chapter 4 - Literature Review

4.1 Materials for Interconnect

Due to the demands placed on the interconnect component, there are many materials that are currently being developed. The most commonly used interconnect materials are lanthanum chromite ($LaCrO_3$ - these belongs to the perovskite family ABO_3) and high chromium content alloys. However, these ceramics do not fulfil some of the requirements: there is a thermal expansion mismatch with zirconia and a poor sinterability in oxidising conditions. To overcome these problems, $LaCrO_3$ is doped with appropriate dopants such as alkaline earth cations (Mg^{2+}, Sr^{2+} etc) and isovalent cations as Al^{3+} and Mn^{3+}. These are then stable in the two extreme environments (oxidising and reducing environments) and have a good compatibility with the electrode materials. With the drive to operate SOFCs at lower temperature, it will be possible to switch from ceramic to metallic materials for the interconnect. Ferritic stainless steels are the most promising alloys.

The ferritic stainless steels contain a minimum of 10.5% chromium, although there are heat-resisting grades with lower chromium and high aluminium contents. Provided the level of austenite stabilising elements, (principally carbon, nitrogen, and nickel), is kept low and the chromium content is above about 14%, then the crystal structure is ferritic (bcc) over normal processing and operating temperatures. The coefficient of thermal expansion of the ferritic materials is around $12 \times 10^{-6}\ K^{-1}$ at 500°C.

These metals appear advantageous over ceramics because of their greater mechanical strength and toughness, much cheaper, easy to fabricate, dense, have excellent electrical conductivity, undergo no phase transformations and have a thermal expansion coefficient, which is similar to the other components in the cell. The main problem for the stainless steel interconnect is the formation of an oxide scale on the cathode side, which introduces a high electrical resistance into the SOFC. Alloying and applying a conducting ceramic coatings on to the stainless steel interconnect will solve these oxide scale problems.

4.2 Materials for Anode

Several metals such as nickel and cobalt and noble metals such as platinum and palladium have been suggested for the anode in the early sixties. The use of these pure metals is impractical due to poor thermal expansion compatibility with the electrolyte. The most commonly selected anode material was then Ni-YSZ cermet because of its relatively low cost. This has several advantages due to its composite structure. Nickel is suggested to be a good catalyst as well as electronically high conductive metal. YSZ provides good thermal compatibility when the electrolyte material is also YSZ. Nowadays porous CGO cermet has been optimised as a state-of-art anode material in place of YSZ. Recent work has shown that the composite Ni/CGO anode has excellent ITSOFC properties at 700°C and below **[1]**. When ceria is placed in a reducing environment, Ce^{4+} tends to reduce to Ce^{3+}, which introduces electrons into the ceria lattice. The ceria structure is no longer insulating, however more electrons in the system should enhance the electronic conductivity **[2]**.

4.3 Materials for Electrolytes

Fluorite-type oxides are commonly ionic conductors and have been considered for use as electrolytes in SOFCs. Traditionally, stabilised-zirconia has been the most common electrolyte material in SOFC operation. Zirconia in its pure form is not a good electrolyte, since it possesses a low ionic conductivity and it has distruptive phase transformations on heating and cooling. However stabilised-zirconia commonly doped with yttria (YSZ) has fully met the requirement of an electrolyte material. Not only does YSZ fulfil the electrical requirements for a SOFC, but it also has good high-temperature mechanical properties for a ceramic. Operational temperatures have been reported around 700-800°C **[3]**. Yttria stabilised zirconia exhibits ionic conductivity higher than 0.1 Scm^{-1} at 1000°C and the electronic conductivity is less than 10^{-4} Scm^{-1} in the entire oxygen potential range used for the SOFC operation. The maximum conductivity is observed at about 10mol% yttria substitution.

It is reported that partially substituted lanthanum gallate based perovskite oxides exhibit high oxide ion conductivity at relatively lower temperature (< 800°C), which is comparable with that of YSZ at 1000°C over a broad range of oxygen partial pressure values in SOFCs **[4]**. These $LaGaO_3$ based powders prepared by glycine nitrate

combustion synthesis in different compositions partially substituted with 10-20 mol% Sr in the "A" site and 15-20 mol% Mg on the "B" site of the perovskite structure exhibited higher conductivity than YSZ. The superior electrical and chemical properties make it a candidate for use as the solid electrolyte in SOFC (for around 600-700°C operation) **[5]**. The increased conductivity in the gallates was attributed to both the greater oxygen ion mobility and a greater concentration of oxygen ion vacancies relative to YSZ **[6 and 7]**.

As stated earlier, reduced operational temperatures will significantly reduce the cost of the fuel cell. Operating at lower temperature will also significantly reduce reported problems of interfacial diffusion between electrodes and the electrolyte **[8]**. Recent works have shown that gadolinia-doped ceria (CGO) has received considerable attention as the most promising electrolyte candidate for operation at 500-600°C **[9 and 10]**. The undoped CeO_2 has n-type electrical conduction, and the conduction takes place by a small polaron hopping mechanism. Pure CeO_2 has negligible ionic conductivity. Similar to Zirconia, ceria doped with divalent or trivalent oxides produces excellent oxygen-ion conductors. Doping with a lower valent metal oxides introduces oxygen vacancies into the host lattice that make these materials potential electrolytes in SOFC operating at approximately 500°C. Figure 4.1 shows the specific ionic conductivities of YSZ compared to CGO as a function of temperature. Assuming a target value of 0.15 Ωcm^2 for the ohmic resistance of the electrolyte, a thin supported CGO electrolyte will have a sufficient electrical property at 500°C. The minimum theoretical temperature for a YSZ electrolyte is approximately 200°C higher.

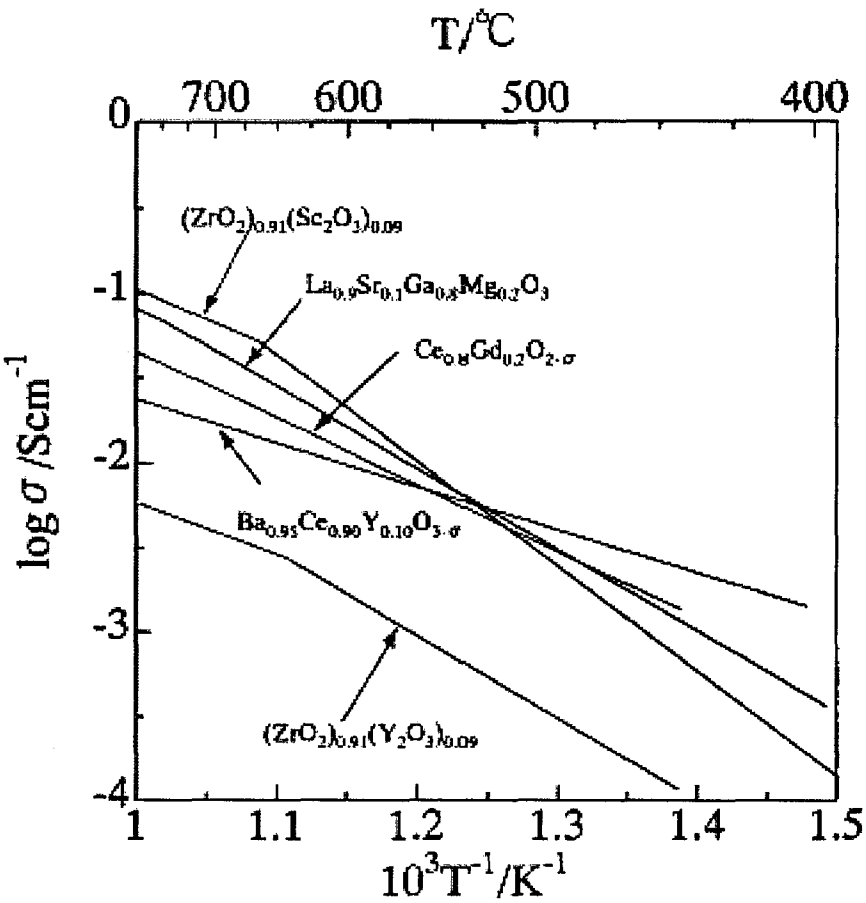


Figure 4.1:- Temperature dependence of electrical conductivity for oxide ion conductors (lower temperature range) [11]

Not only it has a high ionic conductivity, but also a low conduction activation energy. The only problem is that, in reducing conditions (at low oxygen partial pressures, $PO_2 = 10^{-19}$ atm) the Ce^{4+} reduces to Ce^{3+}, introducing electronic conductivity according to the following Kröger-Vink equation:

$$O_O^{\ X} \leftrightarrow V_O^{\bullet\bullet} + \frac{1}{2}O_{2(g)} + 2e^-$$

Under these conditions electronic conductivity is introduced, which causes internal short-circuiting in the cell and lattice expansion which causes associated mechanical stresses. The increase in electronic conductivity due to the formation of Ce^{3+}, severely restricts the ionic domain of CeO_2 based electrolytes so that they cannot be used at high temperatures (> 700°C). This reduction restricts the range of oxygen partial pressure over which the ionic transference number remains close to unity. Thus, at 800°C the

oxygen partial pressure ranges for predominant ionic conduction in CeO_2 limited to about 10^{-12} atm (10^{-7} Pa). In view of the tendency of CeO_2 be reduced in a reducing environment, doped CeO_2 has been considered for use as SOFC electrolyte, especially at reduced temperature, because of its ionic conductivity. Compared to stabilised ZrO_2, doped CeO_2 shows a higher conductivity and a lower conduction activation energy **[12]**. At temperatures of approximately 500°C and below the electrolytic domain is wide allowing efficient fuel cell operation and low electronic conductivity and hence does not affect the cell performance.

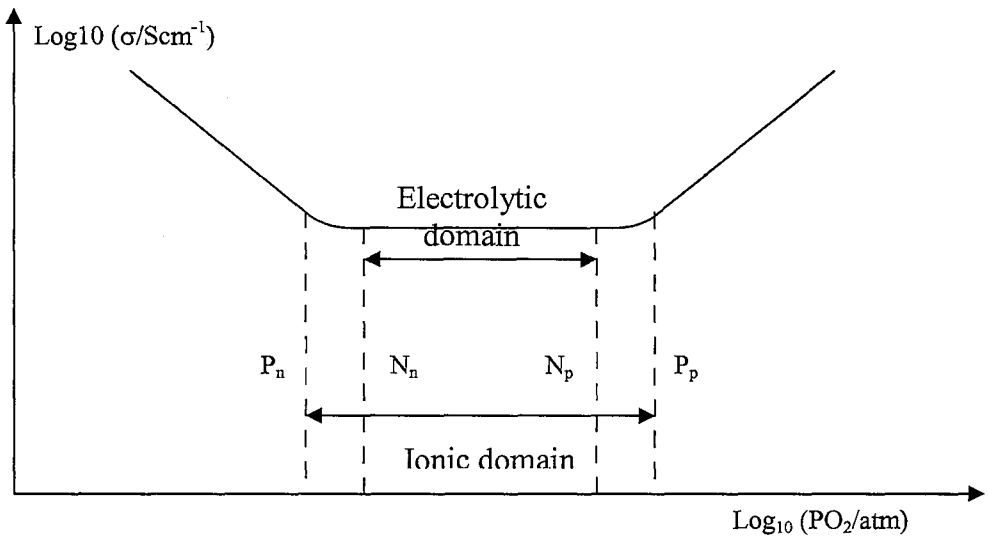


Figure 4.2: - Total electrical conductivity as a function of oxygen partial pressure

The ionic domain boundaries P_p and P_n of a fluorite-type oxide are the oxygen partial pressure at which $PO_2 = P_p$ when $\sigma_i = \sigma_p$ and $PO_2 = P_n$ when $\sigma_i = \sigma_n$. Within this oxygen pressure range and away from the boundaries, the oxide is considered to be an ionic conductor. The electrolytic domain boundaries are the oxygen partial pressures where $PO_2 = N_p$ and $PO_2 = N_n$. Within this oxygen partial pressure range, the conductivity of the oxide is exclusively ionic.

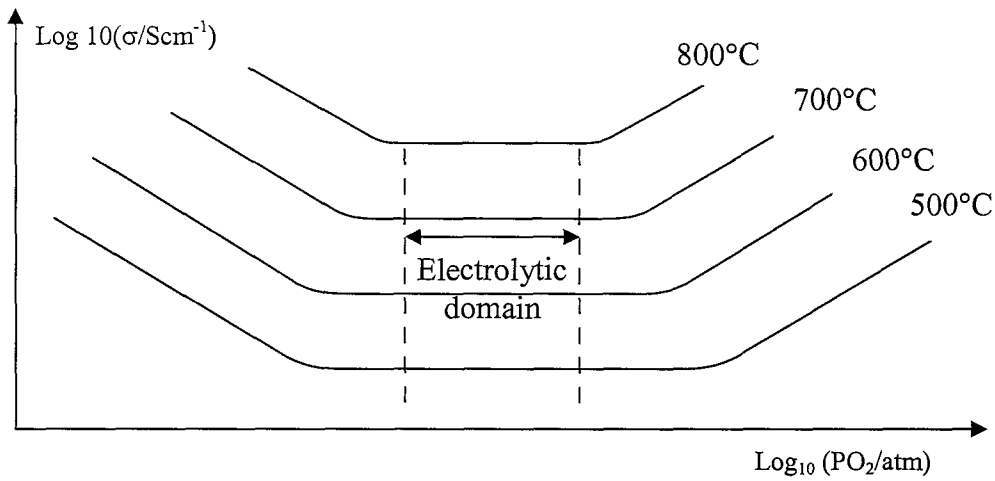


Figure 4.3: - Total electrical conductivity as a function of oxygen partial pressure.

The range of electrolytic domain increases with decreasing temperature as can be seen on Figure 4.3.

4.4 Materials for cathodes

During the early stage of SOFC development, metallic materials were extensively investigated for the cathode of SOFC. However, only noble metals like platinum, palladium, gold, silver, etc can be possible for cathodes because of its highly active oxidising condition. These were however rejected because of their high cost. Silver has relatively good electrode conductivity on YSZ electrolyte. However it is not stable in the long term because of its low melting temperature (T_m = 961°C) and volatility. Composite cathodes consisting of zirconia electrolyte powder and noble metal current collectors exhibited good performance but again were not considered to be economically viable solutions.

Sr – doped $LaMnO_3$ (LSM) for some years has been regarded a good cathode material in the SOFC for high temperature operation. This material has a close thermal expansion match with the YSZ electrolyte, remains stable in oxidising atmospheres, and has sufficient electrical conductivity at 1000°C. $LaMnO_3$ belongs to the class of perovskite oxides. This material melts at about 1880°C. Undoped stoichiometric $LaMnO_3$ is orthorhombic at room temperature and shows an orthorhombic/rhombohedral crystallographic transformation at about 600°C. At the operating temperature, $LaMnO_3$ is stable in oxidising atmospheres but decomposes under highly reducing conditions. $LaMnO_3$ has intrinsic p-type conductivity due to the

formation of cation vacancies. The material has an electrical conductivity of 0.1 Scm^{-1} at 700°C. The electrical conductivity of $LaMnO_3$ has been enhanced for SOFC applications by substituting a lower valence cation on either the A or B sites.

The electronic conductivity and thermal expansion coefficient of LSM increases approximately linearly with increasing Sr concentration. The oxygen diffusion coefficient and surface exchange coefficient for $La_{1-x}Sr_xMn_{1-y}O_3$ at 700°C were found to be 1×10^{-13} cm^2s^{-1} and $2\times10^{-9}cms^{-1}$ **[13]**. Unfortunately, the LSM cathode reacts with the YSZ electrolyte to form $SrZrO_3$ **[14]** for Sr concentrations above about 30mol%. Therefore, LSM compositions have Sr concentrations of 10-20mol%.

At high temperatures the Mn cation is highly mobile and diffuse into the electrolyte changing the electrical and/or structural characteristics of both the electrolyte and the cathode. Another problem associated with the LSM material is the reaction at the LSM/YSZ interface that produces the insulating phase $La_2Zr_2O_7$ **[15 and 16]**. This occurs at temperatures above 1200°C, and hence the cathode fabrication was usually the final step in the cell manufacture to avoid these interfacial reactions between the electrolyte and the cathode.

One approach, which has been taken to improve the performance of the LSM cathode, is to dope the A-site or/and B-site with an ion that promotes the formation of oxygen vacancies. Several first-row transition metals (Co, Fe, Ni or Cu) substituted for the manganese ion in the LSM structure formed wide range of perovskites that have much higher electronic and ionic conductivities (mixed conductivity). A comprehensive comparison between most mixed conducting perovskites has recently been written by Kharton et al. **[15]**, showing that the cobalt-based perovskites display the highest ionic and electronic conductivities among the perovskites and these systems to be evaluated further. For theses cobalt-based perovskites, only CGO electrolytes have shown promise at low temperatures (no interfacial reactions have been detected between these cathodes and the CGO electrolyte when compared to YSZ electrolyte) **[11]**. Several layered cuprates have been studied at the Argonne National Laboratory (ANL), although their long-term stability is still uncertain. LSM and many other cathode compositions have been evaluated for use on YSZ electrolyte at operating temperatures of around 800-1000°C, where severe reactions between the electrolyte and cathode can occur. So the use of CGO electrolyte will shift the SOFCs to operate at relatively low temperatures of around 500-600°C.

A number of doped lanthanum cobaltite ($LaCoO_3$) have been proposed and investigated as potential SOFC cathode material **[17]**. $LaCoO_3$ is rhombohedral from room temperature to 1000°C, but the rhombohedral structure may transform to a cubic phase; the transformation temperature depends on the dopant concentration. $LaCoO_3$ has been to shown to have an intrinsic p-type conductivity, and the electrical conductivity can be enhanced by substituting a lower valence ion on the La site.

Initially, out of all the cobalt-based perovskites, most interesting were the $La_{1-x}Sr_xCoO_{3-\delta}$ (LSC) perovskites **[18]**, these materials possess considerable oxide ion conductivity and sufficient electronic conductivity (to make them of interest as mixed ionic-electronic conductors), when compared to LSM. It is believed that the substitution of Co for Mn, increases the catalytic activity and thus reduces polarisation losses **[19]**. Petrov and kofstad **[20]** have studied the crystal structure and electrical properties of $La_{1-x}Sr_xCoO_{3-\delta}$ with different strontium contents ($0.1 < x < 0.7$) as a function of temperature at PO_2 = 0.21 atm (air). The solid oxide solutions were rhombohedral at reduced temperatures and low values of x; at room temperature the transition taken place for x = 0.55. The electrical conductivity reached a maximum at $x \sim 0.4$. Under these conditions the electrical conductivity was approximately 3000 Scm^{-1} and decreased slowly with increasing temperature. LSC is of little use with the YSZ electrolyte, because it reacts with zirconia, however LSC has been regarded as a suitable cathode material with the $Ce_{0.8}Sm_{0.2}O_{1.9}$ (CSO) or CGO electrolyte for operation between 600-700°C. It has been shown that doping the A and the B sites of LSC, respectively produces a perovskite that can be stable in contact with ceria based electrolytes and produces low electrode resitivities at temperatures between 500-700°C.

One of the most promising systems to date has been produced by doping of the B-site in LSC, Fe for Co **[21-29]**. This perovskite – type oxides behaves as a mixed ionic-electronic conducting material. The substitution of A-site cation in LSCF by a lower valence cation forms both oxygen vacancies and causes a change of valence state in B-site cation to maintain charge neutrality. The concentration of oxygen vacancies can also be tailored by substituting ions of similar sizes but lower valence at B sites. As a result, the materials can exhibit not only high ionic conductivity because of the high concentration of oxygen vacancies but also a high electronic conductivity because of the mixed-valence states. Hence, they are called mixed conductors. It has been confirmed that perovskite-type ABO_3 compositions containing more than two types of transition

metal ions on the B site are always more reactive (for oxygen reduction) than those with only one type of transition metal ion **[30]**. It has been reported that LSCF is a p-type conductor, and Sr^{2+} (acceptor) partially substituting on the La^{3+} sites increases its electronic conductivity due to $Fe^{3+} \rightarrow Fe^{4+}$ and/or $Co^{3+} \rightarrow Co^{4+}$ transitions. Generally, the acceptor dopant (Sr) not only increases the electronic conductivity but also stabilizes the phase. Also, it has been reported that LSCF compositions with higher Sr and Co contents have higher oxygen permeability, which can exceed by more than one order of magnitude than that of YSZ electrolyte. This occurs because Sr on the A-site latice of LSCF acts as an acceptor, enhancing the formation of oxygen vacancies. In addition, Co ions on the B-site appear to have a smaller binding energy for oxygen than do Fe ions. Therefore the degree of oxygen deficiency is expected to be higher in the LSCF compositions with a higher Co content **[31]**. Among the various reports on LSCF compositions, $La_{0.6}Sr_{0.4}Co_{0.2}Fe_{0.8}O_{3-\delta}$ system has been shown to be a good compositional cathode material (based on catalytic activity) for use with ceria-based electrolytes **[32 and 33]**.

Tai et al. **[36 and 37]** have carried out some substantial studies of the $La_{1-x}Sr_xCo_{1-y}Fe_yO_3$ (LSCF) perovskites. It was determined that all compositions in the $La_{1-x}Sr_xCo_{1-y}Fe_yO_{3-\delta}$ (x = 0.2, 0.4) system had a perovskite-type structure. Both the thermal expansion coefficient and the p-type electrical conductivity increased with Co content. It was also shown that the conductivity and the thermal expansion coefficient can be reduced by doping of the B-site with Fe content and suggested that $La_{1-x}Sr_xCo_{0.2}Fe_{0.8}O_{3-\delta}$, with x = 0.2-0.4, were potential cathode compositions for SOFCs operating between 600-800°C. These compositions were single phase and stable throughout a wide range of temperature. Conductivity versus temperature plots showed the conductivity decreasing with Fe content. The peak conductivity of around 350 Scm^{-1} was achieved at the x = 0.4 composition, when studying the effect of the La:Sr ratio **[36]**. It was also found that the peak conductivity occurred around 550°C, which suggests a composition of $La_{0.6}Sr_{0.4}Co_{0.8}Fe_{0.2}O_3$ (LSCF) would be a suitable cathode material for intermediate temperature SOFC operation. Petric et al **[38]** found that for the system, $La_{1-x}Sr_xCo_{1-y}Fe_yO_{3-\delta}$, both the electrical conductivity and the thermal expansion coefficient decreases with iron content.

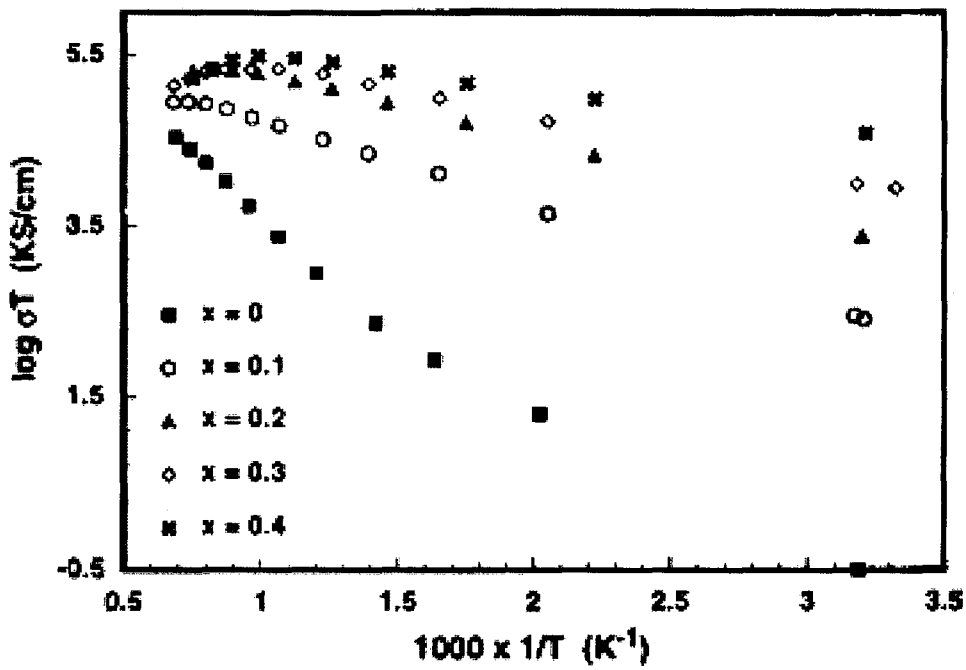


Figure 4.4:- Log σT versus 1000/T in air for $La_{1-x}Sr_xCo_{0.2}Fe_{0.8}O_3$ as function of Sr content (mol) [36]

Teraoka et al **[39]** measured the ionic (σ_i) and electronic (σ_e) conductivity of mixed conducting $La_{1-x}Sr_xCo_{1-y}Fe_yO_{3-\delta}$ materials. At 800°C, for instance, σ_i ranged in the order of 1-10^{-2} Scm^{-1} while σ_e was around 10^2 Scm^{-1}, indicating that the present oxides were good mixed conductors with ionic transport number $10^{-2} - 10^{-4}$. σ_i increases as contents of Sr and Co increased though Sr content was more influential. Ralph et al **[11]** showed that the area specific resistance, ASR of the $La_{0.8}Sr_{0.2}Co_{0.8}Fe_{0.2}O_3$ material on a CGO electrolyte was found to be around 0.3 Ωcm^2 at 700°C, which performed slightly better than $La_{0.8}Sr_{0.2}CoO_3$ on the same electrolyte. However the LSCF's resistance increased rapidly as decrease in temperature when compared to LSC, because it has higher activation energy than LSC. Doshi et al **[40]** investigated the advantages and disadvantages of pyrochlores, perovskites, cermets of silver and doped bismuth oxide cathodes on thin film ceria electrolyte for operation at 500°C. The composite Ag-YDB (25 mol% yittria doped bismuth oxide) and perovskite, $(La_{0.6}Sr_{0.4})_{0.95}Fe_{0.8}Co_{0.2}O_{3-\delta}$ were found to have a promising performance at 500°C (for LSCF the ASR increased from 0.1 Ωcm^2 at 500°C to 5 Ωcm^2 over a testing time of 24 hours).

Bae and Steele **[41]** showed that the performance of the $La_{0.6}Sr_{0.4}Co_{0.2}Fe_{0.8}O_3$ (LSCF) cathode could be improved by microstructural optimisation. They applied a double-

layered cathode of LSCF onto a CGO electrolyte. Separating the dense electrolyte and the thick porous cathode was a thin (1 μm) dense LSCF cathode, which was sprayed on by electrostatic spray assisted vapour deposition (ESAVD). The thick porous LSCF cathode was then tape-cast on the top. Application of the thin film was found to decrease the resistivity of the cathode (ASR as low as 0.5 Ωcm^2 at 520°C was reported **[41]**) and hence enhance the efficiency of the cell. A better performance was achieved because; the thin dense LSCF layer has effectively increased the interfacial contact area between the LSCF cathode and the CGO electrolyte. It was also demonstrated that CGO electrolytes containing different level of SiO_2 content can influence both the electrolyte and cathode resistivities. These resistivities were reduced by etching the electrolyte surface to eliminate the influence of SiO_2 **[42]**. Sahibzada et al **[43]** studied the electrochemical performance of a porous $La_{0.6}Sr_{0.4}Co_{0.2}Fe_{0.8}O_3$ (LSCF) electrode impregnated with small amounts of palladium, Pd on a $Ce_{0.9}Gd_{0.1}O_{2-\delta}$ (CGO) electrolyte. The addition of precious metal like Pd or Pt should increase the catalytic activity of the cathode **[44]**. AC impedance spectroscopy studies from Sahibzada proved that the addition of small amount of Pd (0-15 μg) to the porous LSCF cathodes resulted in 3-4 times lower cathodic impedance in the temperature range 400-750°C.

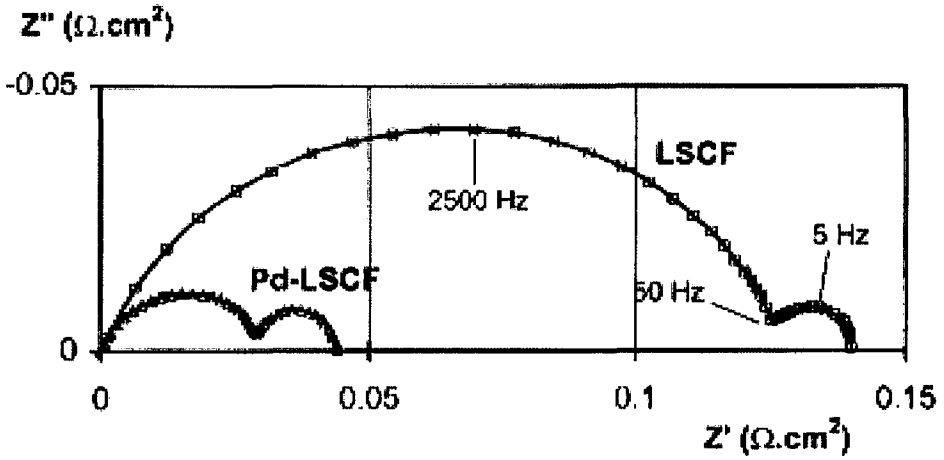


Figure 4.5:- A.C. impedance spectroscopy of LSCF/CGO/LSCF at 700 °C: effect of 7.5 μg/cm₂ Pd addition to LSCF [43]

Replacement of lanthanum on the A-site with Gd, Sm, or Nd has also been investigated to produce materials of greater stability and better performance than LSC or LSCF materials **[45 and 46]**. Ralph et al. **[11]** initial results proved the extremely good performances obtained by all the La-substituted compositions. Firstly $Sm_{0.8}Sr_{0.2}CoO_3$

(SSC) performed similar to LSCF (ASR values were identical), however $Gd_{0.8}Sr_{0.2}CoO_3$ (GSC) and $Nd_{0.8}Sr_{0.2}CoO_3$ (NSC) had a lower ASR than LSCF (approximately 0.1 Ωcm^2 at 700°). Takeda et al **[47]** have studied the electrical conductivity, cathodic polarization and reactivity between $Gd_{1-x}Sr_xCoO_{3-\delta}$ and YSZ (8mol% Y_2O_3 doped ZrO_2). Although the cathodic activity was excellent and similar to $La_{1-x}Sr_xCoO_{3-\delta}$ system, the formation of $SrZrO_3$ at the interface between $Gd_{1-x}Sr_xCoO_{3-\delta}$ and YSZ was observed at higher temperature, which caused deterioration of the cathodic activity. Yamamoto et al **[48]** have studied the electrical conductivity of the sintered samples $Gd_{1-x}A_xMnO_{3-\delta}$ and $Gd_{1-x}A_xCoO_{3-\delta}$ (A = Ca, Sr) as a function of x in the temperature range 30-1000°C. The highest conductivity of 400 Scm^{-1} at 1000°C was found in $Gd_{0.9}Sr_{0.1}CoO_{3-\delta}$. Ralph et al **[49]** tested the $Ln_{1-x}Sr_xCoO_3$ (Ln = Gd, Pr) cathodes on YSZ and CGO electrolytes at the Argonne National Laboratory. The $Pr_{0.5}Sr_{0.5}CoO_3$ and $Gd_{0.5}Sr_{0.5}CoO_3$ cathodes show the best performance on CGO, achieving an ASR between 0.1 and 0.2 Ωcm^2 at 650°C. Samarium doped cobaltite has attracted much attention because of its mixed-conduction characteristics and its relatively high ionic conductivity. $Sm_{1-x}Sr_xCoO_3$ (SSC) shows a higher conductivity, up to 10^3 Scm^{-1} when x = 0.5 **[50]**. Fukunaga et al **[51]** studied the reaction model of dense $Sm_{0.5}Sr_{0.5}CoO_3$ as SOFC cathode. It was shown that the SSC electrodes showed lower overpotential than LSC electrodes. Tu et al **[52]** have examined the perovskite-type oxides of $Ln_{1-x}Sr_xCoO_{3-\delta}$ (Ln = Sm, Dy) for the cathodes of SOFC. The highest conductivity of around 500 Scm^{-1} at 1000°C was found in $Sm_{0.7}Sr_{0.3}CoO_{3-\delta}$, however the conductivity of $Sm_{0.5}Sr_{0.5}CoO_{3-\delta}$ was not measured.

Current research of rare-earth doped manganite cathodes has led to new promising materials such as $Pr_{0.7}Sr_{0.3}MnO_3$ and $Nd_{0.7}Sr_{0.3}MnO_3$ **[53]**. Both have superior conductivity to traditional LSM and importantly there are no interfacial reactions between these cathodes and the CGO electrolyte **[54]**.

4.4.1 Composite Cathode Materials

The use of composite electrodes to improve the performance is very beneficial for intermediate temperature (500-700°C) solid oxide fuel cells (IT-SOFC). Mixing an ionically conducting material with an electronically conducting material to create a two-phase cathode (to try and make the cathode perform as a mixed ionic-electronic conductor) has shown some early success **[55]**. This will extend the surface area over which the oxygen reduction reaction can occur. Kenjo et al and Ostergard et al **[56 and 57]** showed that the composite electrodes comprising a mixture of LSM and YSZ (electrolyte material) might have better performance than electrodes consisting of LSM only.

Jorgensen and Mogensen **[58]** have studied the $La_{1-x}Sr_xMnO_{3-\delta}$/YSZ composite electrodes by impedance spectroscopy. They found that at least five processes affect the impedance. Going from high to low frequency, these processes are, (1), (2) two geometry-related contributions interpreted as transport across $La_{1-x}Sr_xMnO_{3-\delta}$/YSZ interfaces and through the YSZ of the composite, (3) a process reflecting competitive reaction steps such as bond breaking and surface diffusion, (iv) gas diffusion in a stagnant gas layer above the electrode structure, and (v) an activation process (inductive) presumably located at the triple phase boundary of electrode, electrolyte, and gas phase. Recently, Perry et al. **[59 and 60]** tested a 50-weight % LSM-CGO on both CGO and YSZ electrolytes. The area specific resistances were two to three times smaller than the performance of the single-phase cathode.

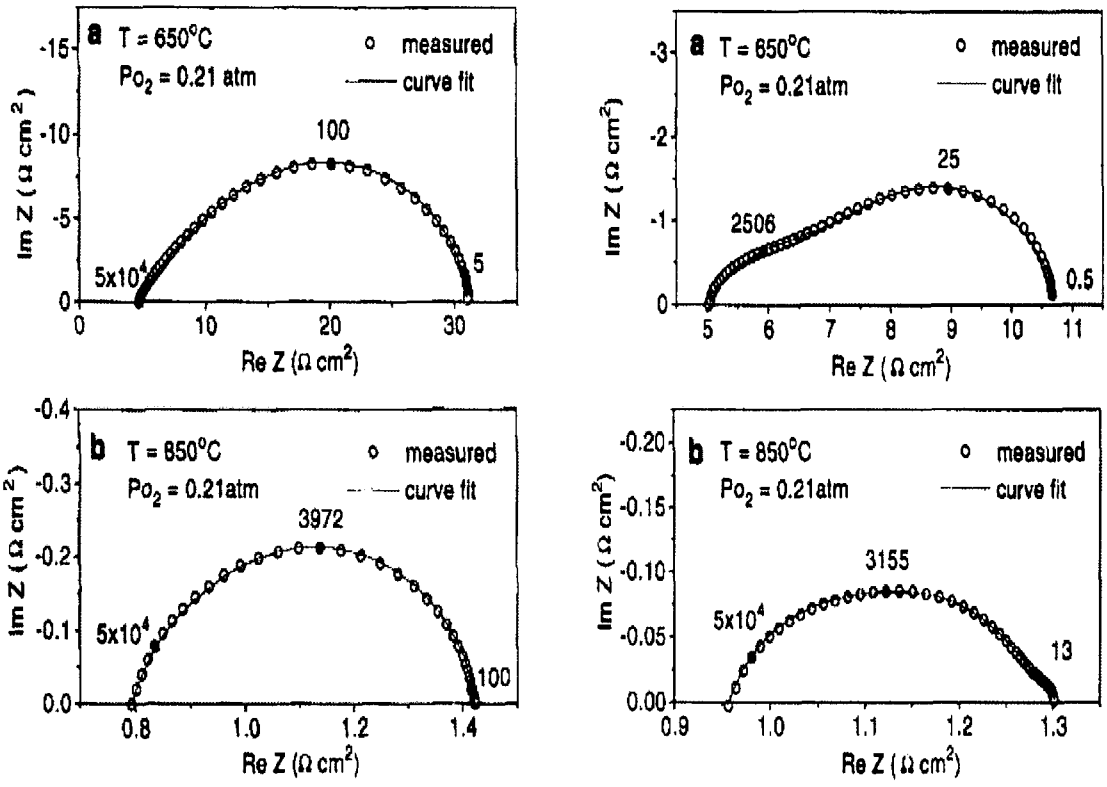


Figure 4.6:- Impedance plot of LSM electrodes (left) and LSM-YSZ electrodes (right) at a) T = 650 °C and b) T = 850 °C in air [60]

Zhao et al **[61]** investigated the electrochemical properties of $La_{0.8}Sr_{0.2}MnO_3$-$Ce_{0.7}Bi_{0.3}O_2$ (LSM-CBO) composite cathode. It was found that the polarisation resistance decreases with the increasing of CBO contents. The optimum value of 50-weight% CBO in LSM results in 1.78 Ωcm^2 ASR at 700°C. However LSM can certainly not be further improved for low operation temperatures because of its low oxygen tracer diffusion and surface exchange coefficient **[62]**.

$Bi_2V_{0.9}Cu_{0.1}O_{5.35}$ (BICUVOX) has been shown to an excellent ionic conductivity than any other ionic conductors such as YSZ or CGO (0.1 Scm^{-1} at 600°C, 50 times higher) **[63]**. Xia et al, mixed BICUVOX with silver for use as a composite cathode for IT-SOFC **[64]**. An area specific resistance of 0.53 Ωcm^2 was measured around 500°C. This is the lowest reported cathode ASR to date at this temperature. Degradation is a big problem with bismuth compounds, so the long-term stability is still needs to be evaluated if this material is going to be used for low temperature SOFC.

The classical cathode material for intermediate temperature solid oxide fuel cell is lanthanum strontium cobalt iron oxide (LSCF). This has been found to possess mixed

ionic-electronic conductivity at 700°C, however it becomes predominantly an electronic conductor at 500°C. Composite electrodes comprising a mixture of LSCF and the electrolyte material ceria gadolinia oxide (CGO) have better performance (had lower ASR and also lower activation energy) than electrodes consisting of LSCF only **[65]**, due to the presence of active triple phase boundary (TPB) points between LSCF, CGO and gas phase in the bulk of the electrode. Dusastre and Kilner **[65]** investigated the electrochemical properties of the interface between composite $La_{0.6}Sr_{0.4}Co_{0.2}Fe_{0.8}O_3$ (LSCF)/$Ce_{0.9}Gd_{0.1}O_{2-\delta}$ (CGO) cathodes on a $Ce_{0.9}Gd_{0.1}O_{2-\delta}$ (CGO) electrolyte at temperatures between 500-700°C using an AC impedance spectroscopy. The optimum composite composition was found to be around 36-volume % (30-weight %) CGO to LSCF. This work resulted in a significant reduction in the ASR typically from 4 Ωcm^2 for LSCF to less that 1 Ωcm^2 at 590°C for the composite CGO/LSCF.

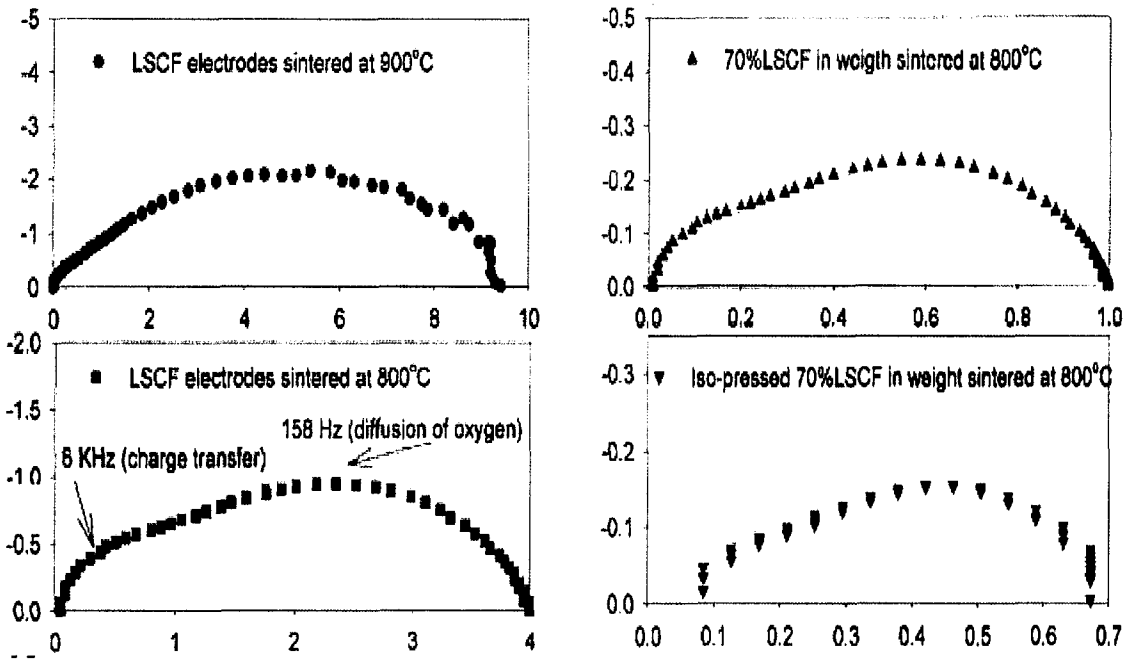


Figure 4.7:- AC Impedance Spectroscopy spectra of LSCF and Composite electrode on CGO electrolyte at 590°C [65]

In theory, porous mixtures of electrode and electrolyte material should increase the triple phase boundary length (tpbl). The polarisation resistance of the composite electrode was decreased by extending the tpbl, which resulted in much lower overpotential toward oxygen reduction in SOFC application than pure LSCF. Composite electrode also provides more pathways for the transport of oxygen to the electrolyte. Barnett and Murray performed impedance measurements on

$La_{0.6}Sr_{0.4}Co_{0.2}Fe_{0.8}O_3$ (LSCF)-$Ce_{0.8}Gd_{0.2}O_3$ composite cathodes on YSZ electrolytes. The LSCF electrodes yielded low-current interfacial resistance values that were a factor of 10 lower than for (La, Sr)MnO_3 cathodes. The addition of 50 vol.% CGO to LSCF resulted in an additional factor of ~ 10 decrease in the polarization resistance. Polarization resistance values for the LSCF-CGO cathodes were as low as 0.01 Ωcm^2 at 750°C and 0.33 Ωcm^2 at 600°C **[66]**.

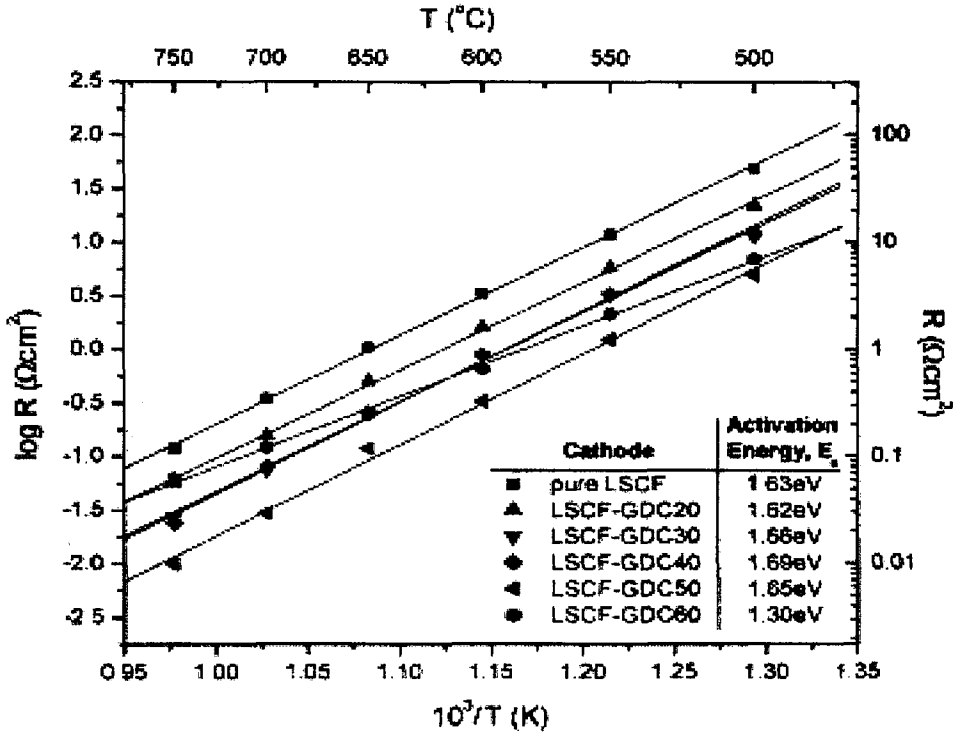


Figure 4.8:- Temperature dependence of the polarization resistance for pure LSCF and various LSCF-GDC cathode composition measured over a temperature range of 500-750°C in air [66]

Liu et al. **[67]** studied the electrochemical properties of the porous composite cathodes consisting of $Sm_{0.5}Sr_{0.5}CoO_3$ (SSC)/$Sm_{0.2}Ce_{0.8}O_{1.9}$ (SDC, samaria-doped ceria) on an $Sm_{0.2}Ce_{0.8}O_{1.9}$ electrolyte. For the sample sintered at the temperature of around 950°C, composite cathode had an area specific resistance of 0.18 Ωcm^2 at 600°C, when compared to a pure SSC electrode; it was 2 Ωcm^2 at 600°C.

4.4.2 Microstructure and Performance of cathodes

It has been shown that the electrochemical performance of the cathode for ITSOFC can be improved from using an electronically conducting cathode to a mixed conducting material or by using a composite cathode. The starting powder characteristics, powder calcination temperature and sintering temperature influence the final microstructure of the cathodes. Electrochemical performance also depends on these processing parameters as well as on the cathode thickness. Sasaki et al **[68]** demonstrated that both the cathodic polarisation and the ohmic loss on the cathode side of the cells depend strongly on the cathode microstructure, influenced by the processing conditions. The cathodic polarisation increases for the cathodes prepared by powders with broad particle size distribution. They also increase in cases of denser cathodes after sintering above 1100°C or very thick cathodes. Fukui et al **[69]** have shown that the cathode performance was strongly influenced by the starting particle size as well as sintering temperature. The smallest cathode polarisation for both 700 and 800°C operations was obtained when using the finer powder (0.53 μm) and sintering at 850°C.

Mogensen et al. **[70]** reported that characteristics such as porosity and thickness of the composite cathode as well as the chemical composition of the cathode have effects on polarisation. Although the results suggest that a correlation between fabrication methods and electrochemical performance exists, the detailed relationships are not fully understood. In another study **[71]**, the composite cathodes made from 60 weight % LSM and 40 weight % YSZ sintered at temperatures between 1100°C and 1300°C were analysed regarding the microstructure and the electrochemical performance at 850° and 1000°C at various oxygen partial pressures in helium, argon and nitrogen. Impedance spectra at 850°C in air change systematically with sintering temperature, where as the polarisation resistance of 0.28 Ωcm^2 to 0.54 Ωcm^2 has no clear dependency on the sintering temperature. Jorgensen et al. **[72]** reported that the microstructure was found to be less dense and to contain smaller grains as the sintering temperature was decreased in the range 1300-1150°C. This increased the active triple phase boundary line (TPBL) between electrode, electrolyte and gas phase, leading to a decrease in the polarisation resistance with decreasing sintering temperature.

Kim et al **[73]** studied the effect of percolation on the electrochemical performance of LSM-YSZ composite cathode. It was identified that the polarisation resistance of the LSM-YSZ composite electrodes is closely related to the connectivity of LSM-YSZ

particles and depends on their size ratio. The polarisation resistance decrease abruptly when YSZ connectivity occurred. The polarisation resistance of the cathode also decreases with the decrease of the particle size of LSM and YSZ, because the three phase boundary is dependent on the particle size of LSM and YSZ. Dusastre and Kilner **[65]** also proved that the observed high performance of the 30 weight % CGO and 70 weight % LSCF composite electrodes is consistent with the effective medium percolation theory **[74]** which predicts the ambipolar transport behaviour of composite mixed ionic-electronic conductors as a function of the volume fraction of each of the randomly distributed constituent phases.

4.5 Summary

The SOFC is a highly efficient device that produces power by means of electrochemical reactions. The materials, design and operating temperature of solid oxide fuel cells have evolved together over several decades of research. A conventional SOFC operates around 1000°C and is composed of a lanthanum manganite cathode, a nickel yittria-stabilized zirconia cermet, a solid yittria-stabilized zirconia electrolyte and an interconnect made of $LaCrO_3$. This temperature results from the need to attain reasonable power density, minimise the ohmic loss through YSZ electrolyte and the need for high reaction rates at the electrodes (especially at their cathode).

The choice of operating temperature has had a profound influence on the selection of the materials. The materials must have the proper stability (chemical, phase, morphological and dimensional), both, alone and together, between room temperature and the fabrication temperature. The requirement for stability at 1000°C places severe constraints on the choice of the materials, and most importantly precludes the use of metals in the fuel cell stack, resulting in all ceramic stacks.

The voltage degradation caused by electrode sintering, mechanical stress due to different thermal expansion coefficients, interfacial diffusion between electrolyte and electrode, maintaining gas tight seals and high temperatures during manufacturing and difficulties in producing large fuel cell structures are some of the materials problems associated with high SOFC operating temperature (1000°C). Although all these problems have been solved by appropriate selection of materials and fabrication techniques, the result is that the capital cost of current cell designs is too high for

SOFCs to be commercially attractive. Therefore, it is desirable to operate a fuel cell at reduced temperatures, while still maintaining the power densities achieved at high temperatures.

A lot of research efforts are now a days focussed towards lowering the operating temperature from 1000°C to 500-600°C (intermediate temperature range) by going in for an appropriate choice of new materials from ceramics and in evolving suitable fabrication techniques. As the temperature is reduced the selection of lower cost alternative materials increases significantly for many of the components within the system. One such component is the interconnect, which could be changed from ceramic to cheap ferritic stainless steel (metallic). A metallic interconnect would not only be less expensive but would provide a much greater flexibility in fuel cell design, having greater strength, toughness, and thermal and electrical conductivity compared to the ceramic interconnect. Metallic manifolding can also be considered in the hot zone of the SOFC, and less insulating material would be required to ensure a comfortable exterior temperature to the fuel cell system, again leading to cost savings and, also, some reduction in unit size. In order to use this type of inexpensive and easily machinable materials in SOFCs, it is necessary to reduce the operating temperature.

Since the chemical stability of stabilised zirconia is excellent in reducing atmospheres at high temperatures, stabilised zirconia has been employed as the electrolyte material of SOFCs from the beginning of the development. SOFCs with yittria stabilised zirconia (YSZ) electrolytes should be operated at about 1000°C for high power density generation. Therefore, it is required that other cell components should be composed of ceramic materials as well as the electrolyte. For significantly reduced operating temperatures, electrolytes with higher ionic conductivity (> 0.1Scm-1) than YSZ are needed. As the operation temperature is reduced, the ohmic loss of the electrolyte can become very considerable **[75]**. The alternate electrolyte material that may exhibit high oxygen ion conductivity than YSZ is ceria godolinia oxide (CGO) and is now used as the electrolyte material for intermediate temperature SOFC operation. CGO's ionic conductivity of 0.1 S/cm at 800°C **[76]** can only be matched by YSZ at 1000°C **[77]**. This also has a thermal expansion coefficient close to steel.

Perovskites-type oxides such as $La_{1-x}Sr_xMnO_{3-\delta}$, $La_{1-x}Sr_xCoO_{3-\delta}$ and related materials for a long time has been intensively studied as cathode materials for SOFC. The use of LSM with YSZ electrolyte is far from being simple. At high temperatures the Mn cation

is highly mobile and diffuses into the electrolyte changing the electrical and/or structural characteristics of both the cathode and the electrolyte. Also the reactions between the manganite and the electrolyte above 1200°C. It is also reported, for example, that the polarisation resistance of LSM increases dramatically from 1 Ωcm2 at 1000°C to 2000 Ωcm2 at 500°C **[40]**. It is therefore a need to find alternative materials that can be used in ITSOFC.

So in the last decade, cobalt-based perovskites were found to be the promising cathode materials for intermediate temperature SOFC operations, displaying the highest ionic and electronic conductivities. For theses cobalt-based perovskites, only CGO electrolytes have shown promise at low temperatures (no interfacial reactions have been detected between these cathodes and the CGO electrolyte when compared to YSZ electrolyte). The peak conductivity of around 350 Scm^{-1} was achieved at 550°C for the $La_{0.6}Sr_{0.4}Co_{0.8}Fe_{0.2}O_3$ (LSCF) composition, when studying the effect of the La:Sr ratio, which suggests that this composition would be a suitable cathode material for intermediate temperature SOFC operation. There are reports that $Gd_{1-x}Sr_xCoO_{3-\delta}$ and $Sm_{1-x}Sr_xCoO_{3-\delta}$ series of materials are also very good cathode materials for use in IT-SOFC operations. All of these materials (LSCF, GSC and SSC) have high conductivity, oxygen transport properties, thermal expansion coefficient match with CGO, mixed ionic electronic conductivity, non-stoichiometry and good electrochemical performance, which have been widely reported in the literature.

The cathode performance can also be improved by adding an ionically conducting second phase, typically YSZ or CGO, to the electronically conducting electrode material, typically LSM or LSCF. The improved performance of composite cathode results from the high density of triple phase boundaries (TPB). This combined with a contiguous ionically conducting phase, allows electrochemical reactions to occur within the electrode.

It has also been shown that the starting powder characteristics, powder calcination temperature, sintering temperature, volume fraction influence the final microstructure (porosity, tortuosity and continuity) of the cathodes. Electrochemical performance also depends on these processing parameters as well as on the cathode thickness.

Figure 8 show a comparison of the area specific resistance for each cobalt-based cathode material on CGO electrolyte sintered at 900°C together with the CGO (30 wt%)-LSCF composite cathode sintered at 800 and 900°C. The $La_{0.8}Sr_{0.2}CoO_3$ cathode

is shown for comparison, displaying the highest resistance of the seven materials. The standard $La_{0.6}Sr_{0.4}Co_{0.2}Fe_{0.8}O_3$ performs better, achieving an area specific resistance of 0.3 Ωcm2 at 700°C. The most surprising results from this comparison have been the extremely good performances obtained by all the La-substituted compositions. For example, $Sm_{0.8}Sr_{0.2}CoO_3$ has a performance similar to $La_{0.6}Sr_{0.4}Co_{0.2}Fe_{0.8}O_3$, while $Gd_{0.8}Sr_{0.2}CoO_3$ and $Gd_{0.6}Sr_{0.4}CoO_3$ have much better performances. The area specific resistance of $Gd_{0.6}Sr_{0.4}CoO_3$ is approximately 0.1 Ωcm^2 at 700°C **[78]**. The development of a series of new electrode microstructures by mixing an ionic conducting phase (CGO) with a mixed conducting phase (LSCF) resulted in a significant reduction of the ASR typically from 4 Ωcm^2 for LSCF to less than 1 Ωcm^2 at 600°C. Therefore further studies are required on composite cathodes of different compositions.

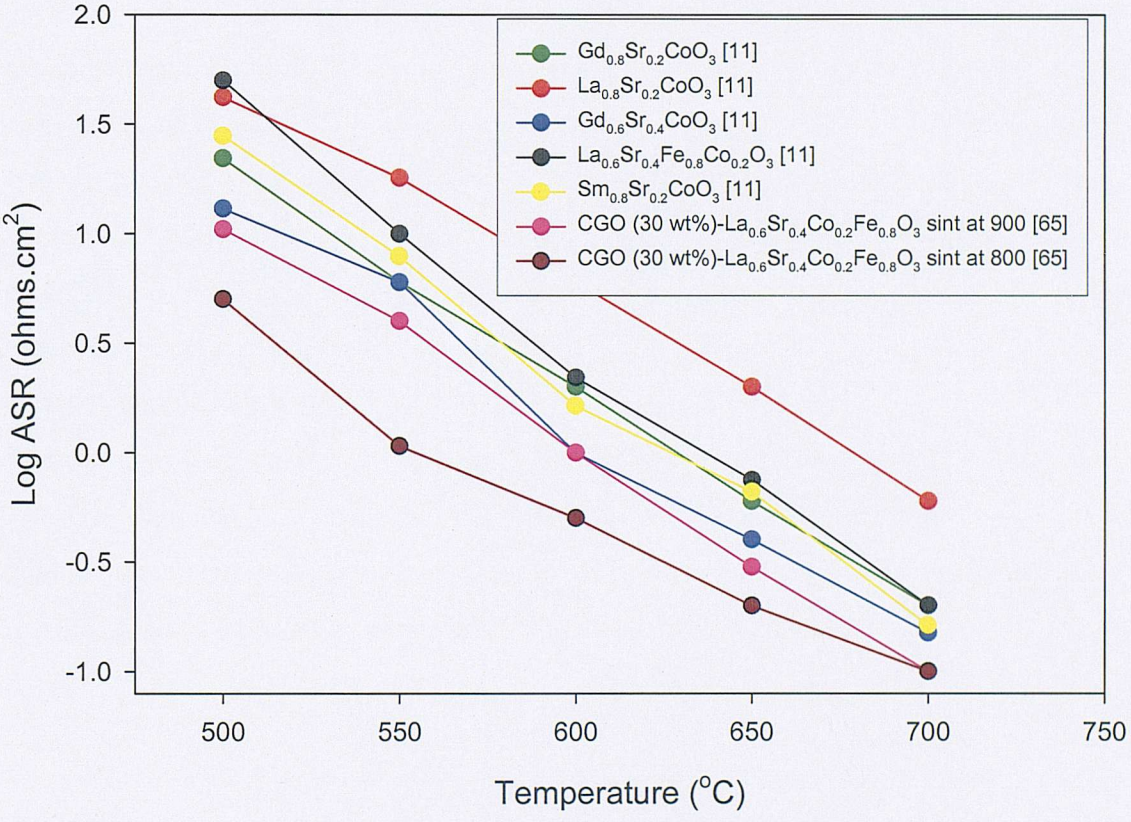


Figure 4.9:- Comparison of the area specific resistance for each cathode material on CGO electrolyte

4.6 Objective of the Research Work

The generation of electricity in SOFC is based on the flow of oxide ions from cathode (which is exposed to air) to the anode (which is exposed to hydrogen rich fuel). The electrolyte plays the main role in facilitating the transfer of oxide ions while blocking the flow of electrons between the electrodes. The research is based on the imperial college program to study the metal-supported SOFC at intermediate temperatures (500-600°C). Since stainless steel is used as the support, there was an aim to co-sinter the whole cell at 1000°C. This will also reduce the processing cost of the SOFC. So the cathodes in this work are all sintered at 1050°C. The electrolyte is CGO as this has been the state-of-the-art electrolyte material at Imperial College SOFC study program and it also has a very good ionic conductivity between 500-600°C. As we know, one of the major problem encountered today to develop IT-SOFC is the large cathode overpotential caused by the reduced operation temperature. One way to overcome this problem is to use a mixed conducting materials, such as LSCF etc, which has shown improved cathode properties due to rapid surface exchange kinetics, high oxygen vacancy concentration and the extended triple phase boundary (TPB) from the electrolyte/electrode interface to the bulk of the electrode. Another way is to form composite electrode. Generally, a high ionic conducting phase is mixed together with an electron-conducting phase.

Therefore in this research, the performance of the $Ce_{0.8}Gd_{0.2}O_2/La_{0.6}Sr_{0.4}Fe_{0.8}Co_{0.2}O_3$, $Ce_{0.8}Gd_{0.2}O_2/Gd_{0.6}Sr_{0.4}CoO_3$ and $Ce_{0.8}Gd_{0.2}O_2/Sm_{0.5}Sr_{0.5}CoO_3$ composite cathode was studied at temperatures between 500-600°C. The aim in this project was to reach an area specific resistance for the cathode in the order of 0.1 Ωcm^2 or lower between 500-600°C.

4.7 References

[1] F.P.F. Van Berkel, G.M. Christie, F.H. Van Heuveln, J.P.P. Huijsmans, in: M. Dokiya et al. (Ed.), SOFC IV, proceedings Volume, Vol. 95-1, Electrochemical Society, NJ, 1995, p1062.

[2] B.C.H. Steele, Solid State Ionics, 129 (2000), p95.

[3] B.C.H. Steele, Journal of Materials Science, 36 (2001), p1053-1068.

[4] V.V. Kharton, E.N. Naumovich, A.A. Vecher, A.V. Nikolaev, Proc of the Fourth International Symposium on SOFCs (SOFC-IV), (Eds. M. Dokiya, O. Yamamoto, S.C. Singhal and H. Iwahara), The Electrochemical Society, Inc., NJ, (1995), p512-519.

[5] T. Fukui, S. Ohara, K. Murata, H. Yoshida, K. Miura and T. Inagaki, Journal of Power Sources, 4543 (2002), 1-4.

[6] T. Ishihara, H. Matsumoto, Y. Takita, J. Am. Chem. Soc. 116 (1994), p3801.

[7] K. Huang, M. Feng, J.B. Goodenough, J. Electrochem. Soc. 144 (1997), p3620.

[8] R. Doshi, V.L. Richards, J.D. Carter, X. Wang and M. Krumpelt, Journal of the Electrochemical Society, 146 (4), 1999, p1273-1278.

[9] J. Will, A. Mitterdorfer, C. Kleinlogel, D. Perednis and L.J. Gauckler, Solid State Ionics, 131 (2000), p79.

[10] J.M. Ralph, PhD. Thesis, University of London, 1998.

[11] J.M. Ralph, J.T. Vaughey and M. Krumpelt, Electrochemical Society Proceedings, 16 (2001), p466-475.

[12] Y. Takeda, H. Y. Tu, N. Imanishi and O. Yamamoto, Solid State Ionics, (1997), 100, p283-288.

[13] R.A.De Souza, J.A. Kilner, Solid State Ionics, 106 (1998), p175-187.

[14] G. Stochniol, E. Syskakis and A. Nauomidis, J. Am. Ceram. Soc. (1995), 78(4), p929.

[15] V.V. Kharton, A.A. Yaremchenko and A.N. Naumovich, J. Solid State Electrochem. (1999), 3, p303.

[16] O. Yamamoto, Y. Takeda, R. Kanno and M. Noda, Solid State Ionics (1987), 22, p241.

[17] E. Ivers-Tiffee, M. Schiessl, H.J. Oel and W. Wersing, in Proceedings of the 14th Riso International Symposium on Materials Science, edited by F.W. Poulsen, J.J. Bentzen, T. Jacobsen, E. Skou and M.J.L. Ostergrad (1993), p69.

[18] Y. Teraoka, T. Nobunaga, K. Okamoto, N. Miura, N. Yamazoe, Solid State Ionics (1991), 48, p207.

[19] H. Taimatsu, K. Wada and H. Kanedo, J. Am. Ceram. Soc. (1992), 75(2), p401.

[20] A.N. Petrov, P. Kofstad, Proc Third International Conference on SOFCs (edited by S.C. Singhal and H. Iwahara), The Electrochemical Society, Inc., NJ, Proc. (1993), vol 63-4, p220-230.

[21] T. Inoue, K. Eguchi and H. Arari, Solid State Ionics (1990), 40-41(1), p407.

[22] Y. Teraoka, H.M. Zhang, K. Okamoto, N. Yamazoe, Mater. Res. Bull. 23 (1988), p51.

[23] Y. Teraoka, H.M. Zhang, K. Okamoto, N. Yamazoe, Mater. Res. Bull. 23 (1985), p1743.

[24] Y. Matsumoto, S. Yamada, T. Nishida, E. Satoi, J. Electrochem. Soc. 127 (1980), p2360.

[25] Y. Teraoka, H.M. Zhang, N. Yamazoe, Chem. Lett. (1985), p1367.

[26] J.D. Sirman and J.A. Kilner, J. Electrochem. Soc, 143, (1996), p. L229.

[27] J.A. Lane, P.H. Middleton, H. Fox, B.C.H. Steele and J.A. Kilner, in Proceedings of the Second International Symposium of Ionic and Mixed Conducting Ceramics, T.A. Ramanarayanan, W.L. Worrell and H.L. Tuller, Editors, p. 489.

[28] E. Maguire, B. Gharbage, F.M.B. Marques and J.A. Labrincha, Solid State Ionics, 127, (2000), p329-335.

[29] Y. Ohno, S. Nagata and H. Sato, Solid State Ionics, 9/10, (1983), p1001.

[30] Y. Teraoka, H.M. Zhang, K. Okamoto and N. Yamazoe, Mat. Res. Bull, (1988), 23, p51-58.

[31] D. Mantzavinos, A. Hartley, I.S. Metcalfe and M. Sahibzada, Solid State Ionics, 134 (2000), p103-109.

[32] C.C. Chen, M.M. Nasrallah and H.U. Anderson, Proc of the Third International Symposium on Solid Oxide Fuel Cells, (1993), (Eds. S.C. Singhal and H. Iwahara), The electrochemical society, Inc. NJ, p252-266.

[33] L.O. Jerdal, R.Turnold and P.H. Middleton, Proc of the Fourth International Symposium on Solid Oxide Fuel Cells (SOFC-IV), (1995), (Eds. M. Dokiya, O. Yamamoto, H. Tagawa and S.C. Singhal), The Electrochemical Society, Inc. NJ, p544-553.

[36] L-W. Tai, M.N. Nasralliah, H.U. Anderson, D.M. Sparlin, S.R. Sehnin, Solid State Ionics (1995), 76, p273-283.

[37] L-W. Tai, M.N. Nasralliah, H.U. Anderson, D.M. Sparlin, S.R. Sehnin, Solid State Ionics (1995), 76, p259-271.

[38] A. Petric, P. Huang and F. Tietz, Solid State ionics 135 (2000), p719-725.

[39] Y. Teraoka, H.M. Zhang, K. Okamoto and N. Yamazoe, Mat Res Bull, (1988), 23, p51-58.

[40] R. Doshi, V.L. Richards, J.D. Carter, X. Wang and M. Krumpelt, J. Electrochem. Soc., 146(4), (1999), p1273-1278.

[41] J. M. Bae PhD thesis, 1996.

[42] J. M. Bae and B.C.H. Steele, Solid State Ionics (1998), 106, p247-255.

[43] M. Sahibzada, S.J. Benson, R.A. Rudkin, J.A. Kilner, Solid State Ionics (1998), 113-115, p285-290.

[44] M. Watanabe, H, Uchida, M. Shibata, M. Mochizuki, K. Amikura, J. Electrochem. Soc. (1994), 141, p342.

[45] H.Y. Tu, Y. Takeda, N. Imanishi, O. Yamamoto, Solid State Ionics (1997), 100, p283.

[46] Y. Takeda, H. Ueno. N. Imanishi, O. Yamamoto, N. Sammes, M.B. Phillipps, Solid State Ionics (1996), 86-88, p1187.

[47] Y. Takeda, H. Y. Tu, N. Imanishi and O. Yamamoto, Solid State Ionics, (1997), 100, p283-288.

[48] O. Yamamoto, S. watanabe, H. Ueno, N. Imanishi, Y. Takeda, N. Sammes and M.B. Phillipps, Proc of the Fourth International Symposium on SOFCs (SOFC-IV), (Eds. S.C. Singhal, M. Dokiya, O. Yamamoto and H. Tagawa), The Electrochemical Society, Inc., NJ, (1995), p414-423.

[49] C. Rossignol, J.M. Ralph, J-M. Bae and J.T. Vaughey, Solid State Ionics, 175 (2004), p59-61.

[50] T. Ishihara, M. Honda, T. Shibayama, H. Minami, H. Nishiguchi and Y. Takita, J. Electrochem. Soc., 145 (9), (1998), p3177.

[51] H. Fukunaga, M. Koyama, N. Takahashi, C. Wen and K. Yamada, Solid State Ionics 132 (2001), p279-285.

[52] H.Y. Tu, Y. Takeda, N. Imanishi, and O. Yamamoto, Solid State Ionics (1997), 100, p283-288.

[53] Y. Sakaki, Y. Takeda, A. Kato, N. Imanishi, O. Yamamoto, M. Hattori, M. Iio and Y. Esaki, Solid State Ionics (1999), 118, p187.

[54] G.C.H. Kostogloudis and C.H. Ftikos, J. Eur. Cera. Soc. (1999), 19, P497.

[55] J.W. Kim, A.V. Virkar, K.Z. Fung, K. Mehta and S.C. Singhal, J. Electrochem. Soc. (1999), 146, p69.

[56] T. Kenjo, M. Nishiya, Solid State Ionics, (1992), 57, p295.

[57] M.J.L. Ostergard, C. Clausen, C. Bagger, M. Mogensen, Electrochim. Acta, (1995), 40, p1971.

[58] M.J. Jorgensen and M. Mogensen, J. Electrochem. Soc., (2001), 148(5), p A443-A442.

[59] E. Perray Murray, S.A. Barnett, Solid State Ionics (2001), 143, p265-273.

[60] E. P. Murray, T. Tsai and S.A. Barnett, Solid State Ionics, (1998), 110, p235.

[61] H. Zhao, L. Huo and S. Gao, Journal of Power Sources, 125 (2004), p149-154.

[62] H. Uchida, M. Yoshida and M. Watanabe, J. Electrochem. Soc., 146 (1), (1999), p1.

[63] J.C. Boivin, G. Mairesse, Chem. Mat. (1998), 10, p2870-2888.

[64] C. Xia, M. Liu, Adv. Mater. (2002), 14, p521-523.

[65] V. Dusastre, J.A. Kilner, Solid State Ionics, 126, (1999), p163-174.

[66] E.P. Murray, M.J. Sever and S.A. Barnett, Solid State Ionics, (2002), 148, p27-34.

[67] M. Liu, C. Xia, W. Rauch, F. Chen, Solid State Ionics (2002), 149, p11-19.

[68] K. Sasaki, J-P. Wurth, R. Gschwend, M. Godickemeier and L.J. Gauckler, J. Electrochem. Soc., vol. 143, 1996, p530.

[69] K. Murata, T. Fukui, H. Abe, M. Naito and K. Nogi, Journal of power sources, 2005, Article in press.

[70] M. Juhl, S. Primdahl, C. Manon, M. Mogensen, J. Power Sources, 61 (1996), p173.

[71] P. Hotappels, M.J. Jorgensen, S. Primdahl, M. Mogensen and C. Bagger, in: P. Stevens (Ed.), Proceedings of the Third European SOFC Forum, France, 1998, p311.

[72] M.J. Jorgensen, S. Primdahl, C. Bagger and M. Mogensen, Solid State Ionics, 139 (2001), p1-11.

[73] J-D. Kim, G-D. Kim, J-W. Moon, H-W. Lee, K-T. Lee and C-E. Kim, Solid State Ionics, 133 (2000), p67-77.

[74] D.S. Mclachlan, M. Blaszkiewicz, R.E. Newham, J. Am. Ceram. Soc. 73 (8) (1990), p2187.

[75] H. Uchida, S-I Arisaka and M. Watanabe, Electrochem Solid State Lett. (1999), 2(9), p428-430.

[76] G.B. Balazs, R.S. Glass, Proc of the second international symposium on Ionic and Mixed Conducting Ceramics, (Eds. T.A. Ramanarayanan, W.L. Worrel, H.L. Tuller), The Electrochemical Society Inc., (1994), vol 94-12, p478.

[77] B.C.H. Steele, Ceramic Oxygen Ion Conductors and their Technological Applications, Ed. B.C.H. Steele, British Ceramic Proceedings, (1996), vol 56, cumbria, p151.

[78] M. Koyama, C-J. Wen, T. Masuyama, J. Otomo, H. Fukunaga, K. Yamada, K. Eguchi and H. Takahashi, J. Electrochem. Soc., (2001), 148(7), PA796-A801.

Chapter 5 - Experimental Procedure

5.1 Introduction

As indicated in the introduction of this thesis, the initial aim of my research is to develop a method that produces porous CGO-LSCF, CGO-GSC and CGO-SSC composite cathode at 1000°C with no deleterious effects on either the mechanical or electrical properties of the material. Initial work concentrated on finding the onset of sintering temperature of these composite materials using dilatometry. Secondly, PMMA and carbon particles were incorporated into the composite material in order to facilitate the development of porosity. Thirdly, the electrical properties of the electrode and the microstructures were examined using an AC impedance spectroscopy and secondary electron microscopy (SEM). Other techniques like particle size analysis, x-ray diffraction and focus ion beam secondary ion electron microscopy (FIB-SIMS) were also used to characterize the samples.

The $Ce_{0.9}Gd_{0.1}O_{2-x}$ (CGO10-90), $Ce_{0.8}Gd_{0.2}O_{2-x}$ (CGO20-80), $La_{0.6}Sr_{0.4}Fe_{0.8}Co_{0.2}O_{3-\delta}$ (LSCF), $La_{0.6}Sr_{0.4}MnO_{3-\delta}$ (LSM) and $Gd_{0.6}Sr_{0.4}CoO_{3-\delta}$ (GSC) powders used were supplied from Rhodia. Impurities contained in the Rhodia powder are minimal (i.e. SiO_2 = 30ppm) and thus the Rhodia powders are considered "clean". $Sm_{0.5}Sr_{0.5}CoO_{3-\delta}$ (SSC) powder was synthesised in the laboratory using the glycine-nitrate synthesis route described below **[1]**.

5.2 Glycine-nitrate combustion synthesis

The Glycine-nitrate combustion route is a particular type of more general combustion methods. In this method a self-sustaining exothermic reaction between a fuel and an oxidant is used for the rapid synthesis of a final product. This synthesis technique consists of two basic steps. First, metal nitrates and glycine are dissolved in water. Second, the solution is boiled down until it thickens and ignites, producing ash that contains the oxide product. Although a variety of reagents can be used, mixtures of metal nitrates and organic reagents appear to be favoured for synthesis of double and ternary oxides of transition metals. In the glycine-nitrate combustion method, as the name suggests, a combustion reaction between metal nitrates and glycine (a low molecular weight amino acid) leads to the formation of a desired product. The glycine serves two important purposes during the synthesis: first, it complexes the metal

cations, increasing their solubility and preventing selective precipitation as the water evaporates: and secondly, it serves as fuel for combustion, being oxidised by the nitrate anions and by oxygen in air. The glycine molecule has a carboxylic acid group at one end and one amine group at the other end. Alkali, alkaline-earth and possibly rare earth cations (La) are largely complexed by the carboxylic acid end of the molecule. Transition metal cations are complexed by the amine group. This method has been used successfully for the synthesis of $Sm_{0.5}Sr_{0.5}CoO_3$ **[2]**.

The appropriate quantities of nitrate salts of each constituent cation ($Sm(NO_3)_3.6H_2O$, $Sr(NO_3)_2$, $CoNO_3.6H_2O$ were weighed accurately, taken in quartz cruicible and dissolved in triple distilled water. Calculated amount of glycine was added to the above solution with continuous stirring and homogenized well. The oxidiser:fuel ratio was caculated based on oxidising (O) and fuel (F) valencies of the reactants keeping O/F = 1 as reported **[3-4]**. The aqueous redox solution containing metal nitrates and glycine was heated on a hot plate in borosilicate beakers. The beaker was covered with a 230 mesh stainless-steel sieve to contain reaction product. During heating, as the last water is evaporated, the solution begins to swell and brown gases appeared. The decomposition of the gels initiated almost simultaneously in a few different locations at the bottom of the beaker and the reaction wave propagated rapidly throughout the mixture without further need of heating as the energy released during the reaction was sufficient for continued heating of the reaction mixture. The exothermic combustion reaction caused the evolution of large amounts of gases. The reaction was completed in a few seconds and produced very fine ash-like powders. The colour of the powder was charcoal black. These ash particles have a foam-like morphology with very low bulk density. After combustion, these soft agglomerates powders were annealed at low temperatures (usually at 700°C in air for 6 hours) in order to remove any organic residue and complete the synthesis. The resultant powders were then characterised by X-ray diffraction.

5.3 Composite Powder Preparation

The CGO20-80/LSCF composite was prepared from the starting powders (manufactured by Rhodia). The average particle size was 1.1 μm and 0.7 μm for LSCF and CGO20-80 respectively. The composition of this composite was 30 weight %

CGO20-80 (the composite containing this composition exhibited the lowest interfacial resistance) **[5]**. The CGO20-80/LSCF powder was prepared by mixing the desired quantities of CGO20-80 and LSCF powders with acetone and ball milled with zirconia balls for 24 hours to ensure even mixing. The paste was then dried and sieved through a 38μ stainless steel mesh. Same procedure was also used to make the CGO20-80/GSC and CGO20-80/SSC composite. The composition here too was 30 weight % CGO20-80. The Pore former was only needed for the CGO20-80/LSCF composite cathode. The pore formers composition, which varied from 10-50 volume % were mixed with the composite and ball milled in acetone for 24 hours. The resultant dried powders with and without a pore former was then used for structural characterisation by X-ray diffraction, microstructural characterisation by SEM and FIB-SIMS, sintering studies by Dilatometry and electrical measurements by AC impedance spectroscopy.

5.4 Sample Preparation

5.41 For Dilatometry

Cylindrical samples of 6 mm in diameter and approximately 4 mm in length were uni-axially pressed from a relatively small 6 mm die at a pressure of about 1 ton.

5.42 For AC Impedance

All the electrodes were sprayed onto an as sintered and a cleaned CGO10-90 electrolyte pellet. The as sintered CGO10-90 pellet was uni-axially pressed at a pressure of about 2 ton from a 13mm die. The density of the green pellet was 55%, measured using the Archimedes method. The pellet, 13mm in diameter was then sintered at 1400°C, heating at a rate of 10°C/min for 5 hours in air. This produced a sintered pellet with an average diameter of 10.5 mm and more than 95% dense.

A cleaned electrolyte was produced by cleaning both the surface of an as sintered electrolyte with a 1200 grid (5-15 micron) silicon carbide paper and then etched by 40 % HF acid for two minutes.

The composite electrode inks for spraying on the electrolyte were made by weighing 10g of the CGO20-80/LSCF powder, together with 0.5g of KD1 dispersant and 25g (approximately 15ml) of acetone. The mix was then ball milled for 24 hours. Finally 2.3g of binder based on terpineol and another 25g of acetone were added to the mix and

further ball milling was carried out for 10 minutes. Then five layers of ink were sprayed on both sides of the dense CGO10-90 pellets with a pressurised sprayer. These cathodes were sintered at 1050°C for 2 hours at a rate of 10°C/minute before studying the electrical properties. The area of the cathode was calculated to be around 0.41 cm^2 (± 0.01).

5.5 Density Measurements

The bulk densities of the green and sintered pellets were calculated using the Archimedes' principle [7]. Sintered pellets were weighed on an electronic scale. A dry pellet was soaked in water and then suspended on copper wire and weighed in water. After drying, the dried pellet and copper wire were reweighed. The bulk density (ρ_{bulk}) of the sintered ceramic was calculated to the following equation (the Archimedes principle):

$$\rho_{Bulk} = \frac{M_{Air}}{M_{Wet} - (M_{water} - M_{Wire})} \times \rho_{water}$$

Where;

M_{Air} is the weight of the dry pellet

M_{Wet} is the weight of the pellet when removed from the beaker (as it is wet)

M_{wire} is the weight of the wire used to suspend the pellet in the water

M_{water} is the weight of the pellet when suspended from a thin wire in a beaker of distilled water.

ρ_{water} is the density of the water at the room temperature (temperature at which the measurement is taken. The measurements were carried out on every four samples and an average density was calculated.

All densities quoted are expressed as percentage of the theoretical density of LSCF, which is 6.6120gcm^{-3}, CGO, which is 7.250gcm^{-3}, and CGO-LSCF, which is 6.8034gcm^{-3}. These were calculated from the X-ray diffraction plot of each powder.

Once the samples had been prepared and sintered they were characterised by the following techniques.

The percentage of porosity measurements were made for all the components with respect to the bulk density measured using the archimedes principle and the theoretical

density of the samples. The percentage of porosity is calculated using the following formula:

$$\text{Percentage of porosity} = \frac{\rho_{theoretical} - \rho_{bulk}}{\rho_{theoretical}} \times 100$$

where, $\rho_{theoretical}$ - theoretical density
ρ_{bulk} - bulk density measured using the Archimedes principle

5.6 Powder Characterisation Techniques

5.61 Particle Size Analysis

The powder particle size distribution was determined using a laser scattering particle sizer (Malver particle sizer model 3600D) fitted with a lens capable of measuring particle sizes in the range 0.1-80μm. The powders were diluted in distilled water, mixed with a magnetic stirrer and diluted again in the analysis cell. The cell had to be kept clean when the measurement is been taken. Once the cell put in place, a solution was mixed to avoid the settling of the particles with a magnetic stirrer and a laser beam crossed the cell. The particle size of the powders were obtained using an automated analysis system connected to the device. The technique is based on the fact that laser light will be scattered by particles in the suspension. The angle of scattering is related to the particle size and the intensity of the scattered light is related to the proportion of particles of that size in suspension **[8]**.

5.62 Dilatometry

Dilatometry is a technique by which the dimensional changes of the sample are monitored as a function of temperature or time during heating or cooling, while the sample may be subjected to an additional mechanical load. An accurate understanding of this behaviour can provide insights on firing processes, the influence of additives and raw materials, densification and sintering properties, reaction kinetics, phase transitions, glaze development, and thermal shock. It can also be used to carry out rate-controlled sintering studies on reactive powders.

The shrinkage behaviour of powders during sintering was investigated using a Netzcsh 402E horizontal dilatometer. Cylindrical samples of approximately 4mm in length and uni-axially pressed at a pressure of 0.5 ton is placed between two high purity alumina

spacers in a special holder inside a moveable furnace. One of the spacers was in contact with a sprung loaded alumina push rod that pushed the other spacer tight against an alumina end plate. A push rod placed directly against the sample transmits length change to a linear variable displacement transducer (LVDT). As the sample was fired, shrinkage occurred resulting in displacement of the push rod. Hence as the sample length changes during the temperature program, the LVDT core is moved, and an output signal proportional to the displacement is recorded. The temperature program is normally controlled using a thermocouple located next to the heating element or next to the sample. Data were recorded between 20-1200°C at a heating rate of 10°C/min in air. The dilatometer software compensated for the expansion of the holder for each measurement.

5.63 X-Ray Diffraction

In crystallised solids, atoms (and molecules) are arranged in a periodic and regular fashion conforming a standard geometry called crystal lattice. In this crystal lattice, the atoms can be thought of as forming different planes taking part in the coherant scattering process. X-ray diffraction is an efficient, non-destructive analytical technique used in this study for identification of phases and also for the information of the crystal orientations of a given phase. X-ray diffraction is one of the most important characterization tools used in solid-state chemistry and materials science. Once the material has been identified, X-ray crystallography may be used to determine its structure, i.e. the size and the shape of the unit cell for any compound, how the atoms pack together in the crystalline state and what the interatomic distance and angle are etc. X-rays are electromagnetic radiation of wavelength about 1 Å (10^{-10} m), which is about the same size as an atom. They occur in that portion of the electromagnetic spectrum between gamma-rays and the ultraviolet. When a X-ray beam is incident on a set of parallel planes (within each crystal) of the crystalline bulk, the electron clouds of these atoms diffract the X-ray beam in a rational approach as shown in Figure 5.1.

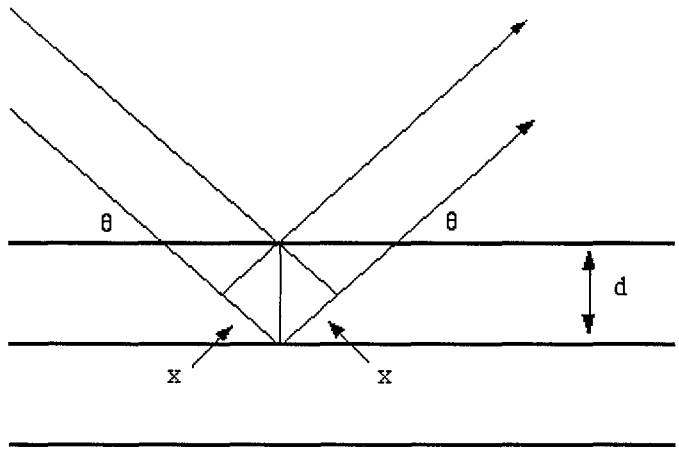


Figure 5.1:- Reflection of x-rays from two planes of atoms in a solid

Only planes parallel to the sample surface diffract in the Bragg-Brentano geometry. Diffraction from the crystal planes occur at well-defined angles that can be described by Bragg equation:

$$n\lambda = 2d\sin\theta$$

where, d – is the interplanar distance (or lattice constant)

λ - is the wavelength of the characteristics X-rays

θ - angle of diffraction

n – is the order of the scattered beam

This famous Bragg's law provides the basic pattern for the XRD methods. For perfect crystals, *I(q)* consists of delta functions (perfectly sharp scattering). For imperfect crystals, the peaks are broadened. For liquids and glasses, it is a continuous, slowly varying function.

The x-ray diffraction measurements were carried out using a diffractometer, philips PW1720 in the Bragg-Brentano geometry and routinely operational voltage of 40 KV and filament current of 40 mA were used. Cu-Kα radiation with a wavelength of 1.54060 Å was used and the measurements of intensity versus 2θ were taken from 20 to 100° at 0.01° intervals every 5 seconds. A nickel filter was used to reduce intensity of Cu-Kβ reflections to less than 0.2% of the intensity of the Cu-Kα reflections.

The sample was placed on a (100) plane cleaved silicon single crystal holder, which does not exhibit a peak in the practical measuring range **[9-10]**. X-ray beam is targeted on the sample while the sample is rotated and tilted. X-ray diffraction pattern for each

sample were collected with the aid of Phillips PC-APD software [11]. XRD pattern was then analysed by using systematic catalogue of powder diffraction file (JCPDS) [12-13]. CELREF, a crystal cell parameters program was used to determine the lattice parameters using a least squares refinement method.

5.64 Scanning Electron Microscope

Scanning electron microscopy (SEM) is a non-destructive method and used primarily for the study of surface topography of solid material. The surface morphology of the sintered components were observed with a jeol-5610v scanning electron microscopy at an accelerating voltage of 20 KV and at the magnification factor ranging between 1000 to 10000. In this study, the SEM was used to characterise the microstructure of the polished and fractured surfaces of the sintered electrolyte/cathode samples. The samples were cleaved to expose their fracture surfaces. Then they were immediately attached on the double-sided carbon tabs, which were stuck on aluminium sample stubs. Subsequently, samples on stubs were gold sputtered so that the gold coating would aid the electrical conduction and not result in charging of samples by the electron beam.

The SEM uses electrons instead of light to form an image. A beam of electrons is produced at the top of the microscope by heating of a metallic filament. The electron beam follows a vertical path through the column of the microscope. It makes its way through electromagnetic lenses, which focus and direct the beam down towards the sample. Once it hits the sample, other electrons (backscattered or secondary) are ejected from the sample. The electrons are collected and used to modulate a synchronous cathode-ray beam and thereby produce point-by-point image on the cathode ray display tube [14]. The intensity of the beam is related to the topography of the sample. The images produced were in the form of micrographs, which were taken to illustrate the effects of heat treatment upon the samples.

5.65 Focussed Ion Beam Secondary Ion Electron Microscopy (FIB-SIMS)

Imaging was done using a fine-focus 5nm beam (FEI-FIB 200 SIMS) scanned over an area of the specimen surface (up to a few mm^2). Because the ion beam (gallium ions from a liquid metal source) used was very fine, FIB-SIMS can be used to see detailed microstructures of our specimens. A cross-section of the specimen was viewed by creating a crater drilled by a high current beam. The crater was then tilted 45° to see the cross section of the specimen. The ion beams irradiated the specimen surface, which

resulted in the emission of secondary electrons, which could be collected in order to determine the composition of specific regions of our specimen.

5.6.6 AC Impedance Spectroscopy

5.6.6.1 Introduction

Electrical measurements of all the pellets sintered at 850°C, 950°C, 1050°C and 1250°C were made via platinum wires attached to fine platinum meshes, which provided the current contacts to each electrode on the pellets. The pellets were held in an alumina holder using springs, which are outside the hot region of the furnace. All the pellets were tested with excitation potentials of 50mV over a frequency range from 1Mhz to 0.01 Hz in the temperature range 400°C to 700°C in air. Each spectrum showed two semicircles that represent the response of the grain interior and grain boundary of these materials. Fitting of semi-circles permits the resistance of these components to be measured and then the Arrhenius graph of Log ASR versus 1/T was plotted. The gradient of each line was used to calculate the activation energy for ionic conductivity.

5.6.6.2 Theory

Impedance spectroscopy (IS) can be used to characterise the electrical properties of materials and their interfaces with electronically conducting electrodes. It has been used extensively in the fields of electrochemistry, solid electrolytes and corrosion for the precise determination of ionic transport properties and for interfacial reaction studies. The first application to solid electrolytes was published by Bauerle in 1969 for the O_2, Pt/YSZ/Pt, O_2 cell **[15]**. Bauerle's results show the separation of grain, grain boundary and electrode resistances. Since then, impedance spectroscopy has become a basic technique for characterising solid electrolyte systems involving crystallised oxides, halides, glasses, polymers and protonic systems.

If a small ac potential is applied to a sample, impedance can be given by as equation, which follows Ohm's law:

$$Z = \frac{V}{I}$$

where Z = the impedance

V = the applied voltage and

I = the resultant current.

It should be noted that the impedance is the time dependent transfer function between the applied voltage and the current, whereas the resistance is the steady state relationship between voltage and current. Thus the impedance is a function of the frequency of the signal, whereas the resistance is independence of frequency. The resistive part is describes as a real number (Z') and the reactance is described as an imaginary number (Z''). This is called complex impedance, Z and it is obtained in the following manner. Normally a small a.c.voltage of angular frequency, ω and amplitude V_o is applied to the sample such that:

$$V = V_o e^{i\omega t} \qquad [1]$$

This induces a current through the sample:

$$I = I_o e^{(i\omega t+\phi)} \qquad [2]$$

where, Vo = the amplitude of the voltage

lo = the subsequent current

ω = the angular frequency of the signal (2πf)

t = the time

ϕ = the phase difference between the two sinusoidal wave function

The complex impedance is simply the ratio of the equation [1] and [2]:

$$Z = \frac{V}{I} = \frac{V_o e^{i\omega t}}{I_o e^{(i\omega t+\phi)}}$$

This can be reduced to:

$$Z = \frac{V_o}{I_o} e^{-i\phi} = |Z| e^{-i\phi}$$

This can also be expressed in Cartesian co-ordinates as,

$$Z = |Z|\cos\phi - j|Z|\sin\phi$$

where, $|Z|$ = Vo/Io

ϕ = the angle between Z and real axis in the complex space.

Z can be defined such that:

$$Z = Z' - iZ''$$

where, $Z' = |Z|\cos\phi$, $Z'' = |Z|\sin\phi$

and the modulus of the impedance can be expressed as,

$$|Z|^2 = |Z'|^2 + |Z''|^2$$

The response of dielectric materials has a characteristics relaxation time constant, τ, which in contrast to the resistance and the capacitance, is independent of the geometry of the measured material and it is given by:

$$\tau = RC = \frac{\varepsilon_o \varepsilon_r}{\sigma}$$

where σ = electrical conductivity of the electrolyte (Scm^{-1})

ε_o = permittivity of free space (8.85×10^{-12} Fm^{-1})

ε_r = relative permittivity

Electrochemical impedance plots often contain several time constants. If the characteristic relation time is significantly longer than the relaxation time of another parallel process (some two to three orders of magnitude difference), then the two responses will be easy to separate in the frequency domain. However, when the relaxation times of the parallel reactions are similar (when the difference is small as one order of magnitude), then the semicircles will be more difficult to separate and becomes convoluted with one another.

In an IS measurement, the specimen is subjected to an ac voltage over a range of frequencies, and the phase (with respect to the applied potential) and amplitude of the current are measured at each frequency. In order to interpret the IS results; the impedance response of a specimen is approximated by an equivalent circuit. The components of the circuit have a physical correspondence to components of the specimen. For a solid electrolyte composed of porous electrodes on both sides of an electrolyte, the impedance response can be approximated by an equivalent circuit composed of resistance, R and capacitance, C. A simple equivalent circuit for an ideal electrolyte and the resulting impedance spectrum is shown in Figure 5.2 and Figure 5.3. The electrode process has been simplified as another parallel RC circuit, but is usually more complicated and will be discussed later in the section. The subscripts "E", "B" and "GB" represent the electrode, the bulk (electrolyte) components and the grain boundary (electrolyte), respectively. The electrode elements R_E and C_E represents the impedance response of the electrodes due to polarisation and charging effects.

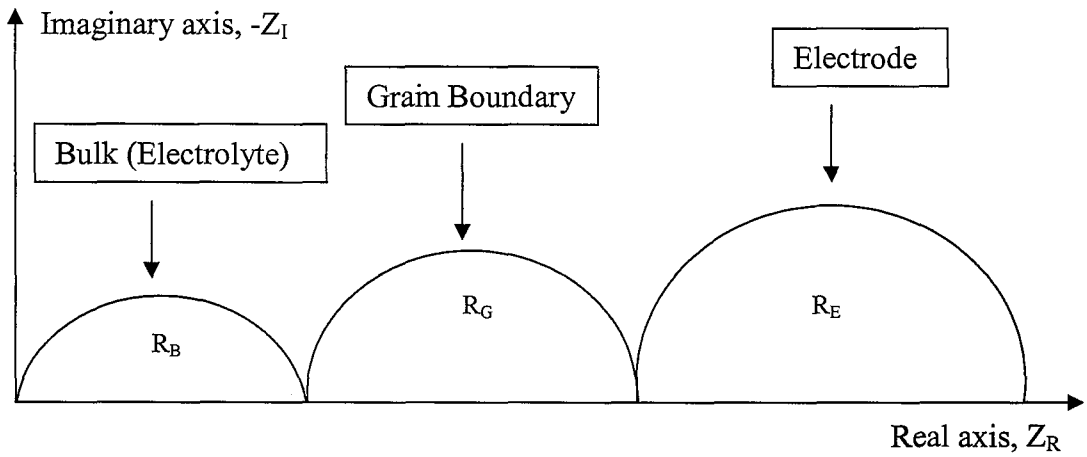


Figure 5.2:- Schematic of an AC measurement result

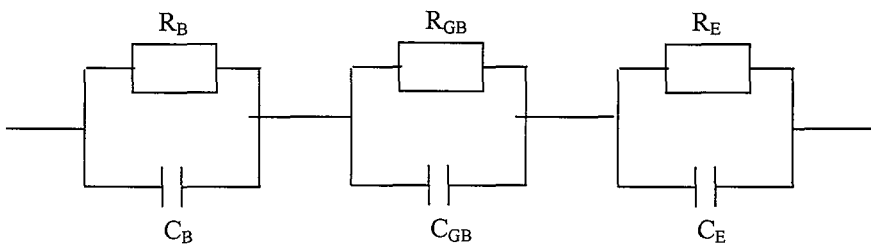


Fig 5.3:- Equivalent circuit

At low temperatures three arcs can normally be resolved in the complex impedance spectra obtained from polycrystalline oxygen ion conducting electrolytes. At moderate temperatures, the high frequency arc originates from the bulk transport and dielectric processes, the lowest frequency arc is due to oxide ion transfer at the electrodes and the intermediate frequency gives information on the grain boundary resistance to oxide ion motion. All these contributions vary with temperatures, and for a given frequency range of measurement, they may or may not all be found. Nevertheless the electrolyte response becomes distorted at high temperatures where the resistance is small and large frequencies are required to perform the measurement. This is because as the temperature is increased, the time constants (RC) of the relaxations associated with the individual polarizations are reduced and the arcs are shifted to even higher frequencies, which cannot be measured by the Solatron equipment in the laboratory.

5.6.6.3 Equivalent circuit model

Impedance spectroscopy (IS) can be a very useful tool to formulate a hypothesis, particularly when the IS data is fit to equivalent circuit models. Often, an equivalent circuit model, which fits the data, will suggest some chemical model, process, or mechanism, which can be proposed and tested. The different semi-circles constituting the spectra could also be deconvoluted using an equivalent circuit model.

The IS data were fitted using a commercial non-linear least square software Z-VIEW and were fitted using the following circuit elements:

Inductor

The electrochemical response mainly comprised of a high frequency induction tail, L, due to the leads connecting the analyser to the holder. The impedance of an inductor increases as frequency increases.

$Z = i\omega L$

$Z' = 0 \qquad Z'' = \omega L$

Resistor

$Z = R$

$Z' = R \qquad Z'' = 0$

The impedance of a resistor is independent of frequency and has only a real component. Because there is no imaginary impedance, the current through a resistor is always in phase with voltage.

Capacitor

$Z = 1 / (i\omega C)$

$Z' = 0 \qquad Z'' = 1 / (\omega C)$

The impedance versus frequency behaviour of a capacitor is opposite to that of an inductor. A capacitor's impedance decreases as the frequency is raised. Capacitors also have only an imaginary impedance component. The current through a capacitor is phase shifted - 90° with respect to the voltage.

Constant Phase Element (CPE) [15]

Capacitors in an impedance spectroscopy measurements often do not behave ideally. Instead they act like a constant phase element (CPE). The constant phase element is a non-intuitive circuit element that was discovered while looking at the response of some systems, where the Nyquist plot is a indeed the arc of a circle, but with the centre some distance below the x-axis (depressed semicircle). Often a CPE is used in a model in place of a capacitor to compensate for non-homogeneity in the system. Each constant phase element is defined by:

$Z = 1/T(j\omega)^n$

The CPE is defined by two values, CPE-T and CPE-n. When this equation describes a capacitor, the constant T = 1/C (the inverse of the capacitance) and the exponent n = 1. For a constant phase element, the exponent n is less than one.

A CPE with CPE-n value of 0.5 can be used to produce an Infinite Length Warburg element.

There are many contributions to the constant phase element and some of these are summarised below:

- Surface roughness
- Inhomogeneous reaction rates on a surface
- Varying thickness or composition of the coating
- Non-uniform current distribution

Warburg

Diffusion can create an impedance known as the Warburg impedance. This impedance depends on the frequency of the potential perturbation. If the material is thin, low frequencies will penetrate the entire thickness, creating a Finite Length Warburg element. If the material is thick enough so that the lowest frequencies applied do not fully penetrate the layer, it must be interpreted as infinite. At high frequencies the Warburg impedance is small since diffusing reactants don't have to move very far. At low frequencies the reactants have to diffuse farther, thereby increasing the Warburg impedance.

The equation for the "infinite" Warburg impedance is:

$$Z = \frac{\sigma}{\omega^{\frac{1}{2}}}(1-j)$$

In the above equation, σ is the Warburg coefficient defined as:

$$\sigma = \frac{RT}{n^2F^2A\sqrt{2}}\left(\frac{1}{C_o^*\sqrt{D_o}} + \frac{1}{C_R^*\sqrt{D_R}}\right)$$

In which,

ω = radial frequency

D_o = diffusion coefficient of the oxidant

D_R = diffusion coefficient of the reductant

A = surface area of the electrode

n = number of electrons transferred

C_o^* = bulk concentration of diffusing species (moles/cm^3)

R = gas constant

F = Faraday's constant

On the Nyquist plot the infinite Warburg impedance appears as a diagonal line with a slope of 0.5.

This form of the Warburg impedance is only valid if the diffusion layer has an infinite thickness. However, if the diffusion layer is bounded, the impedance at lower frequencies no longer obeys the equation above, Instead its in the form:

$$Z_o = \frac{\sigma}{\omega^{\frac{1}{2}}}(1-j)\tanh\left(\delta\left(\frac{j\omega}{D}\right)^{\frac{1}{2}}\right)$$

with,

δ = Nernst diffusion layer thickness

D = an average value of the diffusion coefficients of the diffusing species

This more general equation is called the "finite" Warburg.

References

[1] L.A. Chick, L.R. Pedersen, G.D. Maupin, J.L. Bates, L.E. Thomas and G.J. Exarhos, Mater. Lett. 10, (1990), p6.

[2] C. Xia, W. Rauch, F. Chen and M. Liu, Solid State Ionics, 149, (2002), p11-19.

[3] N. Arul Dhas and K.C. Patil, J. Mater. Sci. Lett, 12, (1993), p1844-1847

[4] L.El. Farh, M. Massot, M. Lemal, C. Julien, S. Chitra, P. Kalyani, T. Mohan and R. Gangadharan, J. Electroceram, 3-4, (1999), p425-432.

[5] V.V. Kharton, F.M. Figueiredo, L. Navarro, E.N. Naumovich, A.V. Kovalevsky, A.A. Yaremchenko, A.P. Viskup, A. Carneiro, F.M.B. Marques and J.R. Frada, Journal of Materials Science, 36, (2001), p1105-1117.

[7] J.H. Chesters, Steeleplant Refractories, United Steele Cos. Sheffield, 1963.

[8] A. Terence, Particle Size Measurement, Chapmen and Hall, London, 1990.

[9] R. Sweeney, Private Communication, Imperial College, London.

[10] G.M. Christie, Ph.D. Thesis, Imperial College, London, 1993.

[11] B.D. Cullity, Elements of X-ray Diffraction, Reading, Mass, London, Addison-Wesley, (1956)

[12] Powder Diffraction File Alphabetical Indexes, Inorganic Phases, Swarthmore, JCPDS, Internal Centre for Diffraction Data, USA.

[13] Inorganic Crystal Structure Data Files, Cambridge Crystallography Data Centre.

[14] P.J. Goodhew, J. Humphreys and R. Beanland, Electron Microscopy and Analysis, Taylor and Francis, London, (2001).

[15] J.R. Macdonald, Impedance Spectroscopy, John Wiley and Sons, New York (1988).

Chapter 6 - Results and Discussion

6.1 Powder Characterisation

6.1.1 Particle Size Measurement

The particle sizes of the powders were characterized as received from the manufacturer. The average values for the median particle size d_{50} (i.e. particle size at which 50% of the particles are larger and 50% are smaller or the so-called median size) distribution are shown in the Table 6.1.1 below.

Material	d_{50} (μm)
LSM ($La_{0.6}Sr_{0.4}MnO_{3-\delta}$)	6.96
Rhodia $La_{0.6}Sr_{0.4}Co_{0.2}Fe_{0.8}O_{3-\delta}$ (LSCF) as received	6.01
Rhodia $Ce_{0.9}Gd_{0.1}O_{2-x}$ (CGO10-90) as received	4.96
Rhodia $Ce_{0.8}Gd_{0.2}O_{2-x}$ (CGO20-80) as received	4.22
Rhodia CGO20-80-LSCF ball milled	1.47
Rhodia 20-80CGO-LSCF cal at 1050°C	24.56
Polymethylmethacrylate (PMMA)	5-10
Milled carbon powder	3.26

Table 6.1.1:- Particle size analysis results of the powders

The size, morphology and degree of agglomeration of the "as received" and calcined powders are all important characteristics when high performance cathodes are required. The median particle sizes of LSM and LSCF powders are very similar to each other. Also the CGO10-90 powder had a very similar particle size to the CGO20-80. The median particle size of CGO20-80/LSCF made from ball milling of the powders for 24 hours are found to be around 1.47μm. In theory ball milling reduces the size of the particles. The zirconia balls used in ball milling were more effective in breaking up the particle sizes of CGO and LSCF powders. The median particle size of the calcined powders are much higher, this is due to sintering of the powders. At 1050°C, the powders are on the brink of sintering and hence the increase in particle size.

6.1.2 Dilatometry

Dilatometry is generally the method used to investigate the sinterability of ceramic powders. There are two heating schedules, which can be employed for the sintering studies of the compact powders. In the first case, the powder compact is heated to a fixed sintering temperature and held at this allocated temperature for a specified time, and finally cooled to room temperature. This schedule is referred to as isothermal sintering. In the other case, referred to as constant heating rate (CHR) sintering, the compact is heated at a fixed rate to the required temperature, after which it is cooled. Densification of a material fired from a green state to high density can be characterised easier using CHR dilatometry.

Figure 6.1.1-6.1.3 shows change in length versus temperature data obtained from a dilatometer during the sintering of green powder compacts of pure CGO, LSCF and LSM. Virtually no shrinkage is seen for all three materials before 500°C. At approximately 600°C the CGO has commenced shrinking, whereas the pure LSCF and pure LSM have commenced shrinking around 750°C and 900°C. There are inflections in the sintering curves in all three materials. This occurs between room temperature and the onset of shrinkage. The small dip in the curve between the room temperature and 200°C is due to the expansion of the sample holder during heating, hence the decrease in sample length. The rise in the curves between 200°C and the onset of shrinkage is due to the small expansion of the material. The appearance of plateau at 1000°C for the CGO pellet in Figure 6.1.1 is due to the sample becoming fully dense at that temperature. Although the dilatometry plot for LSCF ends at around 1000°C, the absence of a plateau at high temperatures in figures 6.1.2 and 6.1.3 indicates that full density had not yet been achieved.

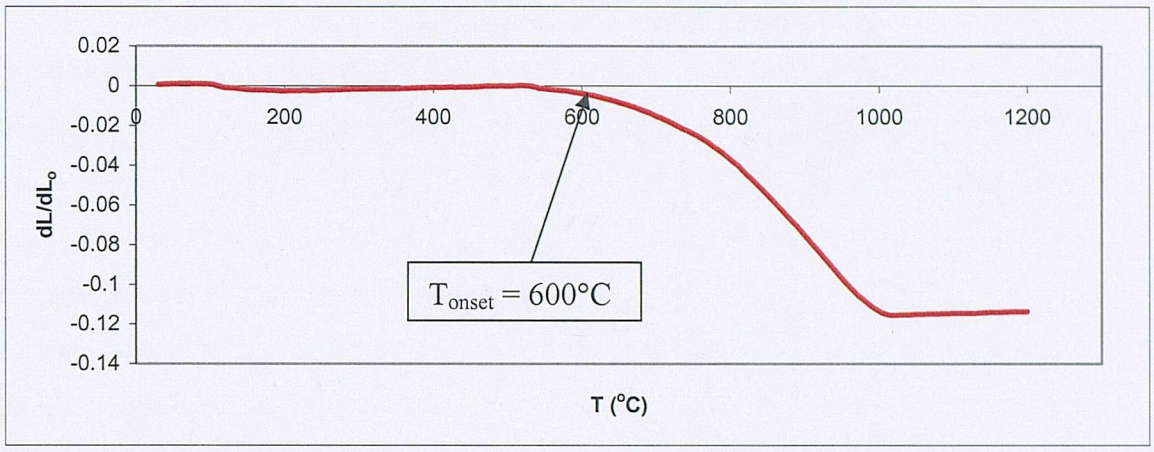


Fig 6.1.1:- Dilatometry trace for a pure CGO20-80 powder sample

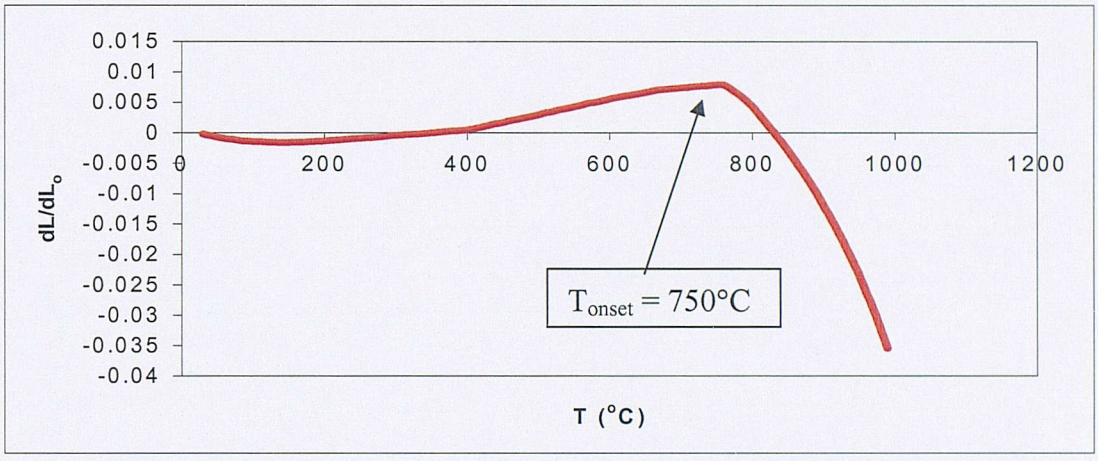


Fig 6.1.2:- Dilatometry trace for a pure LSCF powder sample

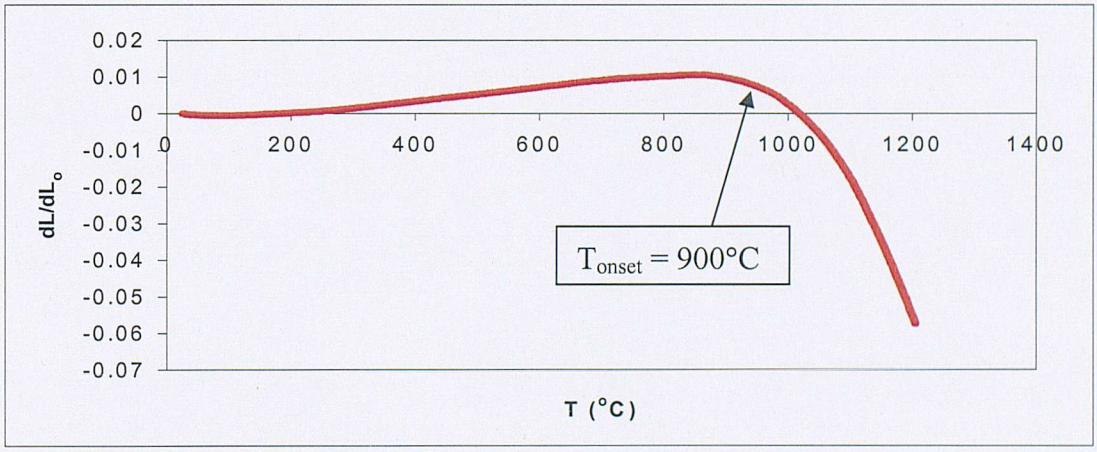


Fig 6.1.3:- Dilatometry trace for a pure LSM powder sample

6.1.3 Electrolyte Characterisation by AC Impedance Spectroscopy

Impedance spectroscopy normally resolves the bulk, grain-boundary and electrode processes by exhibiting successive semicircles (with some distribution) in the complex plane [1]. A high frequency (the left hand side of the AC impedance plot) semicircle originates from the bulk conduction; a low frequency semicircle or arc is due to ion and electron transfer at the surface contacting the electrode, and an intermediate frequency semicircle provides information on the grain-boundary and/or impurity-phase resistance to ionic conduction. All these contributions vary with temperatures, and for a given frequency range of measurement, they may or may not all be found. Nevertheless the electrolyte response becomes distorted at high temperatures where the resistance is small and large frequencies are required to perform the measurement. This is because the time constant of the electrolyte response is small at high temperatures.

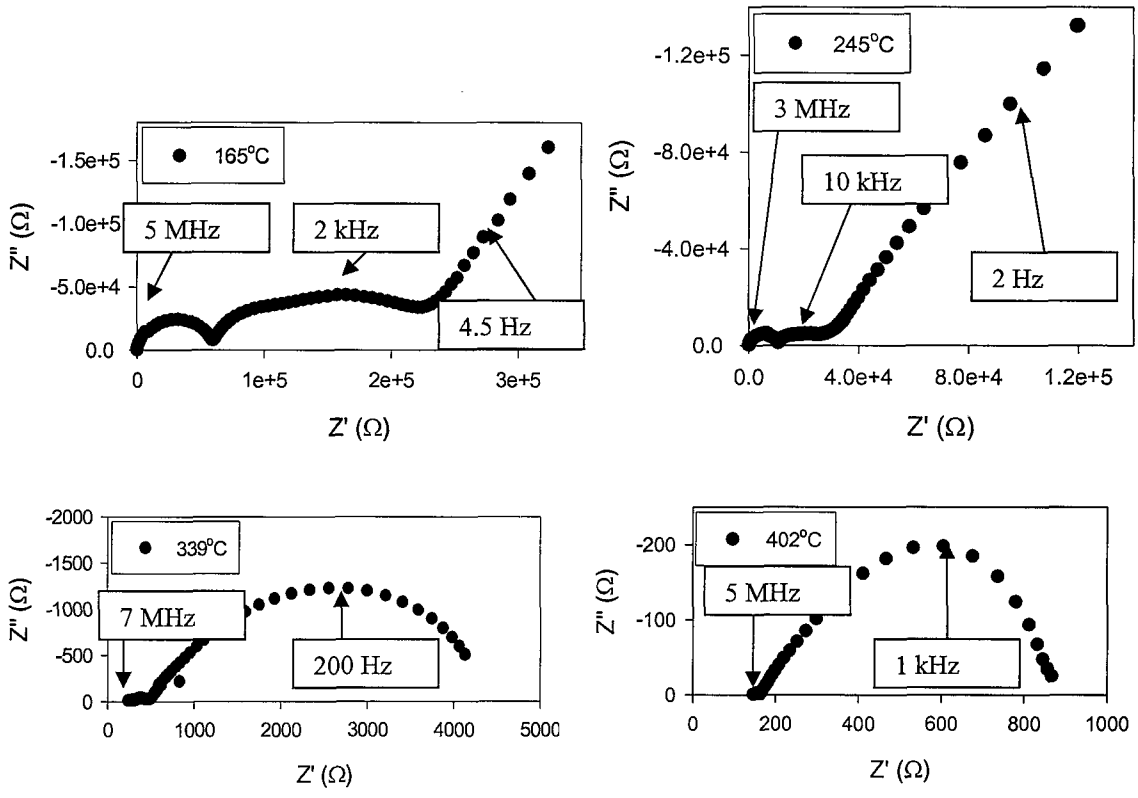


Fig 6.1.4:- Complex impedance spectra of $Ce_{0.9}Gd_{0.1}O_{2-x}$ pellets with silver electrodes

The complex impedance of CGO10-90 electrolyte was measured using silver electrodes, which were fired at 700°C for two hours. AC impedance spectra were measured in air in the temperature range 150-450°C. Figure 6.1.4 shows typical spectra of complex impedance responses of silver coated CGO10-90 electrolyte. As indicated on Figure

6.1.4, at low temperature (165°C) four arcs can be observed. The two arcs observed at higher frequency can be associated with the bulk and grain boundary response of the CGO electrolyte and the two arcs at lower frequency come from the silver electrode. The extra electrode arc observed for the complex impedance plot at 165°C can be due to the electronic current transfer between the current collector and the silver electrode. For each arc observed on the complex impedance plot, three parameters can be obtained: (1) the resistance, R (from the intercept of the real axis, Z'), (2) the capacitance, C (from the frequency at maximum Z'' where $\omega RC = 1$), and (3) the depression angle, α. The values of α and C are independent of the temperature, while the parameter, R, on the other hand is strongly temperature dependent. The values for C were typically in 10^{-12} Farads for the bulk response, 10^{-9} Farads for the grain boundary response and 10^{-5} Farads for the electrode response. The conductivity and the capacitance parameters are compiled in Table 6.1.2. This information was used for finding the offset of the bulk and grain boundary response, and hence later can be used for finding the offset of the CGO/LSCF composite cathode response.

Temperature (°C)	**Bulk resistivity (Ωcm)**	**C (pF)**	**Bulk conductivity (Scm^{-1})**	**Grain boundary resistivity (Ωcm)**	**C (nF)**	**Grain boundary conductivity (Scm^{-1})**
165	2.7×10^{6}	32	3.7×10^{-7}	9.7×10^{6}	3.0	1.03×10^{-7}
245	4.7×10^{5}	38	2.1×10^{-6}	3.7×10^{5}	2.9	2.7×10^{-6}
339				1.5×10^{4}	3.3	6.7×10^{-5}
402				1304	3.0	7.7×10^{-4}

Table 6.1.2:- Resistivity ρ, capacitance C and conductivity σ for bulk and grain boundary of $Ce_{0.9}Gd_{0.1}O_{2-x}$ calcined at 1400°C

Figure 6.1.5 shows the grain boundary resistivity of the CGO10-90 electrolyte as an Arrhenius graph. The Arrhenius graph for the bulk resistivity could not be drawn as only two readings were obtained from the response. The activation energy for the grain boundary resistivity is calculated to be 0.94 ev. This value of activation energy is in good agreement with literature values **[2, 3]**.

At low temperatures, the electrode polarization resistance, electrolyte grain boundary and electrolyte grain interior resistance can be seen in the complex plane as three different semi-circles. By increasing the temperature, the semicircle for the bulk is diminished (time constant of the bulk response is too short and can not be observed with the Solatron equipment) and only the grain boundary semicircle with the electrode semicircle is visible. Finally the grain boundary semicircle also disappears (to higher frequency) at even higher temperatures (above 400°C).

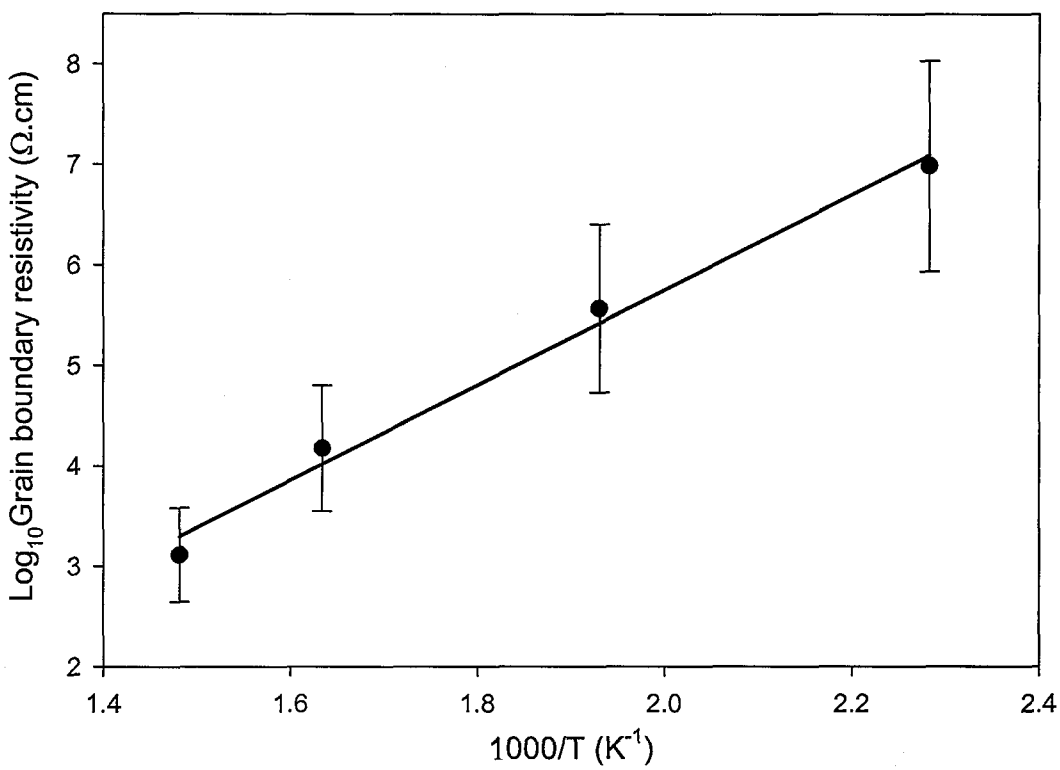


Figure 6.1.5:- Arrhenius graph of the grain boundary resistivity of CGO10-90 electrolyte

6.2 CGO/LSCF

6.2.1 Powder Characterization

Pure CeO_2 has the cubic fluorite structure up to its melting point. Therefore CeO_2, unlike ZrO_2, does not need any stabilization. Depending on temperature and oxygen partial pressure, the material exhibits a large oxygen deficiency with the formula $CeO_{2-\delta}$, where "δ" may be as large as 0.3. The high ionic conductivity and low activation energy for ionic conduction makes doped CeO_2 attractive as a solid electrolyte particularly at temperatures below 800°C. The radius of the Ce^{4+} ion in CeO_2 is sufficiently large (0.97 Å) that a variety of dopants can be incorporated to form solid solutions. Replacing Ce^{4+} with 2+ or 3+ cations result in the creation of anion vacancy sites to compensate in the lattice (because of charge compensation). As a result, a solid electrolyte with ionic conductivity for oxygen over an extended temperature and oxygen pressure range may be produced. The highest ionic conductivity (0.1 to 0.2 Scm^{-1}) was reported for a doping level of 10 mol% of alkaline earth addition **[4, 37]**.

X-ray diffraction was performed on both the nominal $Ce_{0.9}Gd_{0.1}O_{2-x}$ (CGO10-90) and $Ce_{0.8}Gd_{0.2}O_{2-x}$ (CGO20-80) compounds obtained from the commercial suppliers, Rhodia (La Rochelle, France, batch 97162/98 and 99276/98 respectively), with the aim to ascertain phase purity and stoichiometric composition. Figure 6.2.1 and figure 6.2.2 shows the X-ray diffraction data for the "as received" powder. Both the materials were single phase and no impurity peaks can be found. All the peaks are very sharp showing the crystalline nature of the powders. The Bragg peaks were identified using the file $Ce_{0.8}Gd_{0.2}O_2$ (JCPDS 75-0162). The XRD patterns obtained from both the materials studied at room temperature was fitted to a cubic fluorite structure using the software celref **[5]**. The lattice parameters were extracted as 5.39664 (± 0.00005) Å for CGO10-90 and 5.39986 (± 0.00005) Å for CGO20-80 respectively. The theoretical X-ray density calculated for both the CGO10-90 and CGO20-80 cathode powder is 7.3114 gcm^{-3} and 7.3369gcm^{-3}. There is a very slight shift in the peak diffraction angles, relative to pure ceria, to lower 2θ values. These shifts are due to dissolution of the additives (Gd) in the fluorite structure (CeO_2).

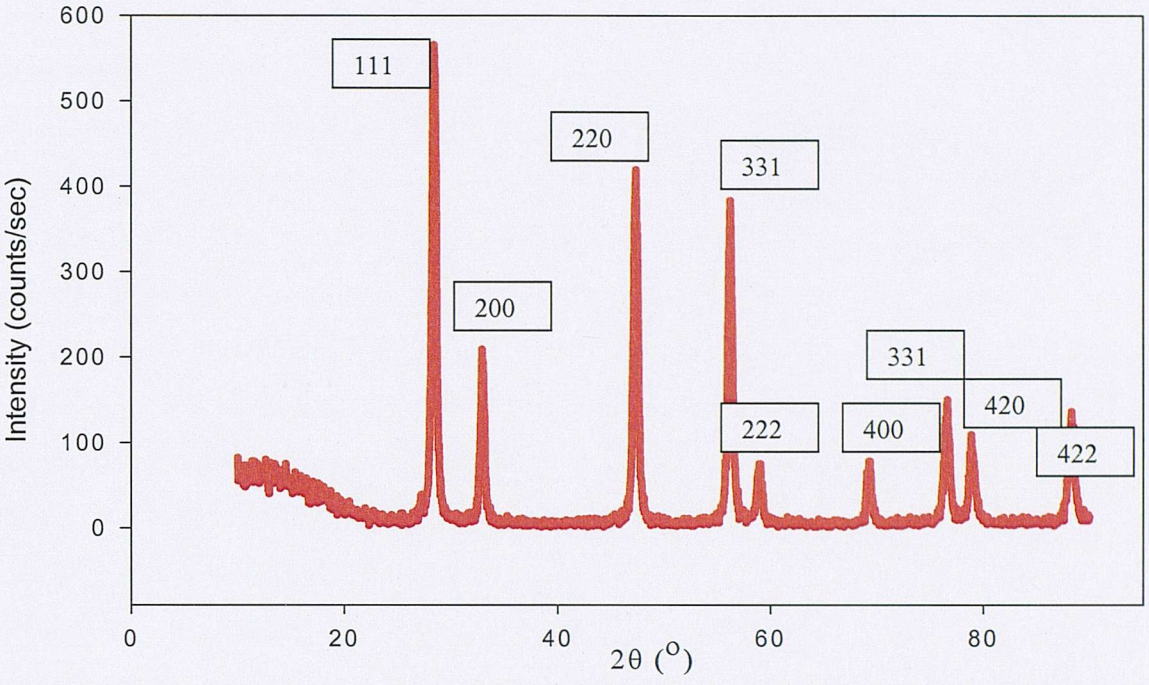


Figure 6.2.1: X-ray diffraction pattern of $Ce_{0.9}Gd_{0.1}O_{2-x}$ (electrolyte material) using Cu-K_α radiation (λ = 1.5406 Å)

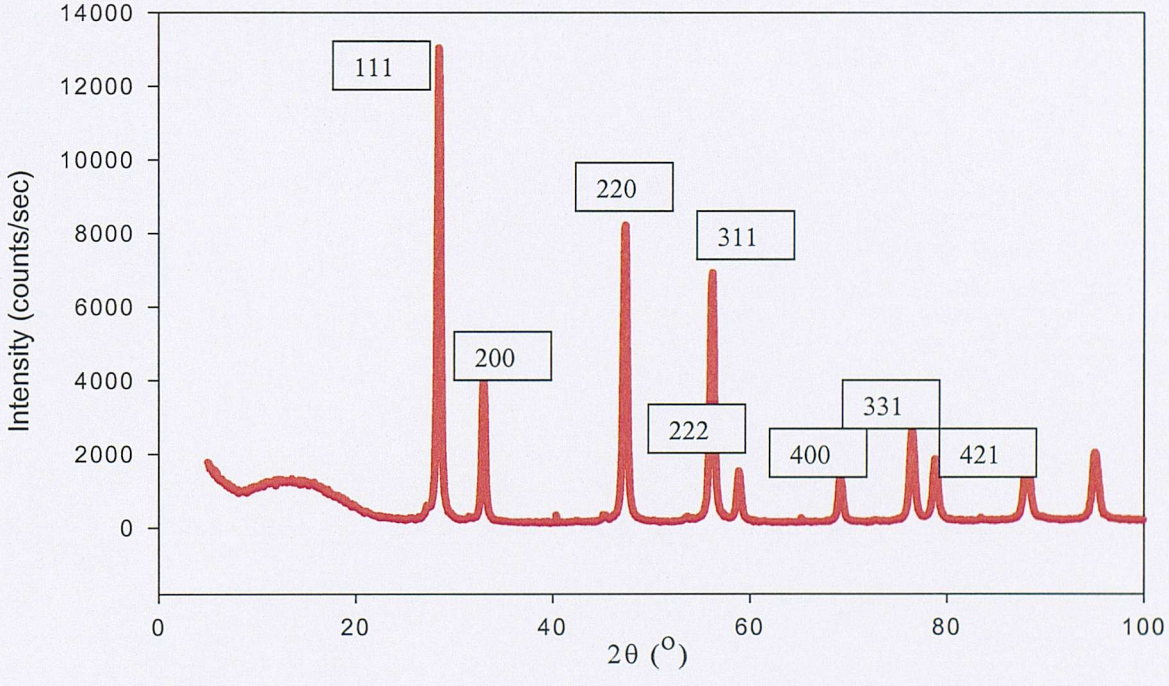


Figure 6.2.2: X-ray diffraction pattern of $Ce_{0.8}Gd_{0.2}O_{2-x}$ using Cu-K_α radiation (λ = 1.5406 Å)

The X-ray diffraction pattern for the "as received" powders from the commercial suppliers, Rhodia (La Rochelle, France, batch FPT-FC2-00), for the $La_{0.6}Sr_{0.4}Fe_{0.8}Co_{0.2}O_{3-\delta}$ (LSCF) powder is shown in Figure 6.2.3. The XRD pattern shows a single-phase perovskite structure and no peak corresponding to any impurity is observed. The Bragg peaks were identified using the file $La_{0.6}Sr_{0.4}CoO_3$ (JCPDS 36-1393). The XRD peaks are found to be very sharp indicating the highly crystalline nature of the perovskite. The LSCF was fitted to a rhombohedral unit cell using the software celref. Tai et al **[6]** report that $La_{0.8}Sr_{0.2}Fe_{0.8}Co_{0.2}O_3$ is orthorhombic, their investigations showed however, that this composition lies directly at the point where the structure changes from the orthorhombic to the rhombohedral unit cell: for iron content up to 70 mol% the perovskite is rhombohedral, while for 80-100 mol% orthorhombic. Moreover, in a subsequent paper of Tai et al **[7]**, where the influence of strontium substitution is studied, we see that compounds with Sr-content up to 10mol% were found to crystallize in the orthorhombic structure whereas compositions with 30-40 mol% in the rhombohedral structure. The a, b and c parameters were extracted as 5.5090 (± 0.0004) Å, 5.5090 (± 0.0004) Å and 13.452 (± 0.0004) Å respectively. The theoretical X-ray density calculated for LSCF cathode powder is 6.29 gcm^{-3} and the reported literature value is 6.36gcm^{-3} **[8]**.

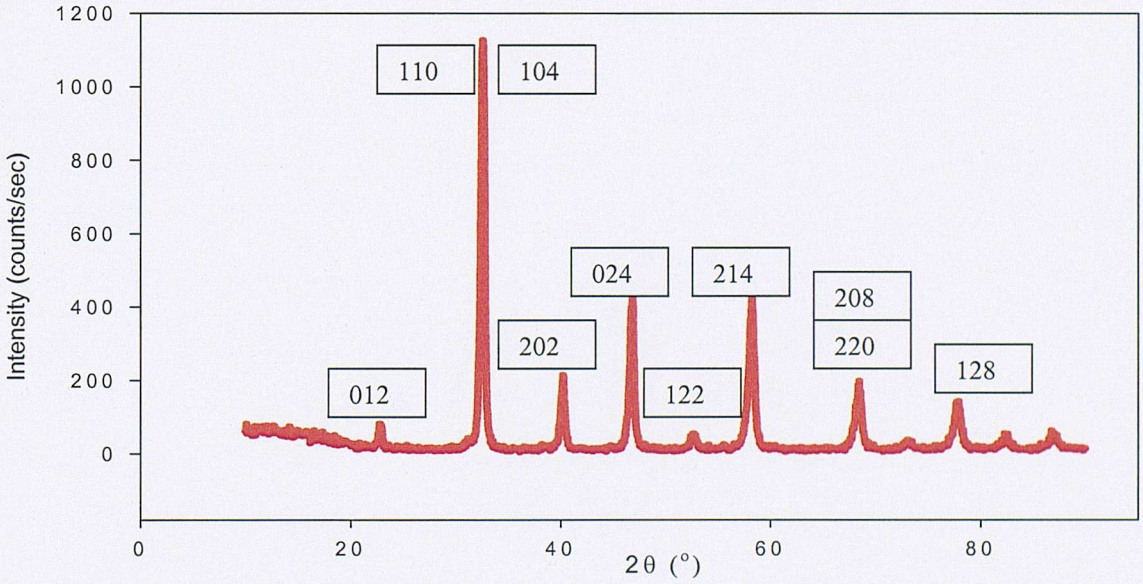


Figure 6.2.3: X-ray diffraction pattern of $La_{0.6}Sr_{0.4}Co_{0.2}Fe_{0.8}O_{3-\delta}$ using Cu-K_α radiation (λ = 1.5406 Å)

Figure 6.2.4 shows the X-ray diffraction pattern of the $Ce_{0.8}Gd_{0.2}O_{2-x}/La_{0.6}Sr_{0.4}Co_{0.2}Fe_{0.8}O_{3-\delta}$ (30 weight% CGO) cathode powder calcined at 1000°C for 2 hours. All the Bragg peaks corresponding to the CGO-20 and LSCF phase could be matched and no secondary phase can be found. LSCF peaks are of greater intensity and overlap a few CGO peaks.

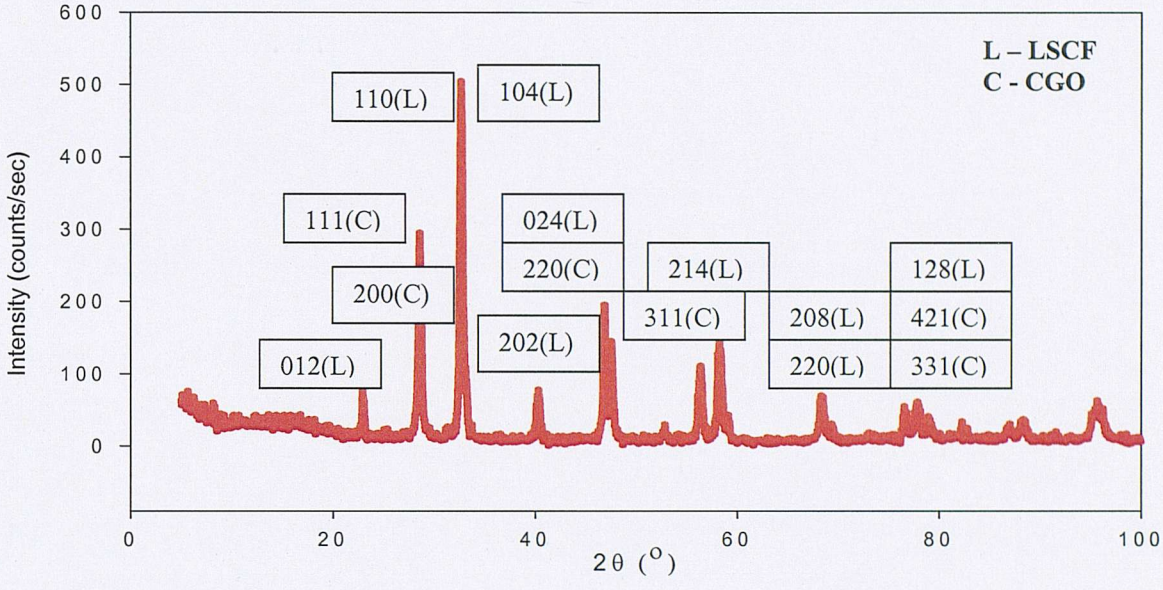


Figure 6.2.4: X-ray diffraction pattern of $Ce_{0.8}Gd_{0.2}O_{2-x}/La_{0.6}Sr_{0.4}Co_{0.2}Fe_{0.8}O_{3-\delta}$ composite using Cu-K_α radiation (λ = 1.5406 Å)

6.2.2 Sintering studies

The dilatometric traces of the CGO20-80/LSCF composite materials are shown in Figure 6.2.5. The change in length versus temperature for CHR sintering at 10°C/min up to 1200°C was measured using the equipment described in the last chapter. At temperatures below 800°C, there is no detectable shrinkage of the specimen. The slight deviation between the room temperature and 800°C is due to the expansion of the instrument and the material. The onset of shrinkage for all three CGO20-80/LSCF composites were around 800°C, also all three plots are very similar to each other. Therefore this indicates that changing the CGO/LSCF compositions does not affect the way CGO20-80/LSCF sinters within this limited composition range.

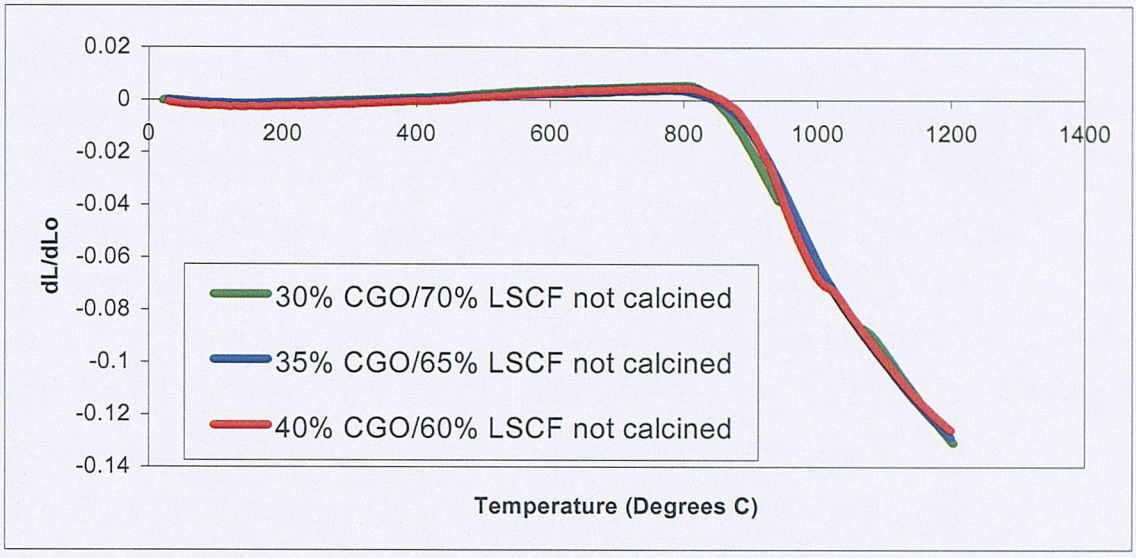


Figure 6.2.5:- Dilatometric traces of 3 CGO/LSCF composite powders

As can be observed in Figure 6.2.6, the sintering behaviour of the composite CGO20-80/LSCF cathode is dominated by the major component, the mixed conducting oxide LSCF. The absence of plateau at high temperature indicates that full density had not yet been achieved. The onset of plateau (>~1200°C) is considered to be the point at which the sample has high density (>95%).

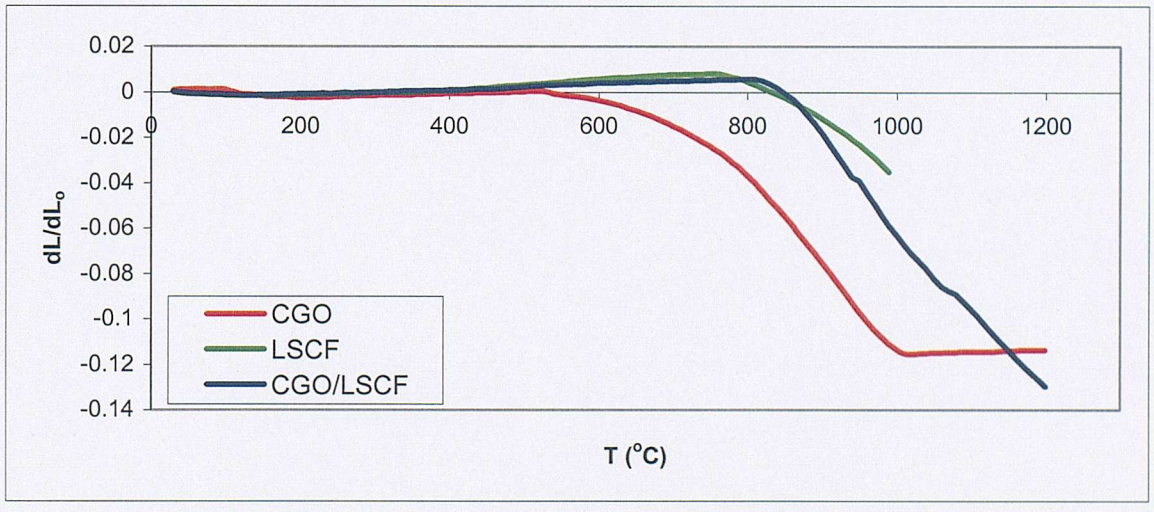


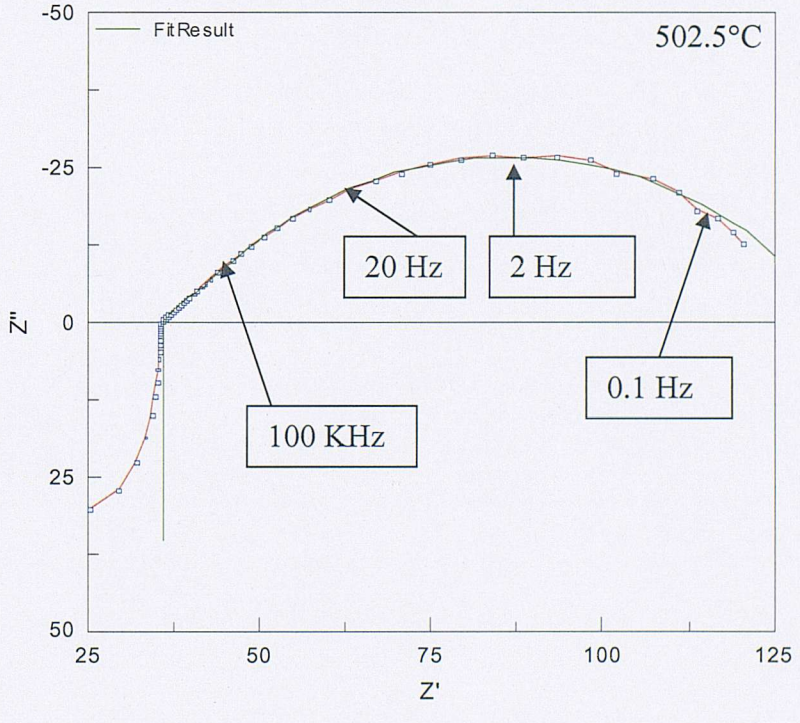
Figure 6.2.6:- Dilatometric traces of CGO, LSCF and CGO (30 weight %)/LSCF composite powders

6.2.3 Electrochemical Performance

6.2.3.1 CGO/LSCF on an as sintered electrolyte

The electrode polarization resistance for symmetrical $Ce_{0.8}Gd_{0.2}O_{2-x}$ (CGO20-80)/$La_{0.6}Sr_{0.4}Co_{0.2}Fe_{0.8}O_{3-\delta}$ (LSCF) electrodes on an as sintered $Ce_{0.9}Gd_{0.1}O_{2-x}$ electrolyte was measured using AC impedance spectroscopy, applying a 20mV alternating signal with zero DC bias. A frequency sweep from 0.01 Hz to 10 MHz was used and the measurements were made in air. Typical AC impedance spectra of CGO20-80/LSCF (70 weight % LSCF) composite coated onto an as sintered CGO10-90 electrolyte pellet and then sintered in air at 1050°C are shown in Figure 6.2.7.

Using the ZVIEW software, all three spectra in Figure 6.2.7 were fitted using the equivalent circuit in Figure 6.2.8. The responses become purely inductive above ~500 kHz at 502.5°C, ~50 kHz at 549°C and ~5 kHz at 599°C. The presence of the inductive tail can be ascribed to the inductance of the measurement leads. The inductance of these leads was measured as 1.25×10^{-6} H and it is represented as L, on the circuit model. The series resistance, R1, is mainly due to the ohmic drop in the electrolyte. The dominant arc is represented by the RCPE1 elements, where R is a resistance and CPE1 is a constant phase element and it might be attributed to the gaseous diffusion and surface exchange in the bulk of the electrode. Although previous work has shown a second, high frequency impedance component in LSCF-based electrodes **[10]**, none were observed under the conditions investigated here at this temperature.



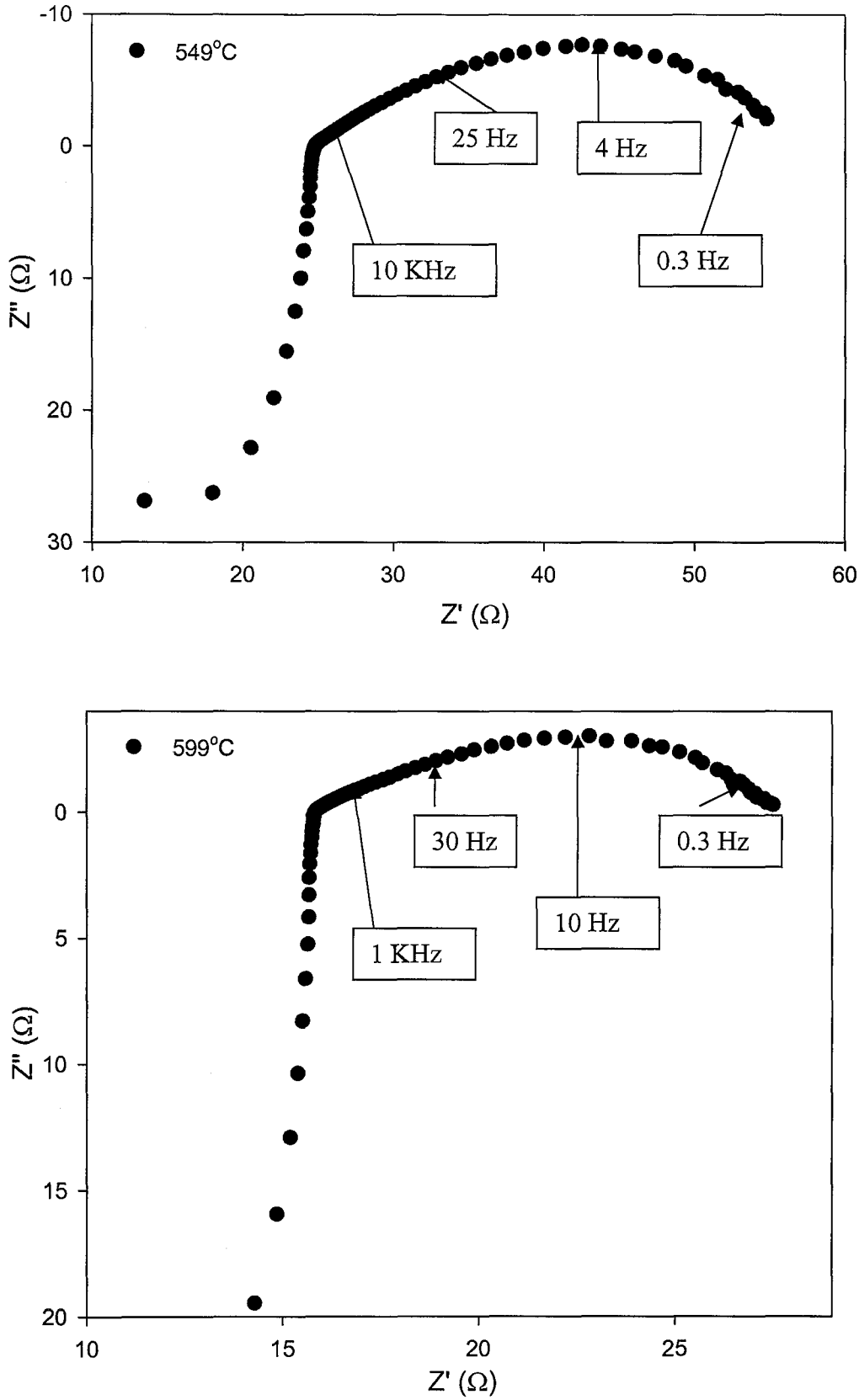


Figure 6.2.7: AC Impedance Spectroscopy spectra of CGO20-80/LSCF Composite cathode on an as sintered CGO10-90 electrolyte at various temperatures

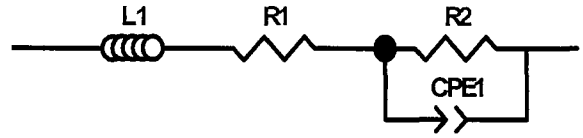


Figure 6.2.8: Equivalent circuit, LR(CPE(R))

The area specific resistance, ASR (the measured resistance between the low and high frequency intercepts of the electrode polarization arc with the x-axis and multiplied by the cross sectional area of the sample and then divided by two due to the symmetrical electrode layers) for the CGO20-80/LSCF composite cathode on an as sintered electrolyte was found to be around 30 $\Omega.cm^2$ at 502.5°C, 10 $\Omega.cm^2$ at 549°C and 5 $\Omega.cm^2$ at 599°C. This was greater, by a factor of 5, when compared to the previous work conducted by Kilner and Dusastre **[10]**. However these authors sintered their cathodes at 800°C and 900°C compared to the cathode studied in the present study where they were sintered at 1050°C. This is because the initial aim of the project was to co-sinter the whole cell at one temperature (around 1000°C) to reduce the processing cost.

The average error in the measured data was calculated to be around 15%. This error includes the weighing of powders of the cathode material (1%), the impedance measurement estimated to be 2% by **[8]**, the measurement of the sample area (2%) and the software fitting (≈10%).

The ASR can be plotted on a graph against the reciprocal of temperature in order to determine activation energy for the electrode response. This is shown in Figure 6.2.9. The activation energy for the electrode polarization resistance was calculated from a linear regression of the data and found to be 1.26 ev ±0.1 ev. The activation energy of CGO20-80/LSCF tracer diffusion coefficient, $E_a^{D^*}$ is 1.62ev **[11]** and activation energy of CGO20-80/LSCF surface exchange coefficient, E_a^{k} is 1.50ev **[11]**. According to Adler-Lane-Steele theory, the activation energy of CGO20-80/LSCF cathode should be the average of these two activation energies, which is about 1.56 ev. The value obtained for activation energy is low compared to the model, however it is in good agreement with the previous experimental studies **[10-12]**. The small differences in the ASR values is associated with the electrode processing quality, governed by parameters such as particle size, porosity, sintering temperature and the extent of particle agglomeration. Also Impurities such as siliceous materials in the CGO electrolyte can also possibly play an important role for the degradation of the electrode property during intermediate

temperature measurement, although where the siliceous materials block the electrode reaction remains ambiguous **[13]**. To overcome this problem, in the next section, we will see how the electrode behaves on a cleaned electrolyte surface.

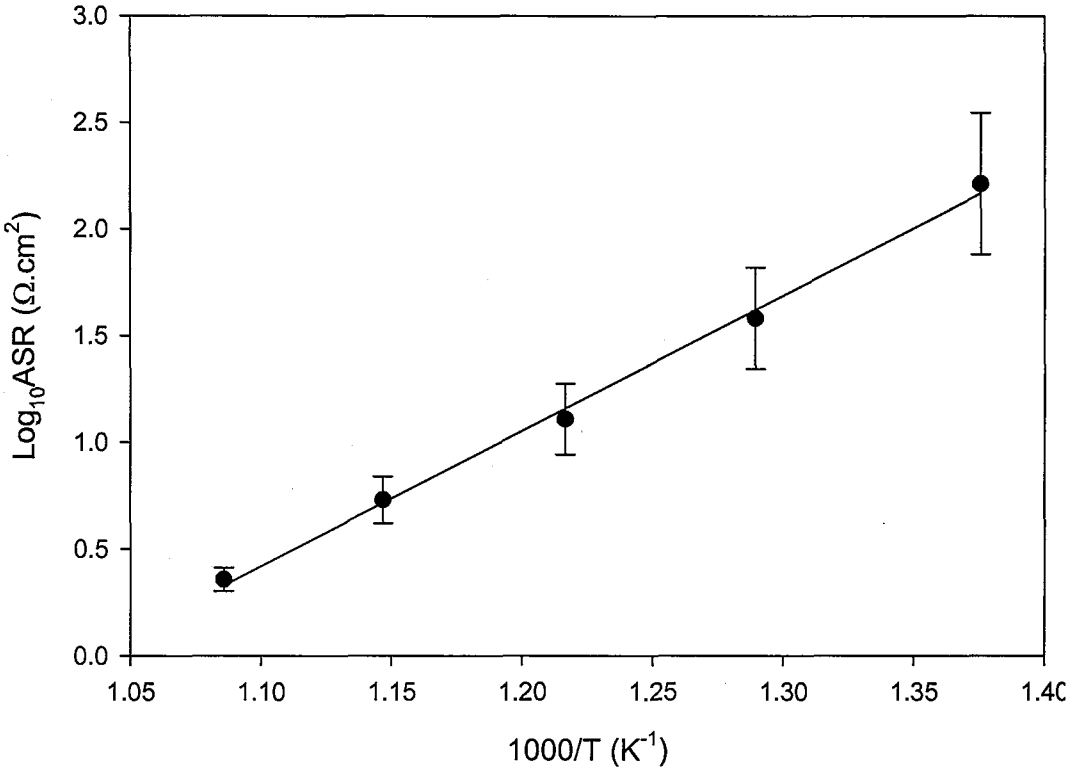


Figure 6.2.9: Arrhenius plot of the CGO20-80/LSCF composite cathode on an as sintered CGO10-90 electrolyte

6.2.3.2 CGO-LSCF on a cleaned electrolyte

Figure 6.2.10 shows the AC impedance spectra of CGO20-80/LSCF composite coated onto a cleaned CGO10-90 electrolyte pellet at 498°C, 547°C and 596°C, together with the response of the CGO20-80/LSCF on an as sintered electrolyte. The same equivalent circuit model as in Figure 6.2.8 fits the data of the CGO/LSCF on a cleaned electrolyte and all three responses can be resolved into one depressed semicircle. Here the inductive tails of the responses are not shown. The shape of the impedance response does not show a great difference between the CGO20-80/LSCF on an as sintered electrolyte and CGO20-80/LSCF on a cleaned electrolyte. The normalized plot in figure 6.2.11 supports this argument. However the offset of the CGO20-80/LSCF on a cleaned electrolyte response has shifted to lower real impedance, when compared to the offset of the CGO20-80/LSCF on an as sintered electrolyte response. This implies that there is

SiO_2 contamination on an as sintered electrolyte and are removed by cleaning the electrolyte.

The ASR value for this cathode was found to be 19.56 $\Omega.cm^2$ at 498°C, 6.54 $\Omega.cm^2$ at 547°C and 2.71 $\Omega.cm^2$ at 596°C. The area specific resistance of a CGO 20-80/LSCF on a cleaned electrolyte shows a significance improvement from that of a CGO 20-80/LSCF on an as sintered electrolyte.

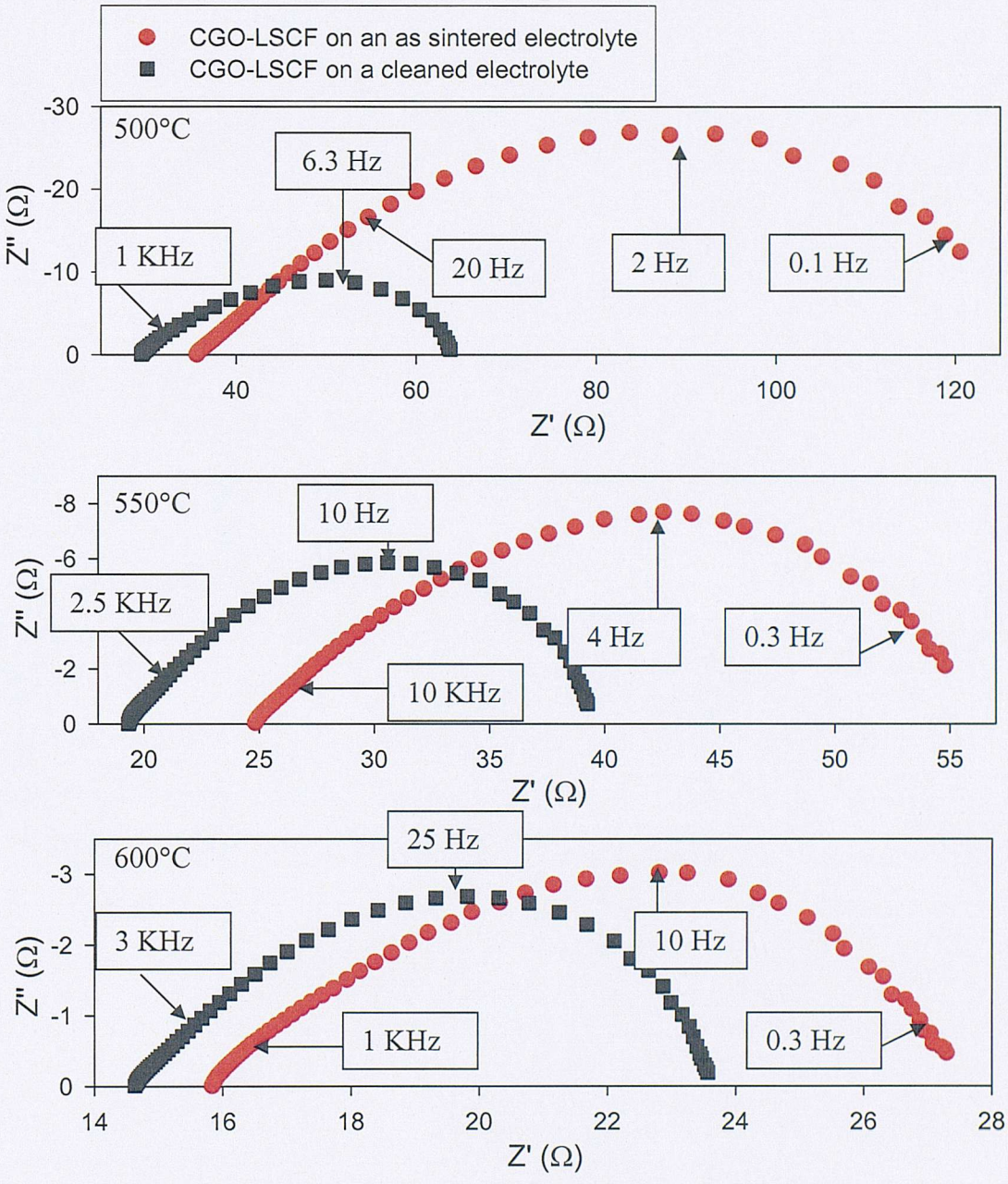


Figure 6.2.10: AC Impedance Spectroscopy spectra of CGO20-80/LSCF composite cathode on a cleaned CGO10-90 electrolyte at various temperatures

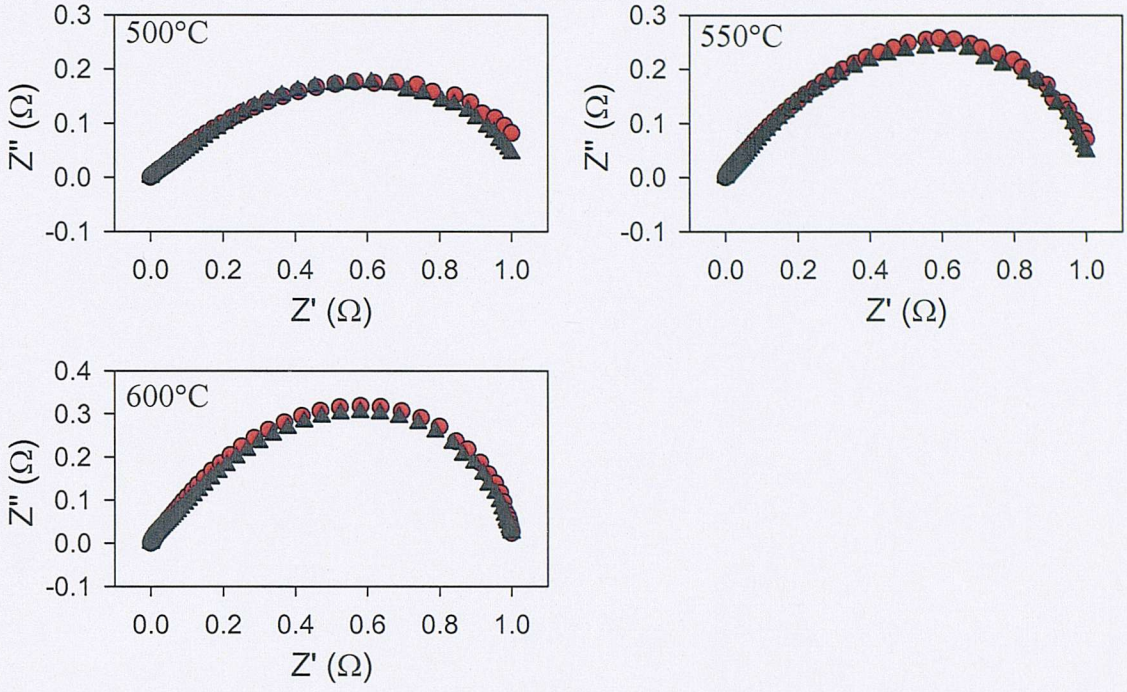


Figure 6.2.11: Normalized AC Impedance Spectroscopy spectra of CGO20-80/LSCF composite cathode on an as sintered and cleaned CGO10-90 electrolyte at various temperatures

The ASR is plotted against the reciprocal of temperature and is shown as Arrhenius plot in Figure 6.2.12. The activation energy for CGO20-80/LSCF composite cathode is found to be 1.22 ev ±0.1ev, which is similar to the activation energy of CGO20-80/LSCF on an as sintered electrolyte. This indicates that same reaction mechanism controls the overall electrode behaviour in the temperature range studied; nevertheless of the processing-induced differences in structure of the electrolyte.

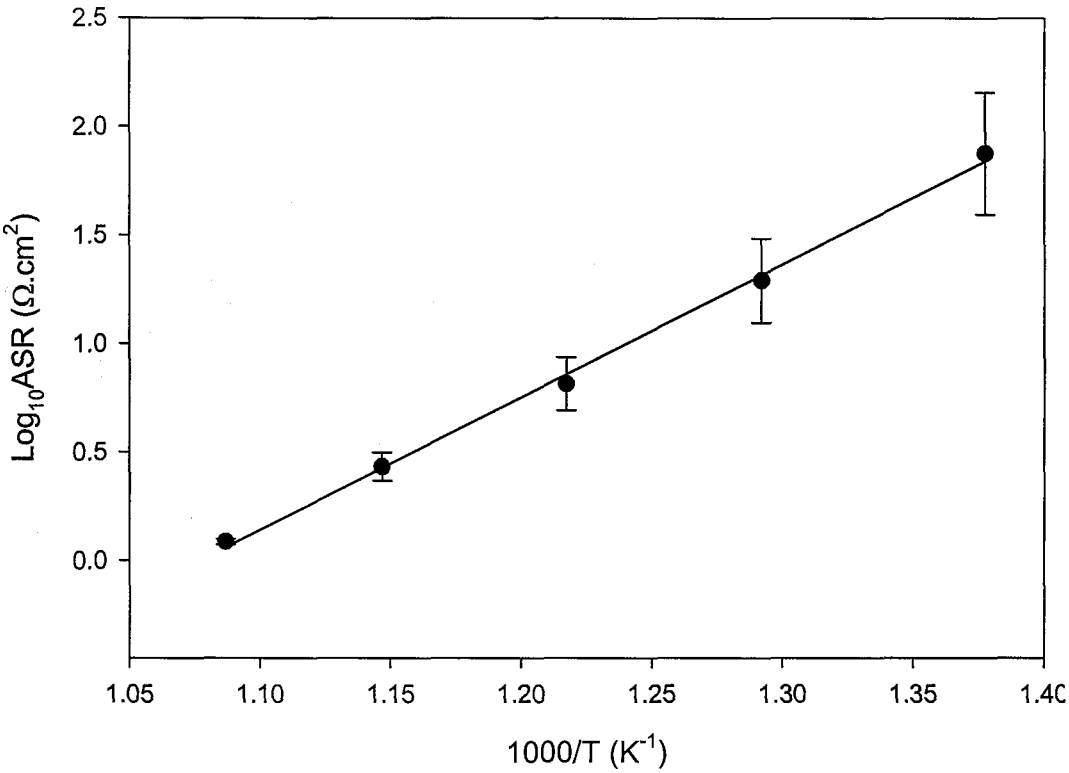


Figure 6.2.12: Arrhenius plot of the CGO20-80/LSCF composite cathode on cleaned CGO10-90 electrolyte

Figure 6.2.13 shows the SEM micrographs of an as sintered CGO10-90 electrolyte sintered at 1400°C for 5 hours. It is evident from the micrograph that there is hardly any porosity. However the grain size is small (~0.5-1.5 microns) and appears to have a bi-modal distribution of grain sizes. The surface of the electrolyte was then cleaned with a 1200 grid (5-15 micron) silicon carbide paper to ensure a clean and relatively rough surface (Figure 6.2.14). The rough surface provides larger practical surface area of the interface between the CGO 20-80/LSCF electrode and the CGO10-90 electrolyte and should provide a sufficiently intimate contact between those two surfaces. The surface of the electrolyte must not be smooth; otherwise the electrode will not adhere properly to the electrolyte. The existence of siliceous materials in CGO10-90 electrolyte plays a significant role in the electrode resistivity as well as the electrolyte resistivity itself. Clearly from the above results, we can say the presence of silicate phase (usually from the furnaces when the electrolytes are sintered at very high temperatures) clearly affects the electrode reaction, however it is very difficult to know exactly which reaction is mostly affected by the existence of siliceous materials **[13-14]**.

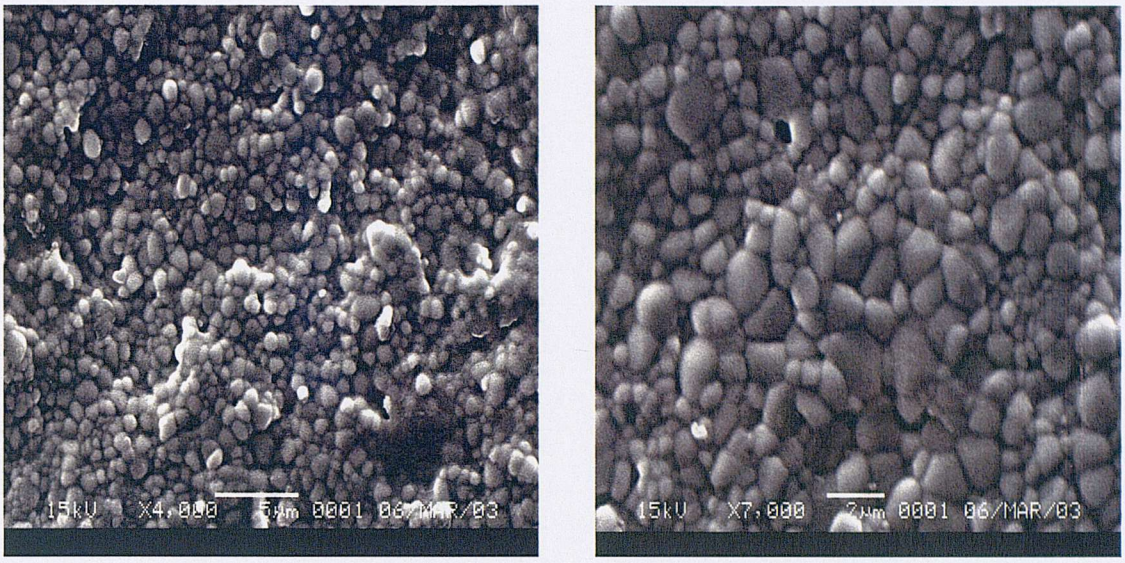


Figure 6.2.13: SEM micrographs taken at low and high magnification of an as sintered CGO10-90 electrolyte at 1400 ℃



Figure 6.2.14: SEM micrographs taken at low and high magnification of a cleaned CGO10-90 electrolyte

Assuming no transport of silica into the CGO 20-80/LSCF electrode, silica would block the transfer of oxygen ions across the interface of the CGO 20-80/LSCF electrode and the CGO 10-90 electrolyte, where space-charge region are created. This may result in reduction in the area of the oxygen transfer path and as a consequence the electrode resistivity may be increased **[13]**.

Hence, by cleaning the surface of the CGO10-90 electrolyte, the existence of siliceous second phase materials at the surface are removed and effectively improving the performance of the electrode on that electrolyte.

6.2.3.3 CGO-LSCF on a cleaned electrolyte and iso-statically pressed

The AC impedance spectra of CGO20-80/LSCF composite coated onto a cleaned CGO10-90 electrolyte pellet, iso-statically pressed and then sintered in air at 1050°C is shown in Figure 6.2.15, together with the responses of the CGO20-80/LSCF on an as sintered and cleaned electrolyte. The equivalent circuit model in Figure 6.2.8 was used to fit the impedance spectra at 498°C, 548°C and 595°C of the CGO20-80/LSCF on a cleaned electrolyte and iso-pressed. The impedance curves were composed of one depressed semi-circle and this may contribute to the non-charge transfer of oxygen, including diffusion and surface exchange. There is no significance difference in the shape of the impedance response at any temperature of all the electrodes with different processing type of electrolytes.

The area specific resistance, ASR for this cathode was found to be 24.86 $\Omega.cm^2$ at 498°C, 7.98 $\Omega.cm^2$ at 548°C and 3.26 $\Omega.cm^2$ at 595°C. There is no improvement in the results compared to the CGO20-80/LSCF on a cleaned electrolyte as can be seen in Table 6.1.3. The iso-statically pressed cathode should provide a better contact with the electrolyte and ensure a better current collection. However it has compressed the cathode making it denser (the density, calculated using Archimedes principle, is 84%) than the unpressed cathode (density is 77%).

	500°C	**550°C**	**600°C**
CGO/LSCF on an as sintered electrolyte	32.41 Ωcm^2	12.84 Ωcm^2	5.37 Ωcm^2
CGO/LSCF on a cleaned electrolyte	19.56 Ωcm^2	6.54 Ωcm^2	2.71 Ωcm^2
CGO/LSCF on a cleaned electrolyte and iso-pressed	24.86 Ωcm^2	7.98 Ωcm^2	3.26 Ωcm^2

Table 6.1.3:- ASR values of the composite cathodes at various temperatures

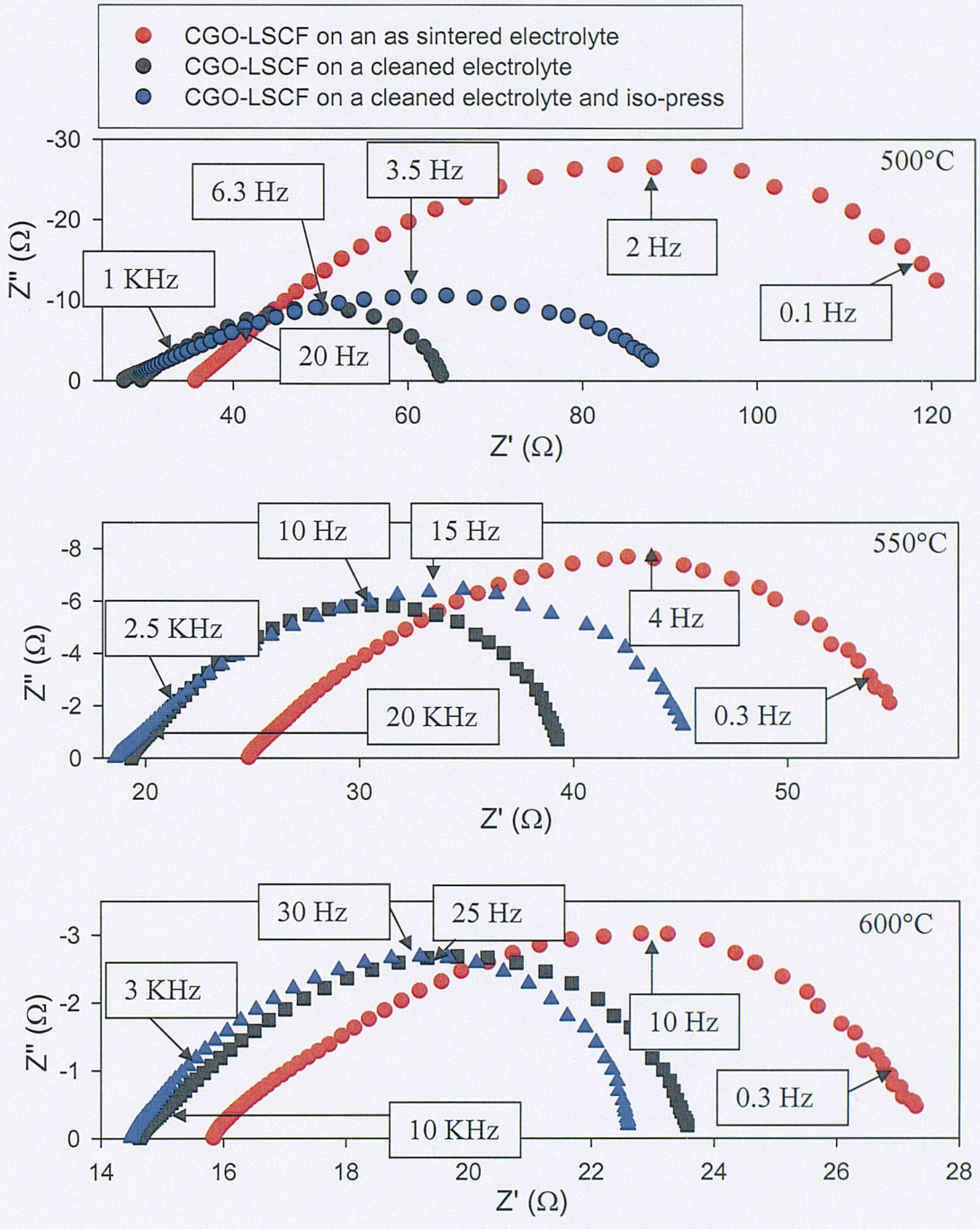


Figure 6.2.15: AC Impedance Spectroscopy spectra of CGO20-80/LSCF Composite cathode on a cleaned CGO electrolyte and iso-statically pressed

The area specific resistance in air as a function of temperature of the CGO20-80/LSCF electrode on a clean CGO10-90 electrolyte and iso-statically pressed is shown in Figure 6.2.16. The activation energy for this composite cathode is found to be 1.23 ev ±0.1ev. Again this activation energy is in good agreement with that of an electrode on an unclean and clean electrolyte.

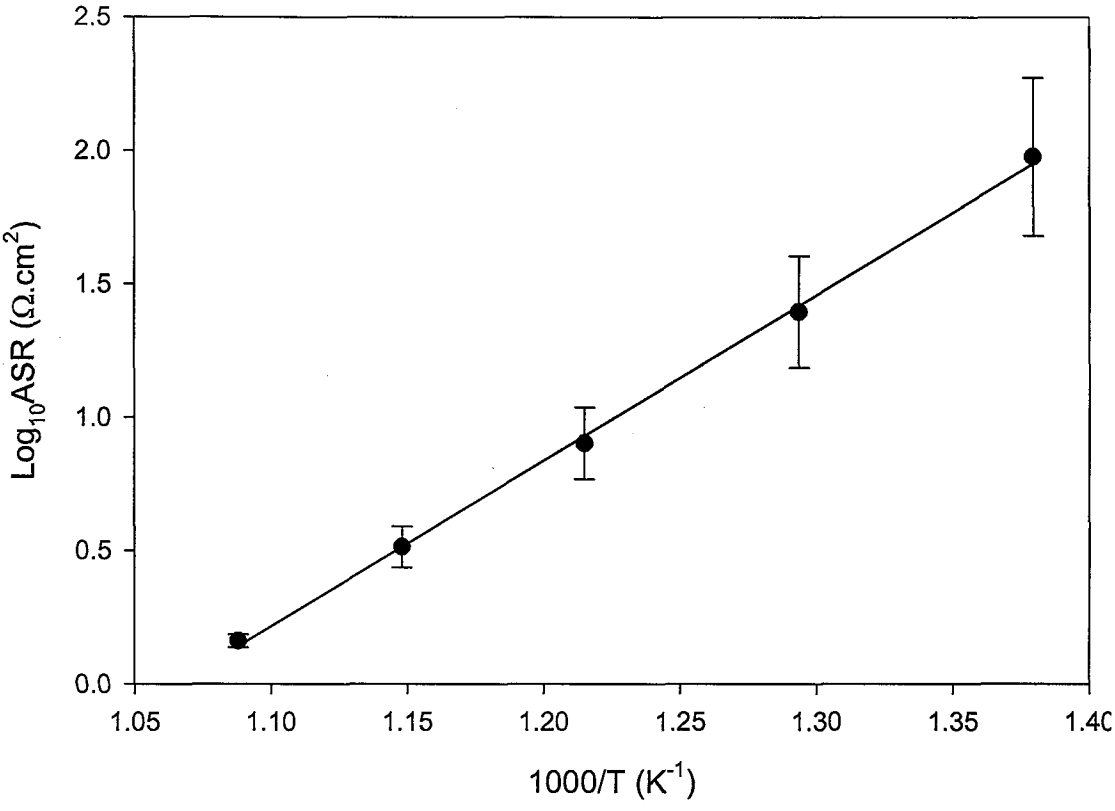


Figure 6.2.16: Arrhenius plot of the CGO20-80/LSCF composite cathode on a cleaned CGO10-90 electrolyte and iso-statically pressed

6.2.4 Microstructural characterisation

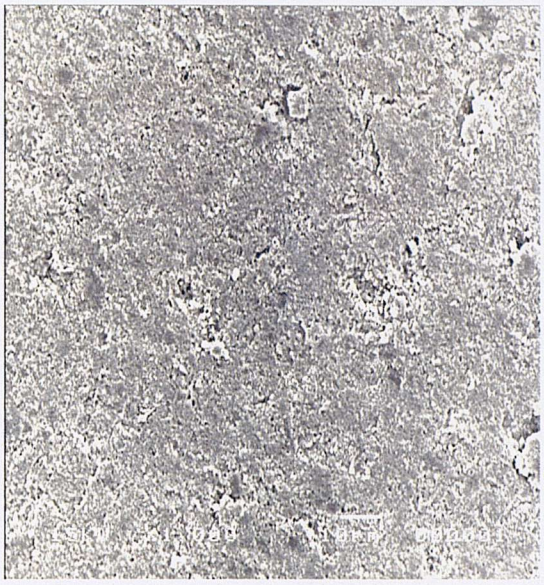


Figure 6.2.17:- SEM micrograph of CGO-LSCF sintered at 1050 ℃. Top surface.

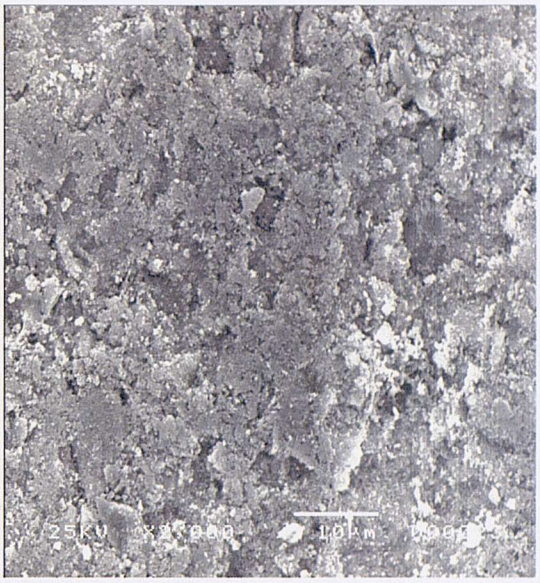


Figure 6.2.18:- SEM micrograph of CGO- LSCF sintered at 1050 ℃. Fractured surface.

Figure 6.2.17 and 6.2.18 shows the SEM micrographs (× 1000) of the smooth and fractured surface of an unaxially pressed CGO 20-80/LSCF cathode sintered at 1050°C for 2 hours. Highly dense electrodes were apparent (> 77 % theoretical density) with very little porosity. The grain distribution in this material is hard to see from these micrographs. Also, from the SEM micrograph, it can be noted that, the very few small pores observed in the pellet sintered at 1050°C will not be sufficient for application as cathode in ITSOFC. Thus, the sintering temperature of LSCF has to be lower than 1050°C in order to obtain a cathode with sufficient porosity (around 40 %) for ITSOFC application. The aim of this thesis is to investigate the co-sintering of the whole cell at around 1000°C to reduce the processing cost. Therefore reducing the sintering temperature to produce porosity will not be considered here and hence the need to find an alternate method to promote porosity into the cathode. The lack of porosity in these samples is also an indication to the higher area specific resistances obtained for this composite cathode.

6.2.5 Comparison with the Adier (ALS) Model

The ALS model [9] has shown evidence that the kinetics of the oxygen reduction in a mixed conductor is dominated by the non-charge transfer oxygen diffusion in the electrode and surface exchange at the electrode/gas interface. Here this model treats the overall electrode reaction, $1/2O_2 + 2e^- \rightarrow O^{2-}$, as a homogenous chemical reaction occurring over the internal surface area of the electrode material. The ALS model is not applicable to a composite material as such, however as a first approximation we can assume that the composite behaves macroscopically as a homogeneous single phase mixed conducting material. Then by using secondary ion mass spectroscopy (SIMS) analysis, we can measure the values for the oxygen diffusion coefficient (D*) and oxygen surface exchange coefficient (K), where these values are used to estimate the response of a composite cathode.

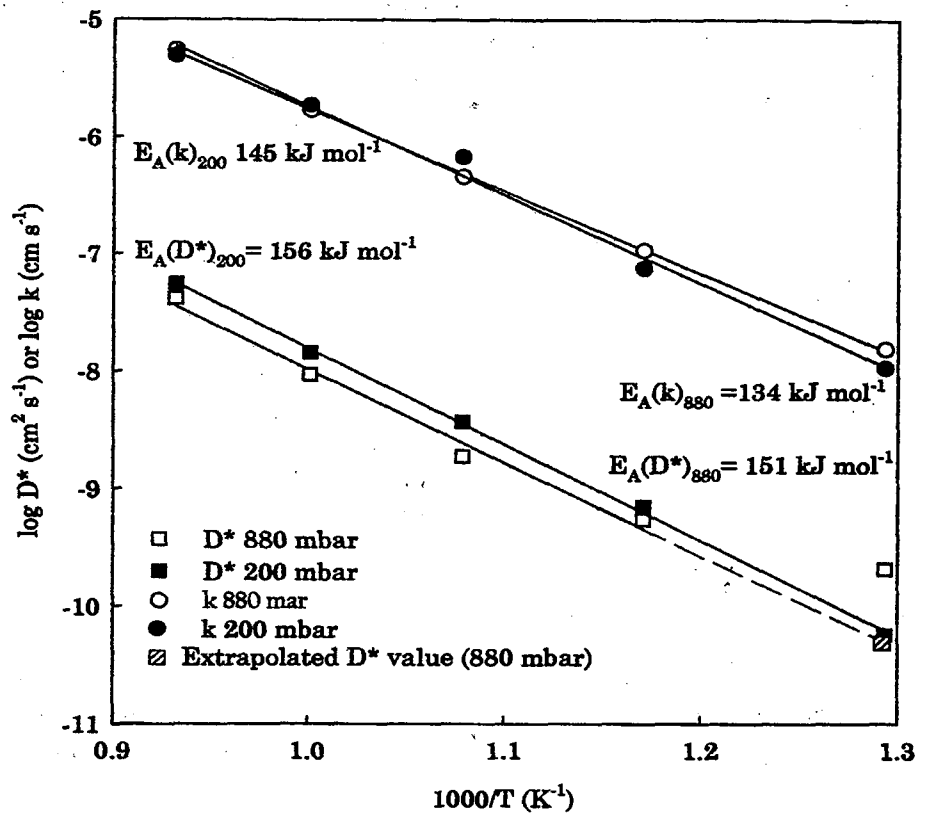


Figure 6.2.19:- Arrhenius plot of the oxygen tracer diffusion coefficients and surface exchange coefficients for the CGO/LSCF samples exchanged around 880 mbar and 200 mbar [11]

If the values of the oxygen diffusion coefficient and the surface exchange coefficient taken from the data of Esquirol (Figure 6.2.19) **[11, 38 and 39]** are substituted into the following equation:

$$R_{chem} = \left[\frac{RT}{2F^2}\right]\sqrt{\frac{\tau}{(1-\varepsilon)aC_o{}^2D^*K}}$$

where, R_{chem} = characteristic resistance

τ = tortuosity

ε = fractional porosity

a = internal surface area/unit volume

Co = concentration of oxygen sites

D* = oxygen diffusion coefficient

K = oxygen surface exchange coefficient

Together with the value of a = 20000 cm^2/cm^3 **[15]**, the porosity (23%) and the tortuosity (1.9) **[15]** then R_{chem} (ASR) values can be generated at different temperatures. The porosity of the cathode on an electrolyte could not be measured, because it was so thin. Therefore, the porosity was measured from a separately made cathode pellet, which was sintered at 1050°C and assumed that the two will be the same. Generated R_{chem} values at different temperatures for CGO/LSCF is shown together along with the experimental ASR values of CGO20-80/LSCF produced under different conditions in Figure 6.2.20. At 500°C, the model's ASR prediction of around 50 Ωcm^2 is higher than all the three electrodes, however at around 550°C the CGO20-80/LSCF on an as sintered electrolyte ASR value of 12.83 Ωcm^2 is similar to the data predicted by the model. Finally at around 600°C, the model's predicted ASR value is very similar to the ASR value of CGO20-80/LSCF on a cleaned electrolyte and also to the CGO20-80/LSCF on a cleaned electrolyte and iso-pressed, which is around 3 Ωcm^2. It therefore appears the model developed by Adler et al, is quantitatively in good agreement for the electrodes studied here.

It is also very important to note that the calculated data is not a fit to the experimental data using electrical equivalent circuits, which is most commonly seen in the literature. This is a response calculated from entirely independent data obtained from diffusion

measurements (literature **[11 and 16]**) and knowledge of the microstructure of the material (where some values were taken from the literature and the porosity was calculated using Archimedes principle)

.

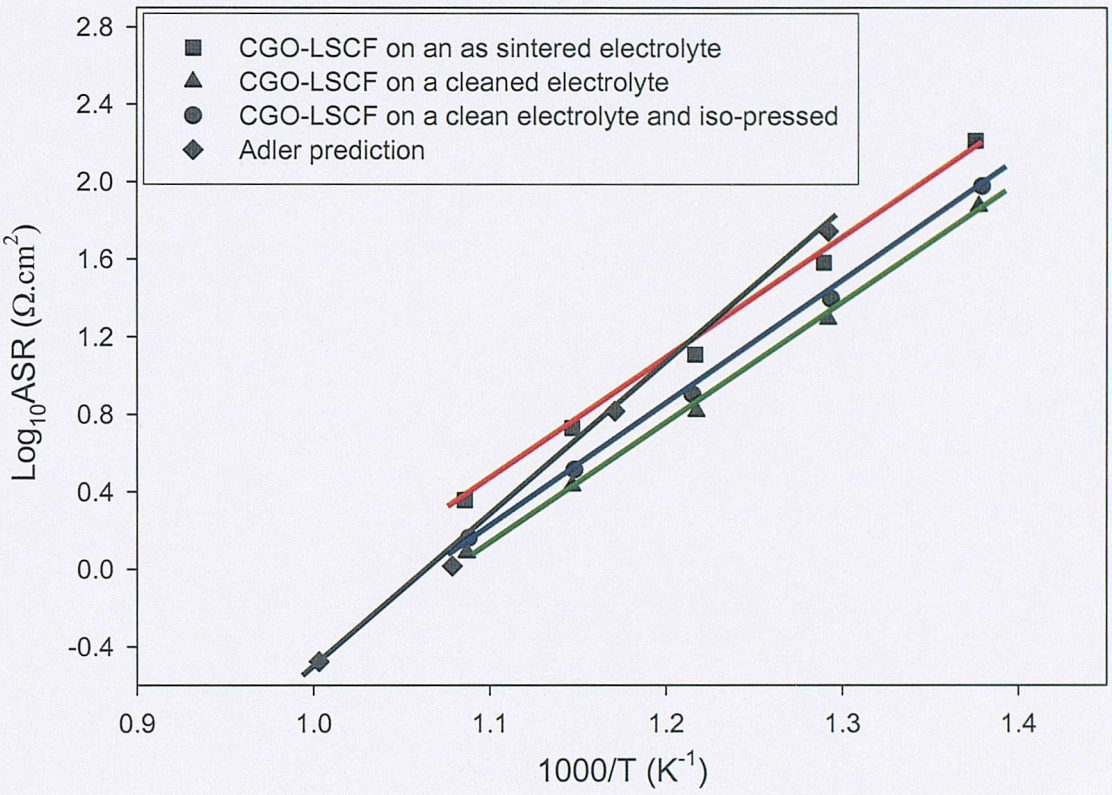


Figure 6.2.20: Comparison of the measured impedance and that predicted by Adler's model

Regarding the Arrhenius plot above, all the composite materials exhibited activation energy in the range 1.22-1.26 ev ±0.1 ev, which are very identical to each other and match well with the literature **[10 and 11]**. The predicted activation energy by the model is 1.53 ev, which is similar to the value obtained by averaging the surface exchange and diffusion coefficient activation energies (1.56 ev). The ALS model has only provided a useful quantitative approach for understanding linear AC polarization values associated with porous single-phase mixed conducting perovskite electrodes. There is still uncertainty about whether; this model is applicable to composite electrodes. However, the morphology of the entire CGO20-80/LSCF electrode studied on different types of electrolytes are very dense, and this may be one of many reasons contributing to the disagreement over the model and the experimental activation energy values.

The other factors can be, firstly the lack of accuracy in the estimation and measurement of the microstructural parameters for the model (porosity, tortuosity, surface area etc). Indeed porosity was calculated using the Archimedes principle, which is accurate, however tortuosity that is estimated varies in the literature between 1.5 and 3. There is no accurate method to measure the tortuosity in an electrode. The surface area of the original powder was measured, but in the case of the cathode itself, it was not possible to measure because the cathode film on the electrolyte was thin. Therefore, the values of surface area and tortuosity were taken from the literature **[15]**.

6.3 CGO/LSCF/LSM

Strontium-doped lanthanum manganite perovskite oxides ($La_{0.6}Sr_{0.4}MnO_3$, LSM) have for some years been known to be a good cathode material for SOFC applications. In contrast to the LSCF materials the LSM oxides have been shown to be very poor oxide ion conductors **[17 and 18]**, but it is mainly an electronic conductor. The strontium dopant in LSM does not increase the oxygen vacancy concentration, but rather oxidizes the manganese ion according to the following equation:

$$SrO(LaMnO_3) \leftrightarrow Sr_{La}^{/} + Mn_{Mn}^{\bullet} + O_O^{X}$$

This reaction effectively increases the electron-hole concentration and improves the electrical conductivity. The absence of oxygen vacancies in LSM results in a conductivity that is almost exclusively electronic. Hence the LSM was mixed the CGO-LSCF composite cathode to increase its electronic conductivity.

Figure 6.30 shows the change in length versus temperature data obtained from a dilatometer during the sintering of green powder compacts of a CGO20-80/LSCF/LSM cathode. The onset of shrinkage commences approximately around 900°C. This is slightly higher than the onset of shrinkage for the CGO20-80/LSCF composites (Figure 6.3.1). The increase in the onset of shrinkage temperature for CGO20-80/LSCF/LSM compared to the CGO20-80/LSCF composites is due to the presence of LSM. So the addition of LSM to the CGO20-80/LSCF composite has increased the onset of shrinkage temperature and hence should provide a more porous microstructure. There are inflections in the sintering curve that occurs between room temperature and the onset of shrinkage. The small dip in the curve between the room temperature and 200°C is due to the expansion of the sample holder during heating, hence an apparent decrease in sample length. The rise in the curves between 200°C and the onset of shrinkage is due to the small expansion of the material. Again the absence of a plateau at high temperature indicates that full density had not been achieved.

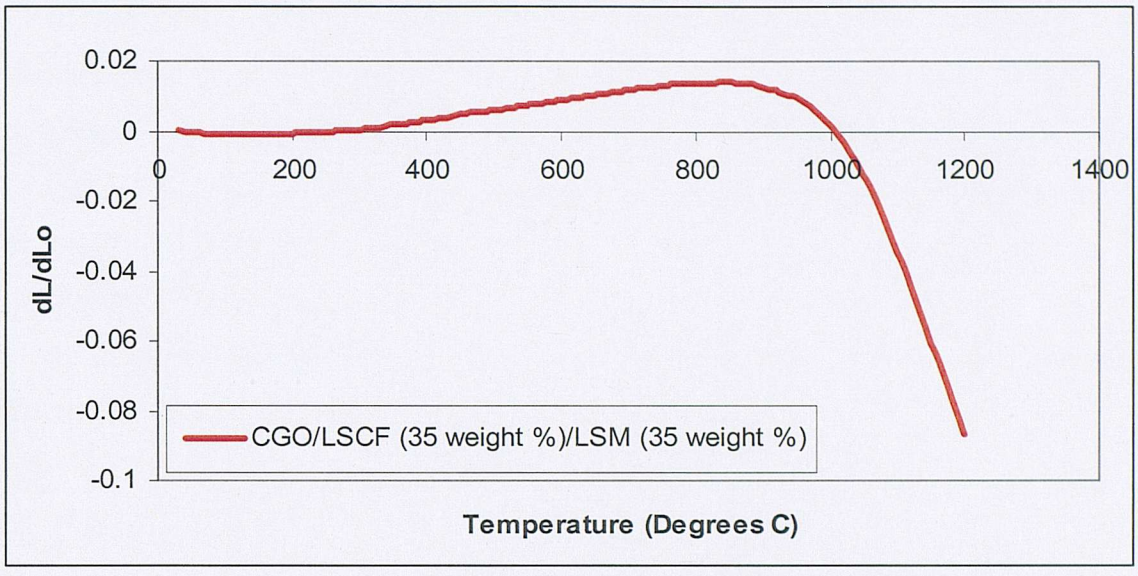


Fig 6.3.1:- Dilatometry trace of CGO20-80/LSCF/LSM

Typical AC impedance spectra of CGO 20-80/LSCF/LSM (35 weight % LSCF and 35 weight % LSM) composite coated onto a cleaned CGO 10-90 electrolyte pellet and then sintered in air at 1050°C are shown in Figure 6.3.2.

The response at 503°C looks very similar to that of Gerischer impedance. However, above 550°C, the complex impedance diagrams consist of two overlapping arcs. The high frequency arc is due the ionic transfer of O^{2-} ions between the electrode and the electrolyte and the low frequency arc is due to the concentration polarization caused by the diffusion and exchange of oxygen species to the electrode/electrolyte interface. This only dominates at low temperatures and decreases with increasing temperature. Hence two arcs only become visible at higher temperatures.

The area specific resistance, ASR for the CGO20-80/LSCF/LSM composite cathode sintered at 1050°C was found to be around 40 $\Omega.cm^2$ at 503°C, 14 $\Omega.cm^2$ at 553.5°C and 7 $\Omega.cm^2$ at 604°C. The CGO20-80/LSCF/LSM cathode showed a poor performance when compared to CGO20-80/LSCF cathode. The ASR values were greater by a factor of two. LSM restricts the reduction of oxygen to the three-phase boundary regions, where the air, cathode and electrolyte are in intimate contact. This restriction and its poor mixed conductivity result in high electrode resistances at lower temperatures. It is well accepted from the literature that a good cathode at lower temperatures must exhibit high mixed ionic-electronic conductivity to maintain an acceptable performance. The oxygen self-diffusion coefficient (D^*) and oxygen surface exchange coefficient (k) for the LSM material are very low when compared to CGO and LSCF material (D* and k

of LSM at 700°C is 3.2E-16 cm^2s^{-1} and 1.0E-9 cms^{-1}) **[15]**. These values are much higher than of CGO and LSCF at 500°C. Hence, the addition of LSM to the CGO/LSCF composite has restricted the ionic flux to the cathode/electrolyte interface. In other words, the electronic conductivity has increased, while the ionic conductivity has decreased due to the addition of LSM **[19]**.

Again the differences in the above ASR values may also be associated with the electrode processing quality, governed by parameters such as particle size, porosity, sintering temperature and extent of particle agglomeration.

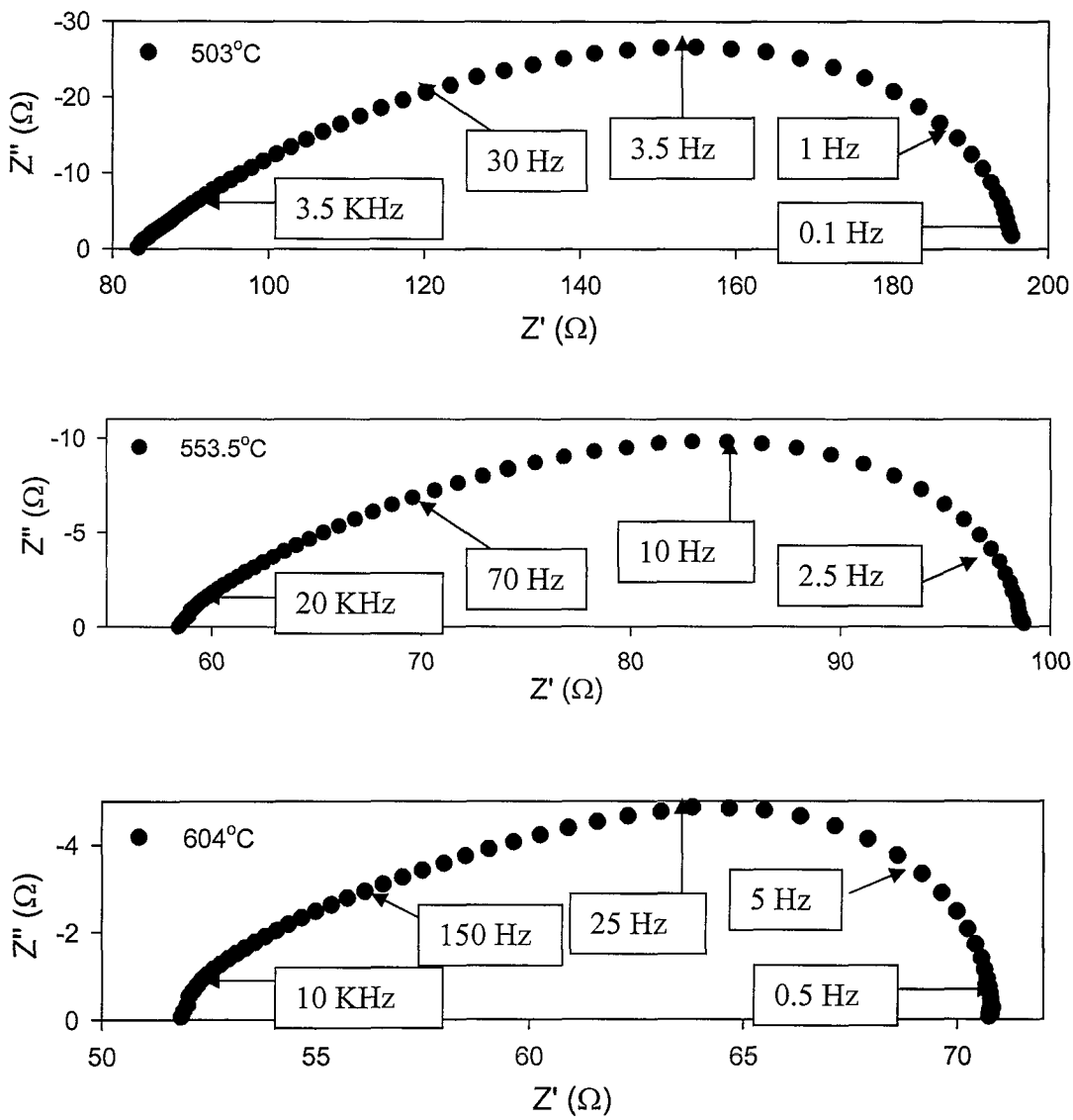


Fig 6.3.2:- AC Impedance Spectroscopy spectra of CGO20-80/LSCF/LSM on CGO10-90 electrolyte calcined at 1050 °C in air.

Area specific resistances, ASR of the CGO 20-80/LSCF/LSM electrode on a CGO 10-90 electrolyte is shown as Arrhenius plot in Figure 6.3.3. The activation energy for this composite cathode is found to be 1.11 ev ±0.15, which is lower than the activation energy of CGO/LSCF.

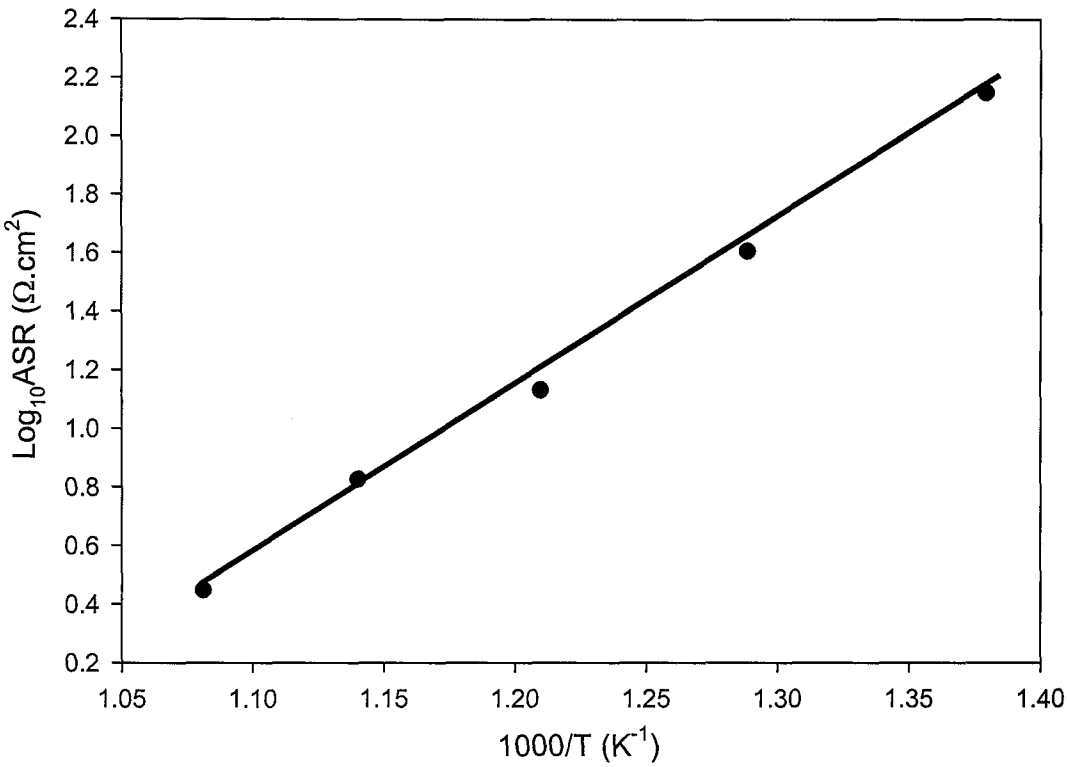


Fig 6.3.3:- Arrhenius plot of the CGO20-80/LSCF/LSM composite cathode on an as sintered CGO10-90 electrolyte

Figure 6.3.4 and 6.3.5 shows the SEM micrographs (× 1000) of the smooth and fractured surface of an uni-axially pressed CGO/LSCF/LSM sintered at 1050°C. Highly dense electrodes are apparent. The experimental density was calculated to be around 65%. This is only slightly better than the CGO/LSCF composite where the experimental density was calculated to be around 71.1%. The lack of porosity in these samples is also an explanation to the high area specific resistances obtained for this composite cathode. Adler predicted that there should be sufficient porosity (around 40%) for the diffusion of oxygen and for a good performance of the cathode. In the next section we will see how the porosity of the electrode can be promoted when sintered at 1050°C and consequently improving the performance of the cathode.



Fig 6.3.4:-SEM micrograph of CGO-LSCF-LSM sintered at 1050℃. Top surface.

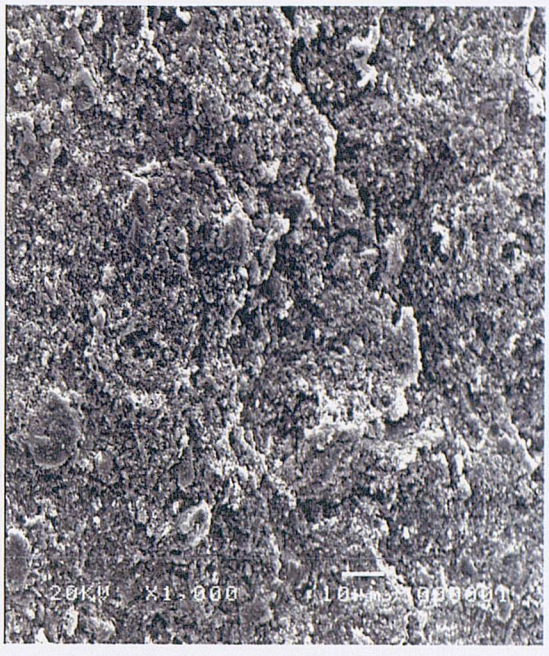


Fig 6.3.5:- SEM micrograph of CGO-LSCF-LSM sintered at 1050℃. Fracture surface.

6.4 CGO/LSCF/PMMA

One way to create porosity in a ceramic sample is to mix a pore former with the ceramic powder and then sinter in a controlled atmosphere. The pore former will burn out before the sintering range of the ceramic to leave residual porosity. Certain organic compounds can be used as the pore former **[20-23]**.

In this project polymethylmethacrylate (PMMA) was used as a fugitive phase, which will burn out around 400-500°C. PMMA of 5-10 μm in particle size were mixed with CGO20-80/LSCF and then sintered in air at 1050°C. Typical microstructures of the porous ceramics after sintering in air are shown in Figure 6.4.1 and 6.4.2. Uniform pores were apparent because of the voids left by the PMMA, while the matrix around these pores appears very dense. The percentage of porosity presented in this composite is calculated to be around 45%. Although high percentage of pores with diameter in the range 5-10 μm was found in this sample, however these pores are not interconnected which will result in no oxygen penetration through this composite when the fuel cell is in operation. Hence an alternate pore former smaller in size should be used to create an interconnected porosity in the electrode structure.

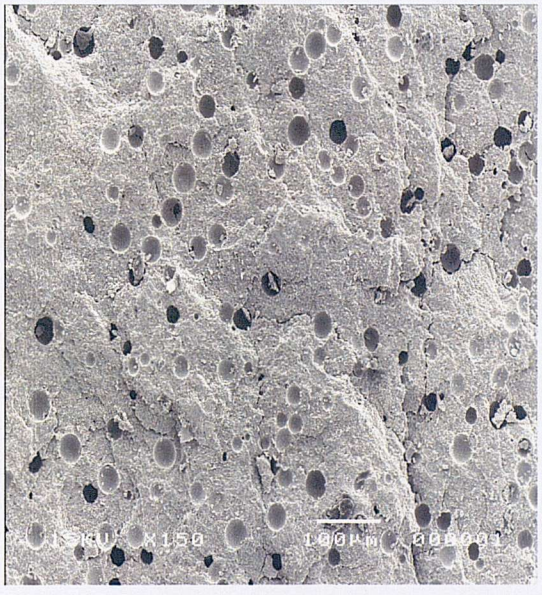


Figure 6.4.1:- SEM micrograph of CGO-LSCF-PMMA sintered at 1050℃. Top surface

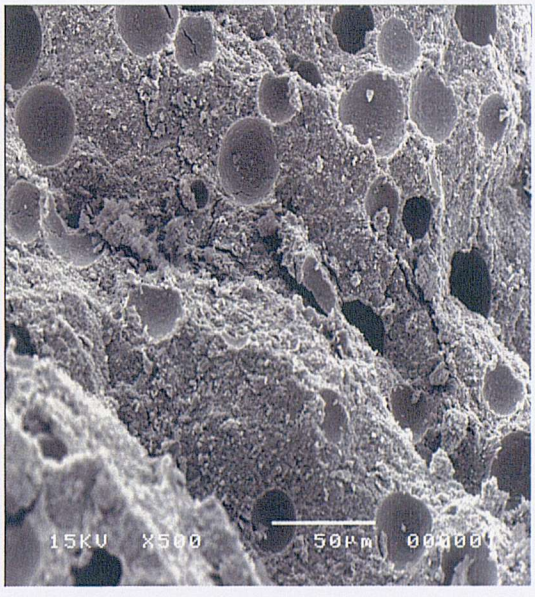


Figure 6.4.2:- SEM micrograph of CGO-LSCF-PMMA sintered at 1050℃. Fractured surface

6.5 CGO/LSCF/Carbon

In the present work, porous CGO/LSCF electrodes are obtained by controlled sintering of CGO/LSCF-carbon powder mixtures. Carbon burn out is more gradual and occurs at a higher temperature (approximately around 500-600°) than some of the organic compounds. This may be seen by a comparison of the sintering-profile (taken from the literature) of polyvinyl butyral (PVB) and carbon in Figure 6.5.1 [23]. Carbon has also negligible solubility in "ink" slurry solvent and is more effective, practical and controllable as a fugitive agent for this purpose. Spherical carbon powders of 1-3.26 μm in particle size was mixed with CGO20-80/LSCF and sintered in air at 1050°C.

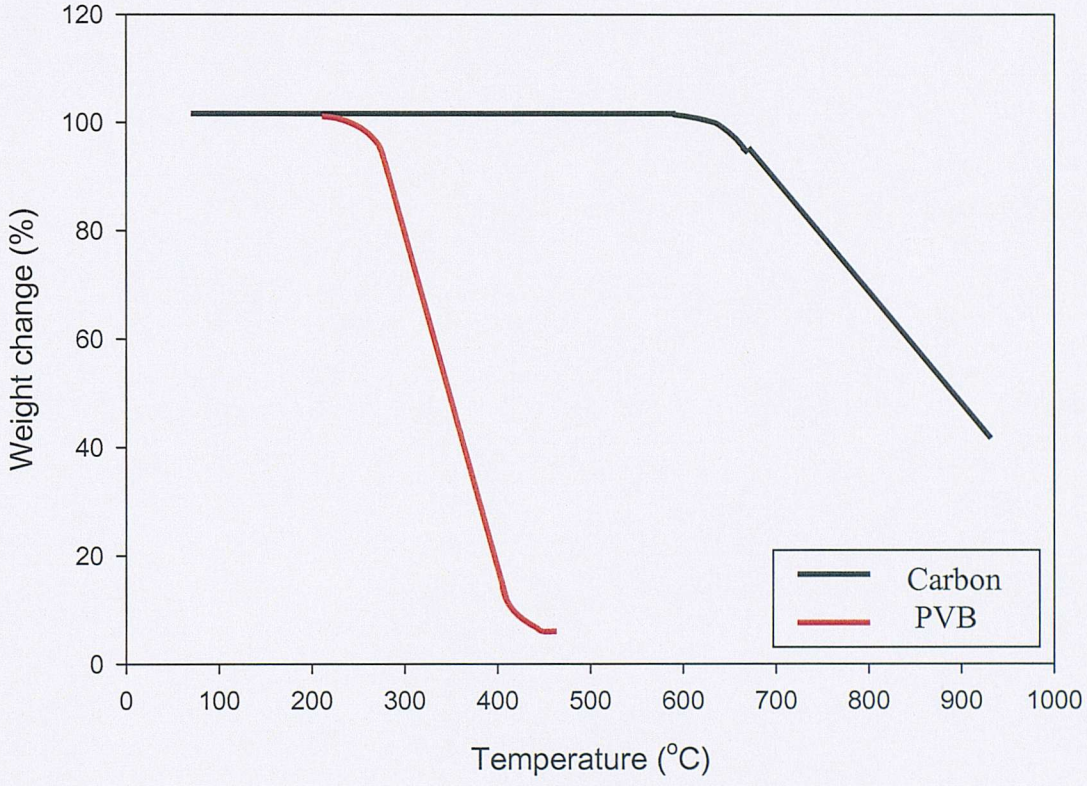


Figure 6.5.1:- Carbon and PVB burn-out profile [23].

6.5.1 Powder Characterisation

X-ray diffraction was performed on both the CGO20-80/LSCF/carbon before sintering and after sintering with the aim to ascertain phase purity and the X-ray diffraction data is shown in Figure 6.5.2 and Figure 6.5.3. In figure 1 where the compound is not sintered, extra additional peak is found at $2\theta = 26°$. This is due to the presence of the carbon in the composite. This peak has disappeared on sintering the sample at 1050°C for 2 hours indicating the burn out of carbon and no impurity peaks can be observed in

Figure 6.5.3. X-ray diffraction data also shows that there are no impurity phases in the CGO/LSCF cathode, even after burning out carbon during sintering. The Bragg peaks were identified using the file $Ce_{0.8}Gd_{0.2}O_{2-x}$ (JCPDS 75-0162) and $La_{0.6}Sr_{0.4}CoO_3$ (JCPDS 36-1393).

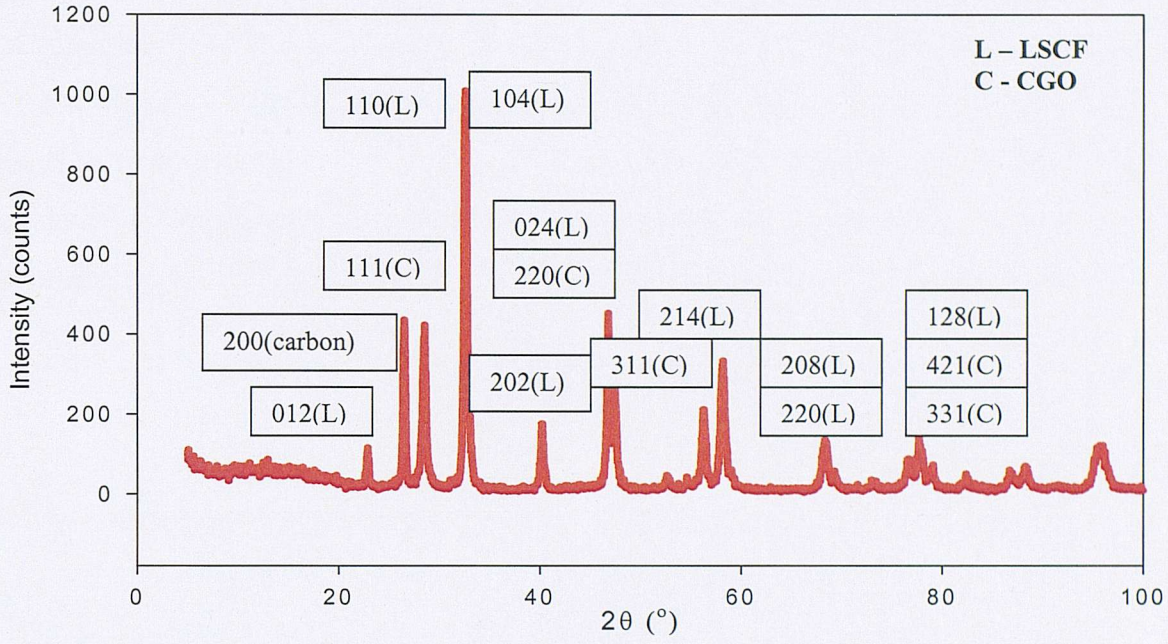


Figure 6.5.2: X-ray diffraction pattern of $Ce_{0.8}Gd_{0.2}O_{2x}/La_{0.6}Sr_{0.4}Co_{0.2}Fe_{0.8}O_{3\delta}$/carbon composite before sintering using Cu-K_α radiation (λ = 1.5406 Å)

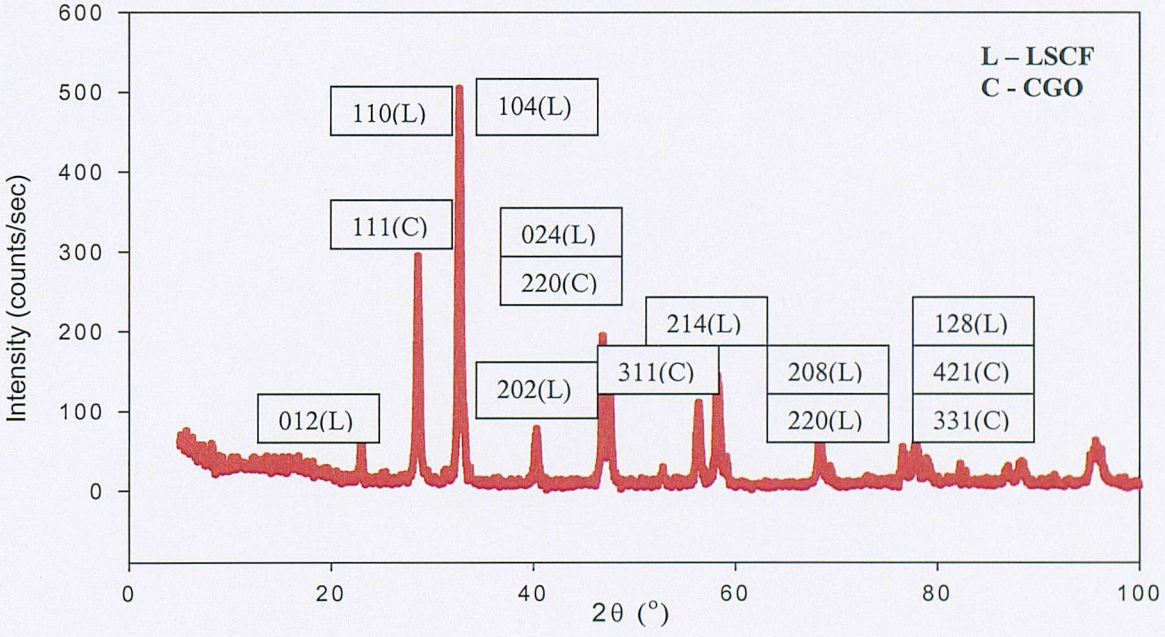


Figure 6.5.3: X-ray diffraction pattern of $Ce_{0.8}Gd_{0.2}O_{2-x}/La_{0.6}Sr_{0.4}Co_{0.2}Fe_{0.8}O_{3-\delta}$/carbon composite after sintering using Cu-K_α radiation (λ = 1.5406 Å)

6.5.2 Sintering Studies

Figure 6.5.4 shows the change in length versus temperature data obtained from a dilatometer during the sintering of green powder compacts of CGO20-80/LSCF/carbon cathode. The rise in the curve between the room temperature and 300°C is due to the small expansion of the material as it is being heated, thus the initial increase in the curve between these points does not suggest a change in the sintering mechanism. The onset of shrinkage commences approximately around 900°C. However, there is a large increase in the change in length between 400°C and 600°C. This is possibly due to the oxidation of carbon, which occurs at these temperatures. The reaction of carbon in an air atmosphere gives rise to carbon monoxide according to the following reaction **[24]**:

$$\underset{\text{solid}}{2(C)} + \underset{\text{gas}}{\{O_2\}} \rightarrow \underset{\text{gas}}{2\{CO\}}$$

followed by carbon monoxide (CO) further oxidizing to carbon dioxide (CO2).

$$CO + 1/2O_2 \rightarrow CO_2$$

It is likely that within the body of the pellet, where the inward oxygen flux is limited by diffusion down pores, the ambient is predominantly carbon monoxide (CO) with a consequent low resultant PO_2. Thus between 400°C and 600°C a substantial portion of the CGO/LSCF material is exposed to a reducing atmosphere due to the presence of carbon monoxide. Hence the large increase in the change in length between 400°C and 600°C shown in Figure 6.5.4 is due to the chemical expansion of the CGO and LSCF material as it loses oxygen.

The linear portion between 600°C and 800°C signifies either the complete reduction of the perovskite phase or the completion of carbon burnout. At around 800°C shrinkage begins and the material starts to sinter.

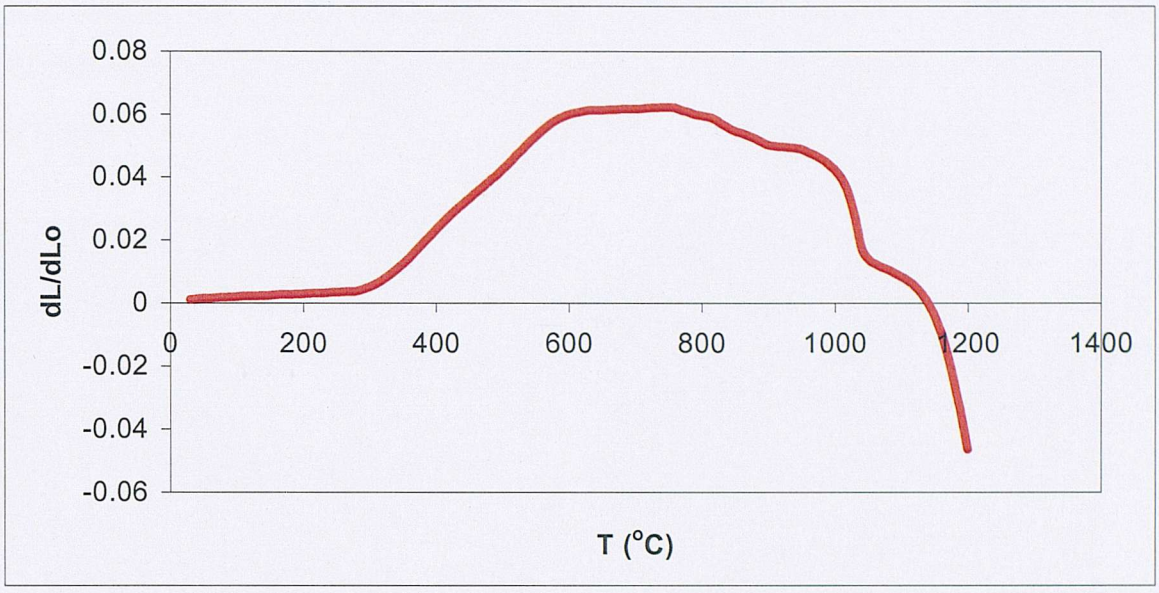


Fig 6.5.4: - Dilatometry trace for a composite CGO/LSCF/carbon sample

6.5.3 Microstructural Studies by SEM

Figures 6.5.5 - 6.5.7 shows the SEM micrographs of the CGO 20-80/LSCF/carbon cathode sintered at 900°C for 2 hours and also the micrographs of unpressed and iso-statically pressed CGO 20-80/LSCF/carbon cathode layer sintered at 1050°C for 2 hours. After sintering at 900°C (Figure 6.5.5), many isolated grains (grain size of ≈ 0.5 μm) in the cathode layer touching neighbouring grains can be identified. After sintering at 1050°C of both unpressed and iso-statically pressed cathode (Figure 6.5.6 and Figure 6.5.7), the grains in the cathode layer were well sintered and there are sufficient connections among the grains. Furthermore the grains remained small in size of around 0.5-1 μm, as observed in Figure 6.5.5 and Figure 6.5.6 leading to long three-phase-boundaries. Hence the sintering of both unpressed and iso-statically pressed CGO 20-80/LSCF cathode at 1050°C for 2 hours resulted in a structure with reasonable porosity that was connected with by narrow bottleneck-type bridges. The percentage of porosity presented in this composite is calculated to be 45.9% at 1050°C, where Adler stated that for a good cathode performance, the porosity should be in the region of 40-50%. The iso-statically pressed cathode in Figure 6.5.7 appears to be denser than unpressed material, however it should provide a better contact with the electrolyte and ensure a better current collection than unpressed cathode. In summary, the carbon oxidised at around 400-500°C, the connections of grains occurred at 900°C and grain growth and

pore closing with further grain coarsening occurred at around 1050°C. In all three micrographs highly porous electrodes are distinguishable with pore diameters between 1-10 μm..

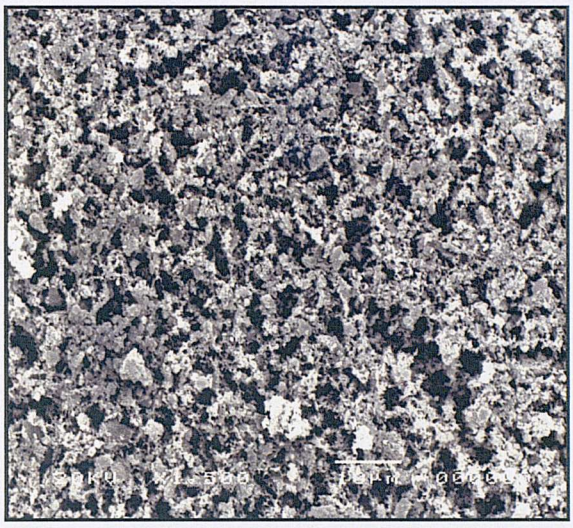


Figure 6.5.5:- SEM micrograph of CGO-LSCF- carbon sintered at 900 ℃.

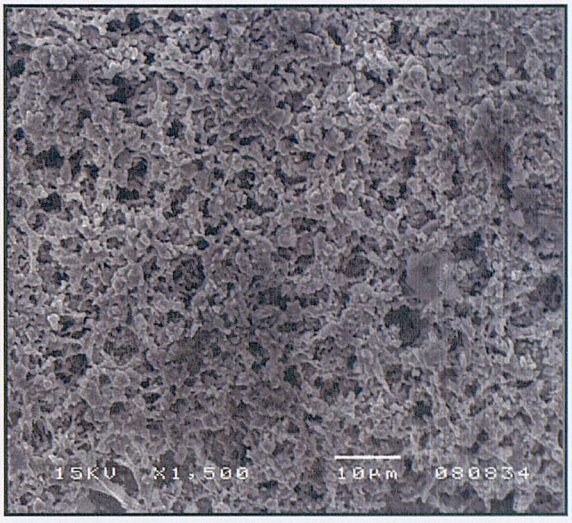


Figure 6.5.6:- SEM micrograph of CGO-LSCF-carbon sintered at 1050 ℃.

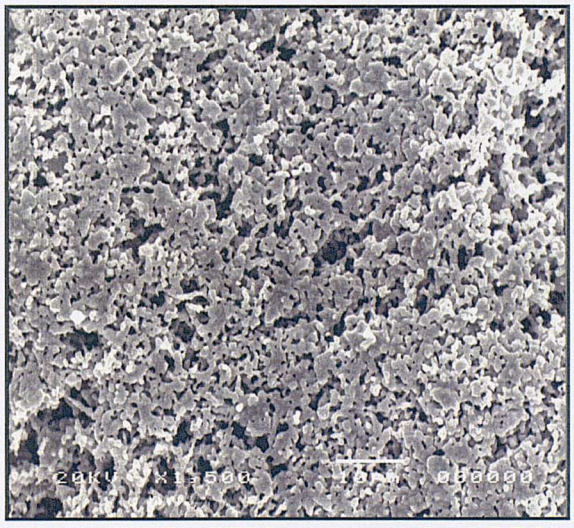


Figure 6.5.7:- SEM micrograph of CGO-LSCF-Carbon sintered at 1050 ℃. Iso-pressed.

SEM images of the resulting electrode/electrolyte interface structures of iso-statically pressed CGO20-80/LSCF/carbon (carbon being burned out at around 500°C) half-cells that were tested are shown in Figure 6.5.8. The micrograph illustrates the fine microstructure of the sprayed layers next to the dense CGO electrolyte. The thickness of

the electrode layer was found to be around 14-17 μm, with high level of interconnected porosity. The electrode microstructure also looks uniform throughout and a very good bonding and continuous contact at the interface between the electrode and the dense electrolyte pellet. The electrodes showed good adherence to the electrolyte because of the similar thermal expansion between the two materials.

In summary the main characteristics easily observed in Figure 6.5.5-6.5.8 are the high percentage of interconnected porosity in the cathode material on a dense electrolyte compared to the previous results obtained from the sintered cathode materials without a pore former.

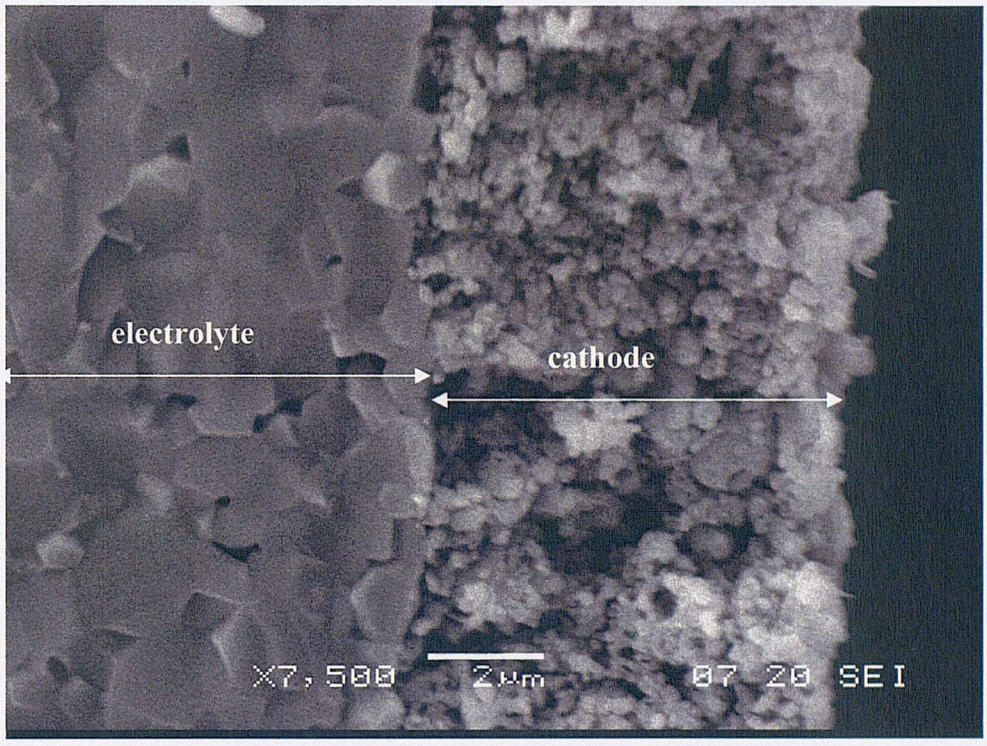


Figure 6.5.8:- SEM micrograph of the cross-section of CGO-LSCF-Carbon onto a CGO electrolyte, iso-statically pressed and sintered at 1050 ℃

6.5.4 Microstructural Studies by FIB SIMS

Figure 6.5.9 and 6.5.10 shows the focussed ion beam (FIB) image of the surface and the cross-section of the CGO20-80/LSCF/carbon composite cathode applied on a CGO10-90 pellet. Better resolution and cross-section images were gathered using this technique. The surface microstructure (Figure 6.5.9 (A)) of the cathode sintered after 1050°C for 2 hours shows a very uniform microstructure with high level of interconnected porosity and all the grains are connected with by narrow bottleneck-type bridges. Figure 6.5.9 (B) shows the same area after a rectangular crater of 20 μm in depth, 30 μm in length and 10 μm in width was produced on the surface of the cathode by a high current ion beam (normally around 500 pAmps), and then polished by a lower current ion beam (around 1-50 pAmps) to give a smoother surface for a better resolution image.

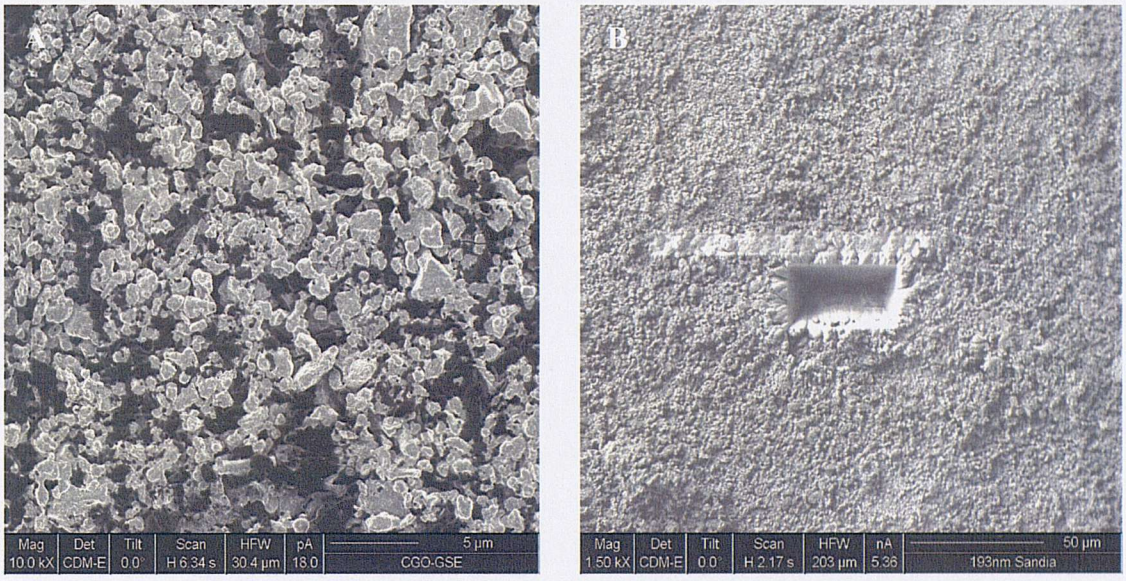


Figure 6.5.9:- (A) Focussed ion beam image (FIB) of the surface of a CGO20-80/LSCF composite cathode sintered at 1050 °C. (B) Focussed ion beam Image (FIB) of the top view of an ion-milled crater on the surface of the cathode (30kev Ga^+ primary bombardment).

Figure 6.5.10 shows the inside of a trench after having tilted the stage at an angle of 30°. The highly porous cathode and a very dense electrolyte are well visible. The particles appeared layered and this was attributed to the number of sprayed layers (in this case about 5-6 sprayed layers). In these layers of cathode, bright and dark areas are visible. The dark areas correspond to the pores while the bright areas are due to presence of the grains. The thickness of the cathode was found to be around 10-14 μm.

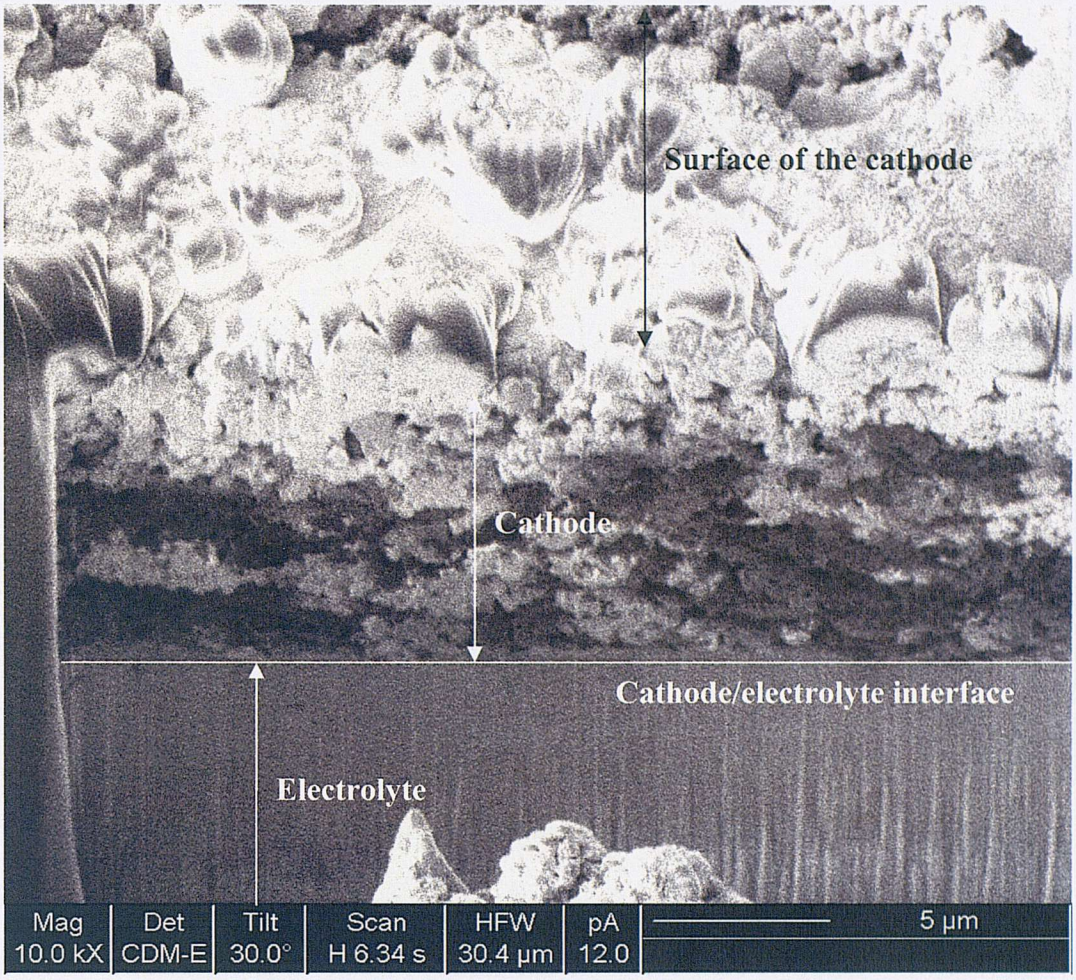


Figure 6.5.10:- Focused ion beam image (FIB) of an ion-milled crater after tilting at 30°((30kev Ga+ primary bombardment).

6.5.5 Electrochemical Performance

6.5.5.1 CGO/LSCF/carbon on an as sintered electrolyte

Figure 6.5.11 shows the typical AC impedance spectra from many repeated experiments of the CGO 20-80/LSCF/carbon composite cathode sprayed onto an as sintered CGO10-90 electrolyte pellet and then sintered in air at 1050°C. The measurements were taken in the temperature range of 400-700°C, but only the responses at 507°C, 553°C and 602°C are shown in the Figure. The shapes of all three responses are different from those produced by the CGO20-80/LSCF on an as sintered electrolyte. Here the impedance spectra are composed of two-depressed overlapping semicircles. Peak frequencies correspond to approximately 500Hz and 4Hz for the response at 507°C, 1KHz and 20Hz for the response at 553°C and 3KHz and 40 Hz for the response at 602°C. The high frequency arc is noticeably smaller than the low frequency arc at all three temperatures. The impedance spectra were therefore fitted to an equivalent circuit containing two constant phase elements, attributed to two different mechanisms involved in the oxygen reduction reaction. The equivalent circuit, which is used to model these responses, is shown in Figure 6.5.12.

The low frequency arc, with a capacitance of the order of 10^{-5} $\Omega^{-1}cm^{-2}$, which becomes more depressed with increasing temperature, is attributed to concentration polarization caused by the diffusion and exchange of oxygen species to the electrode/electrolyte interface **[25]**. This process dominates at low temperatures and decreases with increasing temperature; hence two arcs are more distinguishable at higher temperatures. The high frequency semicircle, with a capacitance of the order of 10^{-4} $\Omega^{-1}cm^{-2}$, is generally attributed to oxygen ions charge transfer across the electrode/electrolyte interface. The resistance of each elementary process occurring on the electrode was determined from the distance between the high-frequency and low-frequency intercepts of the semicircles with the real axis. As the temperature increased, the total impedance of the arc decreased.

At high frequencies the impedance spectra showed induction effects, as indicated by the plot going under the real axis. This represents the inductance of the measurement leads.

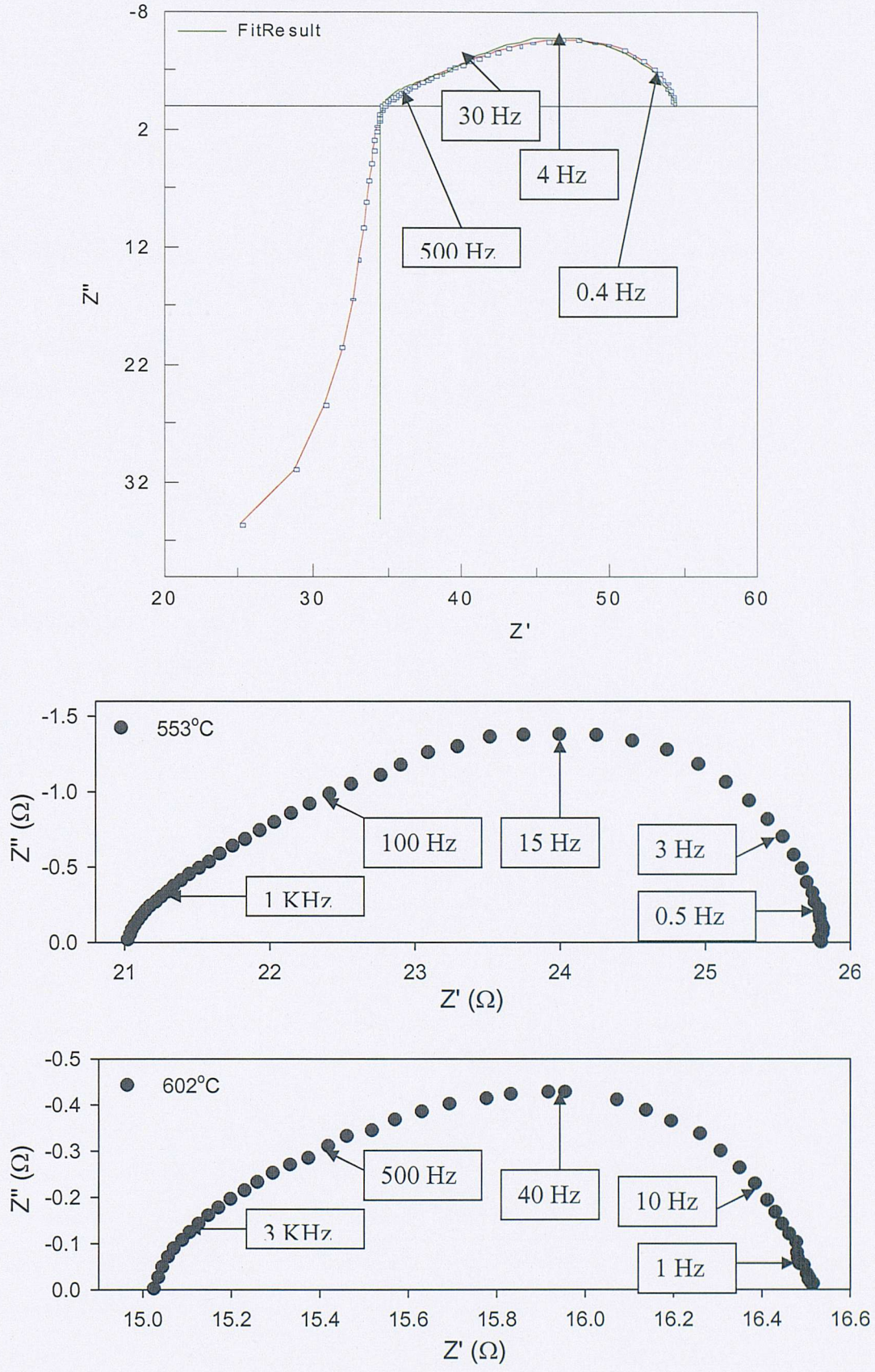


Figure 6.5.11: AC Impedance Spectroscopy spectra of CGO20-80/LSCF/carbon composite cathode on an as sintered CGO10-90 electrolyte at various temperatures

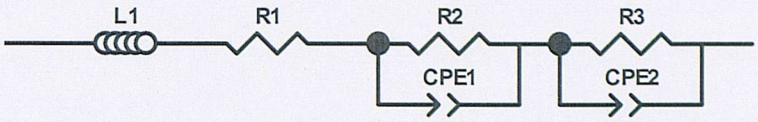


Figure 6.5.12: Equivalent circuit model for the responses in Figure 6.5.11

The normalized AC impedance spectra of the CGO/LSCF/carbon cathode at 503°C, 553°C and 602°C are shown in Figure 6.5.13. It can be noted that with increase in temperature, the high frequency semicircle becomes more distinguishable, however there is no difference in the low frequency component.

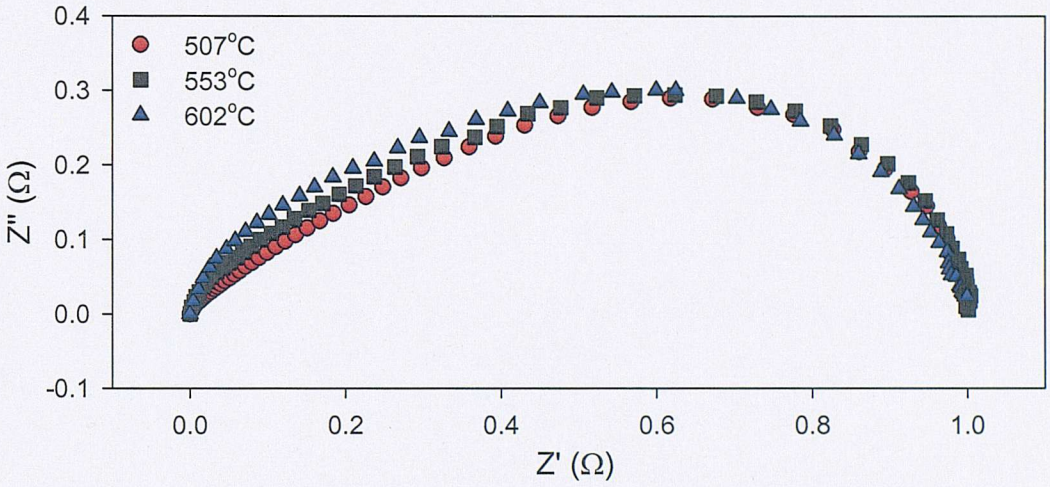


Figure 6.5.13: Normalized AC Impedance Spectroscopy spectra of CGO20-80/LSCF-carbon composite cathode on an as sintered electrolyte at various temperatures

Area specific resistances (ASR) of the CGO20-80/LSCF/carbon electrodes in air was found to be 7.34 $\Omega.cm^2$ at 507°C, 1.86 $\Omega.cm^2$ at 553°C and 0.62 $\Omega.cm^2$ at 602°C. These ASR values are very similar to the previous work conducted by Kilner and Dusastre and also Esquirol **[10-11]**. The shapes of the responses were remarkably similar too between the present study and reference **[10]**, especially given that processing-induced differences in structure can affect electrochemical properties. The microstructure of the electrodes looks similar, which explains the direct similarity of the ASR values. Hence enhancing porosity in the cathode using a pore former has improved the electrical performance of the electrode by a factor of 5 compared to that without a pore former.

Figure 6.5.14 shows the area specific resistance plotted against the reciprocal of temperature as an Arrhenius plot in order to determine the activation energy for the

electrode response. The activation energy for CGO20-80/LSCF composite cathode is calculated from the linear regression of the electrode polarization resistance data and found to be 1.50 ev ± 0.24ev. This activation energy is in agreement with prior studies where activation energies of ~1.4-1.6 ev were reported **[10-12]** and also with activation energy obtained by averaging the surface exchange and diffusion coefficient activation energies of CGO/LSCF (1.56 ev) **[11]**. It therefore appears likely that a combination of diffusion and surface exchange controls the polarization resistance of this composite electrode.

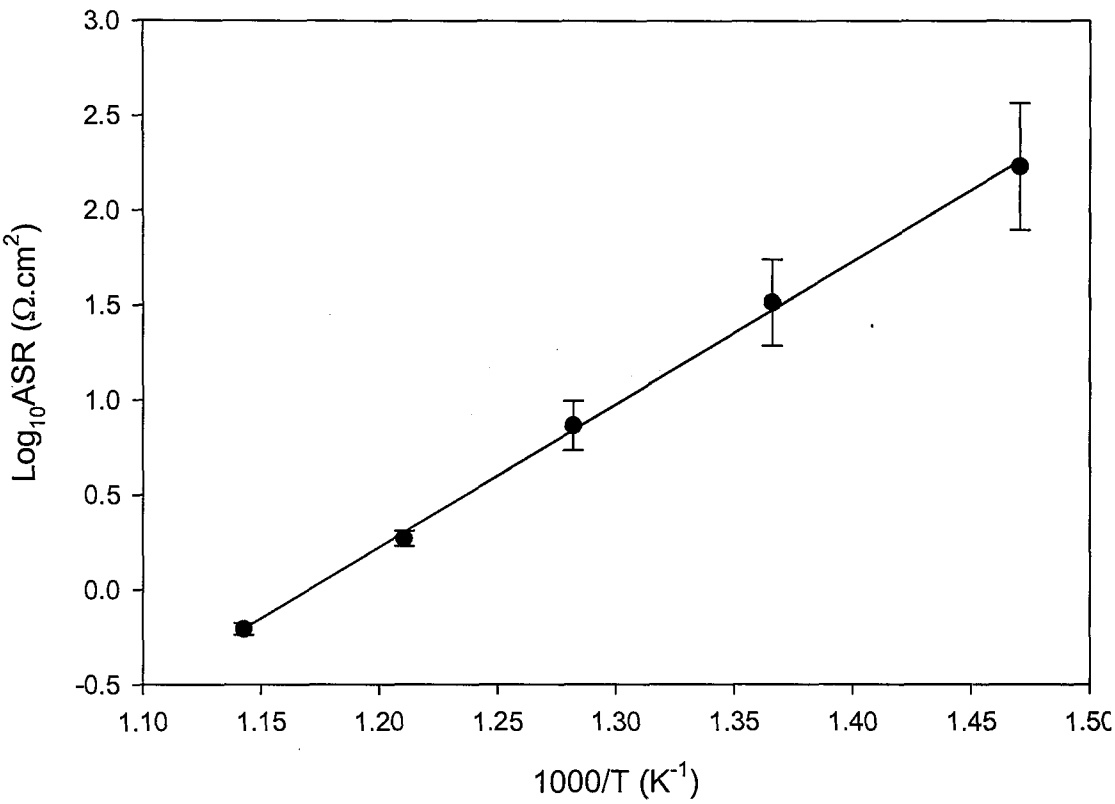
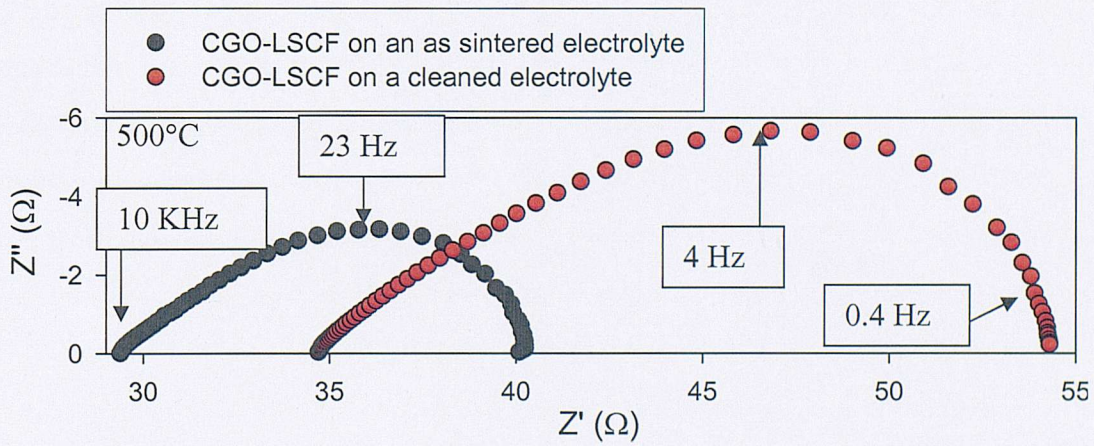


Figure 6.5.14: Arrhenius plot of the CGO20-80/LSCF/carbon composite cathode on an as sintered CGO10-90 electrolyte

6.5.5.2 CGO/LSCF/C on a cleaned electrolyte

Spectra obtained from AC impedance spectroscopy for CGO20-80/LSCF/carbon composite sprayed onto a cleaned CGO10-90 electrolyte pellet and then sintered in air at 1050°C is shown in Figure 6.5.15, together with the responses of the CGO20-80/LSCF/carbon on an as sintered electrolyte. Here also the response at 506°C, 555°C and 604°C can be resolved into two overlapping semicircles using the equivalent circuit model in Figure 6.5.12. The high frequency arc, which peaks at approximately 1 KHZ at

506°C, 2 KHz at 555°C and 3 KHz at 604°C, can be attributed to oxygen ion charge transfer across the electrode/electrolyte interface. The low frequency arc, which peaks at approximately 6 HZ at 506°C, 15Hz at 555°C and 50Hz at 604°C, is due to the non-charge transfer processes including oxygen surface exchange and solid-state diffusion. It must be noted that the shape in the impedance response does not show a great difference between the CGO20-80/LSCF electrode on an as sintered and cleaned electrolyte. Also it can be noted that the high frequency arc decreased in size (polarization resistance decreased) for the CGO20-80/LSCF electrode on a cleaned electrolyte, when compared to the same on an as sintered electrolyte. This is because, assuming that there is no transport of silica into the electrode, then silica at the surface of the electrolyte would block the transfer of oxygen ions across the interface of the CGO20-80/LSCF electrode and the CGO10-90 electrolyte. This may result in reduction in the area of the oxygen transfer path and as a consequence the electrode resistivity may be increased (larger high frequency arc). Hence by cleaning the surface of the electrolyte, the silica is being removed, which would increase the transfer of oxygen ions across the electrode/electrolyte interface. This consequently results in a reduction of electrode resistivity (smaller high frequency arc). The offset of the CGO20-80/LSCF on a cleaned electrolyte response has also shifted to the lower impedance, when compared to the offset of the CGO20-80/LSCF on an as sintered electrolyte response.



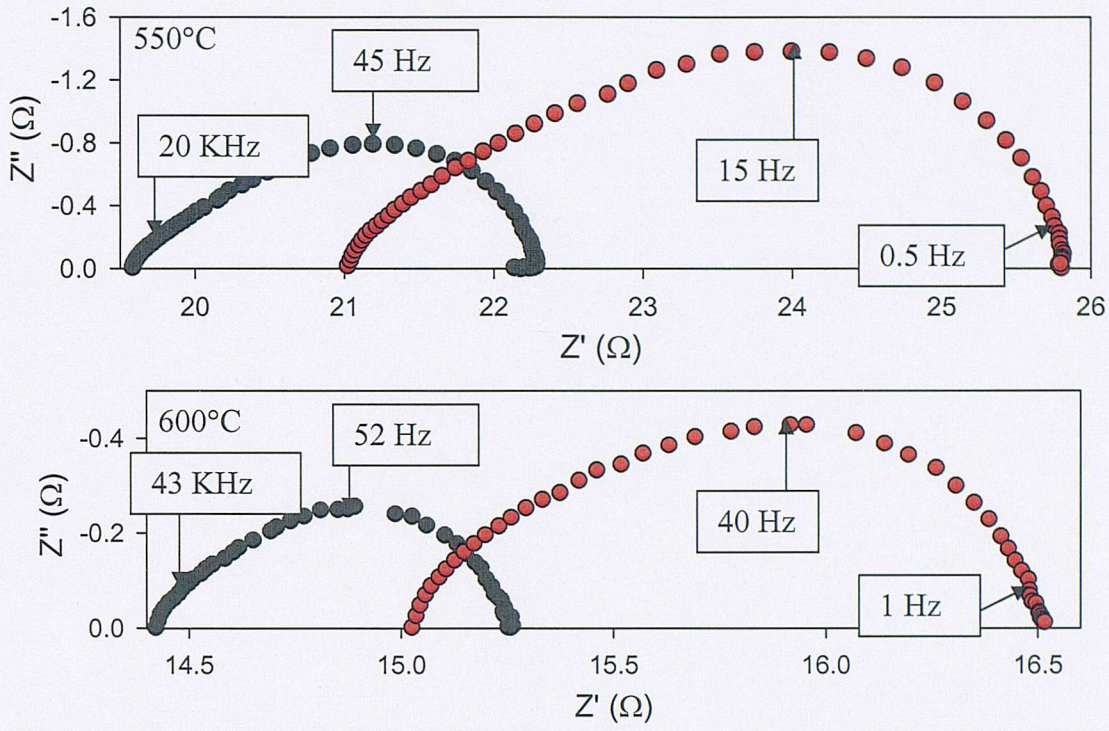


Figure 6.5.15: AC Impedance Spectroscopy spectra of CGO20-80/LSCF/carbon composite cathode on a cleaned CGO10-90 electrolyte at various temperatures

The electrode polarization resistance is calculated from the difference between the low and high frequency intercepts with the real axis. The ASR values for this electrode on a cleaned electrolyte found to be 3.91 $\Omega.cm^2$ at 506°C, 0.96 $\Omega.cm^2$ at 555°C and 0.33 $\Omega.cm^2$ at 604°C. These values are much lower (by a factor of 2) than the ASR values obtained for the cathode on an as sintered electrolyte.

Area specific resistances (ASR) of the CGO 20-80/LSCF/carbon electrodes on a cleaned electrolyte are shown as an Arrhenius plot in Figure 6.5.16. The activation energy for CGO 20-80/LSCF composite cathode is found to be 1.47 ev ±0.24ev.

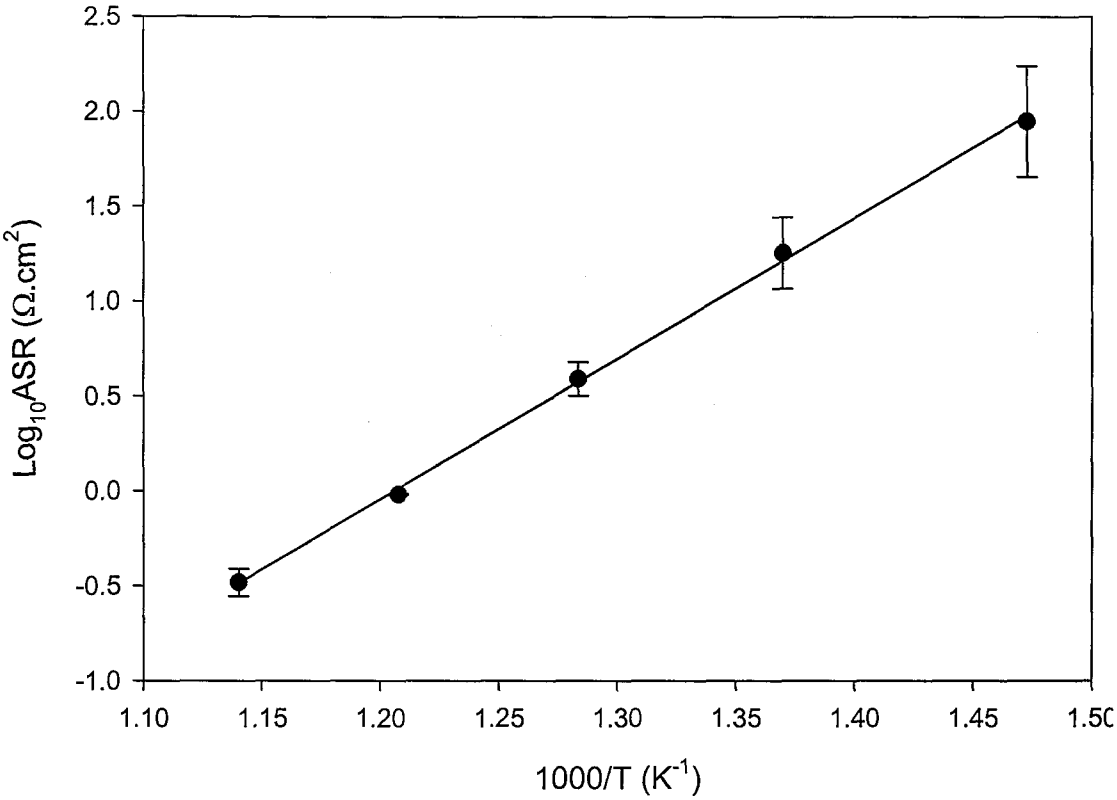


Figure 6.5.16: Arrhenius plot of the CGO20-80/LSCF/carbon composite cathode on a cleaned CGO10-90 electrolyte

6.5.5.3 CGO/LSCF/C on a clean electrolyte and iso-statically pressed

Figure 6.5.17 shows the AC impedance spectra of CGO/LSCF/carbon cathode on a cleaned CGO10-90 electrolyte and iso-statically pressed before sintering at 1050°C in air, together with the impedance responses of the CGO20-80/LSCF on an as sintered and cleaned electrolyte. The impedance spectra of this electrode looks very similar to the responses from the other two electrodes on an as sintered and cleaned electrolyte between 500°C and 600°C. Here also the responses at 503°C, 550°C and 600°C was resolved into two overlapping semicircular arcs using the equivalent circuit model in Figure 6.5.12 and the explanation for the mechanism of each of the semicircle is explained in section 6.5.5.1.

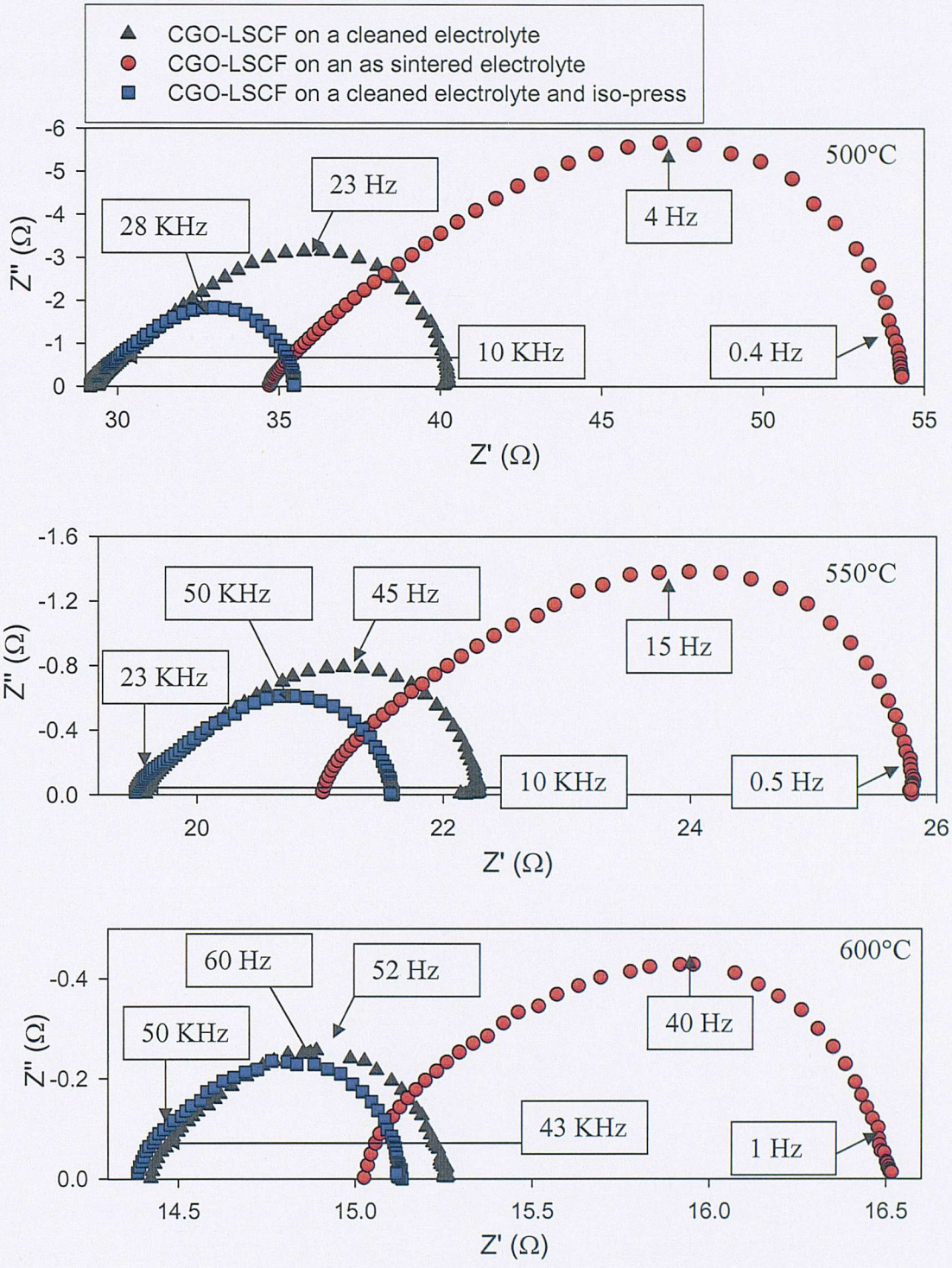


Figure 6.5.17: AC Impedance Spectroscopy spectra of CGO20-80/LSCF/carbon composite cathode on a cleaned CGO electrolyte and iso-statically pressed

The normalized AC impedance spectra of CGO/LSCF-carbon on an as sintered electrolyte, CGO/LSCF-carbon on a clean electrolyte and CGO/LSCF-carbon on a clean electrolyte and iso-statically pressed at 500°C, 550°C and 600°C is shown in Figure 6.5.18. All three responses are identical at the three temperatures shown below. The two

semicircles can easily be resolved above around 550°C. The similarity in the shape of the response indicates that same reaction mechanisms control the overall electrode behaviour in the entire composite cathode studied. These responses are different from that of CGO/LSCF, where only one semicircle is resolved at 500°C, 550°C and 600°C. This might be due to the dense nature of the CGO/LSCF electrode.

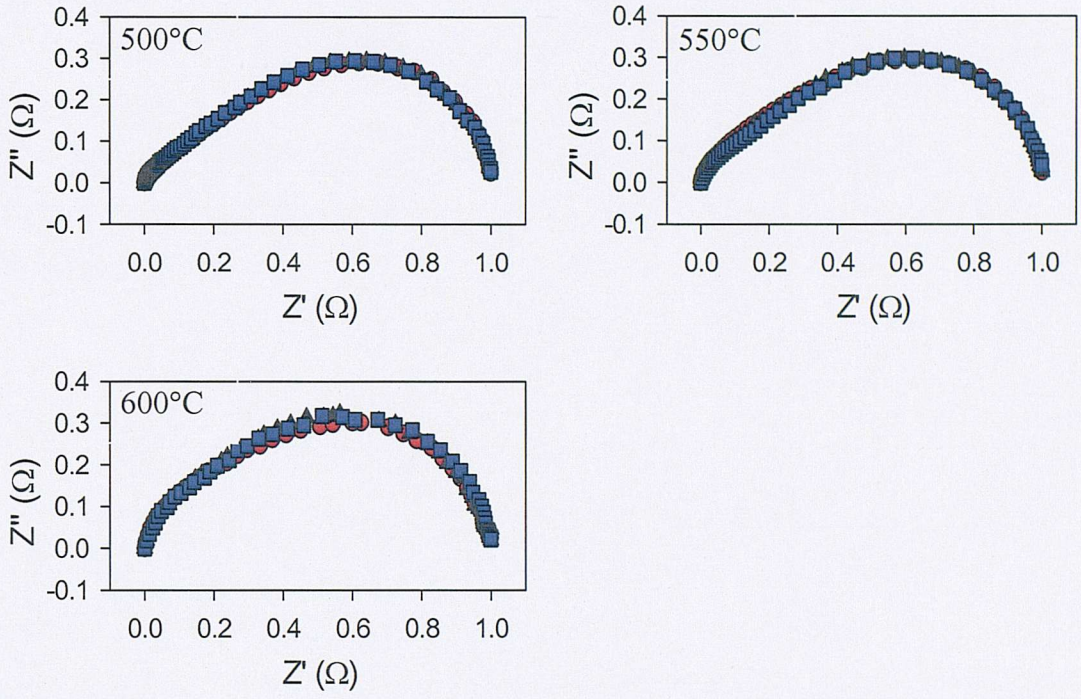


Figure 6.5.18: Normalized AC Impedance spectroscopy spectra of CGO/LSCF-carbon

The CGO20-80/LSCF/carbon electrode on a cleaned electrolyte and iso-statically pressed had an ASR of 2.33 $\Omega.cm^2$ at 503°C, 0.75 $\Omega.cm^2$ at 552°C and 0.29 $\Omega.cm^2$ at 601°C. This is only slightly better than the values obtained for the CGO20-80/LSCF/carbon electrode on a cleaned electrolyte as can be seen in Table 6.1.4. The cathode, which has been iso-statically pressed had provided a better contact with the electrolyte and should ensure a better current collection. Hence a slightly improved performance, when compared to the CGO20-80/LSCF/carbon on a cleaned electrolyte. However, these ASR values are much lower than the reported values in the literature **[10-12]**.

	500°C	550°C	600°C
CGO/LSCF/C on an as sintered electrolyte	7.34 Ωcm^2	1.86 Ωcm^2	0.62 Ωcm^2
CGO/LSCF/C on a cleaned electrolyte	3.91 Ωcm^2	0.96 Ωcm^2	0.33 Ωcm^2
CGO/LSCF/C on a cleaned electrolyte and iso-pressed	2.33 Ωcm^2	0.75 Ωcm^2	0.29 Ωcm^2

Table 6.1.4:- ASR values of the composite cathodes at various temperatures

The activation energy for CGO 20-80/LSCF/carbon composite cathode is calculated from the gradient of the graph shown in Figure 6.5.19 and it was found to be 1.48 ev ±0.24ev.

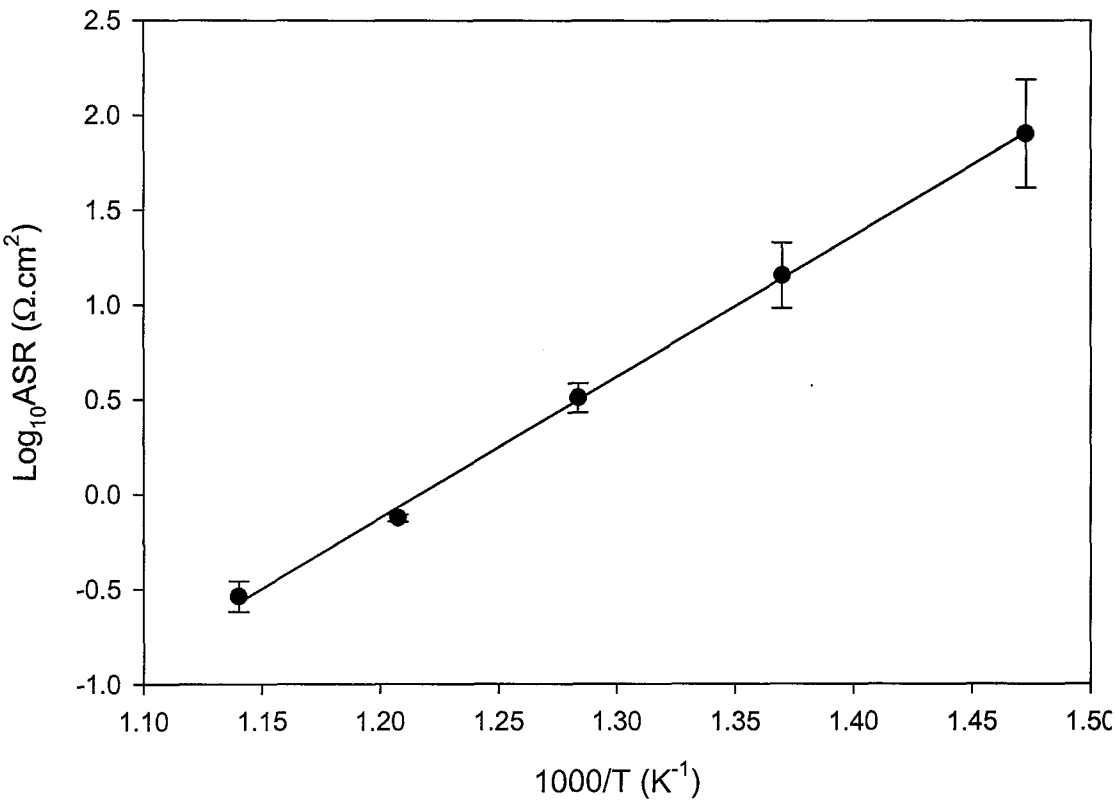


Figure 6.5.19: Arrhenius plot of the CGO20-80/LSCF/carbon composite cathode on a cleaned CGO10-90 electrolyte and iso-statically pressed

Data from the literature **[26]** for $La_{0.6}Sr_{0.4}Fe_{0.8}Co_{0.2}O_{3-\delta}$ sintered at 1000°C and CGO-$La_{0.6}Sr_{0.4}Fe_{0.8}Co_{0.2}O_{3-\delta}$ composite cathode sintered at 800°C and 900°C on a CGO electrolyte **[10]** are shown in Figure 6.5.20 for comparison. This electrode polarization resistance value is very close to the target ASR value of 0.1 $\Omega.cm^2$ between 500-600°C.

As can be observed in the SEM images, the iso-statically pressed cathode has a very uniform microstructure with high level of interconnected porosity and all the grains are connected with by narrow bottleneck-type bridges. This is an ideal microstructure for a good performance cathode.

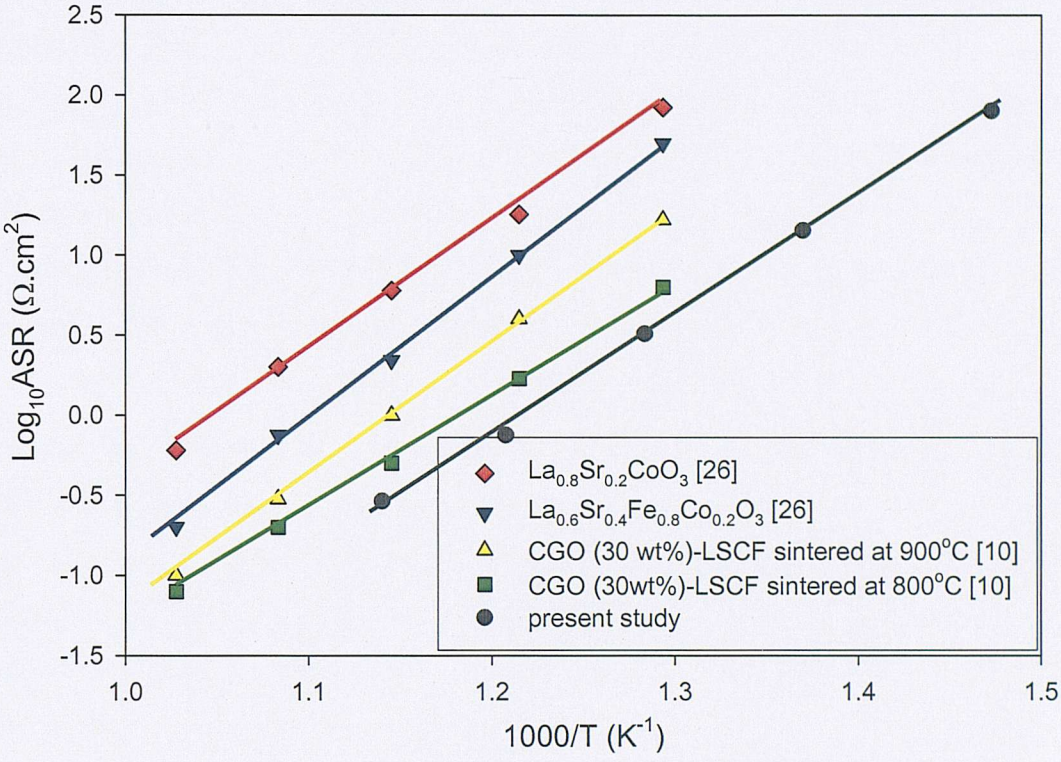


Figure 6.5.20:- Comparison of the ASR values of - from the present study and values reported in the literature

6.5.6 Comparison with the Adler (ALS) Model

The measured ASR values were compared to the generated R_{chem} values for porous electrodes proposed by Adler et al. If the values of the oxygen diffusion coefficient and the surface exchange coefficient taken from the data of Esquirol **[11]** are substituted into the following equation:

$$R_{chem} = \left[\frac{RT}{2F^2}\right]\sqrt{\frac{\tau}{(1-\varepsilon)aC_o{}^2 D^* K}} \qquad [1]$$

together with the value of a = 20000 cm^2/cm^3 **[15]**, the porosity (45.9%) and the tortuosity (estimated at 1.5 from the FIB microstructure) then R_{chem} (ASR) values can be

generated at different temperatures. Here also the porosity of the cathode on a electrolyte could not be measured, because it was so thin. Therefore, the porosity was measured from a separately made cathode pellet, which was sintered at 1050°C. The D and k values have been kept the same because of the same CGO20-80/LSCF electrode material; however microstructural parameters have been changed. Using the pore former, the porosity in the electrode has been improved and hence the tortuosity. Predicted R_{chem} values by the model at different temperatures for CGO/LSCF are shown together along with the experimental ASR values of CGO 20-80/LSCF/carbon cathode in Figure 6.5.21.

As can be seen the model ASR values are higher than the experimental ASR values over the entire temperature range studied. The best measured ASR values of 0.75 Ωcm^2 and 0.29 Ωcm^2 at around 550°C and 600°C for the CGO/LSCF/carbon on a polished electrolyte and iso-statically pressed were much better than the predicted values of 10 Ωcm^2 and 2 Ωcm^2 respectively.

Regarding the Arrhenius plot below, all the lines of the different cathodes are parallel to each other, which indicates that they all have the same activation energies. This further implies that similar processes are involved in both the model description and the experiment but that there are some difficulties in estimating the absolute values of the constants in equation 1. All the CGO20-80/LSCF/carbon composite materials exhibited an activation energy in the range 1.47-1.50 ev ±0.24ev. These activation energies are very comparable to each other and also to the model. From this it is difficult to explain whether the model developed by Adler et al known as ALS model can provide a quantitative approach for understanding the linear AC polarization values associated with a porous composite electrode.

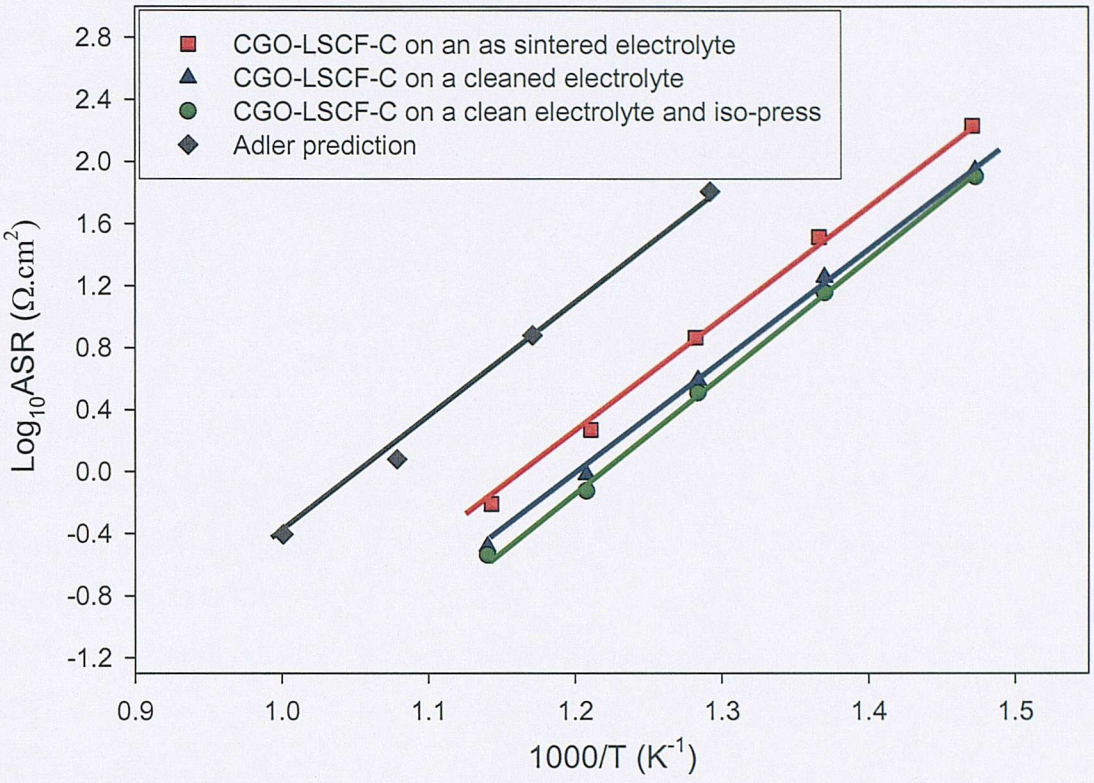


Figure 6.5.21: Comparison of the measured impedance and that predicted by Adler's model

6.6 CGO/LSCF/carbon in water atmosphere

The effect of humidity on the electrode was investigated using the AC impedance spectroscopy technique. Sakai et al **[28]** showed that water could enhance the surface exchange coefficient of YSZ by many orders of magnitude. This was later proved by the performance of the LSM/YSZ composite cathode in the presence of water **[29]**. Benson et al **[30]** used the oxygen isotope exchange combined with SIMS technique to observe the effect of the presence of the gaseous water and carbon dioxide on the tracer diffusion coefficient, D^* and the surface exchange coefficient, k of LSCF at 750°C. An improvement of the oxygen surface exchange coefficient was observed, although the oxygen diffusivity remained the same. Hence this might lead to even lower polarization resistance of the CGO/LSCF/carbon cathode in the humid atmosphere.

Figure 6.6.1 shows typical AC impedance spectra of CGO 20-80/LSCF (70 weight % LSCF) composite coated onto a cleaned CGO10-90 electrolyte pellet and then sintered in air at 1050°C. Here the measurements were taken in dry and wet compressed air. The electrical measurements were first carried out in a flowing atmosphere of dry compressed air, which was passed through a desiccant (anhydrous calcium sulphate). In the next experiment the compressed air was then passed through water to produce a wet atmosphere. This was left overnight to equilibrate to the new atmosphere. Measurements were then carried out in the wet atmosphere for the required temperature range. The response at around 500°C, 550°C and 600°C looks very similar to that of CGO/LSCF on an as sintered electrolyte. At around 500°C the response in both the dry and wet condition looks identical to the Gerisher impedance. However, above 550°C two overlapping semicircles can be observed. The normalized plot in Figure 6.6.2 shows that the responses in dry and wet conditions are identical in shape at all the temperatures studied.

The ASR for this cathode in dry atmosphere was found to be around 6.88 $\Omega.cm^2$ at 508°C, 1.71 $\Omega.cm^2$ at 556°C and 0.63 $\Omega.cm^2$ at 605°C. However in wet atmosphere, the ASR was found to be higher with values of 8.12 $\Omega.cm^2$ at 507°C, 2.03 $\Omega.cm^2$ at 555°C and 0.74 $\Omega.cm^2$ at 601°C. The activation energy for CGO 20-80/LSCF composite cathode is found to be 1.27 ev dry atmosphere and 1.17 ev in wet atmosphere.

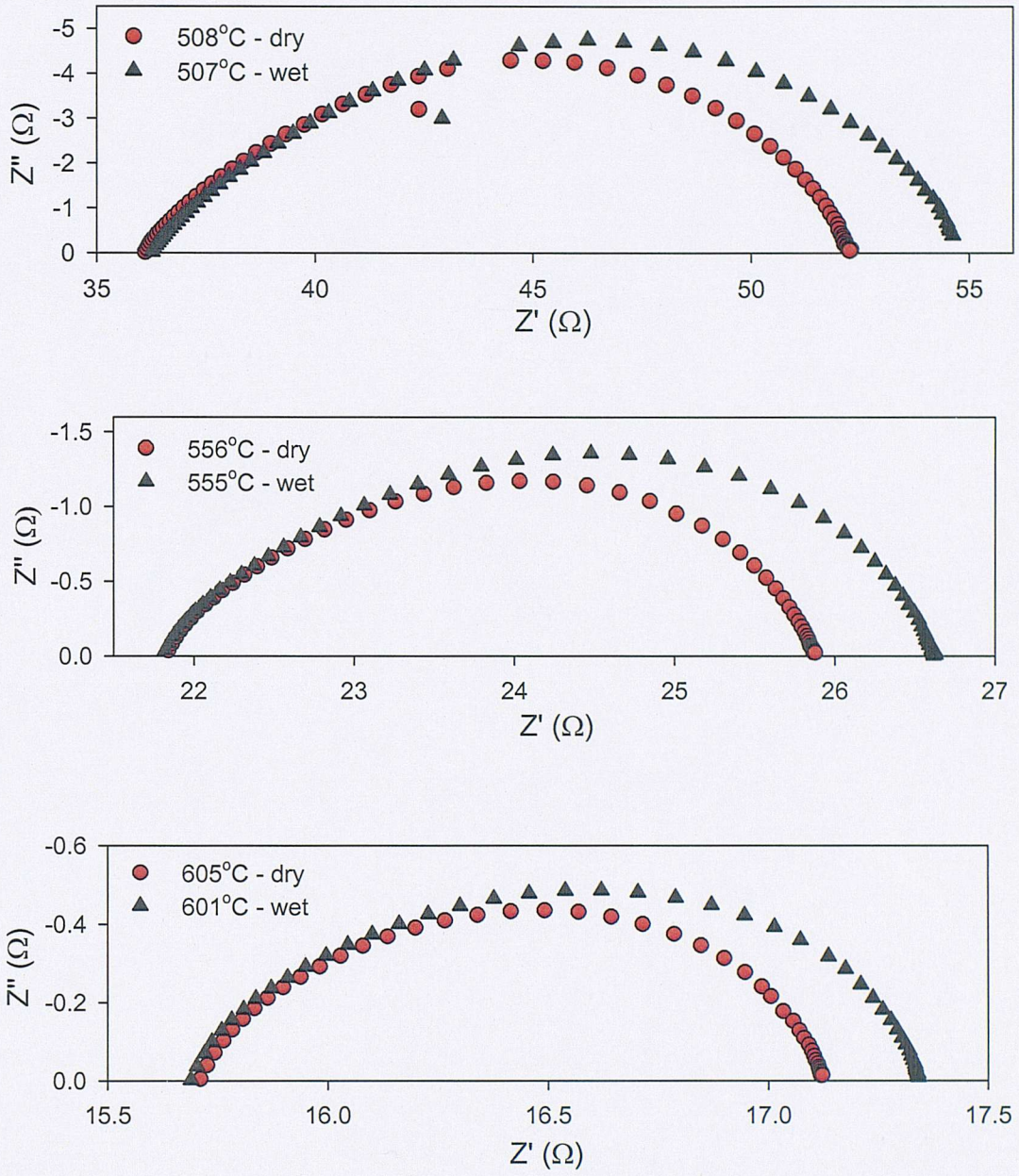


Figure 6.6.1:- AC Impedance Spectroscopy spectra of CGO20-80/LSCF/carbon composite cathode in dry and wet conditions at various temperatures

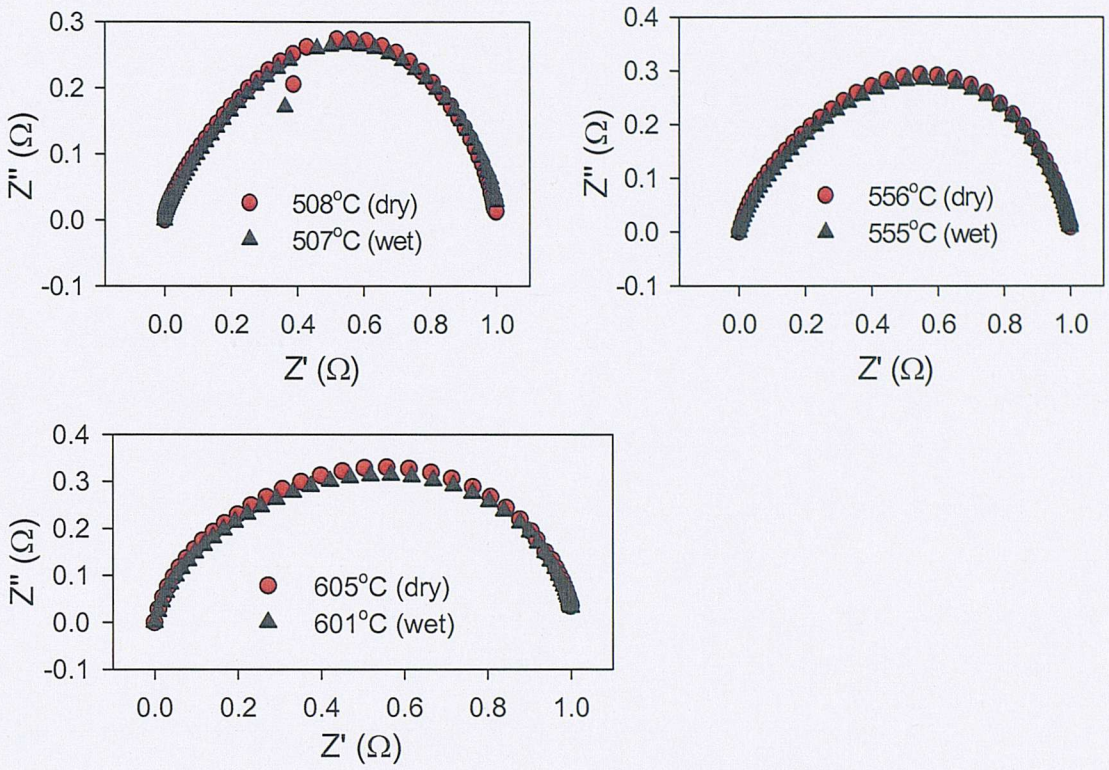


Figure 6.6.2:- Normalized plot of the AC impedance spectra of CGO-LSCF/carbon in dry and wet conditions

Benson et al **[30]** showed that the oxygen surface exchange coefficient is higher in wet conditions; hence the polarization resistance should be lower according to the Adler model. However the AC impedance spectroscopy results obtained from the porous cathode were not in agreement with this finding. The above results show that between 500-600°C, the ASR in wet atmosphere is higher than that of in dry atmosphere. The results of Benson at al are based on the exchange experiments made on dense pellets. Dense and porous samples usually do not behave in the same way and are not controlled by the same rate-determining step **[31-32]**, so water might affect the surface exchange properties of the porous cathode **[11]**.

Below 500°C this composite cathode had a higher ASR values (182.18 $\Omega.cm^2$ at 405°C and 36.82 $\Omega.cm^2$ at 454°C) in dry atmospheres than wet atmospheres (138.38 $\Omega.cm^2$ at 404°C and 35.37 $\Omega.cm^2$ at 455°C as can be seen in Figure 6.6.3.

This phenomenon can be explained as follows: The oxygen exchange reaction at the CGO surface is governed by the interaction between water molecules and oxygen vacancies of CGO.

$$H_2O(g) + V_O^{\bullet\bullet} \Leftrightarrow O_O^{\times} + 2H^{\bullet}$$

Here $V_O^{\bullet\bullet}, O_O^{\times}$ *and* $H^{\bullet}$ represent an oxygen vacancy, an oxide ion and an interstitial proton in CGO lattice. The reaction rate of above equation is considered to be much faster than the reaction, which may be dominant in dry O_2:

$$\frac{1}{2}O_2 + V_O^{\bullet\bullet} \Leftrightarrow O_O^{\times} + 2h^{\bullet}$$

The $h^{\bullet}$ represents an electronic hole in CGO.

Since the existence of water vapour enhances the oxygen exchange reaction on the electrolyte surface, a similar mechanism may enlarge the active zone of the electrochemical reaction on CGO and may reduce the polarization resistance at lower temperatures **[33]**.

The present results indicate that the effect of water vapour on cathode reaction can be explained in terms of the combination of two opposite effects, that is the improvement due to active reaction zone and the degradation due to the prevention of diffusion on electrode. The improvement effect is more significant at lower temperatures and degradation effect becomes dominant at higher temperatures **[34]**.

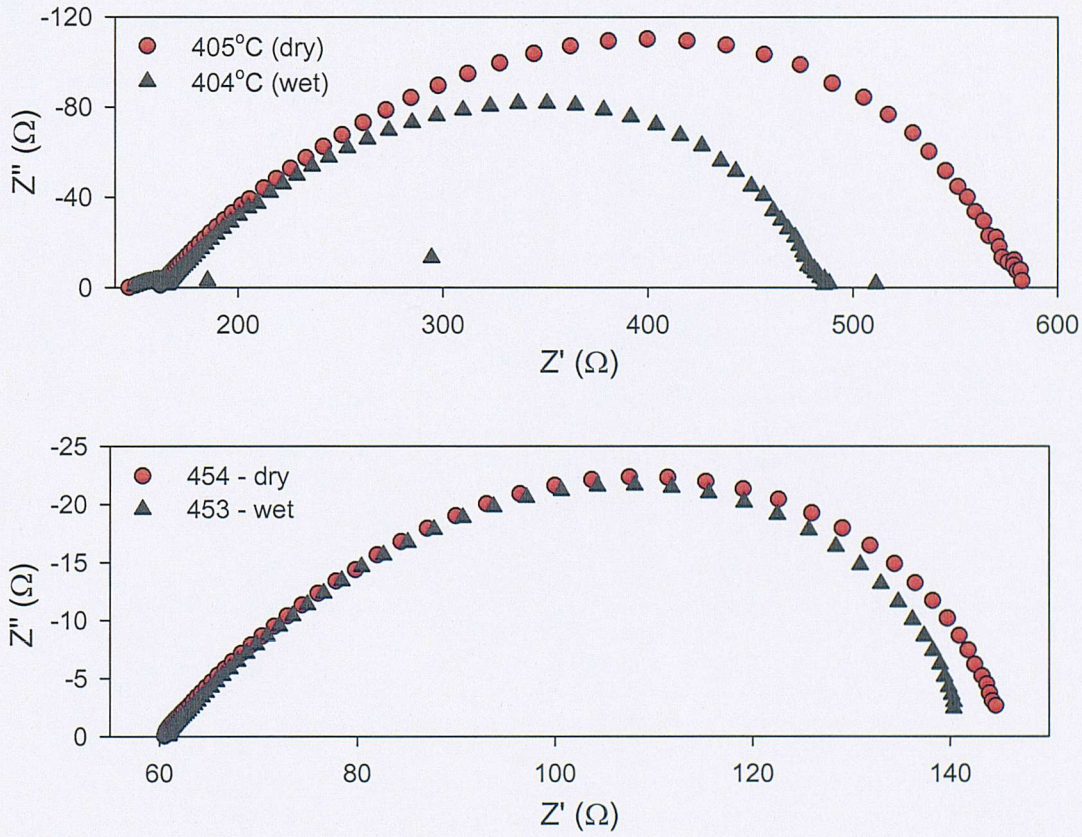


Figure 6.6.3:- AC Impedance Spectroscopy spectra of CGO20-80/LSCF/carbon composite cathode in dry and wet conditions at various temperatures

6.7 CGO/GSC

6.7.1 Powder Characterisation

The XRD pattern of the commercial $Gd_{0.6}Sr_{0.4}CoO_3$ (GSC) powder is shown in Figure 6.7.1. No peak corresponding to any impurity is observed. All the peaks are very sharp showing the crystalline nature of the powders. The Bragg peaks were identified using the file $La_{0.6}Sr_{0.4}CoO_{3-x}$ (JCPDS 48-121). The obtained XRD patterns of the GSC powder studied at room temperature were fitted to a cubic perovskite structure using the software celref. The lattice parameters were extracted as 3.8058 (± 0.0005) Å.

Figure 6.7.2 shows the X-ray spectra of the composite CGO20-80/GSC cathode calcined at 1000°C for 2 hours. All the Bragg peaks from CGO20-80 and GSC could be matched and no secondary phase can be found.

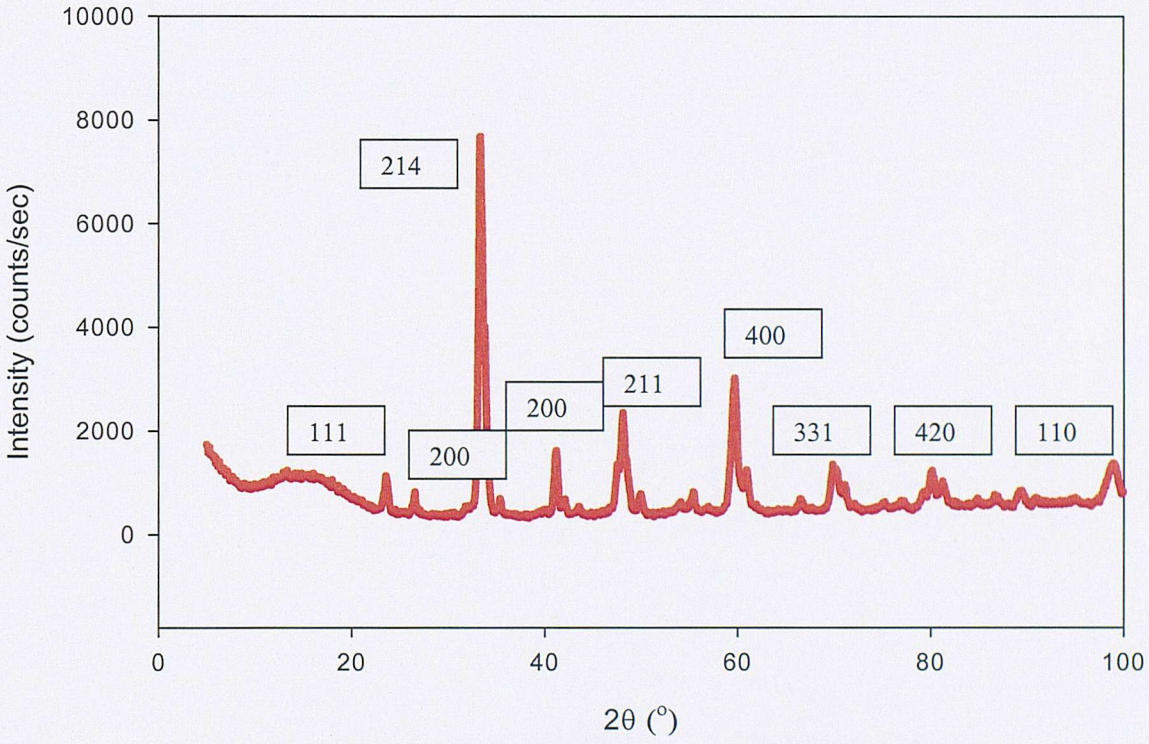


Figure 6.7.1: X-ray diffraction pattern of $Gd_{0.6}Sr_{0.4}CoO_{3-\delta}$ using Cu-K_α radiation (λ = 1.5406 Å)

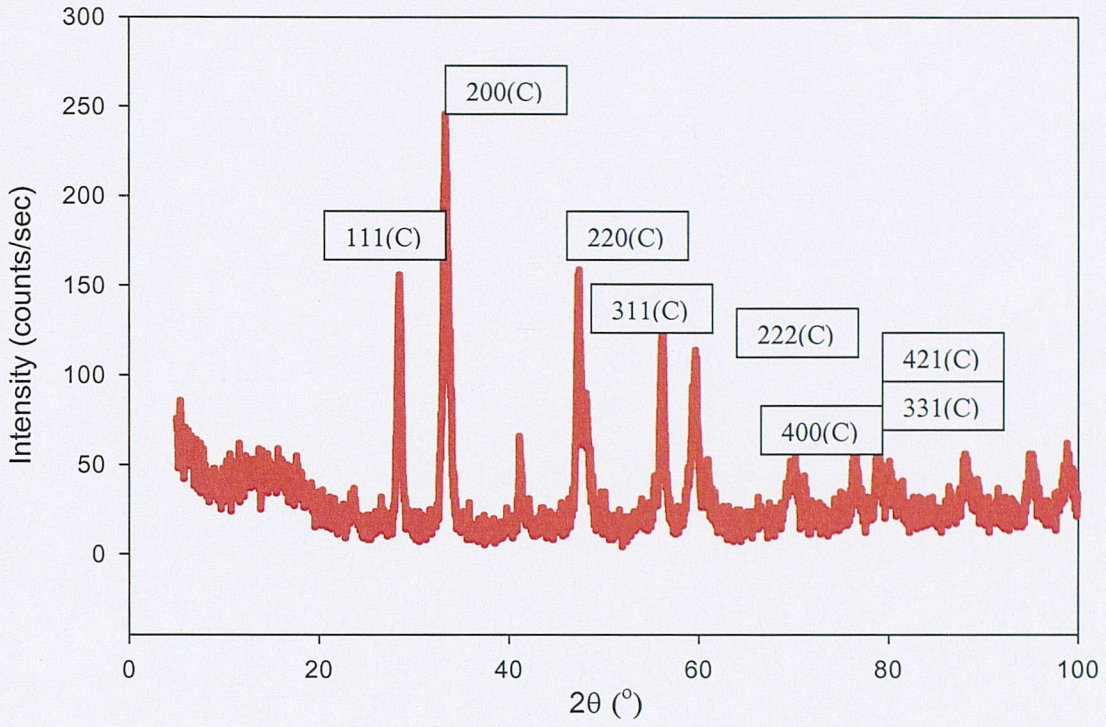


Figure 6.7.2: X-ray diffraction pattern of $Ce_{0.8}Gd_{0.2}O_{2-\delta}/Gd_{0.6}Sr_{0.4}CoO_{3-\delta}$ composite using Cu-K_α radiation ($\lambda = 1.5406$ Å)

6.7.2 Sintering Studies

Figure 6.7.3 shows the change in length versus temperature data obtained from a dilatometer during the sintering of green powder compacts of CGO20-80/GSC cathode. The onset of shrinkage for this composite commences around 950°C, which is about 150°C higher than that which occurs in the CGO/LSCF composite cathodes. This reflects in the higher percentage of porosity seen with the CGO/GSC cathode when sintered at 1050°C, and hence there was no need for the addition of pore former. The rise in the curves between the room temperature and the onset of shrinkage is due to the small expansion of the material. It is also noticeable in the graph that GSC expands more than LSCF (by approximately 300%) **[35-36]**. The absence of plateau at high temperature indicates that full density had not been achieved.

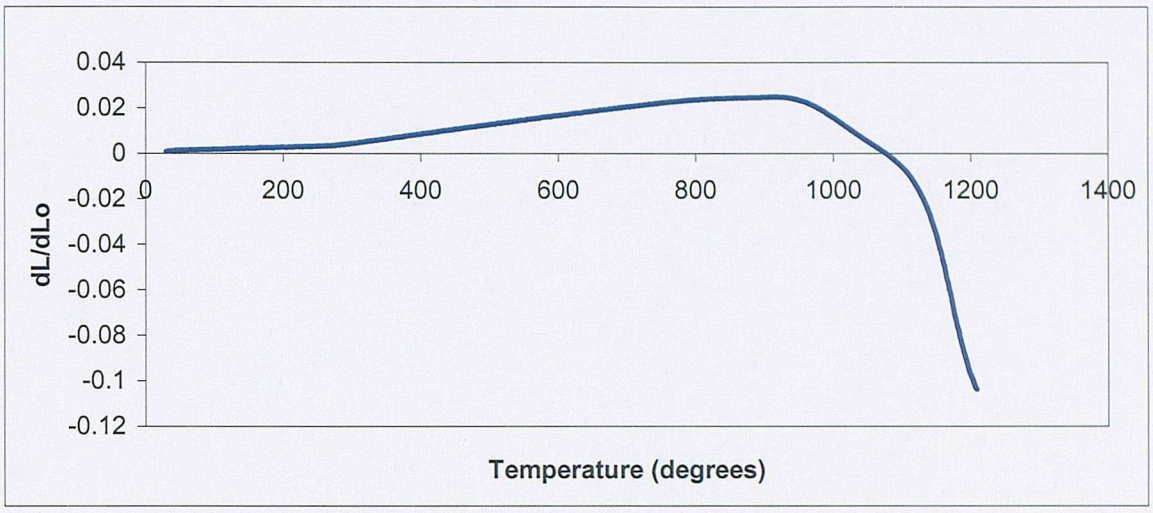


Figure 6.7.3: **Dilatometry trace for a composite *CGO/GSC***

6.7.3 Microstructural Studies by SEM

As we have seen in the previous chapter, the microstructure of the cathode plays a vital role in the performance of the cathode and, thus, in the performance of the whole SOFC. Figures 6.7.4 and 6.7.5 show SEM micrographs of the unpressed and iso-statically pressed CGO 20-80/GSC cathode layer sintered at 1050°C for 2 hours. After sintering at 1050°C of both the unpressed and iso-statically pressed cathode (Figure 6.7.4 and Figure 6.7.5), a uniform microstructure with high level of interconnected porosity can be seen. All the grains are connected, leaving small interconnected pores. Furthermore the grains remained small in size of around 0.5-1 μm, leading to long three-phase-boundaries. Hence the sintering of both unpressed and iso-statically pressed CGO20-80/GSC cathode at 1050°C for 2 hours resulted in a structure with high level of porosity with pore diameters between 0.1-2 μm that was connected with by narrow bottleneck-type bridges. Unlike CGO20-80/LSCF, CGO20-80/GSC did not need a pore former to enhance porosity. The iso-statically pressed cathode in Figure 6.7.5 appears to be denser than unpressed material, however it should provide a better contact with the electrolyte and ensure a better current collection than an unpressed cathode. The percentage of porosity presented in this composite is calculated to be 39% at 1050°C.

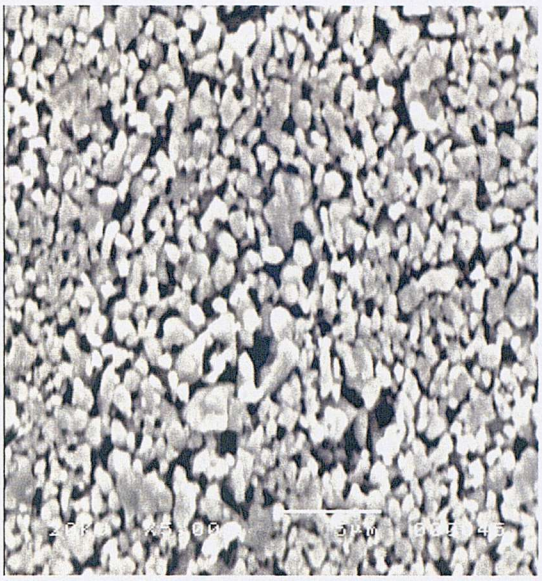


Figure 6.7.4:- SEM micrograph of CGO-GSC sintered at 1050 ℃.

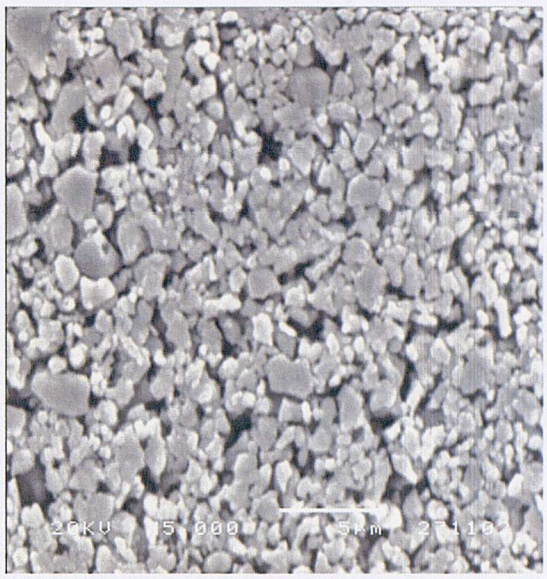


Figure 6.7.5:- SEM micrograph of CGO-GSC sintered at 1050 ℃. Iso-statically Pressed

Figure 6.7.6 and 6.7.7 shows a secondary electron image from SEM of the cross-section of an unpressed and iso-statically pressed CGO20-80/GSC half-cells that were tested on a CGO10-90 electrolyte material. The electrode is approximately 12μm thick in both the micrographs. The electrode shows a high level of interconnected porosity (using Archimedes principle the porosity was calculated to be around 42%), while the CGO electrolyte was very dense (>95%). In Figure 6.7.6 (where the cathode was unpressed), it is apparent that the composite electrode is not a uniform mixture of fine particles where the two oxides are separated from each other, but is, more likely, an agglomerate mixture of the two components. It also shows a good contact to the electrolyte. Figure 6.7.7 shows the SEM micrograph of the iso-statically pressed cathode onto the electrolyte at the same magnification (× 5000). This indicates that the electrode microstructure also looks uniform with a very good bonding and continuous contact at the interface between the electrode and the dense electrolyte pellet. The electrodes showed good adherence to the electrolyte and no reactions could be detected at the interface.

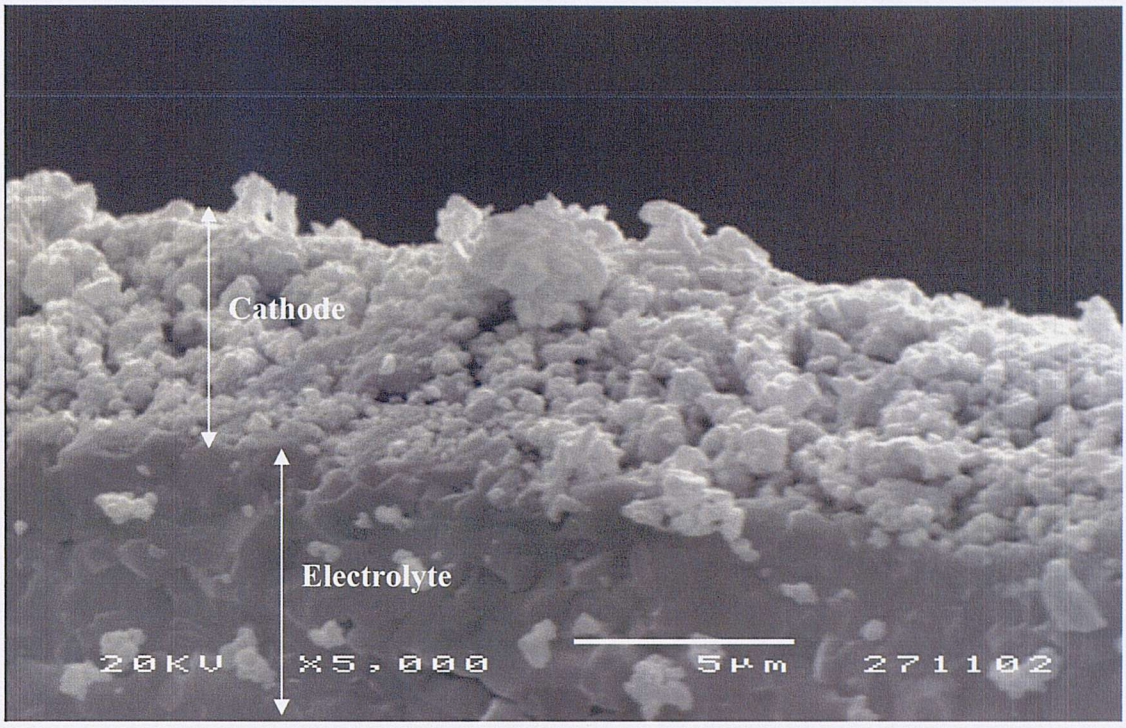


Figure 6.7.6:- SEM micrograph of the cross-section of CGO-GSC onto a CGO electrolyte, sintered at 1050 ℃

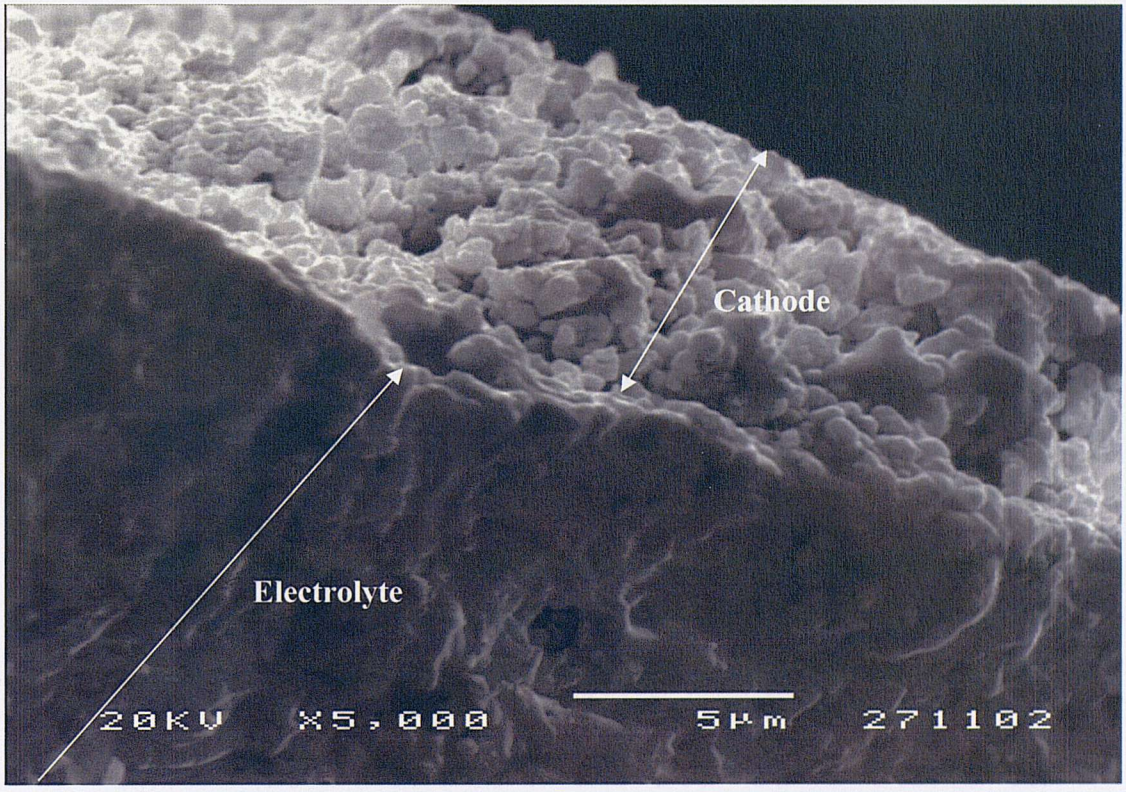


Figure 6.7.7:- SEM micrograph of the cross-section of CGO-GSC onto a CGO electrolyte, iso-statically pressed and sintered at 1050 ℃

6.7.4 Microstructural Studies by FIB-SIMS

Figure 6.7.8 and 6.7.9 shows the focused ion beam (FIB) image of the surface and the ion milled crater of the CGO20-80/GSC composite cathode applied on a CGO10-90 pellet. The surface microstructure (Figure 6.7.8 (A)) of the cathode sintered after 1050°C for 2 hours showed a very uniform microstructure with high level of porosity and all the grains are connected with by narrow bottleneck-type bridges. A rectangular crater of 20 μm in depth, 30 μm in length and 10 μm in width was produced on the surface of the cathode by a higher current ion beam, and then polished by a lower current ion beam to give a smoother surface. This is shown in Figure 6.7.8 (B). Figure 6.7.9 shows the inside of the trench after having tilted the stage at an angle of 30°. The highly porous cathode and a very dense electrolyte are visible. The particles appeared layered and this was attributed to the number of sprayed layers (in this case about 8-9 sprayed layers). The cathode thickness was found to be around 11-15 μm.

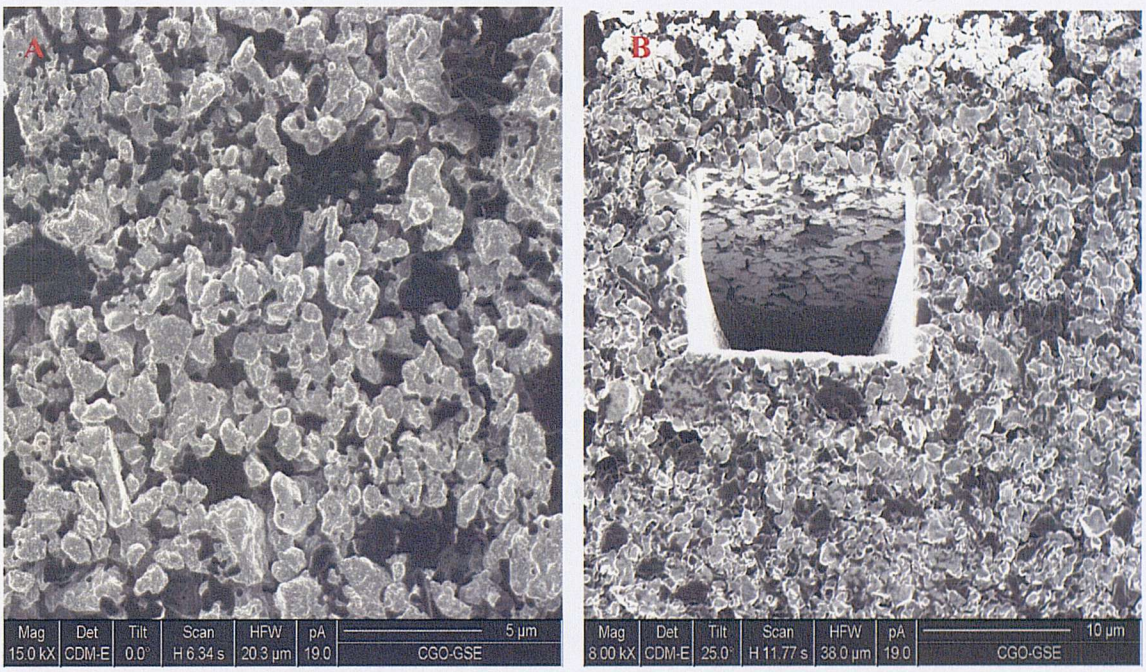


Figure 6.7.8:- (A) Focused ion beam image (FIB) of the surface of a CGO20-80/GSC composite cathode sintered at 1050 °C. (B) Focused ion beam image (FIB) of the top view of an ion-milled crater on the surface of the cathode (30kev Ga^{+} primary bombardment).

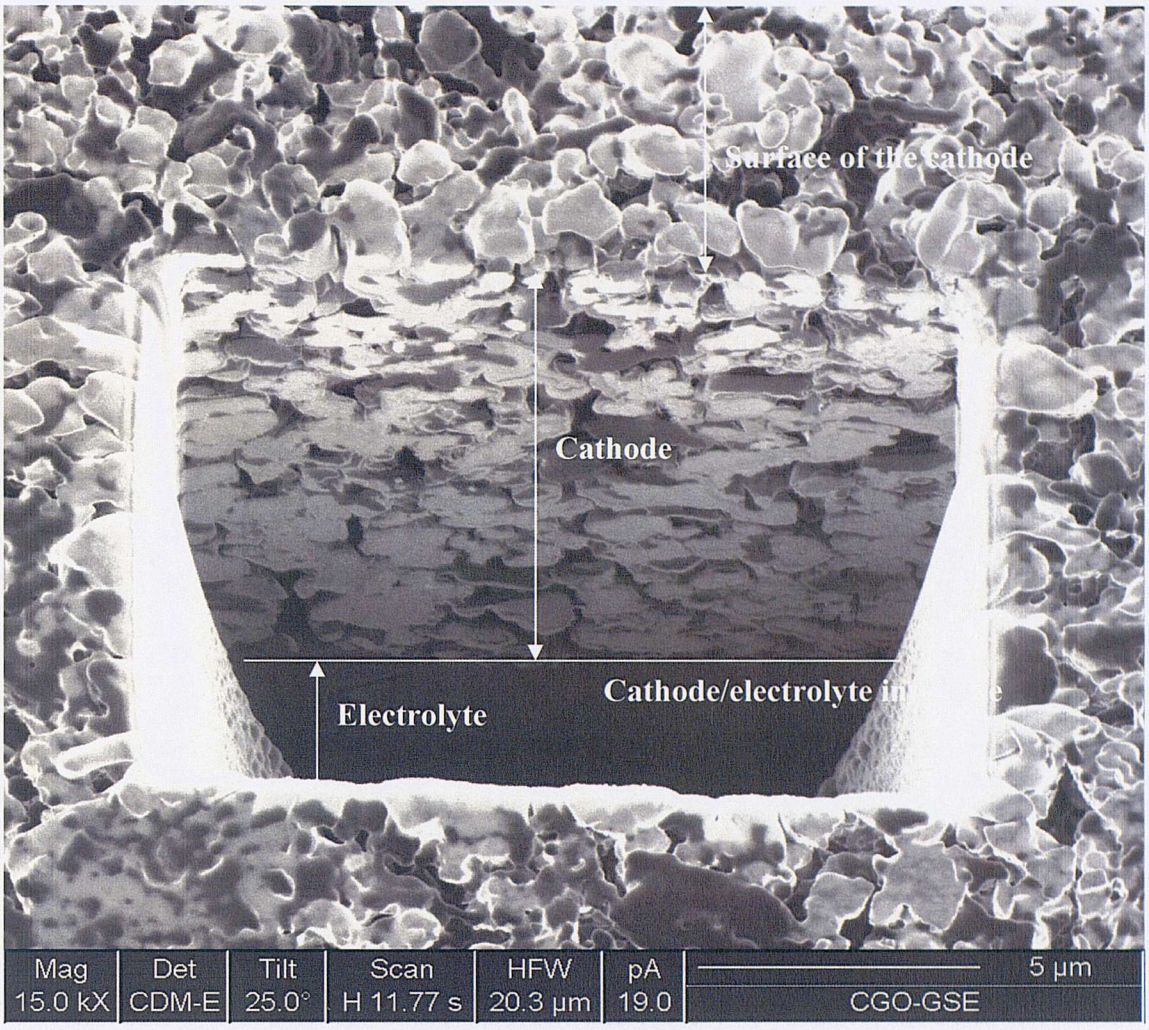


Figure 6.7.9:- Focused ion beam image (FIB) of an ion-milled crater after tilting at 30°((30kev Ga+ primary bombardment).

6.7.5 Electrochemical Performance

Figure 6.7.10 shows the temperature dependence of the total-low current polarization resistance values, given by the difference between the real axis intercepts of the impedance plots, for different $Ce_{0.8}Gd_{0.2}O_2$-$Gd_{0.6}Sr_{0.4}CoO_3$ compositions. As can be observed on the graph, the ASR for the two-phase cathode as a function of weight percent of the mixed conducting phase presented a clear minimum at 70% by weight of GSC. Except for the CGO-GSC (60 weight %), the slopes of the log ASR vs 1/T data were nearly the same for all compositions, yielding activation energies between 1.03-1.13 ev. The substantially lower activation energy for the CGO-GSC (60 weight %) suggests a different reaction mechanism was limiting in this case. The decrease in ASR relative to pure GSC was ≈ 2 times for CGO-GSC (70 weight %).

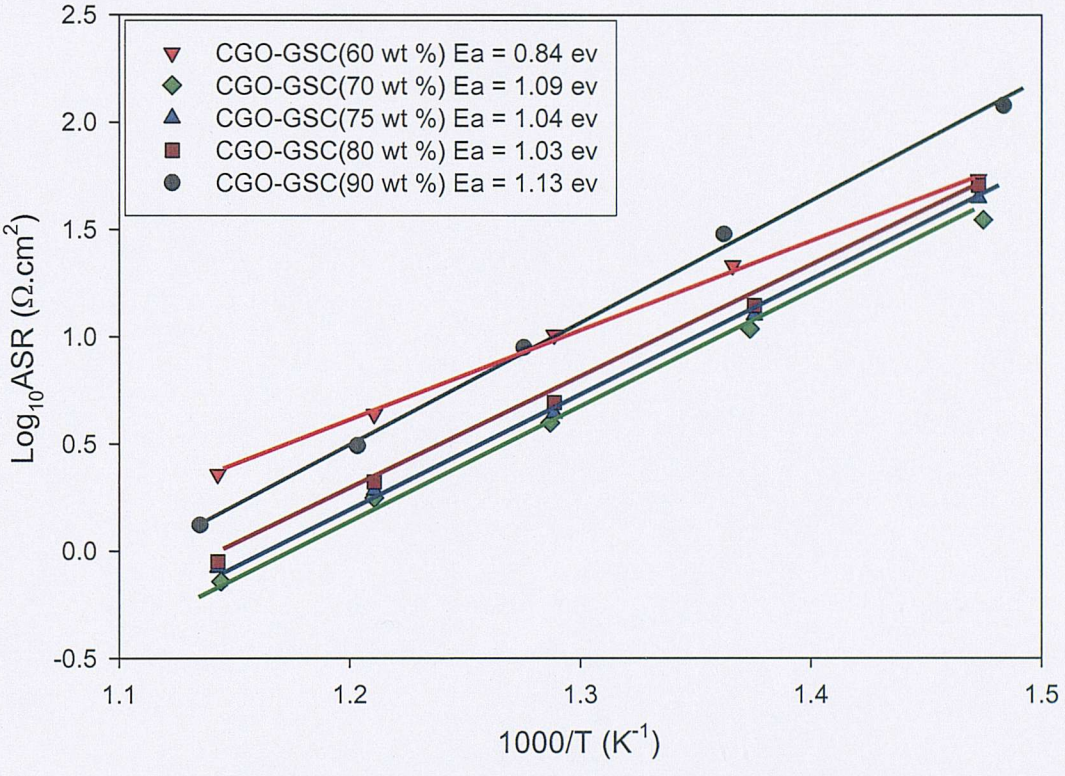


Figure 6.7.10:- Temperature dependence of the polarization resistance for various CGO-GSC cathode compositions measured over a temperature range of 400-650 ℃.

This decrease can be explained in terms of the electrochemical reaction zone of each electrode. GSC is a mixed conductor and the oxygen reduction reactions can thus occur at internal surfaces away from the electrolyte. Penetration depth studies by Adler et al. **[13]** indicate for a mixed-conducting oxide with an average particle size of 1 μm that

the electrode reaction zone extends up to 10 μm from the electrolyte. The addition of CGO, which has 10 times higher ionic conductivity **[31]** than GSC, would presumably extend the reaction zone further into the electrode (the cathodes studied here are approximately 18 μm thick).

6.7.5.1 CGO/GSC on an as sintered electrolyte

The electrode polarization resistance for symmetrical $Ce_{0.8}Gd_{0.2}O_{1.95}$ (CGO20-80)/$Gd_{0.6}Sr_{0.4}CoO_3$ (70 wt %) electrodes on a $Ce_{0.9}Gd_{0.1}O_{1.95}$ (CGO10-90) electrolyte was measured using AC impedance spectroscopy, applying a 20mV alternating signal with zero DC bias. A frequency sweep from 0.01 Hz to 10 MHz was used and the measurements were made in air. Figure 6.7.11 shows the impedance spectra of CGO 20-80/GSC (70 weight % GSC) composite cathode at 500°C, 550°C and 600°C for sintering temperature of 1050°C on an as sintered CGO10-90 electrolyte. The electrode resistances were calculated from the differences between the low and high frequency intercepts of the electrode polarization arc. The ASR decreased with increasing temperature. It is immediately clear that the electrode response is not semicircular in shape and had two overlapping depressed semicircles. The impedance spectra were fitted to an equivalent circuit containing two constant phase elements, which indicates that there are two semicircles and each semicircle represents a reaction step with a different time constant. The equivalent circuit that most closely reproduced the impedance characteristics is shown in Figure 6.7.12. The fitting result is also shown in Figure 6.7.11 for the impedance curve at 503°C. The high frequency arc, which peaks around 1Khz for the response at 502°C and has a capacitance of the order of 10^{-4} $\Omega^{-1}cm^{-2}$, is due to the ionic oxygen charge transfer at the electrode/electrolyte interface. The high frequency semicircle could not be resolved at low temperatures. As the temperature increased, the high frequency arc became distinctively separated from the low frequency semicircle. The low frequency arc, which peaks around 2hz for the response at 502°C and has a capacitance of the order of 10^{-5} $\Omega^{-1}cm^{-2}$, is due to exchange and diffusion of non-charge oxygen in the electrode. The inductance effect due to the measurement leads at high frequency is shown for the response at 503°C.

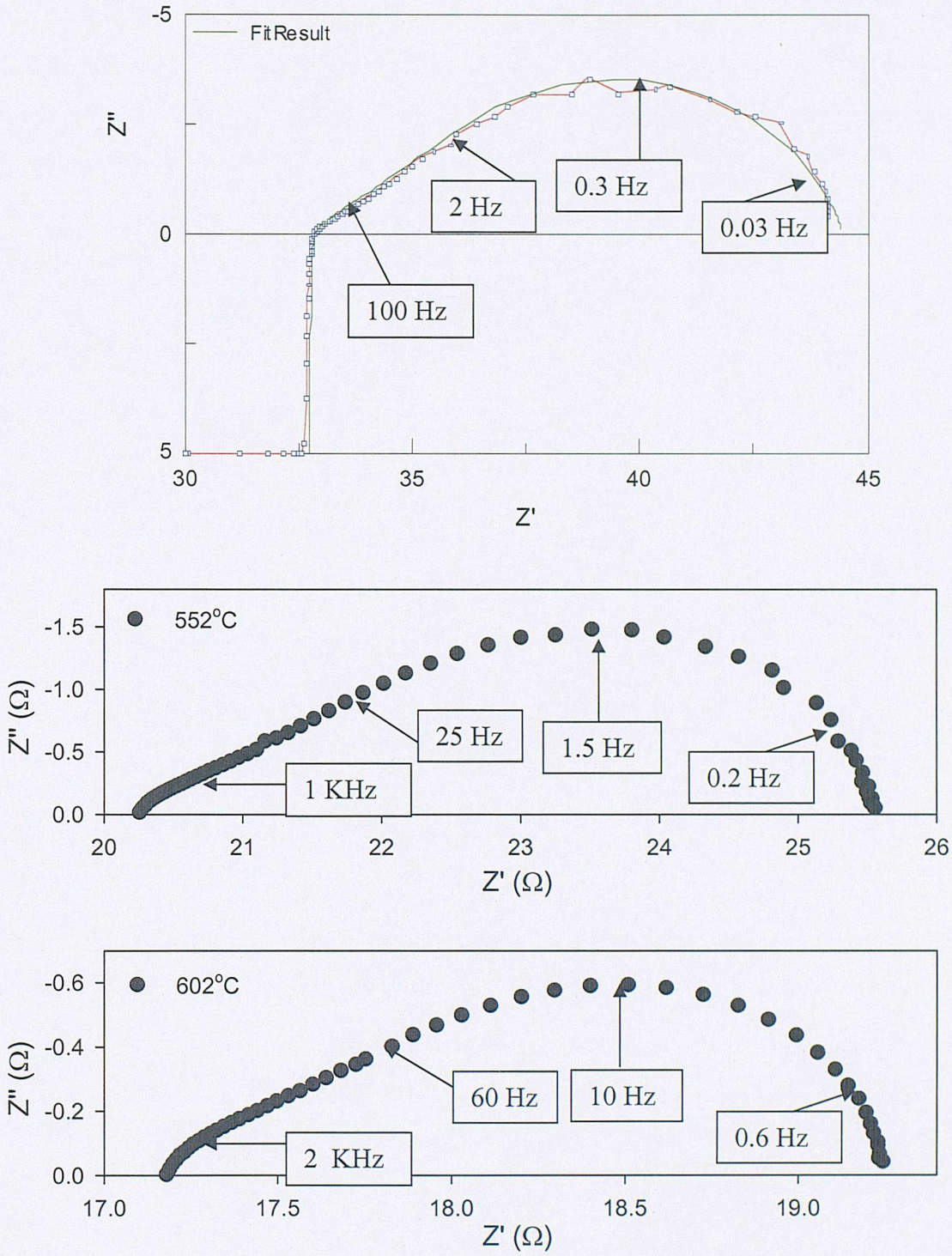


Figure 6.7.11: AC Impedance Spectroscopy spectra of CGO20-80/GSC composite cathode on an as sintered CGO10-90 electrolyte at various temperatures

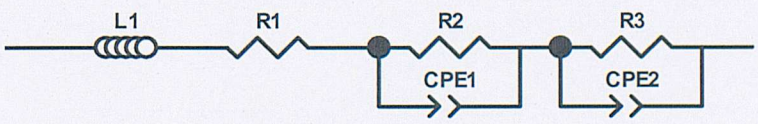


Figure 6.7.12: Equivalent circuit model

Figure 6.7.13 shows the normalized AC impedance spectra of this cathode at 503°C, 552°C and 602°C. It can be noted that the high frequency semicircle becomes more distinguishable with increase in temperature, however there is no difference in the low frequency component.

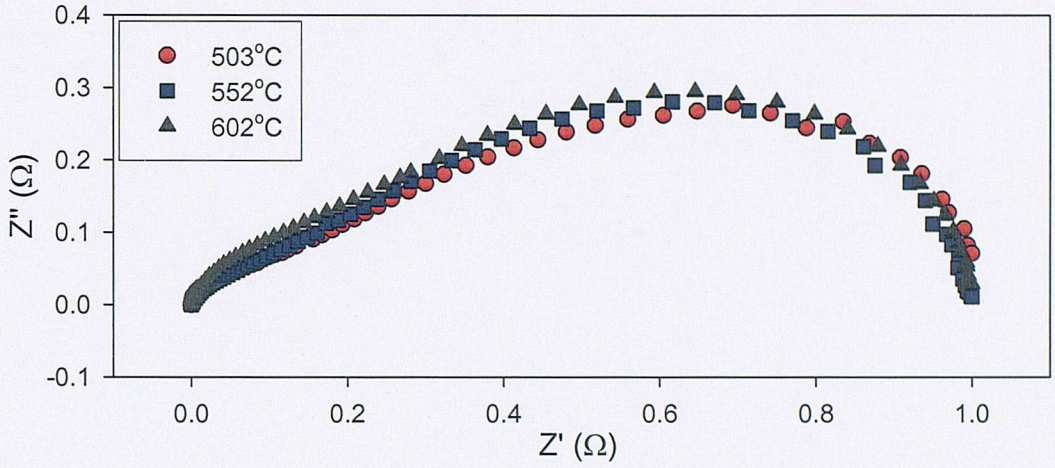


Figure 6.7.13: Normalized AC Impedance Spectroscopy spectra of CGO20-80/GSC composite cathode on an as sintered electrolyte at various temperatures

The area specific resistance (ASR) value for this cathode was found to be 4.18 $\Omega.cm^2$ at 502°C, 1.77 $\Omega.cm^2$ at 553°C and 0.74 $\Omega.cm^2$ at 602°C. These values are 5 times lower than those of CGO/LSCF/carbon conducted under the same conditions. The ASR of the CGO20-80/GSC electrode on a CGO10-90 electrolyte is shown as Arrhenius plot (Figure 6.7.14) against the reciprocal of temperature in order to determine the activation energy for the electrode response. The activation energy for CGO20-80/GSC composite cathode is found to be 1.09 ev ±0.18ev. This value is very similar with that obtained by averaging the activation energy of tracer diffusion coefficient for CGO, $E_a^{D^*}$ is 0.9 ev **[10]** and the activation energy of the surface exchange coefficient for SSC, E_a^{k} is also 0.9 ev **[27]**. Although the value obtained is slightly higher that of predicted, this is because we assume here that GSC have similar properties to SSC and we use the D* and k value of SSC for the GSC.

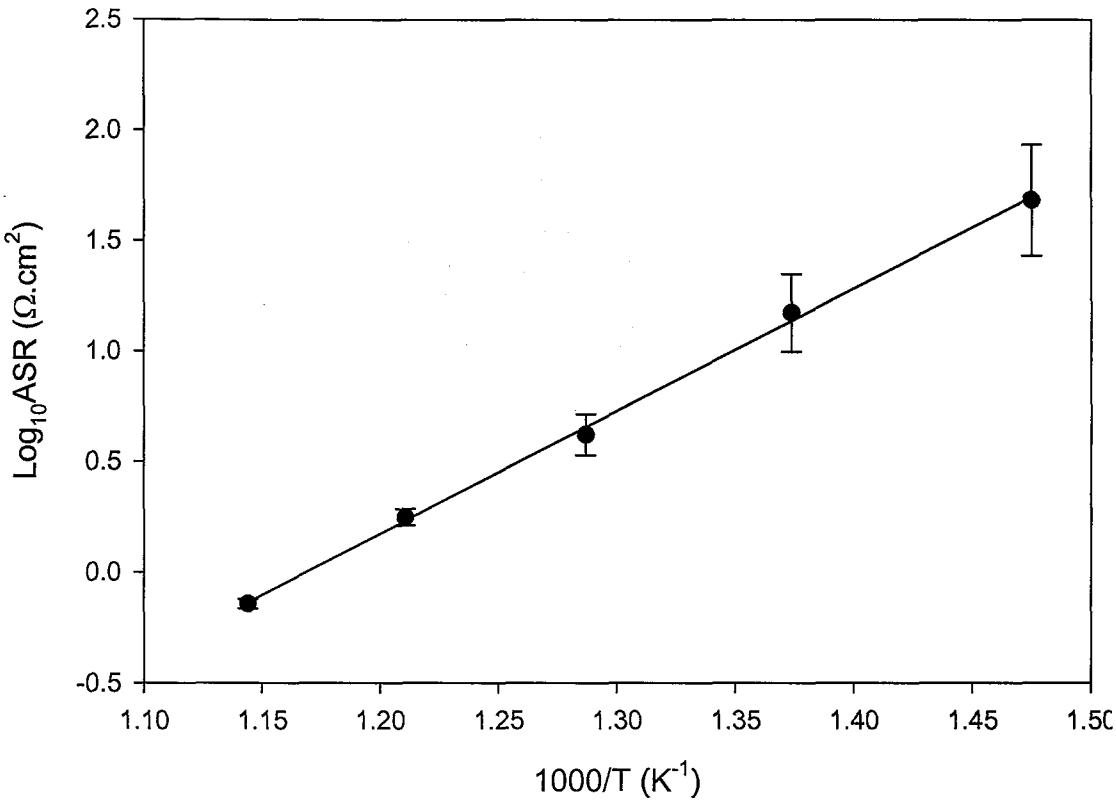


Figure 6.7.14: Arrhenius plot of the CGO20-80/GSC composite cathode on an as sintered CGO10-90 electrolyte

6.7.5.2 CGO/GSC on a cleaned electrolyte

Figure 6.7.15 shows the AC impedance spectra of CGO20-80/GSC composite coated onto a cleaned CGO10-90 electrolyte pellet and then sintered in air at 1050°C. The responses of the CGO20-80/GSC on an as sintered electrolyte are also included for comparison. Here also two overlapping semicircles can be resolved at 503°C, 551°C and 602°C using the equivalent circuit model in Figure 6.7.12. The shape of these responses looks identical to those produced by the CGO/GSC on an as sintered electrolyte. Also it can be noted that the high frequency arc decreased in size (polarization resistance decreased) for the CGO20-80/GSC electrode on a cleaned electrolyte, when compared to it on an as sintered electrolyte. The offset of the CGO20-80/GSC on a cleaned electrolyte response has also shifted to lower impedance, when compared to the offset of the CGO20-80/GSC on an as sintered electrolyte response.

The ASR values for this cathode was found to be 3.47 $\Omega.cm^2$ at 503°C, 1.29 $\Omega.\ cm^2$ at 553°C and 0.56 $\Omega.cm^2$ at 602°C. There is no significance difference in the values from that obtained with a CGO20-80/GSC on an as sintered electrolyte.

Area specific resistances of the CGO20-80/GSC electrodes are shown as Arrhenius plot in Figure 6.7.16. A single slope again implies that the same reaction mechanism controls the overall electrode behaviour in the temperature range studied. The activation energy was calculated from the graph as 1.05 ev ±0.18ev.

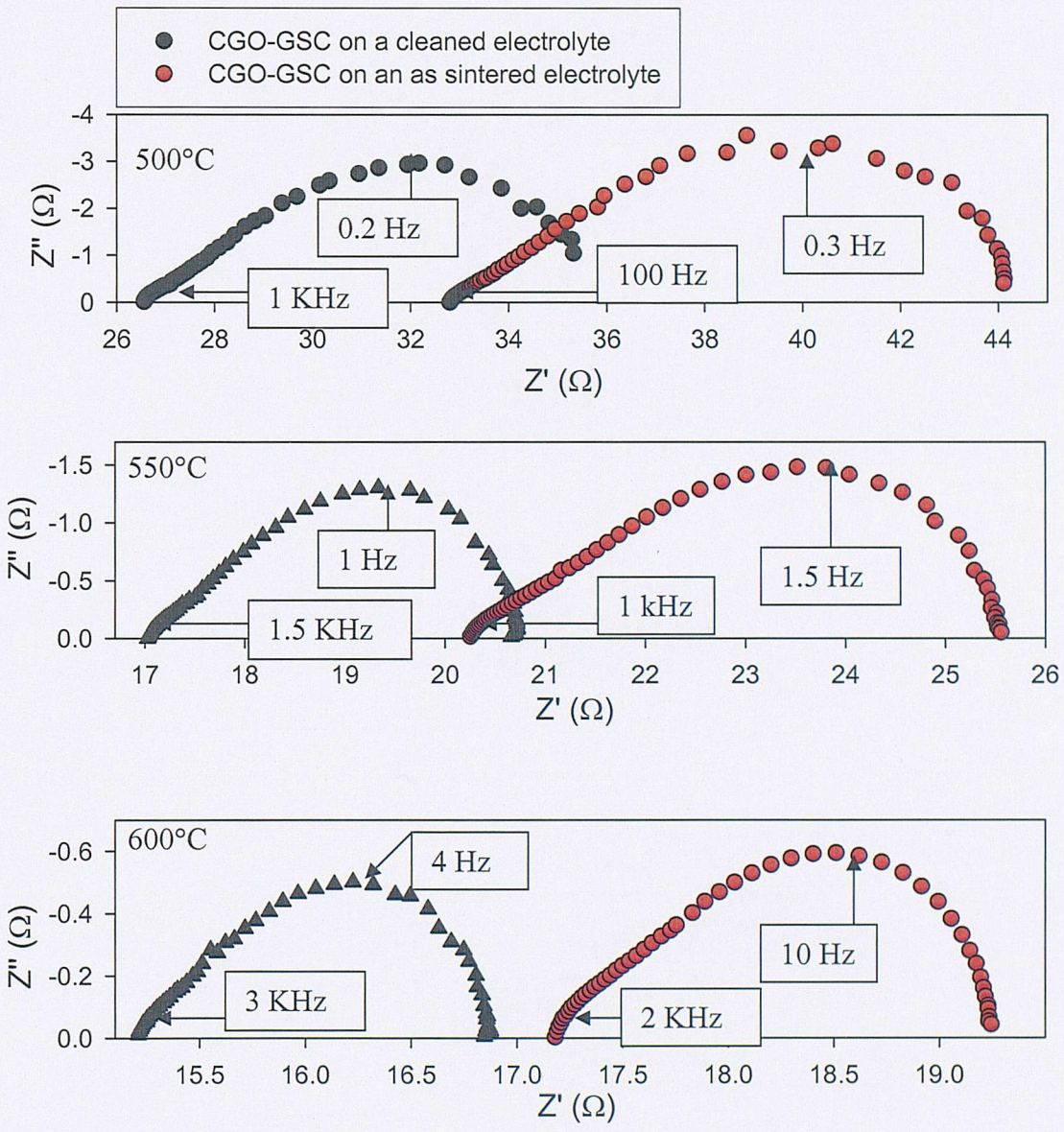


Figure 6.7.15: AC Impedance Spectroscopy spectra of CGO20-80/GSC composite cathode on a cleaned CGO10-90 electrolyte at various temperatures

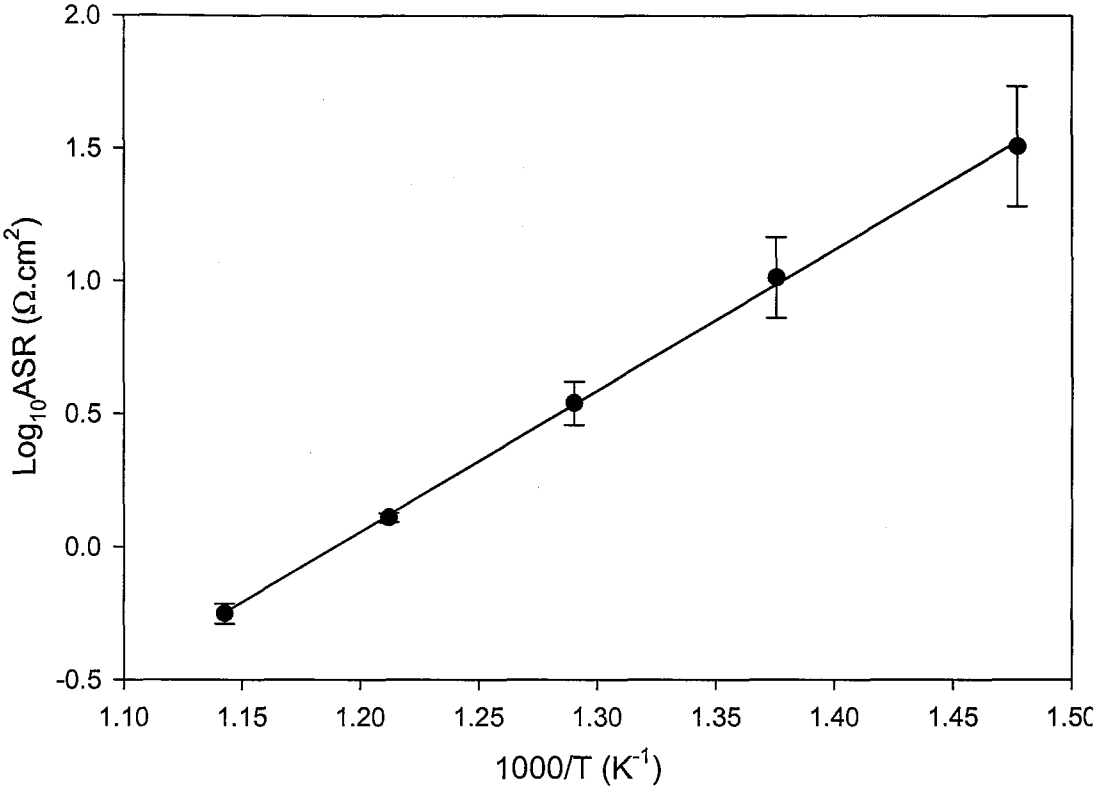


Figure 6.7.16: Arrhenius plot of the CGO20-80/GSC composite cathode on a cleaned CGO10-90 electrolyte

6.7.5.3 CGO/GSC on a cleaned electrolyte and iso-pressed

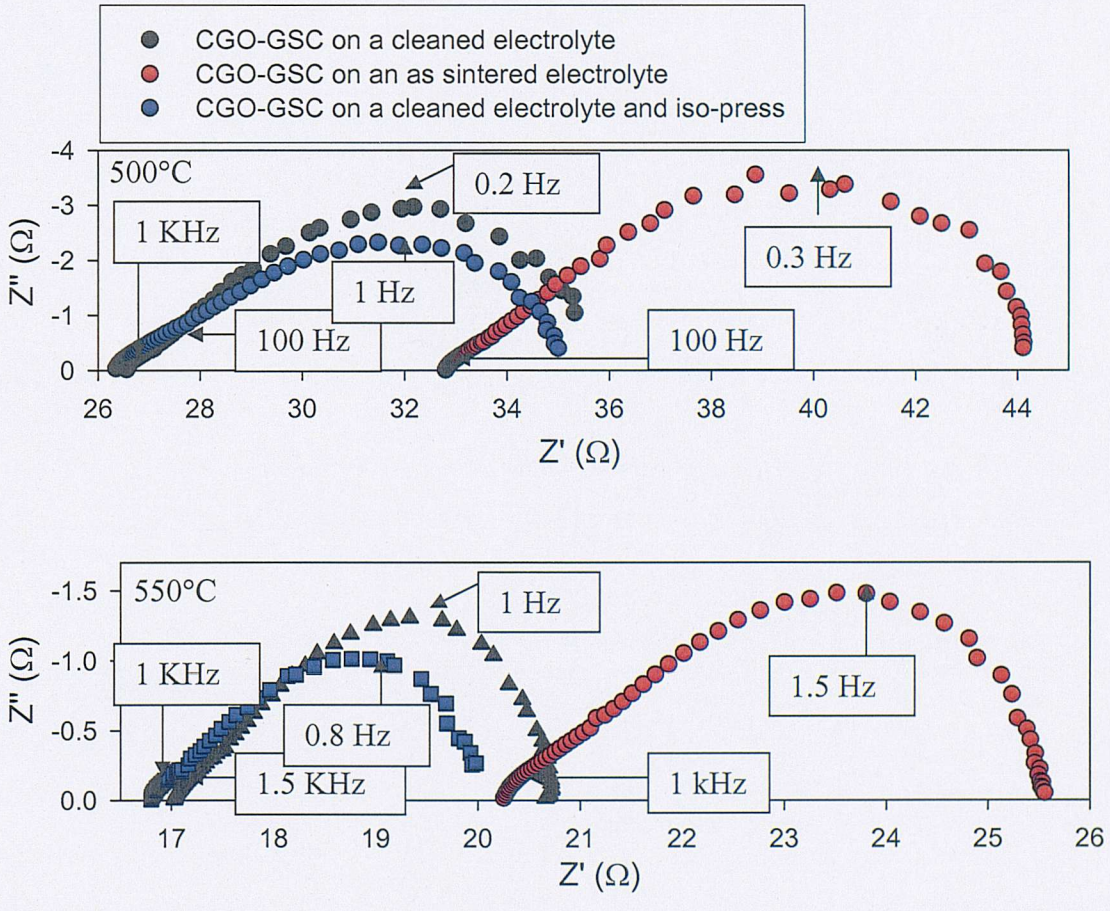
AC impedance spectra of CGO20-80/GSC cathode on a cleaned CGO10-90 electrolyte and iso-statically pressed before sintering at 1050°C in air is shown in Figure 6.7.17. The impedance responses of the CGO20-80/GSC on an as sintered and CGO20-80/GSC on a cleaned electrolyte is also included for comparison. The shape of all three responses at each temperature looks very similar. The equivalent circuit that most closely reproduced the impedance characteristics of the CGO/GSC on a cleaned electrolyte and iso-statically pressed is shown in Figure 6.7.12. The model implies that two depressed semicircles can be resolved for these impedance curves too. The offset of the CGO20-80/GSC on a cleaned electrolyte response and the CGO20-80/GSC on a cleaned electrolyte and iso-statically pressed response appears to occur at a similar point.

	500°C	550°C	600°C
CGO/GSC on an as sintered electrolyte	4.18 Ωcm^2	1.77 Ωcm^2	0.72 Ωcm^2
CGO/GSC on a cleaned electrolyte	3.47 Ωcm^2	1.29 Ωcm^2	0.56 Ωcm^2
CGO/GSC on a cleaned electrolyte and iso-pressed	3.20 Ωcm^2	1.16 Ωcm^2	0.41 Ωcm^2

Table 6.1.5:- ASR of all the CGO20-80/GSC at various temperatures

This electrode had respectively at 503.5°C an ASR of 3.2 $\Omega.cm^2$, 1.16 $\Omega.cm^2$ at 553°C and 0.41 $\Omega.cm^2$ at 602°C. These ASR values are only slightly lower than those obtained with the CGO20-80/GSC on a cleaned electrolyte as can be seen in Table 6.1.5.

The area specific resistance (ASR in $\Omega.cm^2$) in air as a function of reciprocal of temperature for this composite cathode is shown as Arrhenius plot in Figure 6.7.18. The activation energy for CGO20-80/GSC composite cathode is found to be 1.07 ev ±0.18ev.



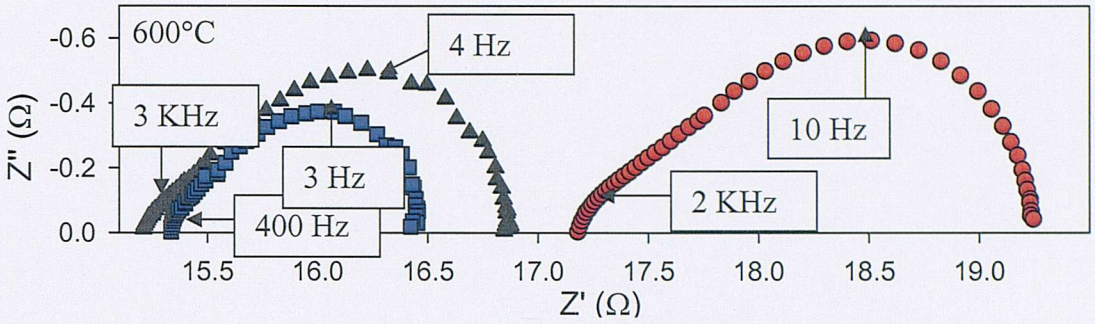


Figure 6.7.17: AC Impedance Spectroscopy spectra of CGO20-80/GSC composite cathode on a cleaned CGO electrolyte and iso-statically pressed

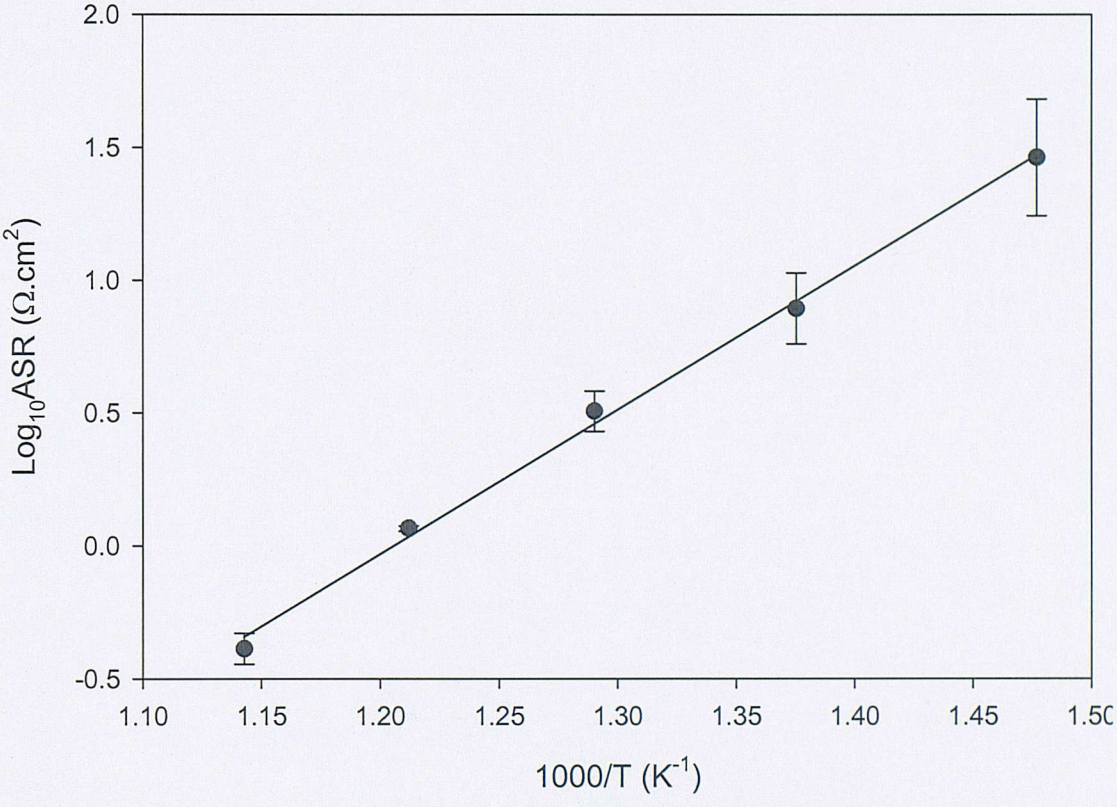


Figure 6.7.18: Arrhenius plot of the CGO20-80/GSC composite cathode on a cleaned CGO10-90 electrolyte and iso-statically pressed

6.7.6 Comparison with Adler Model

The cathode polarisation resistance was compared to the continuum approach for porous electrodes proposed by Adler et al. Here we assume that a composite behaves macroscopically as a single phase mixed conducting material, and used the D* value of the ionically conducting phase, CGO and the k value of the mixed-conducting phase,

GSC. Also we assume that the GSC has the same properties as $Sm_{0.5}Sr_{0.5}CoO_3$ (SSC) and use the same k value of SSC for GSC. Hence if the values of the surface exchange coefficient for SSC taken from the data of Fullarton et al **[6]** and oxygen diffusion coefficient for CGO taken from Steele et al **[15]** are substituted into the following three equations:

$$R_{chem} = \left[\frac{RT}{2F^2}\right]\sqrt{\frac{\tau}{(1-\varepsilon)aC_o{}^2 D^* K}}$$

together with the value of a = 20000 cm^2/cm^3 **[15]**, the porosity (42%) and the tortuosity (estimated at 1.5 from the FIB-SIMS image) then a R_{chem} (ASR) values can be generated at different temperatures. The porosity was measured from a separately made cathode pellet, which was sintered at 1050°C. Generated R_{chem} values at different temperatures for CGO/GSC using the model is shown together along with the experimental ASR values of CGO20-80/GSC cathode produced under different conditions in Figure 6.7.19. The best measured CGO/GSC ASR values of 3.20 $\Omega.cm^2$ at 503.5°C, 1.16 $\Omega.cm^2$ at 553°C and 0.41 $\Omega.cm^2$ at 602°C is three times greater than the predicted values of 1.24 $\Omega.cm^2$ at 500°C, 0.51 $\Omega.cm^2$ at 550°C and 0.15 $\Omega.cm^2$ at 600°C.

It is also very important to note that the calculated data is not a fit to the experimental data using electrical equivalent circuits, which is most commonly seen in the literature. This is a response calculated from entirely independent data obtained from diffusion measurements (literature) and knowledge of the microstructure of the material from microscopy.

Regarding the Arrhenius plot below, it is noticeable that the predicted and measured activation energies are very close. CGO20-80/GSC composite materials exhibited activation energy in the range 1.05-1.09 ev ±0.18ev, which is slightly higher than the model's activation energy (0.88 ev) and also the activation energy obtained by averaging the diffusion coefficient activation energy of CGO ($E_a^{D^*}$ = 0.9 ev) and the surface exchange coefficient activation energy of GSC (E_a^{k} = 0.9 ev).

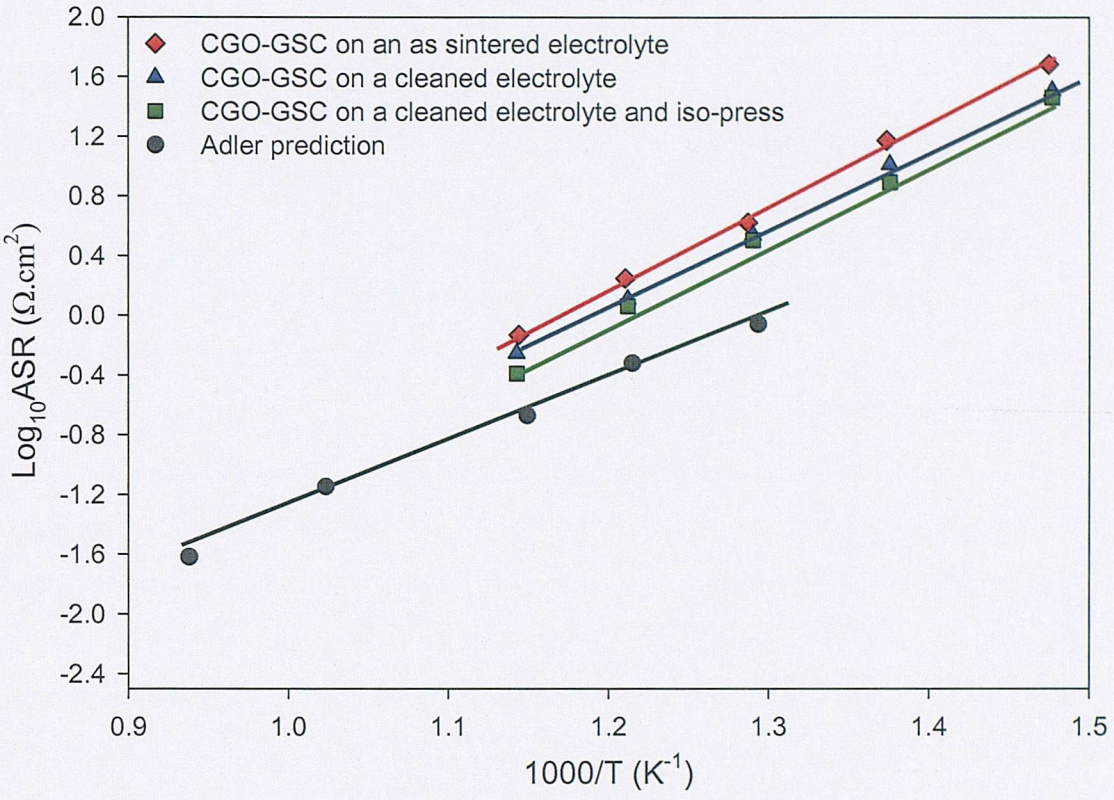


Figure 6.7.19: Comparison of the measured impedance and that predicted by Adler's model

The differences between the experimental and predicted ASR values can be attributed to several factors. First there is a lack of accuracy in the estimation and measurement of the microstructural parameters. Indeed porosity was calculated using Archimedes principle, which is accurate, however tortuosity that is estimated varies in the literature between 1.5 and 2.5. There is no accurate measurement to measure the tortuosity in an electrode. Secondly we assumed that a composite behaves macroscopically as a single phase mixed conducting material, and we used the D* value of the CGO and k value of the GSC, however uncertainty still remains about which processes occurs at which phases and comparing composite cathode behaviour with that of a single-phase MIEC.

6.8 CGO/SSC

6.8.1 Powder Characterisation

$Sm_{0.5}Sr_{0.5}CoO_3$ (SSC) powders were prepared by glycine-nitrate method **[40]**. Stoichiometric amount of $Sm(NO_3)_3.6H_2O$, $Sr(NO_3)_2$ and $Co(NO_3)_2.6H_2O$ were dissolved in distilled water to form an aqueous solution, to which glycine (0.5 mol glycine per mol NO_3^-) was then added in solid state. Combustion of the metal nitrate/glycine solution was subsequently performed in glass beakers on a hotplate. The precursors were heated to evaporate excess water, yielding a red viscous liquid. Further heating caused the viscous liquid to autoignite, resulting in rapidly and self-sustaining combustion. The resultant black ash was then collected and heated in air at 800°C for 2 hours to remove the carbon residue and to convert it to the desired $Sm_{0.5}Sr_{0.5}CoO_3$ phase of perovskite structure. This was then measured by X-ray diffraction to study the structural and purity properties of the perovskite.

The XRD pattern of the resultant SSC powder is shown in Figure 6.8.1. No peak corresponding to any impurity is observed. All the peaks are very sharp showing the crystalline nature of the powders. The Bragg peaks were identified using the file $La_{0.5}Sr_{0.5}CoO_3$ (JCPDS 48-122). The obtained XRD patterns of the SSC powder produced by glycine-nitrate method studied at room temperature were fitted to a cubic perovskite structure using the software celref. The lattice parameters were extracted as 3.8042 (± 0.0004) Å.

Figure 6.8.2 shows the X-ray spectra of the composite CGO20-80/SSC cathode calcined at 1000°C for 2 hours. All the Bragg peaks from CGO20-80 and SSC could be matched and no secondary phase can be found.

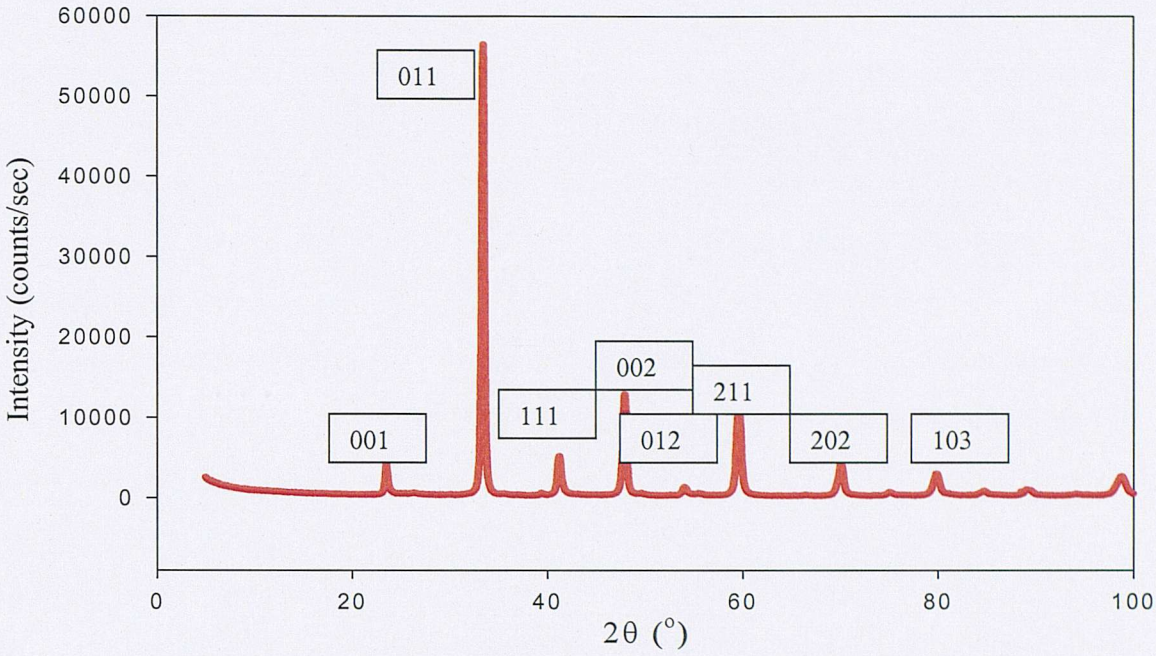


Figure 6.8.1: X-ray diffraction pattern of $Sm_{0.5}Sr_{0.5}CoO_{3-\delta}$ using Cu-K_α radiation ($\lambda = 1.5406$ Å)

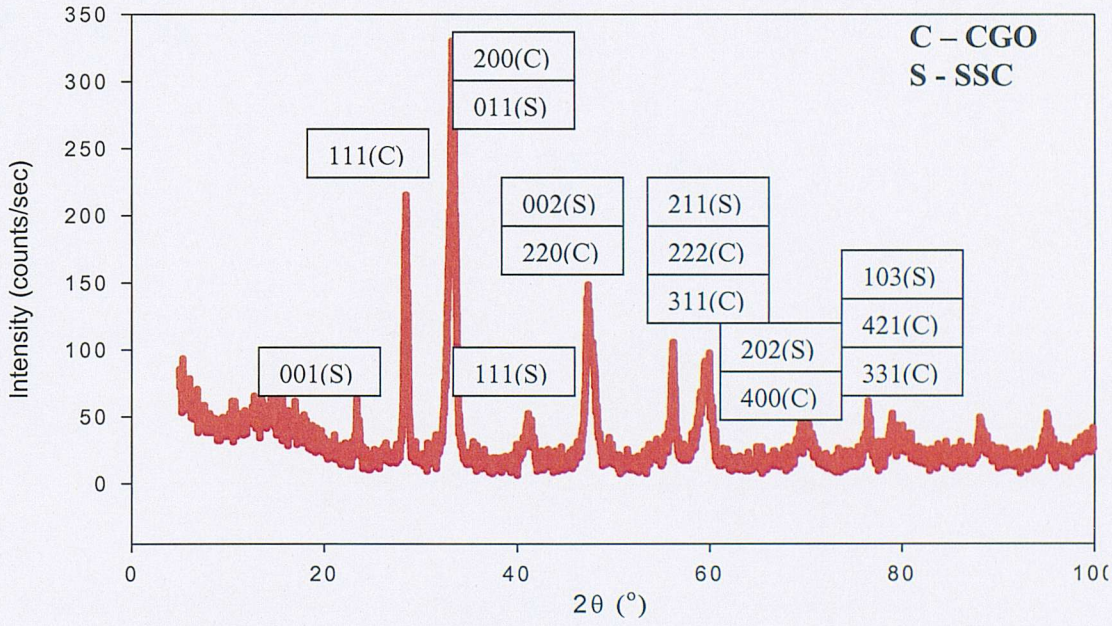


Figure 6.8.2: X-ray diffraction pattern of $Ce_{0.8}Gd_{0.2}O_{2-\delta}/Sm_{0.5}Sr_{0.5}CoO_{3-\delta}$ composite using Cu-K_α radiation ($\lambda = 1.5406$ Å)

6.8.2 Sintering Studies

Figure 6.8.3 shows the change in length versus temperature data obtained from a dilatometer during the sintering of green powder compacts of CGO20-80/SSC cathode. The onset of shrinkage for this composite commences around 1000°C, which is about 200°C higher than that occurs in the CGO/LSCF composite cathode. This reflects in the higher percentage of porosity seen with the CGO/SSC cathode when sintered at 1050°C, and hence there was no need for the addition of pore former. There are inflections in the sintering curve between the room temperature and the onset of shrinkage. The small dip in the curve between the room temperature and 200°C is due to the expansion of the sample holder during heating. The rise in the curve between 200°C and the onset of shrinkage is due to the small expansion of the material. Therefore the increase in the curves between these points does not suggest a change in the sintering mechanism. The absence of plateau at high temperature indicates that full density had not been achieved.

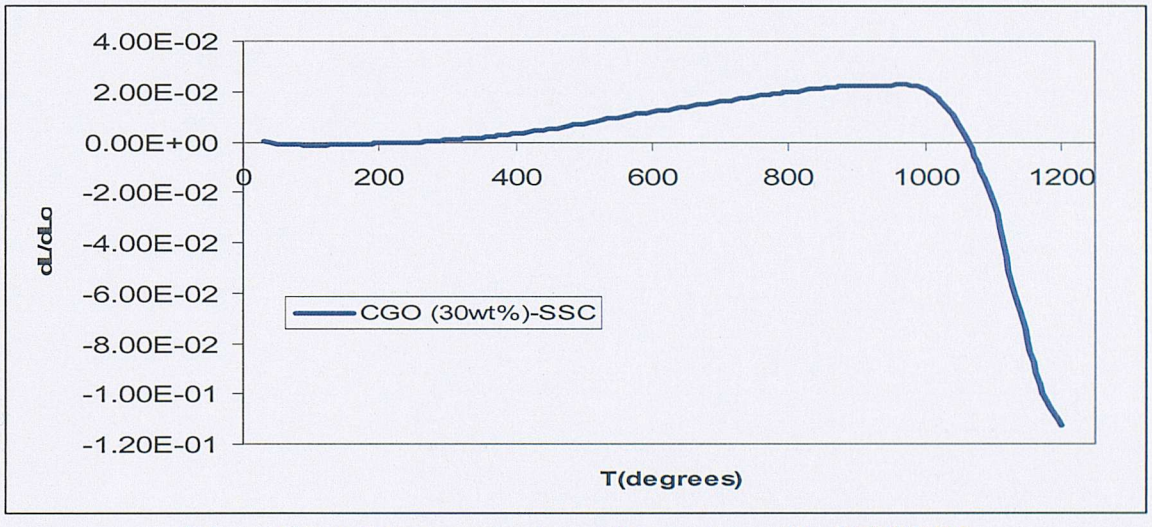


Figure 6.8.3: **Dilatometry trace for a composite *CGO/SSC***

6.8.3 Microstructural Studies by SEM

Figures 6.8.4 shows a secondary electron image of an unpressed CGO 20-80/SSC cathode sintered at 900°C for 2 hours. The high level of agglomeration, 1-2μm in size, with high level of interconnected porosity is distinguishable. Many isolated grains (grain size of ≈ 0.5 μm) in the cathode layer touching neighbouring grains can be identified.

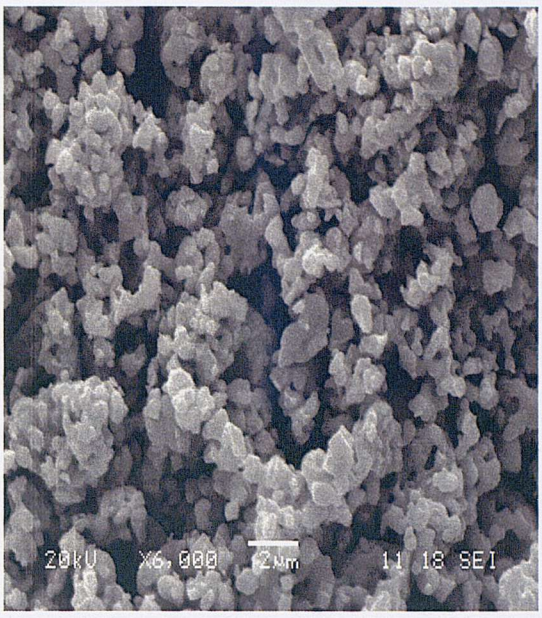


Figure 6.8.4:- SEM micrograph of CGO-SSC, sintered at 900 ℃

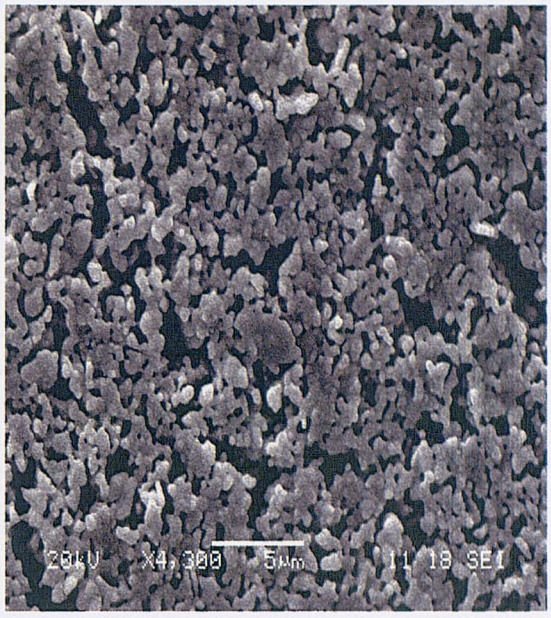


Figure 6.8.5:- SEM micrograph of CGO-SSC, sintered at 1050 ℃

The micrographs of unpressed and iso-statically pressed CGO 20-80/SSC cathode layer sintered at 1050°C for 2 hours at lower and higher magnification are shown in Figure 6.8.5 and 6.8.6. This indicates that neck formation had occurred between adjacent particles, and there was evidence that smaller particles had coalesced to form larger aggregates. Furthermore, the grains remained small in size of around 0.5-4 μm. There was a high level of interconnected porosity. Hence the sintering of iso-statically pressed CGO 20-80/SSC cathode at 1050°C for 2 hours resulted in a structure with high level of porosity (using Archimedes principle the porosity was calculated to be 45%) that was connected with by narrow bottleneck-type bridges. In all three micrographs highly porous electrodes are distinguishable with pore diameters between 1-10 μm. The percentage of porosity in this composite was calculated to be around 40% at 1050°C. Also like GSC, SSC did not need a pore former to enhance porosity. It had sufficient porosity when the material was sintered at 1050°C.

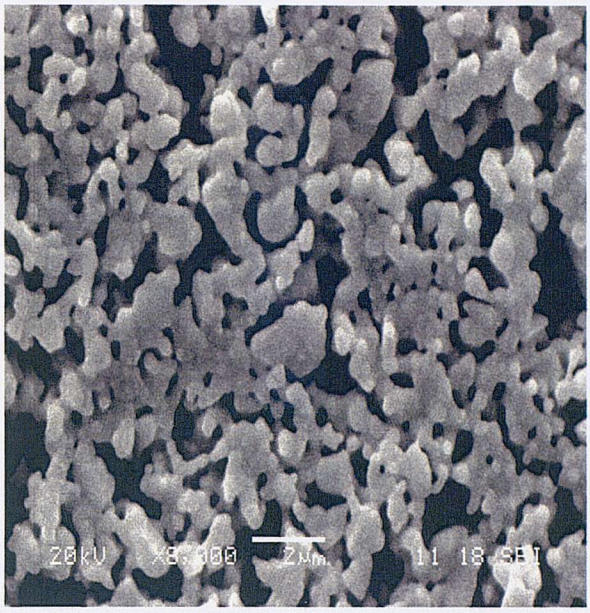


Figure 6.8.6:- SEM micrograph of CGO-SSC, sintered at 1050 ℃. Iso-statically pressed

SEM images of the resulting electrode/electrolyte interface structures of iso-statically pressed CGO20-80/GSC half-cells that were tested are shown in Figure 6.8.7. Fine microstructure of highly porous electrodes sprayed onto a dense electrolyte is apparent. The electrode microstructure also looks uniform with a very good bonding and continuous contact at the interface between the electrode and the dense electrolyte pellet. The electrodes showed good adherence to the electrolyte because of the similar thermal expansion between the two materials. The thickness of the electrode layer in both the micrographs were found to be around 15 μm.

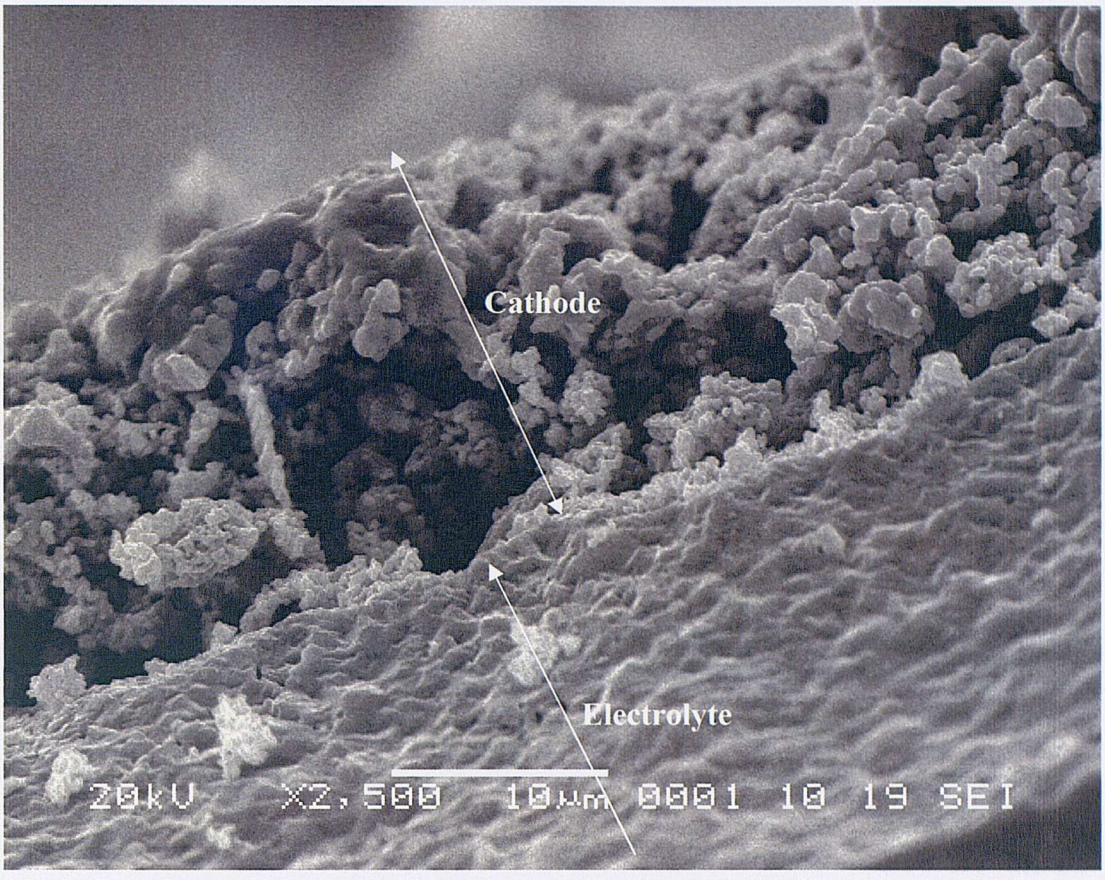


Figure 6.8.7:- SEM micrograph of the cross-section of CGO-SSC onto a CGO electrolyte, iso-statically pressed and sintered at 1050 ℃

6.8.4 Microstructural Studies by FIB-SIMS

Figure 6.8.8 and 6.8.9 shows the focused ion beam (FIB) image of the surface and the cross-section of the CGO20-80/LSCF composite cathode applied on a CGO10-90 pellet. The surface microstructure (Figure 6.8.8 (A)) of the cathode sintered after 1050°C for 2 hours showed a very uniform microstructure with reasonable porosity and all the grains are connected with by narrow bottleneck-type bridges. Figure 6.8.8 (B) shows the same area after a rectangular crater of 20 µm in depth, 30 µm in length and 10 µm in width was produced on the surface of the cathode by a lower current ion beam, and then polished by a lower current ion beam to give a smoother surface for better resolution image. Figure 6.8.9 shows the inside of a trench after having tilted the stage at an angle of 30°. The highly porous cathode and a very dense electrolyte are visible. The particles appeared layered and this was attributed to the number of sprayed layers (in this case about 5-6 sprayed layers). The thickness of the cathode was found to be around 15-17 µm.

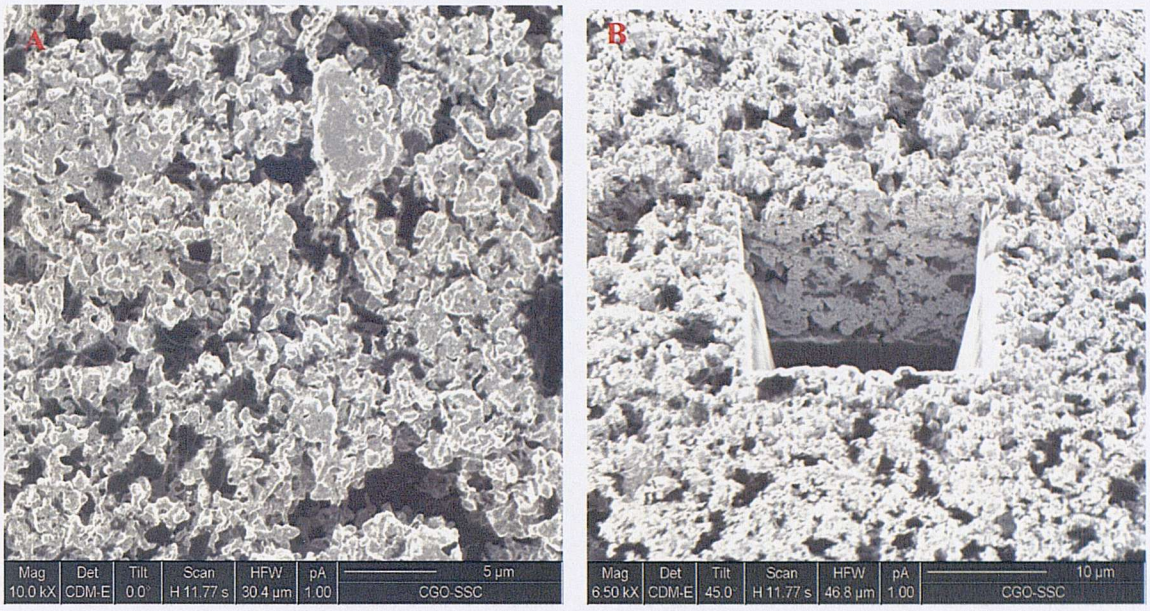


Figure 6.8.8:- (A) Focused ion beam image (FIB) of the surface of a CGO20-80/SSC composite cathode sintered at 1050 ℃. (B) Focused ion beam image (FIB) of the top view of an ion-milled crater on the surface of the cathode (30kev Ga^{+} primary bombardment).

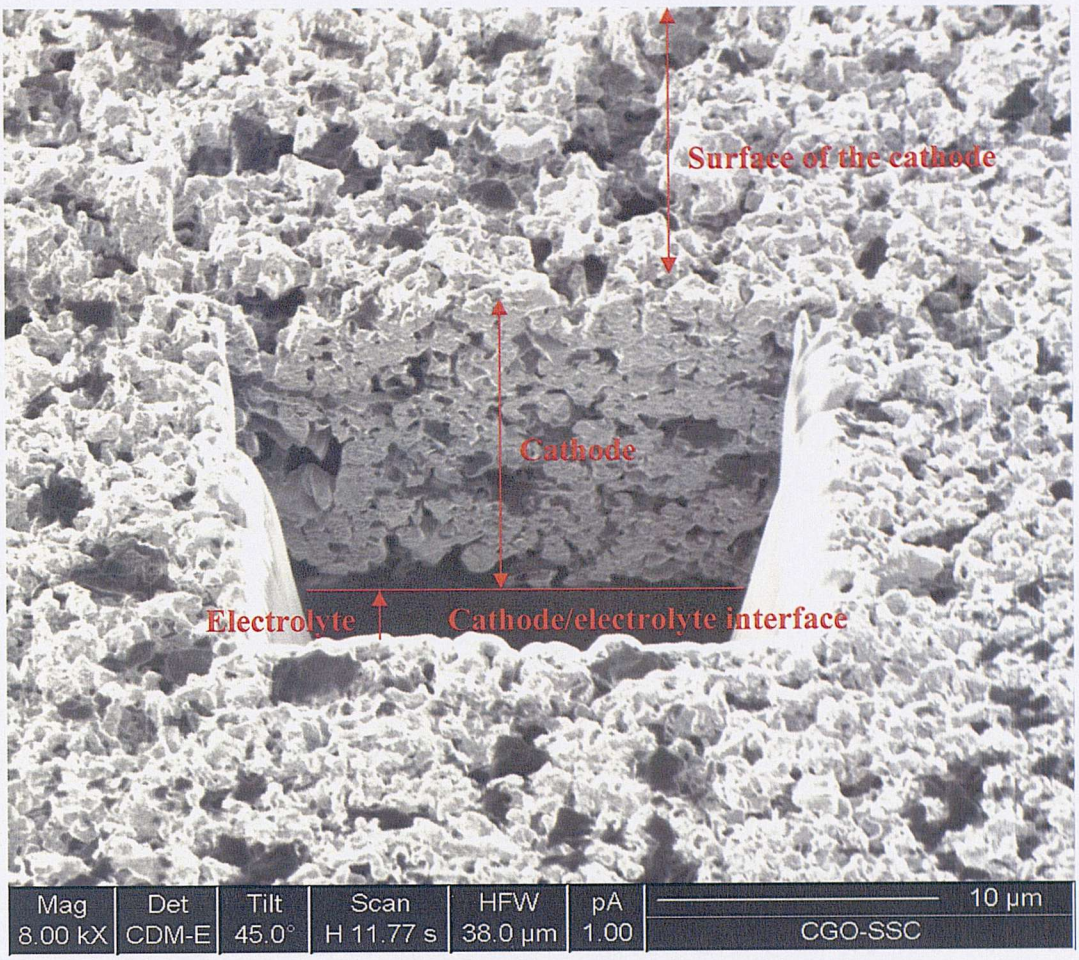


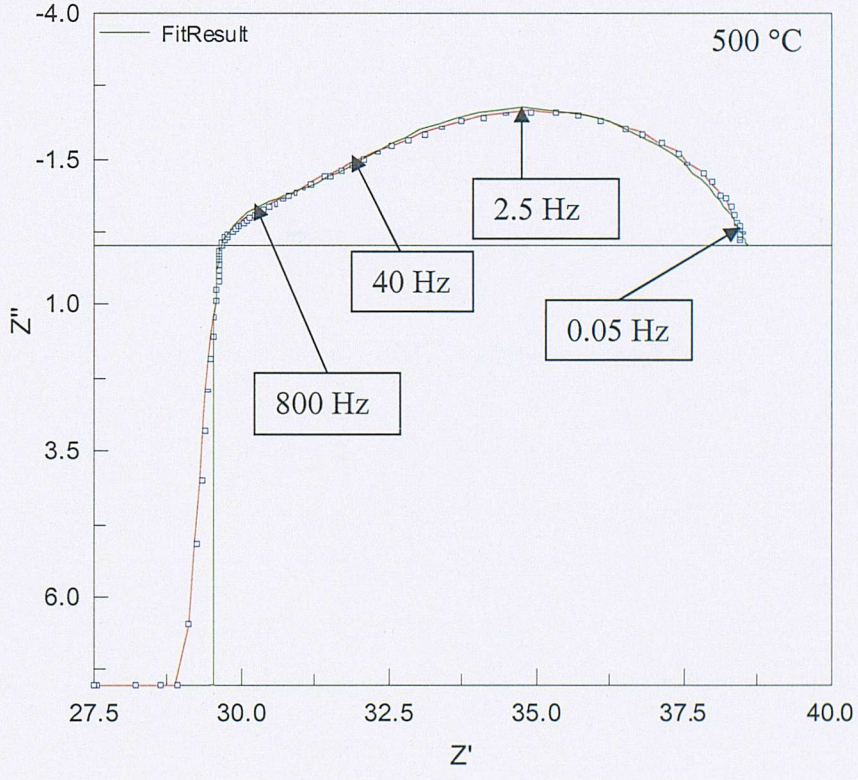
Figure 6.8.9:- Focused ion beam image (FIB) of an ion-milled crater after tilting at 30° ((30kev Ga+ primary bombardment)

6.8.5 Electrochemical Performance

6.8.5.1 CGO/SSC on an as sintered electrolyte and iso-pressed

The electrode polarization resistance for symmetrical $Ce_{0.8}Gd_{0.2}O_2$ (CGO20-80)/$Sm_{0.5}Sr_{0.5}CoO_3$ (SSC) electrodes on a $Ce_{0.9}Gd_{0.1}O_2$ (CGO10-90) electrolyte was measured using AC impedance spectroscopy, applying a 20mV alternating signal with zero DC bias. A frequency sweep from 0.01 Hz to 10 MHz was used and the measurements were made in air. Typical AC impedance spectra of CGO 20-80/SSC (70 weight % SSC) composite coated onto an as sintered CGO10-90 electrolyte pellet and then sintered in air at 1050°C are shown in Figure 6.8.10. The electrode resistances were calculated from the differences between the low and high frequency intercepts of the electrode polarization arc.

All three impedance curves can be resolved into two overlapping semicircular arcs using the ZVIEW software. One semicircle is clearly distinguishable in all three spectra at low frequency and the other one at high frequency is not distinctively separated and became convoluted with the low frequency semicircle **[41]**. The equivalent circuit of the type LR(RQ)(RQ) that most closely fitted to all three data is shown in Figure 6.8.11. The inductance of the leads is calculated to be around 1.36×10^{-6} H.



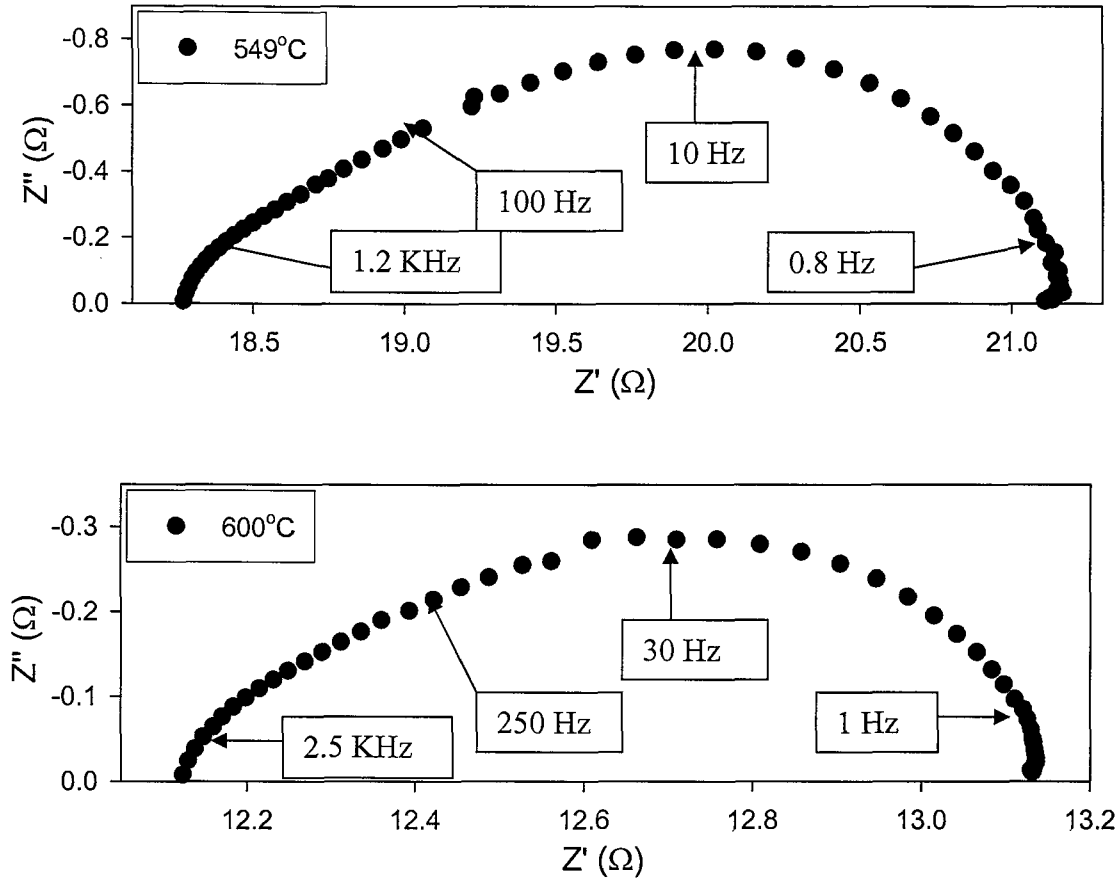


Figure 6.8.10: AC Impedance Spectroscopy spectra of CGO20-80/SSC composite cathode on an as sintered CGO10-90 electrolyte at various temperatures

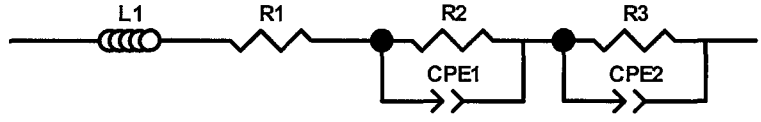


Figure 6.8.11: Equivalent circuit model

Figure 6.8.12 shows the normalized AC impedance spectra of the three temperature responses. It can be noted that the high frequency arc increases in size as the temperature is increased from 500°C to 600°C. This is because, the concentration polarization caused by the diffusion and exchange of oxygen species to the electrode/electrolyte interface, which contributes to the low frequency component only dominates at lower temperatures and decreases as the temperature increases and so the two arcs are more clearly seen at higher temperatures. The low frequency component looks very similar at all three temperatures.

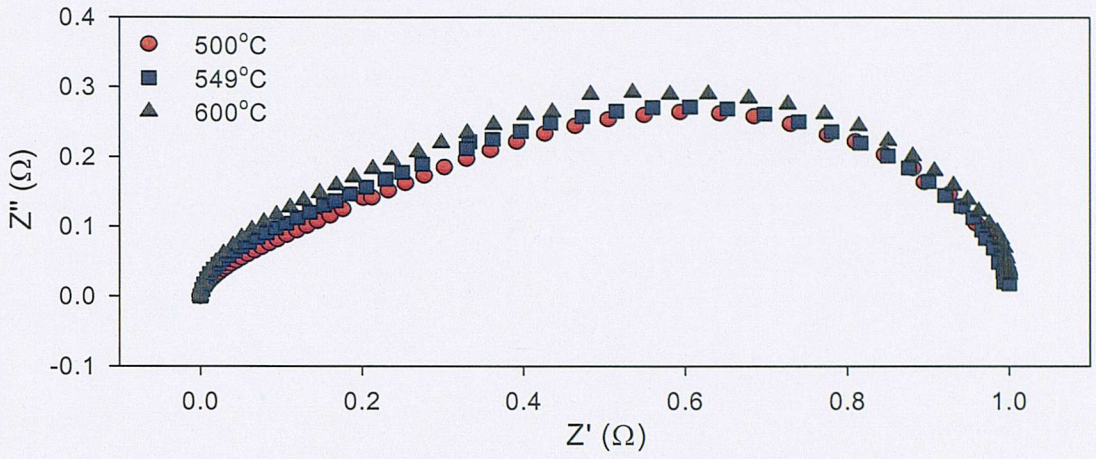


Figure 6.8.12: Normalized AC Impedance Spectroscopy spectra of CGO20-80/SSC on an as sintered CGO10-90 electrolyte at various temperatures

Area specific resistances of the CGO 20-80/SSC electrode on a CGO 10-90 electrolyte are shown as Arrhenius plot in Figure 6.8.13. The ASR value for this cathode was found to be 3.58 $\Omega.cm^2$ at 500°C, 1.20 $\Omega.cm^2$ at 549°C and 0.44 $\Omega.cm^2$ at 600°C. The activation energy for CGO 20-80/SSC composite cathode is found to be 1.21 ev ±0.15ev.

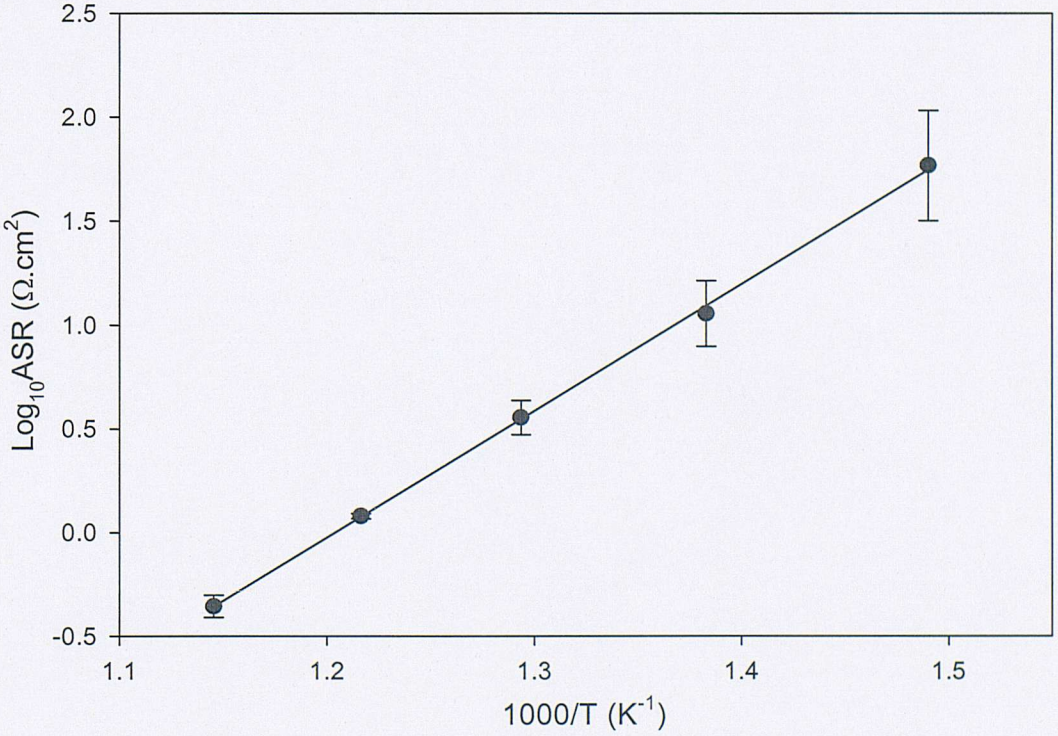


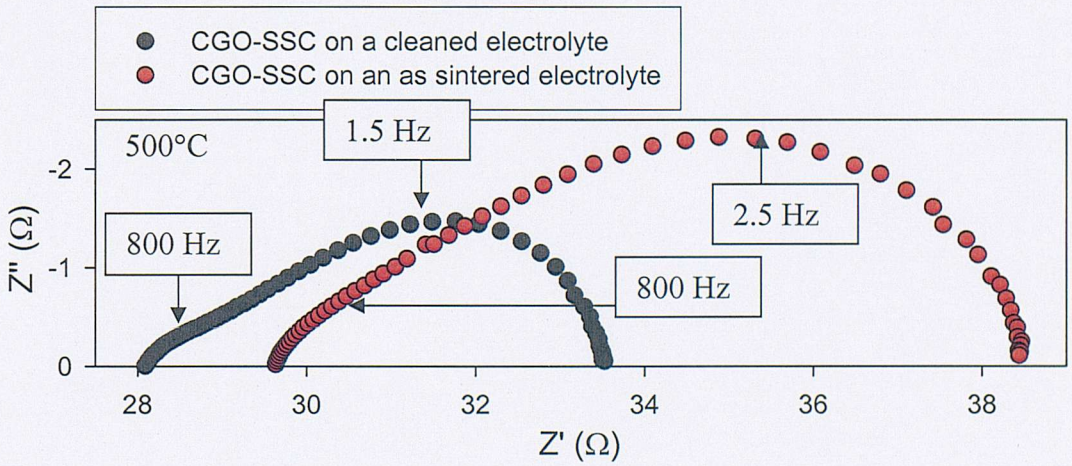
Figure 6.8.13: Arrhenius plot of the CGO20-80/SSC composite cathode on an as sintered CGO10-90 electrolyte

6.8.5.2 CGO/SSC on a cleaned electrolyte

Figure 6.8.14 shows typical AC impedance spectra of CGO20-80/SSC composite coated onto a cleaned CGO10-90 electrolyte pellet and then sintered in air at 1050°C, together with the responses of the CGO20-80/SSC on an as sintered electrolyte for comparison. It must be noted that the shape of the impedance response does not show a great difference between the CGO20-80/SSC on an as sintered electrolyte and a cleaned electrolyte. However the size of the high frequency arc response is smaller for the CGO20-80/SSC on a cleaned electrolyte than that of it on an as sintered electrolyte. Using the equivalent circuit model in Figure 6.8.11, the three impedance curves were resolved into two semicircles and each semicircle represents a reaction step with a different time constant. The low frequency arc was attributed to gaseous diffusion, while the high frequency arc, which flattened with decreasing temperature is generally attributed to charge transfer.

The ASR for this cathode was found to be 2.02 $\Omega.cm^2$ at 503°C, 0.64 $\Omega.cm^2$ at 550°C and 0.24 $\Omega.cm^2$ at 602°C. The area specific resistance of a CGO20-80/SSC on a cleaned electrolyte shows a significance difference from that of a CGO20-80/SSC on an as sintered electrolyte. These results are about 2 times lower than the ASR values obtained for the cathode on an as sintered electrolyte.

Area specific resistances (ASR) of the CGO20-80/SSC electrode on a CGO10-90 electrolyte is shown as Arrhenius plot in Figure 6.8.15. The activation energy for CGO20-80/SSC composite cathode is found to be 1.25 ev ±0.15ev.



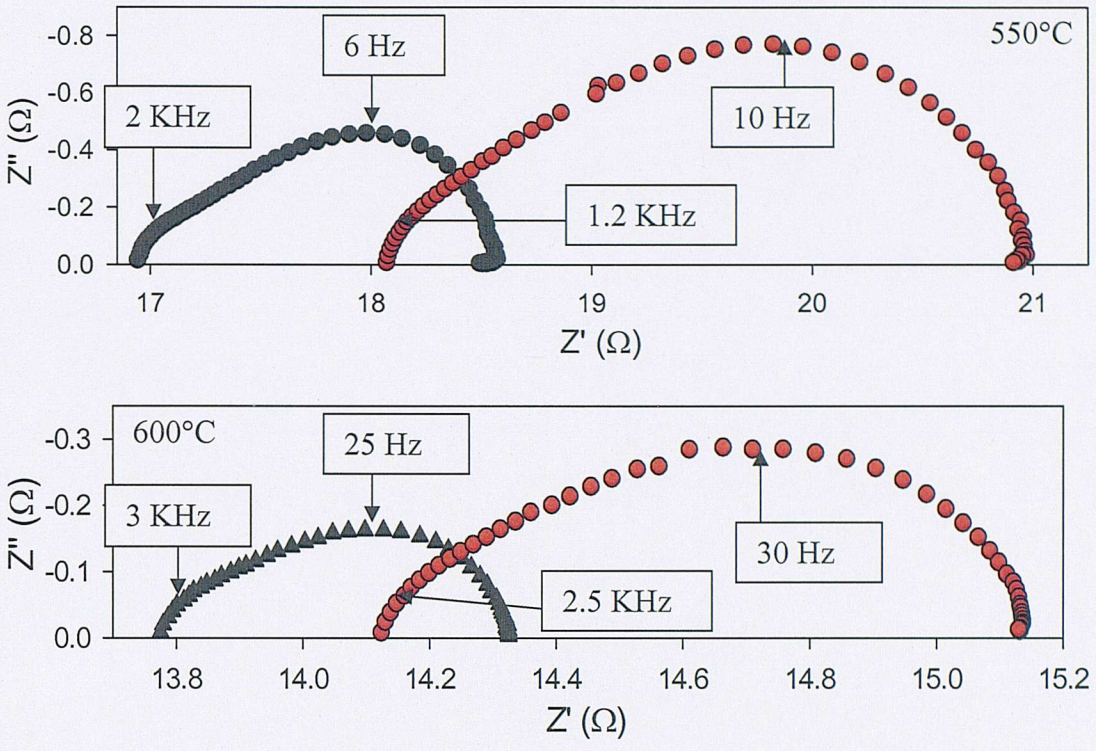


Figure 6.8.14: AC Impedance Spectroscopy spectra of CGO20-80/SSC composite cathode on a cleaned CGO10-90 electrolyte at various temperatures

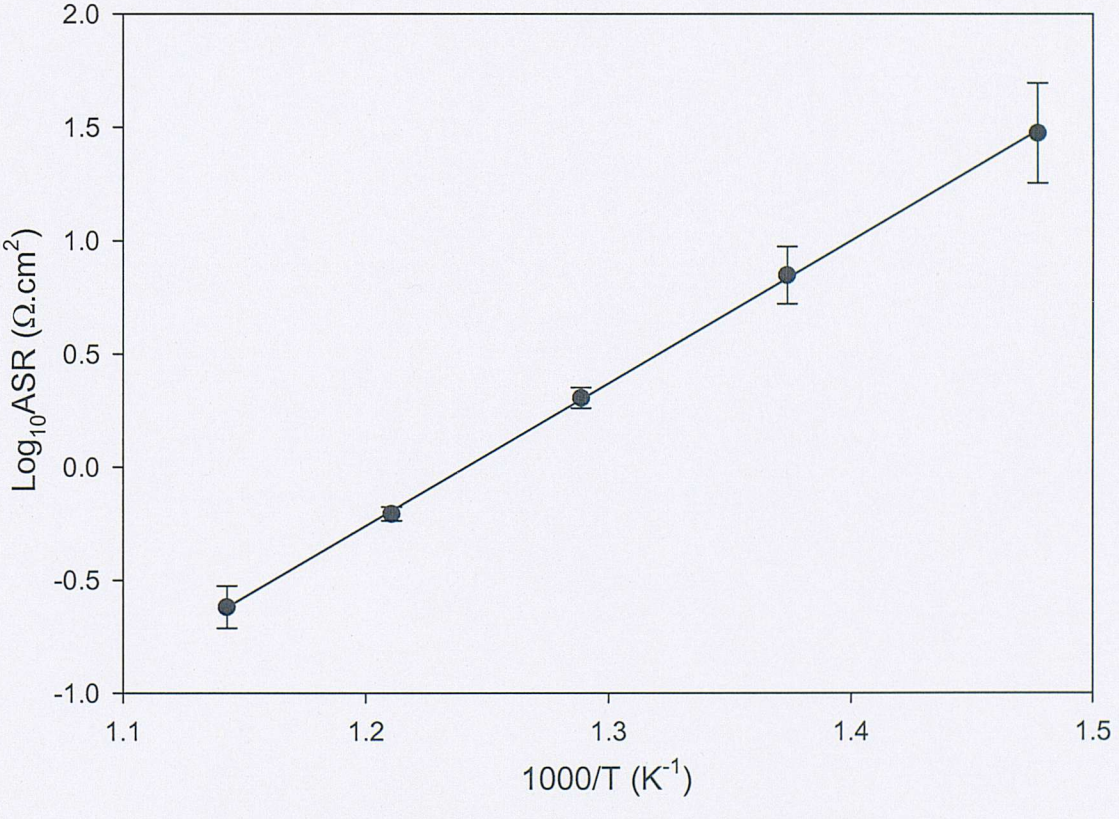
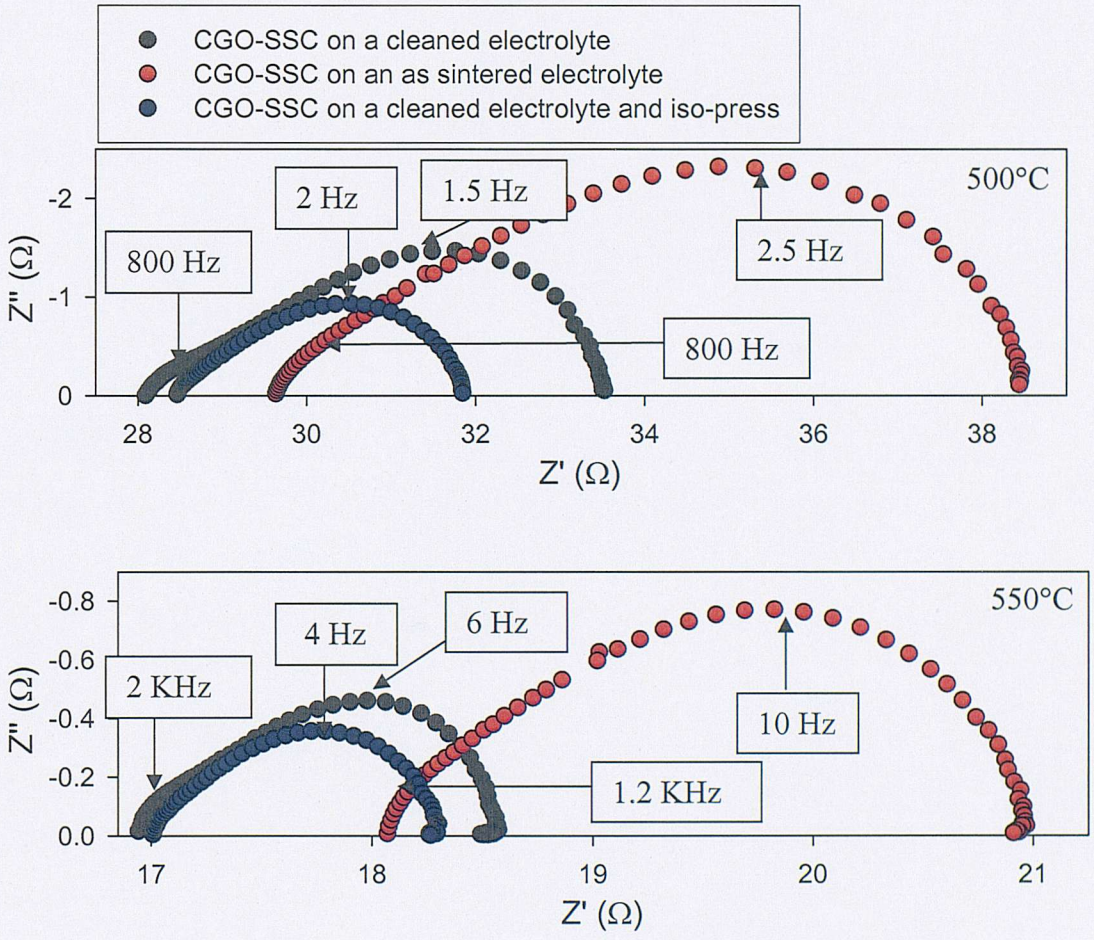


Figure 6.8.15: Arrhenius plot of the CGO20-80/SSC composite cathode on a cleaned CGO10-90 electrolyte

6.8.5.3 CGO/SSC on a cleaned electrolyte and iso-pressed

Figure 6.8.16 shows the AC impedance spectra of CGO20-80/SSC cathode on a cleaned CGO10-90 electrolyte and iso-statically pressed before sintering at 1050°C in air together with the responses of the CGO20-80/SSC on an as sintered and CGO20-80/SSC on a cleaned electrolyte for comparison. Again all three impedance spectra can be resolved into two semicircular arcs using the equivalent circuit of the type LR(RQ)(RQ) in Figure 6.8.11. The offset of the CGO20-80/SSC on cleaned electrolyte and the CGO20-80/SSC on a cleaned electrolyte and iso-statically pressed occur at a similar point, which is slightly lower than the offset of the CGO20-80/SSC on an as sintered electrolyte response.



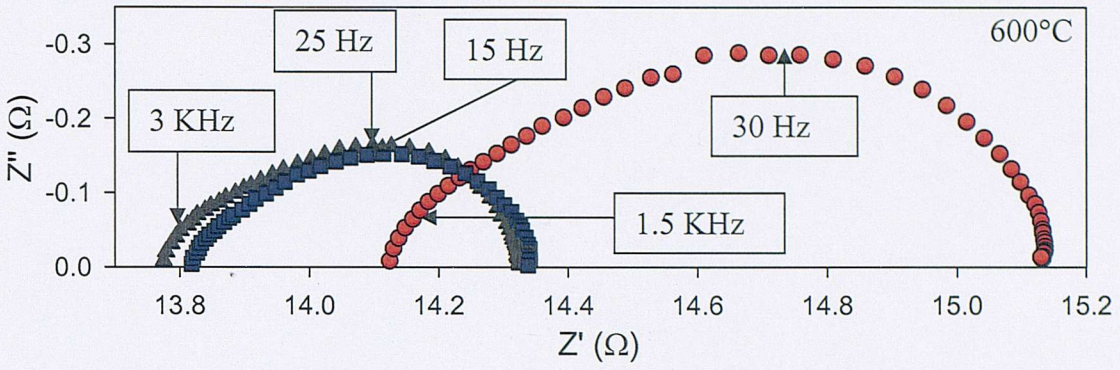


Figure 6.8.16: AC Impedance Spectroscopy spectra of CGO20-80/SSC composite cathode on a cleaned CGO electrolyte and iso-statically pressed

This electrode had respectively at 502°C an ASR of 1.40 $\Omega.cm^2$, 0.53 $\Omega.cm^2$ at 551°C and 0.23 $\Omega.cm^2$ at 599°C. These ASR values are much lower than the any of the values obtained with the other cathodes. This is very close to the target ASR value of 0.1$\Omega.cm^2$ between 500-600°C as can be seen in Table 6.1.6.

	500°C	**550°C**	**600°C**
CGO/GSC on an as sintered electrolyte	3.58 Ωcm^2	1.20 Ωcm^2	0.44 Ωcm^2
CGO/GSC on a cleaned electrolyte	2.02 Ωcm^2	0.64 Ωcm^2	0.24 Ωcm^2
CGO/GSC on a cleaned electrolyte and iso-pressed	1.40 Ωcm^2	0.53 Ωcm^2	0.23 Ωcm^2

Table 6.1.6:- ASR of all the CGO20-80/SSC at various temperatures

The area specific resistance (ASR in $\Omega.cm^2$) in air as a function of reciprocal of temperature for this composite cathode is shown as Arrhenius plot in Figure 6.8.17. The activation energy for CGO20-80/SSC composite cathode is found to be 1.19 ev ±0.15ev.

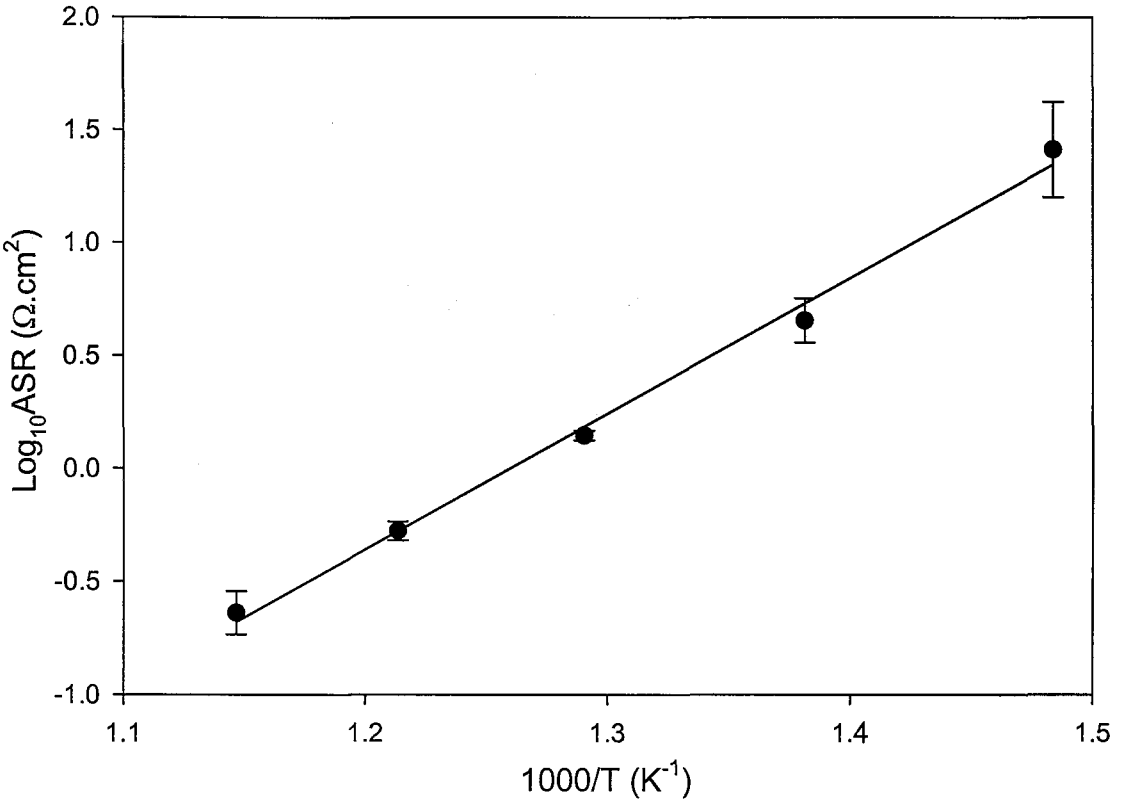


Figure 6.8.17: Arrhenius plot of the CGO20-80/SSC composite cathode on a cleaned CGO10-90 electrolyte and iso-statically pressed

6.8.6 Comparison with Adler's Model

The ALS model has shown evidence that the kinetics of the oxygen reduction in a mixed conductor is dominated by the non-charge transfer oxygen diffusion in the electrode and surface exchange at the electrode/gas interface. The ALS model is not applicable to a composite material as such, however as a first approximation we can assume that the composite behaves macroscopically as a homogeneous single phase mixed conducting material. If the values of the oxygen diffusion coefficient for CGO is taken from Steele et al [15] and the surface exchange coefficient for SSC is taken from the data of Fullarton et al [6] are substituted into the following three equations:

$$R_{chem} = \left[\frac{RT}{2F^2}\right]\sqrt{\frac{\tau}{(1-\varepsilon)aC_o{}^2D^*K}}$$

together with the value of a = 20000 cm^2/cm^3 [15], the porosity (45%) and the tortuosity (estimated at 1.5 from the FIB-SIMS) then a R_{chem} (ASR) values can be generated at

different temperatures. Generated R_{chem} values at different temperatures for CGO/SSC is shown together along with the experimental ASR values of CGO20-80/SSC in Figure 6.8.18. As can be seen the model values at two temperatures are in good agreement with the experimental ASR values of CGO20-80/SSC on a polished electrolyte and iso-statically pressed. The best measured CGO/SSC ASR values of 0.64 $\Omega.cm^2$ at 553°C and 0.23 $\Omega.cm^2$ at 602°C is in good agreement with the predicted values of 0.48 $\Omega.cm^2$ at 550°C and 0.21 $\Omega.cm^2$ at 600°C. However the best measured value of 2.02 $\Omega.cm^2$ at 503.5°C is much higher than the predicted value of 0.87$\Omega.cm^2$ at the same temperature. Therefore, the measured and the predicted values are in good agreement over the temperature range studied.

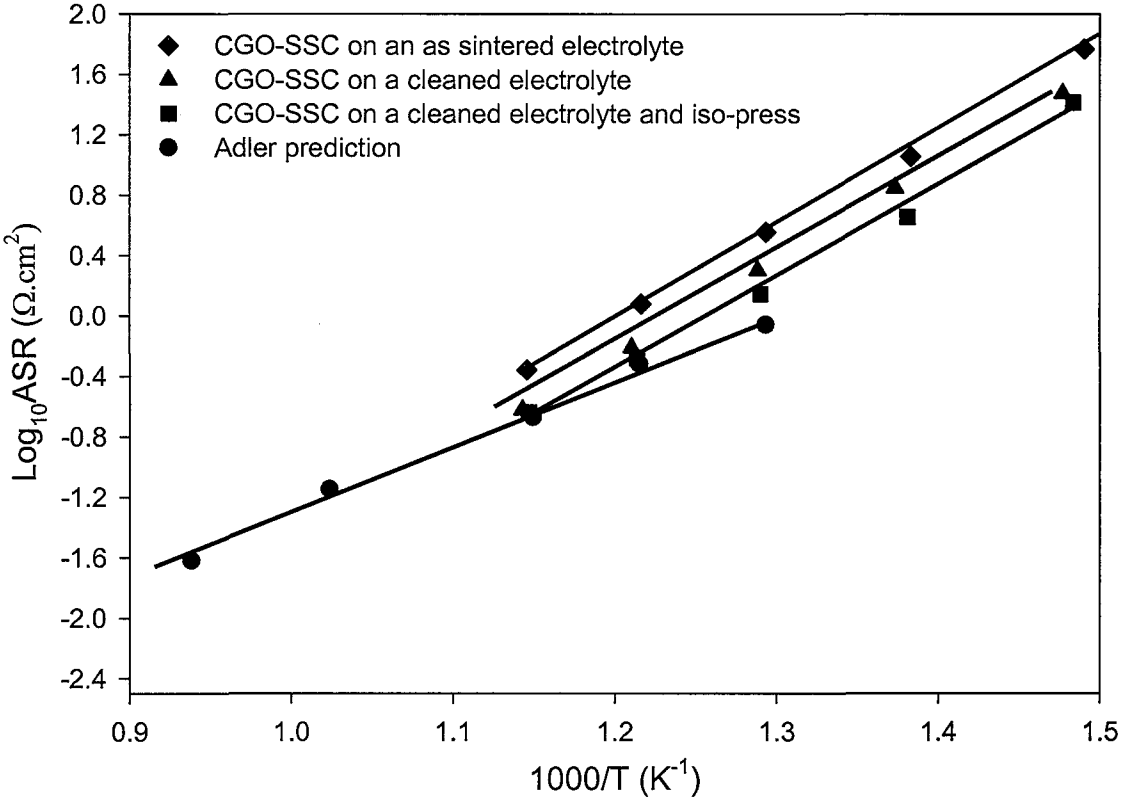


Figure 6.8.18: Comparison of the measured impedance and that predicted by Adler's model

All three CGO20-80/SSC exhibited an activation energy in the range 1.19-1.25 ev ±0.15ev. The activation energy obtained is higher than the model's value (≈ 0.88 ev) and also higher than the activation energy obtained by averaging the diffusion coefficient activation energy of CGO (E_a^{D*} = 0.9 ev) and the surface exchange coefficient activation energy of SSC (E_a^{k} = 0.9 ev).

6.9 References

[1] K. Huang, M. Feng, and J.B. Goodenough, J. Am. Ceram. Soc, (1996), 79 (4), p1100-1104.

[2] I. Reiss, D. Braunshtein, D.S. Tannhauser, J. Am. Ceram. Soc. 64 (1981), p479.

[3] K. Huang, M. Feng, and J.B. Goodenough, J. Am. Ceram. Soc, (1998), 81(2), p357.

[4] J.M. Ralph, Ph.D. Thesis, University of London (1998).

[5] http://www.ccp14.ac.uk/tutorial/lmgp/celref_manual_hkl_peaks.html.

[6] L-W. Tai, M.M. Nasrallah, H.U. Anderson, D.M. Sparlin and S.R. Sehlin, Solid State Ionics, 1995, 76, p259-271.

[7] L-W. Tai, M.M. Nasrallah, H.U. Anderson, D.M. Sparlin and S.R. Sehlin, Solid State Ionics, 1995, 76, p273-283.

[8] N. Hart, PhD thesis in Materials, Brunel University (2001).

[9] S.B. Adler, J.A. Lane and B.C.H Steele, J. Electrochem. Soc., vol 143 (1996), p3554-3564.

[10] V. Dusastre, J.A. Kilner, Solid State Ionics, 126, (1999), p163-174.

[11] A. Esquirol, Ph.D thesis in Materials, Imperial College, London (2003).

[12] E.P. Murray, M.J. Sever and S.A. Barnett, Solid State Ionics, (2002), 148, p27-34.

[13] J-M. Bae, Properties of Selected Oxide Cathodes for Solid Oxide Fuel cell, Ph.D thesis in Materials, Imperial College, London (1996).

[14] J. M. Bae and B.C.H. Steele, Solid State Ionics (1998), 106, p247-255.

[15] B.C.H. Steele, K.M. Hori, S. Uchino, Solid State Ionics (2000), 135, p445-450.

[16] S.J. Benson, R.J. Chater and J.A. Kilner, in proc. of the 3rd Int. Symp. On Ionic and Mixed Conducting Ceramics, Eds. T.A. Ramanarayanan, W.L. Worrel, H.L. Tuller, M. Mogensen and A.C. Khandkar, The Electrochemical Society, Inc., Pennington, NJ, PV 97-24, Paris (1997).

[17] J. D. Sirman, J.A. Lane, and J.A. Kilner, in ionic and mixed conducting ceramics, III (T.A. Ramanarayanan, W.L. Worrell, H.L. Tuller, A.C. Khandkar, M. Mogenson, W. Gopel, Eds., PV 97-24, 57-72, Electrochemical Society, Pennington, 1997).

[18] A. Endo, S. Wada, C. Wen, H. Komiyama, K. Yamada, J. Electrochem. Soc., 145 (1998), pL35-L37.

[19] R.A. De Souza, J.A. Kilner, Solid State Ionics, 106 (1998), p175-187.

[20] J.K. Yamamoto, K. Kata, Y. Shimada, Mater. Lett. 8(8), 1989, p278-282.

[21] D.J. Roth, E.R. Generazio, G.Y. Baaklini, Mater. Eval. 45(8), 1987, p958-966.

[22] D.M. Liu, J. Mater. Sci. Lett. 15, 1996, p419-421.

[23] R.A. Lopes, A.M. Segadaes, Mater. Sci. Eng. A209, 1996, p149-155.

[24] K. Maca, P. Dobsak and A.R. Boccaccini, Ceramic International 27 (2001), p577-584.

[25] S.B. Adler, Solid State Ionics, 111 (1998), p125-134.

[26] J.M. Ralph, J.T. Vaughey and M. Krumpelt, Electrochemical Society Proceedings, 16 (2001), p466.

[27] I.C. Fullarton, J.A. Kilner, B.C.H. Steele and P.H. Middleton, Ionic and Mixed Conducting Ceramics, Second International Symposium, (1994), (Edited by: T.A. Ramanarayanan, W.L. Worrell, H.L. Tuller), p9-26.

[28] N. Sakai, K. Yamaji, T. Horita, Y.P. Xiong, H. Kishimoto and H. Yokowa, Journal of the Electrochemical Society, 150 (6) (2003), A689-A694.

[29] M. Mogensen, K.V. Jensen, M.J. Jogensen and S. Primdahl, Solid State Ionics, 150, (2003), p123-129.

[30] S.J. Benson, D. Waller and J.A. Kilner, Journal of the Electrochemical Society, 146 (4), (1999), p1305-1309.

[31] J.D. Sirman, J.A. Lane and J.A. Kilner in proceedings of Ionic and Mixed Conducting Ceramics III, T.A. Ramanarayanan, W.L. Worrell, H.L. Tuller, A.C. Khandkar, M. Mogensen, W. Gopel, Eds., PV97-24, 57-72, Electrochemical Society, Pennington, (1997).

[32] A. Endo, S. Wada, C. Wen, H. Komiyama, K. Yamada, J. Electrochem. Soc., 145 (1998), L35-L37.

[33] N. Sakai, K. Yamaji, H. Negishi, T. Horita, Y.P. Xiong and H. Yokokawa, Electrochemical Society Proceedings, 16 (2001), p511-516.

[34] R. Doshi, V.L. Richards, J.D. Carter, X. Wang, M. Krumpelt, J. Electrochem. Soc. 146 (1999), p1273.

[35] W. Chen, T. Wen, H. Nie and R. Zheng, Materials Research Bulletin (2003), available online at www.sciencedirect.com, p1-10.

[36] M.B. Phillipps, N.M. Sammes, O. Yamamoto, Solid State Ionics, 123 (1999), p131-138.

[37] L-W. Tai, M.M. Nasrallah, H.U. Anderson, D.M. Sparlin and S.R. Sehlin, Solid State Ionics, (1995), 75, p273-283.

[38] S.J. Benson, D. Waller, J.A. Kilner, J.A. Lane, presented at the 11th Int. Conf. On Solid State Ionics, Honolulu (1997).

[39] S.J. Benson, D. Waller, J.A. Kilner, J. Electrochem. Soc., 146 (1999), p1305-1309.

[40] C. Xia, W. Rauch, F. Chen, M. Liu, Solid State Ionics, 149 (2002), p11-19.

[41] M. Koyama, C-J. Wen, T. Masuyama, J. Otomo, H. Fukunaga, K. Yamada, K. Eguchi and H. Takahashi, Journal of the Electrochemical Society, 148(7), A795-A801 (2001).

7 Summary and Conclusion

This thesis has investigated the performance of the $Ce_{0.8}Gd_{0.2}O_2/La_{0.6}Sr_{0.4}Fe_{0.8}Co_{0.2}O_3$, $Ce_{0.8}Gd_{0.2}O_2/Gd_{0.6}Sr_{0.4}CoO_3$ and $Ce_{0.8}Gd_{0.2}O_2/Sm_{0.5}Sr_{0.5}CoO_3$ composite cathode on a $Ce_{0.9}Gd_{0.1}O_2$ electrolyte at temperatures between 500-600°C. The project aimed at reaching an area specific resistance for the cathode in the order of 0.1 Ωcm^2 or lower between 500-600°C.

In chapter 6, section 6.2 the performance of the CGO/LSCF composite cathode has been studied using an AC impedance spectroscopy. The values of ASR are summarised in table 7.1.

	ASR at 500°C (Ω.cm2)	**ASR at 550°C (Ω.cm2)**	**ASR at 600°C (Ω.cm2)**
CGO/LSCF on an as sintered electrolyte	32.41	12.84	5.37
CGO/LSCF on a cleaned electrolyte	19.56	6.54	2.71
CGO/LSCF on a cleaned electrolyte and iso-pressed	24.86	7.98	3.26

Table 7.1:- ASR values CGO/LSCF

The CGO/LSCF on an as sintered electrolyte had an ASR greater by a factor of 5 at all three temperatures, when compared to the previous work conducted by Kilner and Dusastre **[10]**. However these authors sintered their cathodes at 800°C and 900°C compared to the cathode in the present study where they were sintered at 1050°C. This is because; the initial aim of this project was to co-sinter the whole cell at 1000°C, which will reduce the processing cost. The microstructure of the electrode is very dense and around 23% of porosity is calculated to be in this cathode using Archimedes principle. The very similar microstructure is seen with the CGO/LSCF cathode on a cleaned electrolyte too. The better performance of this cathode when compared to the CGO/LSCF electrode on an as sintered electrolyte is due to the cleaned electrolyte surface. Impurities such as siliceous materials from the furnaces during sintering of the CGO electrolyte can play an important role for the degradation of the electrode property during intermediate temperature measurement. Hence, by cleaning the surface of the electrolyte, the existence of siliceous second phase materials are removed and

effectively improving the performance of the cathode on that electrolyte. The iso-statically pressed cathode should provide a better contact with the electrolyte and ensure a better current collection. However it has compressed the cathode making it denser (the density, calculated using Archimedes principle, is 84%) than the unpressed cathode (density is 77%) and hence the poor performance, when compared to the other cathodes. The activation energy for all three electrodes were calculated to be between 1.22-1.26 ev ±0.1 ev, which indicates that same reaction mechanism controls the overall electrode behaviour in the temperature range studied. The experimental ASR values of CGO20-80/LSCF produced under different conditions were compared to the generated R_{chem} values using the Adler model at different temperatures. At 500°C, the model's ASR prediction of around 50 Ωcm^2 is higher than all the three electrodes, however at around 550°C the CGO20-80/LSCF on an as sintered electrolyte ASR value of 12.83 Ωcm^2 is similar to the data predicted by the model. Finally at around 600°C, the model's predicted ASR value is very similar to the ASR value of CGO20-80/LSCF on a cleaned electrolyte and also to the CGO20-80/LSCF on a cleaned electrolyte and iso-pressed, which is around 3 Ωcm^2. It therefore appears the model developed by Adler et al, is quantitatively in good agreement with experimental ASR values for the electrode morphology used here.

In section 6.3 the LSM material was mixed with CGO/LSCF composite in order to improve the electrical conductivity and hence to improve the performance of the cathode. However it was found to exhibit poor performance with an ASR of 40 $\Omega.cm^2$ at 500°C, 14 $\Omega.cm^2$ at 550°C and 7 $\Omega.cm^2$ at 600°C. The poor performance of this cathode was also due to the dense structure, where there are lack of porosity for the oxygen exchange and diffusion. The activation energy for this composite cathode is found to be 1.11 ev ±0.15, which is lower than the activation energy of CGO/LSCF.

The main drawback for the poor performance of the entire cathode is the lack of porosity. One way to optimise the porosity in a sintered body is to add a pore former and burn them out during sintering. In section 6.4, the addition of PMMA as a pore former to the CGO/LSCF cathode was investigated. Although high percentage of pores with diameter in the range 5-10 μm was found in this sample, these pores are not, however, interconnected which will result in no oxygen penetration through this composite when the fuel cell is in operation.

In section 6.5 CGO/LSCF cathodes with reasonable interconnected porosity (about 40-45%) were fabricated using the carbon pore former. X-ray diffraction data shows that there are no impurity phases in the CGO/LSCF cathode, even after burning out carbon during sintering.

	ASR at 500°C (Ω.cm2)	**ASR at 550°C (Ω.cm2)**	**ASR at 600°C (Ω.cm2)**
CGO/LSCF/C on an as sintered electrolyte	7.34	1.86	0.62
CGO/LSCF/C on a cleaned electrolyte	3.91	0.96	0.33
CGO/LSCF/C on a cleaned electrolyte and iso-pressed	2.33	0.75	0.29

Table 7.2:- ASR values CGO/LSCF/C

These ASR values for the cathodes with a pore former are summarised in table 7.2. The CGO/LSCF/C on an as sintered electrolyte had an ASR, which is very similar to the previous work conducted by Kilner and Dusastre and also Esquirol **[10-11]**. The microstructure of this cathode is very porous, and very similar to the cathode microstructure produced by Kilner and Dusastre, which explains the direct similarity of the ASR values. The ASR values of the CGO/LSCF/C on a cleaned electrolyte are lower (by a factor of 2) than the ASR values obtained for the cathode on an as sintered electrolyte. The same electrode on a clean electrolyte and iso-statically pressed had the ASR than the CGO/LSCF/C on an as sintered electrolyte and cleaned electrolyte. This is because the iso-pressing had made the cathode a better contact with the electrolyte, which should ensure a better current collection and also resulted in an ideal structure with reasonable porosity, where the grains are connected with narrow bottleneck-type bridges. This ASR value is very close to the target ASR of 0.1 $\Omega.cm^2$ at 500°C. The activation energy for all three composite cathodes is calculated to be between 1.47-1.50 ev ± 0.24ev. This activation energy is in agreement with prior studies where activation energies of ~1.4-1.6 ev were reported **[10-12]** and also with activation energy obtained by averaging the surface exchange and diffusion coefficient activation energies of CGO/LSCF (1.56 ev) **[11]**. These results were compared to the Adler model and are in good agreement over the entire temperature range.

The effect of water on the performance of the CGO/LSCF cathode was investigated in section 6.6. Some literature **[30]** stated that an improvement of the oxygen surface exchange coefficient was observed in the presence of the water, although the oxygen diffusivity remained the same. The AC impedance spectroscopy results obtained from the porous cathode were not in agreement with this finding. The ASR of the CGO/LSCF cathode in dry atmosphere was found to be around 6.88 $\Omega.cm^2$ at 508°C, 1.71 $\Omega.cm^2$ at 556°C and 0.63 $\Omega.cm^2$ at 605°C. The ASR of this cathode, however in wet atmosphere was found to be higher with values of 8.12 $\Omega.cm^2$ at 507°C, 2.03 $\Omega.cm^2$ at 555°C and 0.74 $\Omega.cm^2$ at 601°C. The above results show that between 500-600°C, the ASR in wet atmosphere is higher than that of in dry atmosphere. But below 500°C the ASR of this composite cathode is lower (138.38 $\Omega.cm^2$ at 404°C and 35.37 $\Omega.cm^2$ at 455°C) than that in dry atmosphere (182.18 $\Omega.cm^2$ at 405°C and 36.82 $\Omega.cm^2$ at 454°C).

In section 6.7 the performance of the CGO/GSC was investigated. Unlike CGO20-80/LSCF, CGO20-80/GSC did not need a pore former to enhance porosity. The ASR for the CGO-GSC composite cathode as a function of weight percent of the mixed conducting phase presented a clear minimum at 70% by weight of GSC. The performance of the CGO/SSC cathode is investigated in section 6.8. The $Sm_{0.5}Sr_{0.5}CoO_3$ (SSC) powders were prepared by glycine-nitrate method. Again unlike CGO20-80/LSCF, CGO20-80/SSC also did not need a pore former to enhance porosity. An ideal microstructure with reasonable porosity (around 40%) and the grains are connected with narrow bottleneck-type bridges were obtained with the CGO/GSC and the CGO/SSC cathode.

The ASR values for both these cathodes at 500, 550 and 600°C are summarised in table 7.3. The CGO/GSC ASR values are very similar to those of CGO/LSCF/carbon conducted under the same conditions, however the ASR values of CGO/SSC are slightly lower than those of CGO/LSCF/C and CGO/GSC cathodes. This is because the SSC had the highest oxygen diffusion coefficient and oxygen surface exchange coefficient when compared to LSCF. The activation energy for all three CGO20-80/GSC composite cathodes is found to be between 1.05-1.09 ev ±0.18ev. The experimental ASR values were compared to the generated results from the Adler's model. The experimental and calculated results were very similar, suggesting that the model provides an accurate description of the electrode behaviour.

The ASR value obtained at 600°C for CGO/SSC cathode on a cleaned electrolyte and iso-statically pressed is very close to the target ASR value of 0.1 $\Omega.cm^2$ between 500-600°C and the ASR values obtained with this cathode is the lowest ever reported at 500, 550 and 600°C. The activation energy for all three CGO20-80/SSC composite cathodes is found to be between 1.19-1.25ev ±0.15ev. These results were compared to the generated results from the Adler's model and are quantitatively in good agreement over the entire temperature range studied.

	ASR at 500°C (Ω.cm2)	**ASR at 550°C (Ω.cm2)**	**ASR at 600°C (Ω.cm2)**
CGO/GSC on an as sintered electrolyte	4.18	1.77	0.74
CGO/GSC on a cleaned electrolyte	3.47	1.29	0.56
CGO/GSC on a cleaned electrolyte and iso-pressed	2.02	0.88	0.33
CGO/SSC on an as sintered electrolyte	3.58	1.20	0.44
CGO/SSC on a cleaned electrolyte	2.02	0.64	0.24
CGO/SSC on a cleaned electrolyte and iso-pressed	1.40	0.53	0.23

Table 7.3:- ASR values CGO/GSC and CGO/SSC

The best ASR results for each of the composite material studied in this thesis are summarised as Arrhenius plot in Figure 7.1. From the results we can conclude that, the most important factor, which affects the cathode polarization resistance is the oxygen diffusion coefficient and the oxygen surface exchange coefficient. The microstructural parameters, including tortuosity and porosity also make a minor contribution to the cathode polarization resistance.

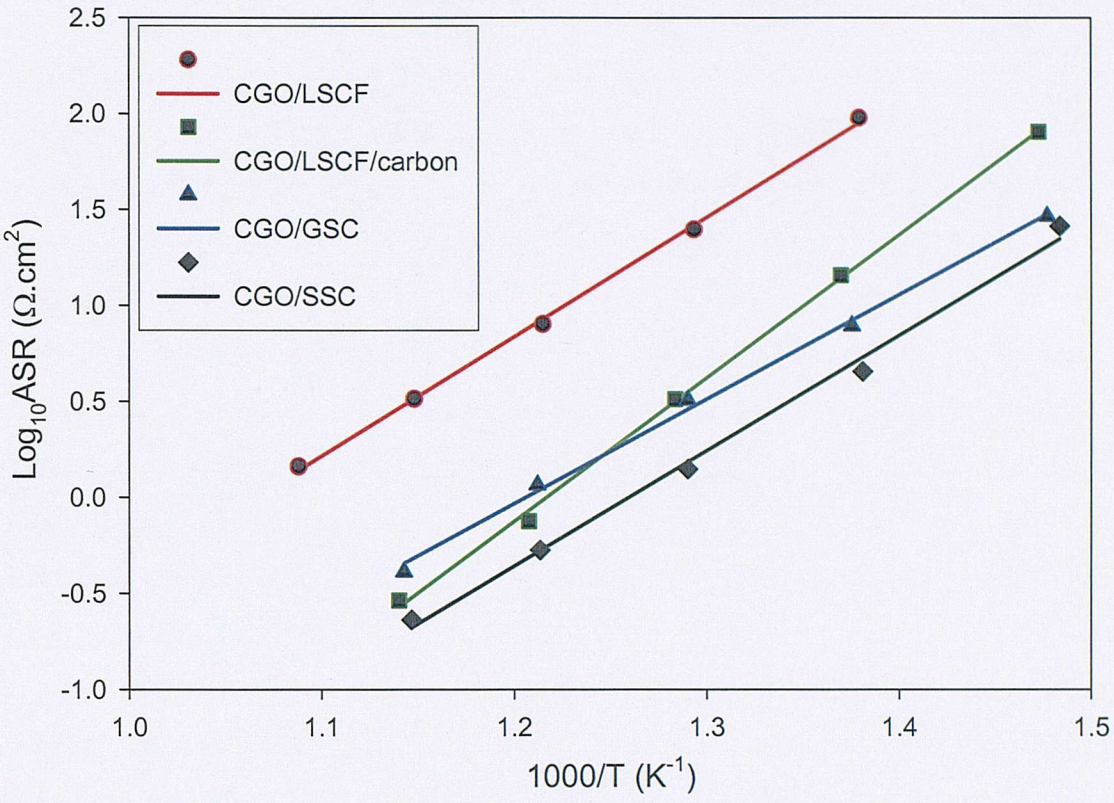


Figure 7.1:- Arrhenius plot of CGO/LSCF, CGO/LSCF/C, CGO/GSC and CGO/SSC composite cathodes

8 Suggestions for Future Work

The three composite cathode materials studied in this thesis are found suitable for use in intermediate temperature SOFC. Alternate fabrication process (screen printing/tape casting) for preparing thin cathode structure with adequate porosity (30-40%) on densified electrolyte substrate is to be standardised for used in ITSOFC.

Further experiments could be performed in order to calculate the microstructural parameters accurately. The porosity of the cathode on an electrolyte could not be measured, because it was too thin. In addition, tortuosity was estimated from the FIB-SIMS image, hence an alternative method needs to be found to measure these parameters. Using these more accurate measurements, more precise R_{chem} values can be obtained using the Adler model.

Further exchange measurements should be carried out in order to verify the surface exchange coefficient and tracer diffusion coefficient for the CGO20-80/GSC and CGO20-80/SSC composite cathode. This would enable us to gain a better understanding of oxygen diffusion within the material.

AC impedance needs to be performed on different CGO20-80/SSC compositions in order to find the optimum composition with the lowest area specific resistance.

Another task for future work would be to study the long-term effect of these cathodes. This then could be set up with the electrolyte, anode and interconnect after which the cell could be performance tested.